

Numerical Studies of Inertial Particles in Turbulence and Buoyancy-Driven Bubbly Flows



Vikash Pandey

Numerical Studies of Inertial Particles in Turbulence and Buoyancy-driven Bubbly Flows

A thesis

Submitted to the
Tata Institute of Fundamental Research, Mumbai
for the degree of
Doctorate of Philosophy in physics

by

Vikash Pandey



TATA INSTITUTE OF FUNDAMENTAL RESEARCH
TIFR CENTER FOR INTERDISCIPLINARY SCIENCES

Hyderabad, India

August, 2021

埼玉へ

Publications

1. Vikash Pandey, Prasad Perlekar, and Dhrubaditya Mitra, “Clustering and energy spectra in two-dimensional dusty gas turbulence”, In: Phys. Rev. E, **100**, 013114, 2019. Selected as Editor’s suggestion.
2. Vikash Pandey, Rashmi Ramadugu, and Prasad Perlekar, “Liquid velocity fluctuations and energy spectra in three-dimensional buoyancy-driven bubbly flows”, In: J. Fluid Mech., **884**, R6, 2019.
3. Jan Meibohm, Vikash Pandey, Akshay Bhatnagar, Kristian Gustavsson, Dhrubaditya Mitra, Prasad Perlekar, B. Mehlig, “Paths to caustic formation in turbulent aerosols”, In: Phys. Rev. Fluids, **6**, L062302, 2021
4. Vikash Pandey, Dhrubaditya Mitra, and Prasad Perlekar, “Turbulence modulation by large weakly buoyant bubbles”, In: arXiv:2105.04812, 2021
5. Rashmi Ramadugu, Vikash Pandey, and Prasad Perlekar “Pseudo-turbulence in two-dimensional buoyancy-driven bubbly flows: A DNS study”, In: Eur. Phys. J. E **43** (11) 73 (2020).

Acknowledgements

The work presented in this thesis took almost four years to complete and would not have been possible without my supervisor Prasad. I thank him for all the trust and belief he showed in me, and all the fruitful discussions. During Ph.D. only the successful outcomes counts, but underneath lies uncountable hypotheses and theories that fails. I express my gratitude to the supervisor for all the extended support during all the failures and making Ph.D. interesting. I would like to acknowledge my collaborator Dhrubaditya for all the physics discussions and being critical of all the mistakes I have made. I thank my other collaborators Navdeep, Rashmi, Gaurav, Jan, Akshay, for all the help and interesting discussions. Finally, I thank my thesis monitoring committee Rama, and Smarajit for all scientific discussions.

The time spent here at TIFR has been long, and I have been fortunate to meet many people here. I thank Hari Dass, Madhu, Mustansir, Sriram, Surajit, Rama, Smarajit, Subha, M. Krishnamurty, Raji, Aprotim for all the interesting lectures and discussions. I especially would like to extend my gratitude to Raji for all the tasty meals she made for us during festivals. I carried out one of my MS project with Smarajit, where where studied the dynamics of a mixture of rod and sphere using Molecular Dynamics (MD). I thank him for being patient and teaching me MD. Finally I thank Kabir for all the interesting discussions over coffee in the canteen.

I received lot support from my seniors during the time I joined Tifr-Hyderabad. I express my gratitude to Jose (the zen-master) for all the interesting discussions on Manga and movies. I would also like to thank Harsh, Croor, Rayan for the support. I acknowledge all my friends, Rajsekhar, Pappu, Pankaj,

Navdeep, Bhanu, Nikita, Kesavan, Mrinmoy, Indrajit, Samashree, Debankur, Sumit, Mukul, Aditya, Bharti, SV Rahul, Gupta, Archit, Lokrishi, Saptarishi, Sumit Birwa, Ganga, Anusheela, Maiti, Abhijeet, Kallol, JK for making the stay in Tifr-Hyderabad fun and interesting. Especial thanks goes to Nikita for being there always for me during all the happy and not so happy moments. The vibrant culture in TIFR-Hyderabad allows for people of different disciplines to work under a single roof. In the process, I had the opportunity to meet people of different fields.

As I sit here at TIFR-Hyderabad, typing this acknowledgment to finish the thesis, I realize almost (or nearly) half of my life has been spent. It has been a long journey, so long that the starting point almost feels like dark (at least iron) ages. There have been a lot of people who have influenced me to pursue a Ph.D. I have tried my best to thank all the people who have helped me throughout. I apologize if anyone has been missed.

After a very long thought, I realize that many memories from the beginning, very-beginning, have faded. Of course, the most influential people then (and even now) are my parents. They supported me throughout my life till here (I guess they will do so in the future as well), and hence I would like to express my gratitude towards them. Next, I would like to thank my sibling Bhumika and immediate cousins Shailesh, Yunita, and Monica for all the discussions I could have with them, which otherwise was impossible with parents. Finally, I thank all my school teachers for nurturing the researcher (not there yet) in me during the early days. I have lost contact from almost all my school and college friends and only a handful remain. I thank Nayan, Dependra, Sandeep and Amir for making my stay at home fun.

Finally, I would like to thank the funding agency and the computational facility at Tifr-Hyderabad, without which this work would be impossible. I extend my thank to all the TIFR-family as well. This acknowledgment has been long and therefore, I thank the reader for patiently reading it.

Contents

Publications	iii
Acknowledgements	v
1 Introduction	1
1.1 Turbulence	3
1.1.1 Kolmogorov’s theory of turbulence	6
1.1.2 Multifractal model	8
1.1.3 Energy spectra and transfer functions in the spectral space	10
1.1.4 Two-dimensional turbulence	11
1.2 Multiphase flows	12
1.2.1 Caustics in turbulent flow	14
1.2.2 Dusty gas turbulence	14
1.2.3 Buoyancy-driven bubbly flows	15
1.3 A guide to the thesis	22
References	24
2 Numerical methods for multiphase flows	31
2.1 Introduction	31
2.2 Single phase flow	33
2.2.1 Pseudo-spectral solver	33
2.2.2 The nonlinear term and the aliasing error	34
2.2.3 Two-dimensions	35

2.3	One- and two-way coupling	36
2.3.1	Test case	38
2.4	Buoyancy-driven bubbly flows	40
2.4.1	Non-dimensional numbers	40
2.4.2	Boussinesq approximation	41
2.4.3	Front-tracking (FT)	41
2.5	PARIS	45
2.6	Test Cases	46
2.6.1	Method-1	47
2.6.2	Method-2	51
2.6.3	Bubble shape and the Reynolds number	54
2.6.4	Two-dimensional test	56
2.6.5	Multiple bubbles	58
2.7	Conclusion	60
	References	62
3	Caustics in turbulent flow	65
3.1	Introduction	65
3.2	Model	66
3.3	Simulation details	69
3.4	Rate of caustics formation	74
3.5	Statistical properties of \mathbb{Z} and \mathbb{A}	76
3.6	Path to caustics formation	79
3.7	Conclusion	84
	References	86
4	Clustering and energy spectra in dusty-gas turbulence	89
4.1	Introduction	89
4.2	Simulation details	91
4.3	Clustering	96
4.4	Energy spectra	97
4.5	Enstrophy budget	100
4.6	Conclusion	105

References	108
5 Statistical properties of pseudo-turbulence generated by buoyancy-driven bubbly flows	111
5.1 Introduction	111
5.2 Model and simulation details	113
5.3 Single bubble dynamics	114
5.4 Bubbles suspension	116
5.5 Total kinetic energy	118
5.6 Liquid and bubble velocity fluctuations	120
5.6.1 Probability distribution of the liquid velocity	120
5.6.2 Probability distribution of the bubble velocity	122
5.7 Energy spectra and scale-by-scale budget	125
5.7.1 Energy spectra	125
5.7.2 Scale-by-scale energy budget	125
5.7.3 Low At (runs R1 – R4)	127
5.7.4 High At (runs R5 – R7)	131
5.7.5 Frequency spectrum of pseudo-turbulence	132
5.8 Length scales of pseudo-turbulence	133
5.9 Clustering of bubbles	134
5.10 Topological properties of fluid	137
5.11 Conclusion	140
References	142
6 Turbulence modulation by large buoyant bubbles	147
6.1 Introduction	147
6.2 Numerical Simulations	149
6.3 Results	150
6.3.1 Bubble trajectories and rise velocity	152
6.3.2 Liquid velocity fluctuations	156
6.3.3 Energy spectrum and flux	157
6.4 Conclusion	160
References	162

7 Conclusion	165
References	168

Introduction

‘Multiphase flows’ where particles of a different phase are dispersed in a fluid medium are observed in many human-made and natural processes. A few common examples are (1) ‘Aeolian’ process, or the transport of dust, sand, etc., by the wind [1]. An example of such a process that occurs in the Saharan desert is shown in Fig. 1.1 [2]. (2) Bubble column reactors (Fig. 1.2), used in industrial processes to carry out controlled gas-liquid reactions [3]. In other applications, the bubbles are also used to mix the fluid in a cost-efficient way compared to mechanical stirring. (3) An extraordinary example of bubbly flows is observed during hunting by the humpback whales. This hunting process is depicted in the fourth episode of the “Netflix” series “*Our Planet*” by Sir David Attenborough [4]¹.

The multiphase flows are diverse and depending on the thermodynamic state (solid, liquid or gas) of the phases, it can be broadly classified into the following categories [5]:

1. Gas-solid flows (dust in storms),
2. Gas-liquid flows (rains drops in atmosphere, boiling),

¹To quote Sir Attenborough from the episode, “*These whales have a remarkable way of collecting the bounty. They work as a team; the lead whale dive first and blows a curtain of bubbles to concentrate the fish. A [whale] call synchronizes the attack. By coordinating this way, each whale can eat up to a ton of fish a day.*”

3. Liquid-liquid flows (oil-water mixture),
4. Liquid-solid flows (mudflows),
5. Gas-liquid-solid flows (fluidized bed).

Further division based on the geometric property of the dispersed phase, its size distribution, concentration, etc., are also possible. These classifications are board and does not imply that each category can be studied separately [5]. For instance, the mist, a mixture of tiny droplets in the air which falls under gas-liquid category, shares many similar features with pollutants dispersed in the atmosphere – a gas-solid mixture.

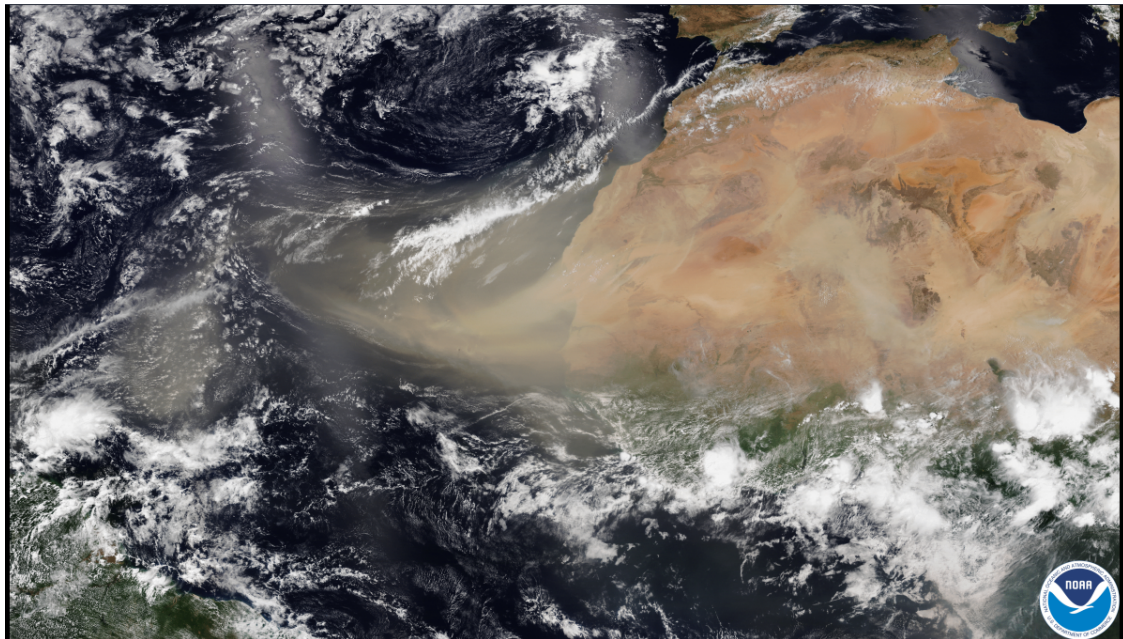


Figure 1.1: Satellite image of the Saharan dust plumes carried by trade winds. Image by National Oceanic and Atmospheric Administration [2].

A common feature, that can be observed in all the discussed examples of multiphase flows is that the background flow is, almost always, turbulent. Turbulence is characterized by the presence of the flow structures of all scales [6, 7]. The presence of a dispersed phase is known to alter the statistical properties of turbulence dramatically. For instance, as noted above, the swarm of bubbles rising in a turbulent flow enhances mixing [8–10].

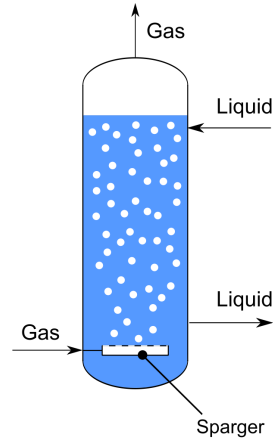


Figure 1.2: A schematic diagram of the bubble column reactor. The gas bubbles are pumped through sparger at the bottom of the tube to carry out gas-fluid reactions. Image taken from Wikipedia [11, 12].

In this thesis, we use direct numerical simulations to study: (i) Particle-laden turbulent flow where the particle size is minuscule compared to the smallest eddy. (ii) Statistical properties of buoyancy-driven bubbly flows, where the size of bubbles are comparable to a typical eddy.

The rest of this chapter is organized as follows: We begin by briefly introducing the single phase turbulence in [Sec. 1.1](#). In [Sec. 1.2](#), we will discuss the specific multiphase flows of our interest and review the important results from the earlier studies. In the last [Sec. 1.3](#), we give a brief outline of all the chapters in this thesis.

1.1 Turbulence

The Navier-Stokes equations [7, 13, 14] which describes the motion of fluids are,

$$\partial_t \mathbf{u} + \mathbf{u} \cdot \nabla \mathbf{u} = -\nabla p + \nu \nabla^2 \mathbf{u} + \mathbf{f}, \quad (1.1)$$

$$\nabla \cdot \mathbf{u} = 0, \quad (1.2)$$

where \mathbf{u} is the velocity field, p is the pressure, ν is the kinematic viscosity, \mathbf{f} is the external force, and [1.2](#) gives the incompressibility condition. We assume

that the density $\rho = 1$ in Eq. 1.1. The Navier-Stokes equations are symmetric under following transformations [7, 14].

- Space and time translations; $\mathbf{u}(\mathbf{x}, t) \rightarrow \mathbf{u}(\mathbf{x} + \mathbf{r}, t)$ and $\mathbf{u}(\mathbf{x}, t) \rightarrow \mathbf{u}(\mathbf{x}, t + T)$
- Gallilean transformation; $\mathbf{u}(\mathbf{x}, t) \rightarrow \mathbf{u}(\mathbf{x} + \mathbf{U}t, t) + \mathbf{U}$
- Parity; $\mathbf{u}(\mathbf{x}, t) \rightarrow -\mathbf{u}(-\mathbf{x}, t)$
- Rotation; $\mathbf{u}(\mathbf{x}, t) \rightarrow \mathbf{A}\mathbf{u}(\mathbf{A}\mathbf{x}, t)$ $\mathbf{A} \in \text{SO}(n)$ ($\text{SO}(n)$ are the rotational group.)
- Scaling; $\mathbf{u}(\mathbf{x}, t) \rightarrow \gamma^h \mathbf{u}(\gamma \mathbf{x}, \gamma^{1-h} t)$, where γ is any positive real number and h is any real number.

In the inviscid unforced limit, 1.1 gives,

$$\begin{aligned} \frac{1}{2} \partial_t \langle u^2 \rangle &= 0, \\ \frac{1}{2} \partial_t \langle \mathbf{u} \cdot \boldsymbol{\omega} \rangle &= 0, \end{aligned}$$

where $E = \frac{1}{2} \langle \rho u^2 \rangle$, the total kinetic energy, and $H = \frac{1}{2} \langle \mathbf{u} \cdot \boldsymbol{\omega} \rangle$, the total helicity are the constants of motion. Here $\boldsymbol{\omega} = \nabla \times \mathbf{u}$ is the vorticity and $\langle \cdot \rangle$ represents averaging over space and time. At finite non-zero viscosity the energy gets dissipated at a rate $\epsilon_v = \nu \langle |\nabla \mathbf{u}|^2 \rangle$.

The fluid motion as described by 1.1 and 1.2 can have different flow regimes; laminar and turbulent. This was first demonstrated by Reynolds [15] in an experiment of water flowing through a cylindrical pipe. Reynolds [15] observed that upon increasing the ‘Reynolds number’,

$$\text{Re} = \frac{u_a d_{\text{pipe}}}{\nu}, \quad (1.3)$$

a laminar flow become turbulent. In 1.3, d_{pipe} is the diameter of pipe, and u_a is velocity of the flow at inlet.

In fluid mechanics photographs or images are often used to describe different flow regimes. The best snapshots of the fluid flows can be found in ‘An Album of Fluid Motion’ by Dyke [16], and Refs. [17, 18]. Here, we shall use the images taken from Refs. [18, 19] to describe the laminar and turbulent flows. We show the snapshot of the flow, obtained using coloring dye, behind bluff bodies in Fig. 1.3. These dye follow the streaklines, which indicates the direction of flow [19].

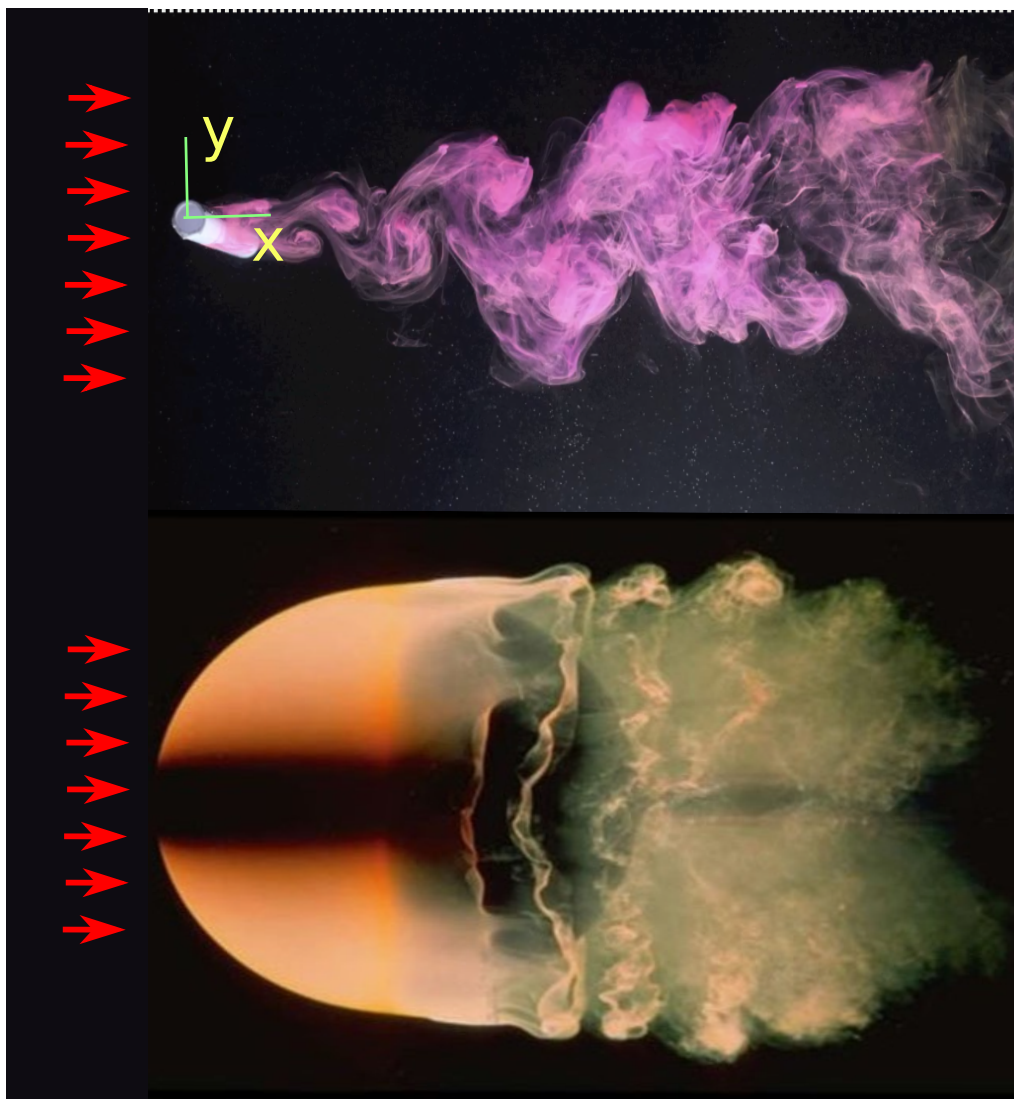


Figure 1.3: The turbulent flow behind a cylinder and a spherical body. The red arrows indicates the direction of flow. Image taken from Ref. [12, 18–20].

Let us first consider the flow behind a cylinder at $Re = 485$ as shown in Fig. 1.3 (top). We choose a coordinate system where, the origin coincides with the center of the cylinder. As we move towards $x < 0$ (or region towards the left of the cylinder), the streamlines are expected to be parallel indicating a laminar flow. In this region all the symmetries of Navier-Stokes equations will be satisfied. Now consider the flow at $x > 0$ (towards the right). Here we observe Von-Karman vortices initially which transition into random and chaotic motion. This random or chaotic fluid motion is also known as turbulence. One can easily distinguish the top ($y > 0$) from the bottom ($y < 0$); thus, the top-bottom symmetry no longer exists. We can also see large swirling

motions or eddies along the edge of the wake but, as we move towards $y = 0$, line one can observe the eddies of smaller sizes as well. A similar observation can be made for the flow behind sphere in Fig. 1.3 (bottom).

Based on these observations, turbulence can be defined as a random and chaotic fluid motion where individual flow realizations are statistically similar [14, 21]. Thus, this field is often studied using a statistical description with the assumptions of homogeneity and isotropy [21–24]. These assumptions implies that the statistical properties of a turbulent flow are invariant under translation and rotation. As a consequence of homogeneity and isotropy all the moments of longitudinal velocity increment,

$$\delta u_{||}(\ell) \equiv [\mathbf{u}(\mathbf{x} + \ell \hat{\mathbf{e}}_\ell) - \mathbf{u}(\mathbf{x})] \cdot \hat{\mathbf{e}}_\ell, \quad (1.4)$$

is a function of ℓ only. In 1.4, \mathbf{x} and $\mathbf{x} + \ell \hat{\mathbf{e}}_\ell$ are the position vectors. The moments of $\delta u_{||}(\ell)$ are known as the structure functions, $S_p(\ell) = \langle [\delta u_{||}(\ell)]^p \rangle$.

1.1.1 Kolmogorov's theory of turbulence

In a series of papers [25–27], Kolmogorov put forward two similarity hypotheses that has been the basis for understanding turbulent flow properties. Here we list both the hypothesis and discuss their consequences.

Kolmogorov's first similarity hypothesis states that “the statistical property of small scale turbulent structure is universal and determined uniquely by ν and ϵ_v .” The first postulate allows us to construct the following scales of the turbulent motion, solely from ν and ϵ_v [7]:

$$\text{Kolmogorov length scale } \eta = \left(\frac{\nu^3}{\epsilon_v} \right)^{1/4}, \quad (1.5)$$

$$\text{Kolmogorov time scale } \tau_\eta = \left(\frac{\nu}{\epsilon_v} \right)^{1/2}, \text{ and} \quad (1.6)$$

$$\text{velocity scale } u_\eta = (\nu \epsilon_v)^{1/4}. \quad (1.7)$$

The Kolmogorov [25] second similarity hypothesis states that; “In every turbulent flow at sufficiently high Reynolds number, the statistics of the motions

of scale ℓ in the range $\ell_0 \gg \ell \gg \eta$ have a universal form that is uniquely determined by ϵ_ν and is independent of ν ." Here, ℓ_0 is the large integral length scale or the forcing scale.

The range $\ell_0 \gg \ell \gg \eta$ is also known as the ‘inertial range’. Since the statistical properties of the turbulence in the inertial range depends only on ϵ_ν , a simple dimensional analysis gives,

$$S_2(\ell) \sim \epsilon_\nu^{2/3} \ell^{2/3}. \quad (1.8)$$

The same scaling in S_2 is observed in the experiments and numerical studies on homogeneous and isotropic turbulence [7, 28].

Here, it is worth noting the Richardson cascade [29] picture that describes Kolmogorov’s hypothesis. It states that the energy injected at scale ℓ_0 gets transferred to dissipative scale η via a self-similar breakdown of eddies. The schematic of the Richardson cascade, depicting the different scales of turbulent motion, is shown below in Fig. 1.4.

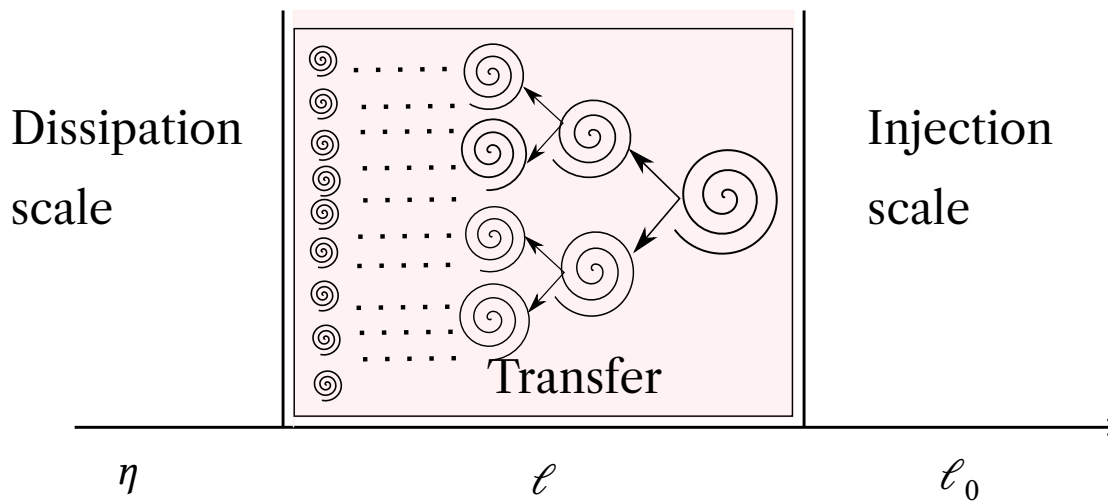


Figure 1.4: The different length scales of turbulent flow. In the inertial range, the energy is transferred to small scales by the breakdown of eddies (shown as spirals). The process continues till the size of each eddy is comparable to η , where the energy gets dissipated.

Although the 1.8 is derived using the dimensional arguments, Kolmogorov from his second similarity hypothesis and using Karman and Howarth [30] equation was able to derive an exact relation for the third order structure

function,

$$S_3(\ell) = \frac{4}{5}\epsilon_v\ell. \quad (1.9)$$

1.1.2 Multifractal model

Kolmogorov theory assumes that a turbulent flow is self similar which implies that the structure function of order n scales according to,

$$S_n(\ell) \sim \ell^{\zeta_n}, \quad (1.10)$$

where the exponent ζ_n satisfies,

$$\zeta_n = nh, \quad \text{and, } h = 1/3. \quad (1.11)$$

Later studies [31–34] have found that this relation does not hold (except for $n = 3$) and has large deviations specially at large n . In Fig. 1.5, we show a representative snapshot of $|\omega|$ and the exponent ζ_n versus n upto $n \leq 6$. Clearly $\zeta_n \neq n/3$ and the Kolmogorov theory needs modifications.

The simple assumption of self-similarity breaks because turbulent flow is ‘intermittent’ and multifractal [14, 35, 36]. This leads to corrections in the scaling exponents of the structure functions. Using a multifractal model Parisi and Frisch [37] showed that,

$$\zeta_n = \inf_n [nh + 3 - D(h)], \quad (1.12)$$

where $D(h)$ is the fractal dimension.

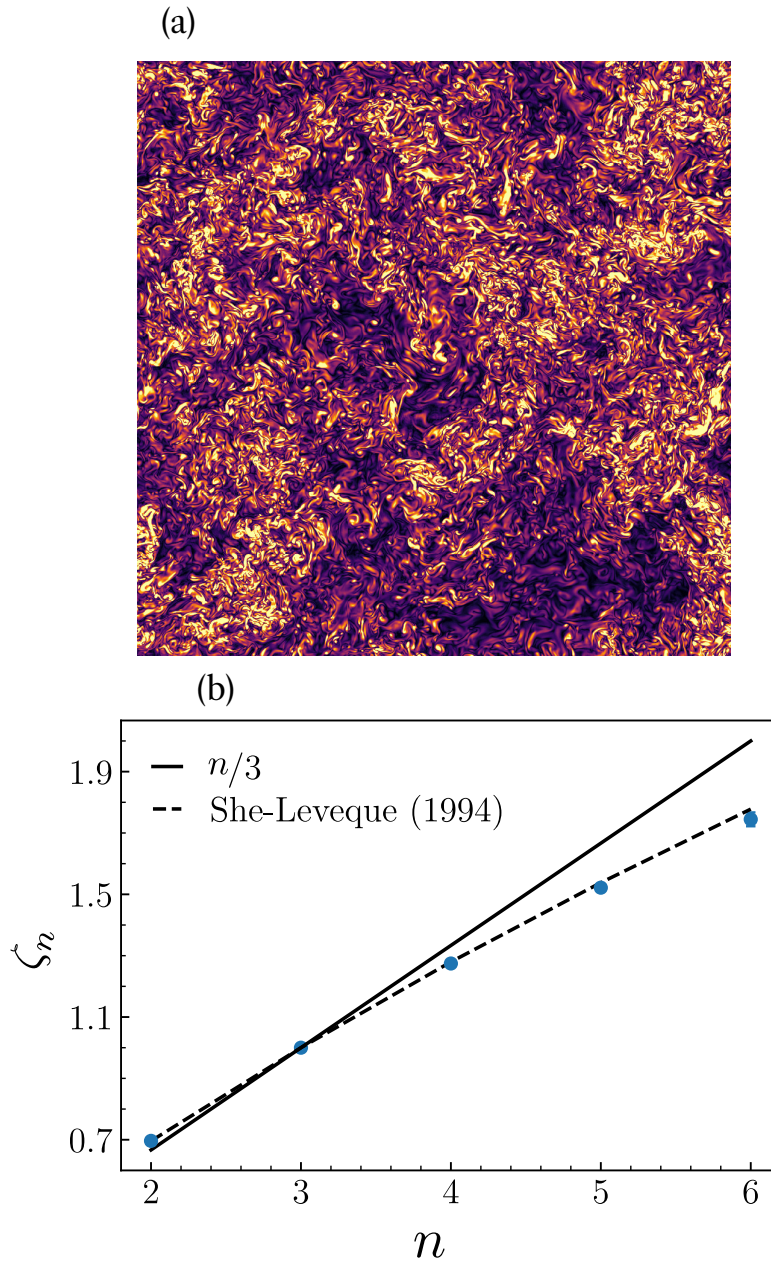


Figure 1.5: (a) Representative pseudo-color plot of the vorticity $|\omega|$ and (b) the plot of ζ_n vs. n obtained from the numerical simulation of turbulence in 1024^3 grids (JHU turbulence database [38]). In (a) the bright color represents region of intense vorticity. In (b) the black continuous line shows the Kolmogorov relation and the black dashed line shows the She and Leveque [34] relation for ζ_n .

1.1.3 Energy spectra and transfer functions in the spectral space

The study of turbulent flow in the Fourier instead of physical space has seen much success [7, 14]. Here we shall introduce some of the key concepts which are extensively used in this thesis. We first define the Fourier amplitudes of the velocity field,

$$\mathbf{u}_{\mathbf{k}} = \int \exp(i\mathbf{k} \cdot \mathbf{x}) \mathbf{u}(\mathbf{x}) d\mathbf{x}. \quad (1.13)$$

The kinetic energy spectrum $[E(k)]$ is defined using the velocity field in the Fourier space,

$$E(k) = \frac{1}{2} \int d\mathbf{k} |u_{\mathbf{k}}|^2 \delta(|\mathbf{k}| - k). \quad (1.14)$$

In spectral-space Kolmogorov's second similarity hypothesis implies that the kinetic energy spectra,

$$E(k) \sim \epsilon_v^{2/3} k^{-5/3}, \quad (1.15)$$

in the inertial range. The above 1.15 gives the distribution of the turbulent kinetic energy among the eddies of size $\ell = 2\pi/k$. In Fig. 1.6(a) we show a representative kinetic energy spectrum for homogeneous and isotropic turbulent flow and mark the 5/3 scaling range. The scaling in energy spectra can be understood using the energy transfer relation. Using 1.1, we write the Navier-Stokes equation for the Fourier amplitude $\mathbf{u}_{\mathbf{k}}$,

$$\partial_t \mathbf{u}_{\mathbf{k}} + [\mathbf{u} \cdot \nabla \mathbf{u}]_{\mathbf{k}} = -ikp_{\mathbf{k}} - \nu k^2 \mathbf{u}_{\mathbf{k}} + \mathbf{f}_{\mathbf{k}}. \quad (1.16)$$

Taking a scalar product of Eq. 1.16 with $\mathbf{u}_{\mathbf{k}}$ and using the incompressibility condition we obtain the energy transfer relation as,

$$T(k) = -D(k) + \mathfrak{F}(k), \quad (1.17)$$

where,

$$T(k) = \int d\mathbf{k} \delta(|\mathbf{k}| - k) \mathbf{u}_{\mathbf{k}} \cdot [\mathbf{u} \cdot \nabla \mathbf{u}]_{-\mathbf{k}}, \quad (1.18)$$

is the nonlinear transfer at scale k ,

$$D(k) = \nu k^2 E(k), \quad (1.19)$$

is the energy dissipation rate at scale k , and

$$\mathfrak{F}(k) = \int d\mathbf{k} \delta(|\mathbf{k}| - k) \mathbf{u}_{\mathbf{k}} \cdot \mathbf{f}_{-\mathbf{k}}. \quad (1.20)$$

is the contribution at k from the external forces. Since the energy injected at large scales is dissipation only at small scales, 1.17 suggests that in the inertial range the nonlinear flux $\Pi(k) = \int_0^k dq T(q)$ is constant. This is verified in Fig. 1.6(b), where we show a representative plot of Π_k .

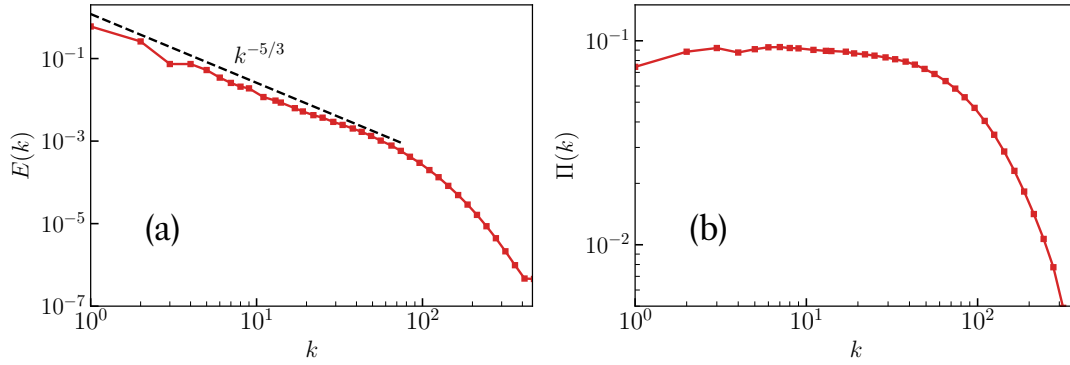


Figure 1.6: Log-log plot of the (a) kinetic energy spectrum (b) nonlinear flux $\Pi(k)$ obtained from the direct numerical simulation of homogeneous and isotropic turbulence on 1024^3 grids (JHU turbulence database [38]). In the inertial range, the $E(k) \sim k^{-5/3}$ and $\Pi(k)$ is constant.

1.1.4 Two-dimensional turbulence

Two-dimensional turbulence is used to model many natural systems such as atmospheric and oceanic flows. In laboratories two-dimensional turbulence can be realized in soap films [39, 40] or stratified layers [41, 42].

In the inviscid limit along with the total kinetic energy, the total enstrophy, $\Omega = \frac{1}{2} \langle |\omega|^2 \rangle$ is also a constant of motion [43–45]. Consequently, one observes an inverse energy cascade from the forcing scale $k_f = 2\pi/\ell_0$ to larger scale and the forward enstrophy cascade from k_f to smaller scales. Simple dimensional arguments, gives the following scaling relation for kinetic energy spectrum [43–45],

$$E(k) \sim \begin{cases} C \epsilon_v^{2/3} k^{-5/3}, & \text{for } k < k_f \\ C' \beta^{2/3} k^{-3}, & \text{for } k > k_f \end{cases} \quad (1.21)$$

where, C, C' are the constants and $\beta \equiv \nu \langle |\nabla \omega|^2 \rangle$ is the enstrophy dissipation rate.

1.2 Multiphase flows

The key objectives in the research of dispersed multiphase flows involve characterizing the statistical properties of the dispersed phase and understanding the flow modulation due to its interaction with the embedded medium [46, 47]. These studies are relevant to many industrial and natural process, e.g., turbulent dispersion of pollutants, pollinations in plants, mixing and combustion, etc.

In multiphase flows, both the statistical properties of flow and the particles depend upon several parameters such as the ratio of particle-fluid length-scale, particle-fluid density, particle Reynolds number (Re_p), [46, 48] etc. For example, a neutrally buoyant particle of diameter $d \ll \eta$, basically follows the fluid as tracers. However, when the particle-fluid density ratio is significant, its behavior deviates from that of a tracer.

In a very simplified picture, each particle in a multiphase flow can be assumed to be a sphere of diameter d_p . At a sufficiently low $Re_p \ll 1$, the acceleration of this spherical particle in the fluid is given by the Maxey and Riley [49] equation,

$$\begin{aligned} \frac{d\mathbf{V}(t)}{dt} = & \frac{18\rho_f\nu}{\rho_p d_p^2} \left[\mathbf{u}(\mathbf{X}, t) - \mathbf{V}(t) \right] + \frac{3\rho_f}{4\rho_p} \nabla^2 \mathbf{u}(\mathbf{X}, t) \\ & + \frac{\rho_f}{\rho_p} \left. \frac{D\mathbf{u}}{Dt} \right|_{\mathbf{x}} + \frac{\rho_f}{2\rho_p} \frac{d}{dt} \left[\mathbf{u}(\mathbf{X}, t) + \frac{d_p^2}{40} \nabla^2 \mathbf{u}(\mathbf{X}, t) - \mathbf{V}(t) \right] \\ & + \frac{9\rho_f\nu}{\rho_p d_p} \int_0^t d\tau \frac{1}{[\pi\nu(t-\tau)]^{1/2}} \frac{d}{d\tau} \left[\mathbf{u}(\mathbf{X}, \tau) + \frac{d_p^2}{24} \nabla^2 \mathbf{u}(\mathbf{X}, \tau) - \mathbf{V}(\tau) \right], \end{aligned} \quad (1.22)$$

where, $\mathbf{u}(\mathbf{X}, t)$ is the undisturbed fluid velocity at the particle position \mathbf{X} and time t , $\mathbf{V}(t)$ is the velocity of the particle, and ρ_p (ρ_f) is the fluid (particle) density. The terms in RHS of 1.22 are arranged in the following manner; the first line represents the Stokes drag, the second line gives the Faxen correction [50], and the third line represents the Basset history force [51].

For a micron sized particle with density, $\rho_p \gg \rho_f$, we obtain the following equations of motion for a heavy inertial particle,

$$\frac{d\mathbf{X}(t)}{dt} = \mathbf{V}(t), \quad (1.23)$$

$$\frac{d\mathbf{V}(t)}{dt} = \frac{1}{\tau_p} [\mathbf{u}(\mathbf{X}, t) - \mathbf{V}(t)], \quad (1.24)$$

where $\tau_p = \rho_p d_p^2 / 18 \nu \rho_f$ is the particle relaxation time. The above 1.23 and 1.24 can be used to model solid-particles or droplets (e.g., clouds) in a turbulence provided $d_p \ll \eta$ and the flow experienced by a particle is laminar. The main non-dimensional number governing the dynamics is the Stokes number, $St = \tau_p / \tau_\eta$. We shall often refer to the particles obeying 1.23 and 1.24 as ‘heavy inertial particles’.

The level of carrier flow modulation by the particles obeying 1.23 and 1.24 is determined by the particle volume fraction Φ_V and the mass-loading parameter $\phi_m = \rho_p \Phi_V / \rho_f$ [48, 52]. When $\Phi_V \leq 10^{-6}$, and ϕ_m is also small the suspension is considered dilute and the effect of particles on turbulence is negligible. In this regime the dynamics of the particle is affected by the flow but its back-reaction can be ignored (one-way coupling). At moderately dense regime $10^{-6} \leq \Phi_V \leq 10^{-3}$ and $\phi_m \sim \mathcal{O}(1)$, the influence of the particle on carrier phase becomes significant (two-way coupling). For $\Phi_V > 10^{-3}$ the inter-particle collisions increases by a considerable amount (four-way coupling).

When the size of the particles are finite, or $d_p > \eta$ and $Re_p > 1$, then 1.23 and 1.24 are no longer a valid model. Here the turbulence modulation cannot be studied using a single non-dimensional number, St [53]. Moreover, for $Re_p \geq \mathcal{O}(100)$, the vortex shedding behind the particles further adds to the fluctuations in the carrier phase [54]. In this regime, we study the fluctuations generated by a swarm of rising bubbles in an otherwise stagnant or turbulent flow.

In the following sub-sections, we will describe the problems investigated in this thesis in greater detail.

1.2.1 Caustics in turbulent flow

In a turbulent flow, the inertial particles governed by 1.23 and 1.24 show many interesting behaviors, one of the most notable being preferential clustering. Maxey [55] using 1.24, showed that the particles of density greater than the fluid tends to cluster in regions dominated by strain.

The inhomogeneous distribution of the inertial particles in turbulent flow is known to have consequences in increasing the rate of raindrop formation [56–59]. In clouds, the raindrops are believed to grow by the process of coalescence that occur as tiny droplets collide with each other [59, 60]. The collision rate between droplets is highly enhanced by the formation of singularities in the particle velocity gradients, also known as caustics [60]. This caustic formation also plays a key role in the growth of planetisimals in astrophysical dusts [61]. In chapter 3, we study the rate of caustic formation in the turbulent flow. Previous studies have mostly studied this problem in synthetic flows [62–64]. We show that in the turbulent flows, the rate of caustic formation falls exponentially with $1/St$.

1.2.2 Dusty gas turbulence

In astrophysical plasma, the inclusion of back-reaction from dusts allows for the streaming instability [65, 66], to manifest itself. Thus, in a suspension at moderate dense regime, the back-reaction from particles can not be ignored.

The turbulence modulation by heavy inertial particles at high mass loading has been studied both numerically [52, 67–70] and experimentally [71]. In the decaying turbulence the for a fixed mass-loading parameter $\phi_m = 1$, it was observed that particle with $St < 0.1$ tends to increase both the total turbulent kinetic energy and the total dissipation rate, compared to single-phase flow. The particles with $0.1 < St < 0.5$ increases, the dissipation rate but the turbulent kinetic energy remain unchanged. Particles whose $St \approx 1$ reduce turbulent kinetic energy but the total dissipation rate remain unchanged. Large particles $St > 1$ reduces both turbulent kinetic energy and dissipation rate relative to their values in the single-phase flow. These modulation in to-

tal kinetic energy and dissipation rate can be explained on the basis of time spent by a particle of given St in vortical or strain region of the fluid [67]. Similarly, an increase in the dissipation rate was also reported by Muramulla *et al.* [70] in a recent study on channel flow.

Much fewer studies exist where the scaling in kinetic energy spectra in the particle-laden flow is investigated. In turbulence the scaling in the kinetic energy spectra is universal, i.e., $E(k) \sim k^{-5/3}$ in three-dimension. How does this scaling changes in the presence of back-reaction from dust is not understood fully. It is also difficult to answer this question from the earlier studies as not enough scaling range was resolved. Only recently, Gualtieri *et al.* [68] observed a new power-law scaling regime in the kinetic energy spectra where $E(k) \sim k^{-4}$ in three-dimensions. In two-dimensional particle-laden turbulence Bec *et al.* [72] observed a spectral exponent of ≈ -2 in kinetic energy spectra. The question that remain is, how does this new scaling regime and the scaling-exponent depend upon the mass loading parameter and the Stokes number? In chapter 4, we investigate this problem in a two-dimensional particle-laden turbulent flow.

1.2.3 Buoyancy-driven bubbly flows

In this thesis, we study the statistical properties of the buoyancy-driven bubbly flows using a fully resolved simulation. The Navier-Stokes equations governing the motion of bubbles in fluid [73–75] are,

$$\rho(\partial_t \mathbf{u} + \mathbf{u} \cdot \nabla \mathbf{u}) = -\nabla p + \nabla \cdot [2\mu \mathcal{S}] + \mathbf{F}^\sigma + \mathbf{F}^g, \quad (1.25)$$

$$\nabla \cdot \mathbf{u} = 0, \quad (1.26)$$

where μ is the dynamic viscosity, $\mathcal{S} = \frac{1}{2}(\nabla \mathbf{u} + \nabla \mathbf{u}^T)$, is the strain-rate tensor, $\mathbf{F}^\sigma = \sigma \kappa \mathbf{n}$, is the force density due to surface tension, defined in terms of σ , the coefficient of surface tension, κ , the curvature and \mathbf{n} , the unit normal to the interface, and $\mathbf{F}^g = (\rho - \rho_a)\mathbf{g}$, is the buoyancy force density, in which \mathbf{g} is the acceleration due to gravity, ρ_a is the average density.

A set of four non-dimensional numbers governs the dynamics of bubbly flows. The density and the viscosity ratios of the two-fluid, $\frac{\rho_b}{\rho_f}$ and $\frac{\mu_b}{\mu_f}$ respectively, are the first two. Here, the subscript b is used to denote the bubble phase and f the liquid phase. For an air bubble in water, $\frac{\rho_b}{\rho_f} \sim 10^{-3}$ and $\frac{\mu_b}{\mu_f} \sim 10^{-2}$. The usual choice of the other two, in buoyancy-driven flows, are the Galilei number (Ga) and the Bond (Bo), [also known as the Eotvos (Eo)] number, defined as,

$$\text{Ga} \equiv \sqrt{\frac{\rho_f |\rho_f - \rho_b| g d^3}{\mu_f^2}}, \quad (1.27)$$

$$\text{Bo} \equiv \frac{|\rho_f - \rho_b| g d^2}{\sigma}, \quad (1.28)$$

where d is the diameter of a bubble. The Reynolds number $\text{Re} = \frac{\rho_f V_0 d}{\mu_f}$ is defined using the rise velocity V_0 of an isolated bubble.

Experimental and numerical studies on bubbly flows

We begin by discussing the studies on the dynamics of a single bubble. A single spherical bubble while rising does-not necessarily remain spherical and can also undergo path instability, where a rectilinear motion transverses into zigzag. The first documented observation of these phenomena is found in Leonardo Da Vinci's book 'Codex Leicester.' [76].

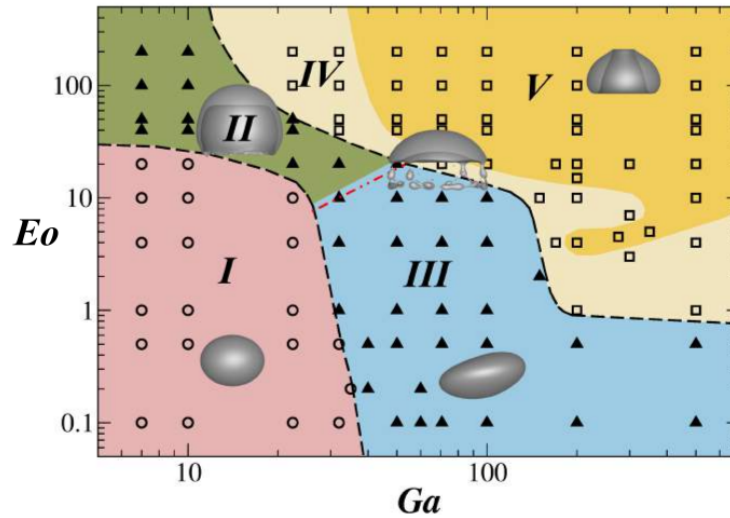


Figure 1.7: The bubble shape and trajectory in the $Ga - Eo$ (or $Ga - Eo$) plane. The different regions are: (I) spherical bubble and rectilinear trajectory, (II) asymmetric bubble with non-oscillatory trajectory, (III) asymmetric bubble shape with oscillatory trajectory, (IV) and (V) breakup regime. Figure published from Tripathi [77] with permission.

Many studies have explored the subject of path instabilities and bubble shapes of a rising bubble numerically [78, 79], experimentally [80, 81], and theoretically [82]. Initially Bhaga and Weber [80] and more recently Tripathi *et al.* [78] have identified five distinct regimes of bubble shape and trajectories in the $Ga - Eo$ (Eo is same as Bo) phase space. We show the phase plot as obtained by Tripathi *et al.* [78] in Fig. 1.7. In the figure, region-I (shown in pink) bubble has a constant ellipsoidal shape and rises in a rectilinear trajectory. Region II (marked in green color), the bubble rise in a straight line, and the bubble shape is an axisymmetric cap with a thin trailing skirt. Region III (blue color), the bubble rises in a zigzag or a spiral trajectory and shows shape oscillation. Region IV and V (light and dark yellow color) represent peripheral and central breakup regime. Not only the bubble shape and trajectory but also the wake structure is distinct at each regime.

In a homogeneous bubble swarm, the wakes of individual bubbles interact giving rise to a complex flow structures resembling turbulence. Such flows are often known as pseudo-turbulence [83] or Bubble Induced Agi-

tation (BIA) [9, 84]. Although the wake structure of a single bubble is distinct for a given $Ga - Bo$ pair, the statistical properties of pseudo-turbulence are observed to be universal. For instance, almost all the studies have shown that the probability distribution function of the transverse component of the liquid velocity fluctuations is exponential, and the horizontal component is skewed [8, 9].

Energy spectra in pseudo-turbulence

The earliest experiment to study the statistical properties of pseudo-turbulence was performed by Lance and Bataille [83]. In the experiment, the bubbles at volume fractions ($\Phi_V = 1 - 4\%$) was released in a turbulent fluid. In Fig. 1.8 we show the liquid kinetic energy spectra obtained by Lance and Bataille [83]. The single phase turbulent spectra, marked as 1, show a clear $-\frac{5}{3}$ scaling in the inertial range. The spectra obtained for volume-fraction $\Phi_V = 1, 3,$ and 4% are marked as 2, 3, and 4 respectively. Once the bubbles interact with the underlying turbulence, a new scaling region is observed for scales smaller than d . Over this region, the kinetic energy spectra, $E(k) \sim k^{-8/3}$ and this scaling of ~ -3 is also known as the pseudo-turbulent scaling.

Later, Rensen *et al.* [85] introduced the term bubble parameter (b) to characterize the amount of pseudo-turbulent fluctuations present in a turbulent flow. The bubble parameter is defined as,

$$b \equiv \frac{\Phi_V V_0^2}{u_0^2}, \quad (1.29)$$

where u_0^2 is the root mean square velocity of the turbulent fluctuations in the absence of bubbles. In an experiment similar to Lance and Bataille [83], Rensen *et al.* [85] did not observe any change in the spectral slope. This observation was attributed to the fact that b explored by Rensen *et al.* [85] ($b < 1$) was much lower than that of Lance and Bataille [83] ($b > 1$). In both the experiments, the bubble $Re \sim \mathcal{O}(10^3)$.

The direct numerical simulation of bubbly flows poses considerable challenges. A lot of computational resources are spent in simulating the sharp interfaces accurately. Thus, earlier numerical studies of pseudo-turbulence

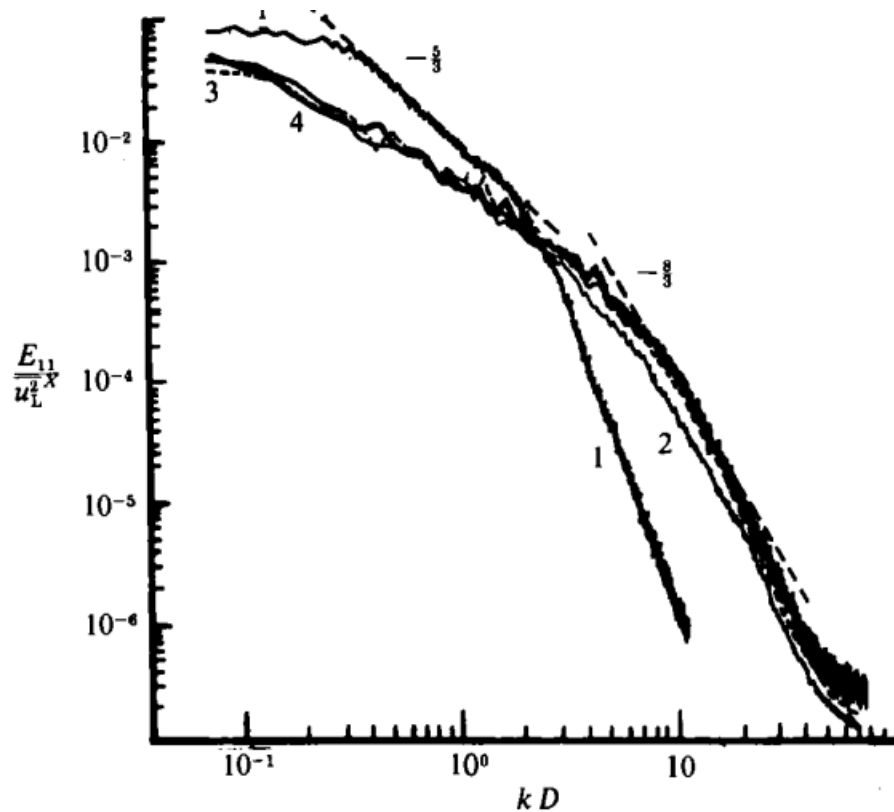


Figure 1.8: The kinetic energy spectra as obtained from the experiments of Lance and Bataille [83]. The spectra for different volume-fractions are marked as (1) $\Phi_V = 0$, (2) $\Phi_V = 1.0\%$, (3) $\Phi_V = 3\%$ and (4) $\Phi_V = 4\%$. Figure published with permission from Lance and Bataille [83]

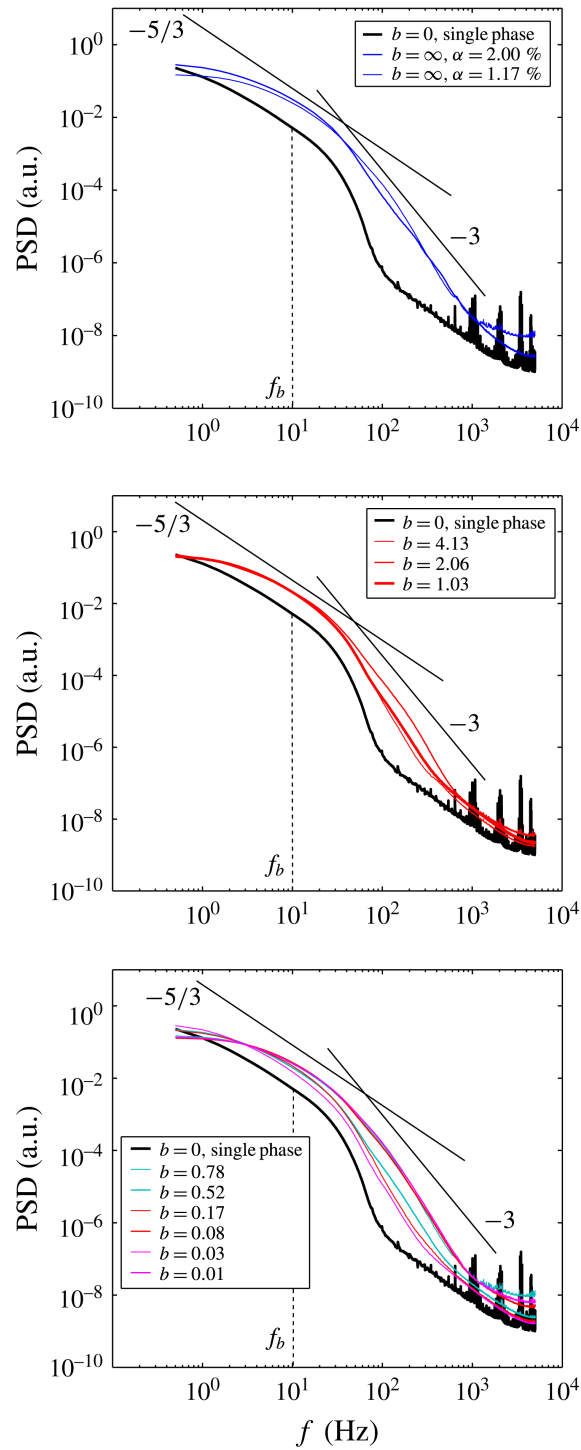


Figure 1.9: The kinetic energy spectra obtained from the experimental study of Prakash *et al.* [86]. The top panel shows spectra for $b = \infty$, middle $b > 1$, and bottom $b < 1$. For comparison, single phase turbulent spectra $b = 0$ is plotted in black. The horizontal dotted line marks the frequency corresponding to bubble diameter. Figure published with permission from Prakash *et al.* [86].

were restricted to low $Re \sim \mathcal{O}(10)$. In the first of a numerical study at $b = \infty$ in two-dimension Esmaeeli and Tryggvason [87] observed a kinetic energy spectra of k^{-3} . Later studies in three-dimensions [88–90], at similar $Re \sim \mathcal{O}(10)$, observed a steeper scaling of $k^{-3.6}$ for scales smaller than the bubble diameter. At high $Re \sim \mathcal{O}(10^3)$ the scaling of k^{-3} was again recovered in the numerical study of Roghair *et al.* [91].

In the experimental studies, the scaling range has remained controversial. Mercado *et al.* [92] and Ref. [8, 86] reported a scaling of -3 for scales smaller than the bubble diameter whereas Riboux *et al.* [84], and Ref. [93] reported the scaling for the scales larger than d . The main difference between the two was that the former measured the fluctuations within the swarm while the measurement was taken behind the swarm in the latter. A Kolmogorov scaling of $k^{-5/3}$ was also observed by Riboux *et al.* [84] for scales $k > k_d$ (k_d bubble diameter mode), which is not observed in any other experiments or simulations.

In a recent study, Prakash *et al.* [86] explored a range of bubblance parameter ranging from $b = 0 - \infty$. In the experiment, the b was varied by changing both the turbulence intensity and the volume fraction Φ_V . We show the spectra as obtained by Prakash *et al.* [86] in Fig. 1.9. In all the cases, the pseudo-turbulent scaling of -3 was observed even for $b \approx 0.01$. The most recent investigation of Alm eras *et al.* [8] also made a similar observation for a range of bubblance $0.1 \lesssim b \lesssim 1.3$.

The pseudo-turbulent scaling of k^{-3} is robust and was observed in almost all the experiments and simulations. Lance and Bataille [83], studied the energy transfer relation to help understand this scaling behavior,

$$T(k) = D(k) + \mathfrak{F}(k), \quad (1.30)$$

where, \mathfrak{F} is the production due to all the forces (gravity and surface tension) present in pseudo-turbulence. Lance and Bataille [83] argued that the production term is local in spectral space, implying that its balance with the dissipation term gives the scaling of k^{-3} . All the studies that followed have attributed the scaling to the balance of production with dissipation. The role of the nonlinear forces and the contribution of different forces at each scale

in the energy budget remain unclear.

In chapter 5 of the thesis, we conduct a comprehensive study of the bubbly flows using Direct Numerical Simulations (DNS). We validate our analysis by showing the distribution of the liquid velocity fluctuations fits precisely with the experimental observation. We then study the energy transfer relation in the pseudo-turbulent flows. The main advantage of using DNS is that it allows us to disentangle the contribution of various forces at each scale, which otherwise is very difficult in the experiments. We show that the production due to gravity is present only at scales larger than d . The combined transfer of energy by the surface tension and fluid nonlinearity leads to the observed scaling of k^{-3} in pseudo-turbulence. In chapter 6, we extend these ideas to study the turbulence modulation by a swarm of rising bubbles for different bubble parameter.

1.3 A guide to the thesis

We summarize in brief all the chapters that constitute this thesis.

In the next chapter (chapter 2) we discuss in detail the numerical methods to study different multiphase flows.

In chapter 3, we start with the simplest scenario in which the volume fraction of the embedded particles is small and does not modify the flow properties. Here we study the statistical properties of the particle velocity gradients. We show the rate at which singularities occur in the gradients falls exponentially with the $1/St$.

In the following chapter (chapter 4), we study the statistical properties of the flow in the regime of two-way coupling. The mass-loading is significant and modifies the turbulent flow significantly. We show that a new scaling regime appears in the kinetic-energy spectra, and the scaling depends upon both the Stokes number and the mass-loading.

In chapter 5, we present the statistical properties of flows generated by a homogeneous swarm of buoyant bubbles rising under gravity using three-dimensional direct numerical simulations. In a suspension, the bubbles' wake

interaction leads to complex flow structures known as pseudo-turbulence. Using an energy budget analysis we show that the balance of the viscous dissipation and the net production by surface tension and fluid nonlinearity gives the k^{-3} scaling in pseudo-turbulence.

In chapter 6, we study the interaction of a swarm of buoyant bubbles with turbulence generated by large-scale driving. We show that $E(k) \sim k^{-5/3}$ for scales larger than the bubble diameter, whereas the pseudo-turbulent scaling, $E(k) \sim k^{-3}$ is present only for scales smaller than d . We use the energy budget analysis to understand the energy transfer mechanism. We also present the results for the acceleration statistics of the center-of-mass of bubbles.

In the final chapter (chapter 7), we conclude the thesis and provide future research prospects.

References

- [1] J. F. Kok, E. J. R. Parteli, T. I. Michaels, and D. B. Karam, *Rep. Prog. Phys.* **75**, 106901 (2012).
- [2] National Oceanic and Atmospheric Administration, <https://www.nesdis.noaa.gov/content/dust-plume-blowing-west-sahara-atlantic-ocean> (2010).
- [3] N. Kantarci, F. Borak, and K. O. Ulgen, *Process biochemistry* **40**, 2263 (2005).
- [4] Sir D. Attenborough, *Our Planet*, <https://www.imdb.com/title/tt9253866/>.
- [5] R. F. Mudde, *Annu. Rev. Fluid Mech.* **37**, 393 (2005).
- [6] P. Davidson, *Turbulence: An Introduction for Scientists and Engineers* (Oxford University Press, 2004).
- [7] S. Pope, *Turbulent Flows* (Cambridge University Press, 2012).
- [8] E. Alm eras, V. Mathai, D. Lohse, and C. Sun, *J. Fluid Mech.* **825**, 1091 (2017).
- [9] F. Risso, *Annu. Rev. Fluid Mech.* **50**, 25 (2018).
- [10] V. Mathai, D. Lohse, and C. Sun, *Annu. Rev. Condens. Matter Phys.* **11**, 1 (2019).
- [11] Image by Daniele Pugliesi, https://en.wikipedia.org/wiki/Bubble_column_reactor.
- [12] Creative Commons Attribution Licence, <https://creativecommons.org/licenses/by-nc-nd/4.0/>.
- [13] L. Landau and E. Lifshitz, *Course of Theoretical Physics, Volume 6* (Elsevier Science, 2013).

- [14] U. Frisch, *Turbulence, A Legacy of A. N. Kolmogorov* (Cambridge University Press, 1997).
- [15] O. Reynolds, *Philosophical Transactions of the Royal society of London* **174**, 935 (1883).
- [16] M. V. Dyke, *An Album of Fluid Motion*, 12th ed. (Parabolic Press, Inc., 2008).
- [17] V. S. of Japan and K. J. Gakkai, *Fantasy of Flow: The world of fluid flow captured in photographs* (Ohmsha, 1993).
- [18] Flow Visualization: a Course in the Physics and Art of Fluid Flow by Jean Hertzberg and students at CU Boulder, <https://www.flowvis.org>.
- [19] M. Fermigier, *Comptes Rendus Mécanique* **345** (2017).
- [20] H. Werlé, ONERA Cinema Film (1974).
- [21] A. Tsinober, *An informal introduction to turbulence* (2004) OCLC: 70726392.
- [22] G. I. Taylor, *Proceedings of the Royal Society A: Mathematical, Physical and Engineering Sciences* **151**, 421 (1935).
- [23] G. K. Batchelor, *The theory of homogeneous turbulence*, Cambridge science classics (Cambridge University Press).
- [24] A. S. Monin and A. M. Yaglom, *Statistical fluid mechanics: mechanics of turbulence vol-1* (MIT Press, 1971).
- [25] A. Kolmogorov, *Proceedings: Mathematical and Physical Sciences* **434**, 9 (1991).
- [26] A. Kolmogorov, *Dokl. Akad. Nauk SSSR* **31**, 538 (1941).
- [27] A. Kolmogorov, *Proceedings: Mathematical and Physical Sciences* **434**, 15 (1991).
- [28] A. Noullez, G. Wallace, W. Lempert, R. B. Miles, and U. Frisch, *J. Fluid Mech.* **339**, 287 (1997).

- [29] L. F. Richardson, *Weather prediction by numerical process*, edited by University of California Libraries (Cambridge University press, 1922).
- [30] T. Karman and L. Howarth, Proceedings of the Royal Society of London. Series A-Mathematical and Physical Sciences **164**, 192 (1938).
- [31] F. Anselmet, Y. Gagne, E. J. Hopfinger, and R. A. Antonia, J. Fluid Mech. **140**, 63 (1984).
- [32] R. Benzi, G. Paladin, G. Parisi, and A. Vulpiani, J. Phys. A: Mathematical and General **17**, 3521 (1984).
- [33] K. R. Sreenivasan, Annu. Rev. Fluid Mech. **23**, 539 (1991).
- [34] Z.-S. She and E. Leveque, Phys. Rev. Lett. **72**, 336 (1994).
- [35] C. Meneveau and K. R. Sreenivasan, J. Fluid Mech. **224**, 429 (1991).
- [36] C. Meneveau and K. R. Sreenivasan, Phys. Rev. Lett. **59**, 1424 (1987).
- [37] G. Parisi and U. Frisch, Turbulence and Predictability of Geophysical Flows and Climate Dynamics **88**, 84 (1985).
- [38] Y. Li, E. Perlman, M. Wan, Y. Yang, C. Meneveau, R. Burns, S. Chen, A. Szalay, and G. Eyink, J. Turbul. **9**, N31 (2008).
- [39] P. Vorobieff, M. Rivera, and R. E. Ecke, Phys. Fluids **11**, 2167 (1999).
- [40] M. Rivera, P. Vorobieff, and R. E. Ecke, Phys. Rev. Lett. **81**, 1417 (1998).
- [41] G. Boffetta and R. E. Ecke, Annu. Rev. Fluid Mech. **44**, 427 (2012).
- [42] G. Boffetta, A. Cenedese, S. Espa, and S. Musacchio, Europhys. Lett. **71**, 590 (2005).
- [43] G. K. Batchelor, Phys. Fluids **12**, 233 (1969).
- [44] C. E. Leith, Phys. Fluids **11**, 671 (1968).
- [45] R. H. Kraichnan, Phys. Fluids **10**, 1417 (1967).
- [46] S. Elghobashi, Annu. Rev. Fluid Mech. **51**, 217 (2019).

- [47] F. Toschi and E. Bodenschatz, *Annu. Rev. Fluid Mech.* **41**, 375 (2009).
- [48] S. Balachandar and J. K. Eaton, *Annu. Rev. Fluid Mech.* **42**, 111 (2010).
- [49] M. R. Maxey and J. J. Riley, *Phys. Fluids* **26**, 883 (1983).
- [50] H. Faxen, *Annalen der Physik* **373**, 89 (1922).
- [51] A. B. Basset, *A treatise on hydrodynamics: with numerous examples*, Vol. 2 (Deighton, Bell and Company, 1888).
- [52] S. Elgobashi, in *IUTAM Symposium on Computational Approaches to Multiphase Flow* (Springer Netherlands, Dordrecht, 2006) pp. 3–10.
- [53] F. Lucci, A. Ferrante, and S. Elghobashi, *Phys. Fluids* **23**, 025101 (2011).
- [54] P. Ern, F. Risso, D. Fabre, and J. Magnaudet, *Annu. Rev. Fluid Mech.* **44**, 97 (2012).
- [55] M. R. Maxey, *J. Fluid Mech.* **174**, 441 (1987).
- [56] B. J. Devenish, P. Bartello, J.-L. Brenguier, L. R. Collins, W. W. Grabowski, R. H. A. IJzermans, S. P. Malinowski, M. W. Reeks, J. C. Vassilicos, L.-P. Wang, and Z. Warhaft, *Q. J. R. Meteorol. Soc.* **138**, 1401 (2012).
- [57] P. G. Saffman and J. S. Turner, *J. Fluid Mech.* **1**, 16 (1956).
- [58] S. Sundaram and L. R. Collins, *J. Fluid Mech.* **335**, 75 (1997).
- [59] E. Balkovsky, G. Falkovich, and A. Fouxon, *Phys. Rev. Lett.* **86**, 2790 (2001).
- [60] G. Falkovich, A. Fouxon, and M. G. Stepanov, *Nature* **419**, 151 (2002).
- [61] K. Gustavsson and B. Mehlig, *J. Turbul.* **15**, 34 (2014).
- [62] M. Wilkinson and B. Mehlig, *Phys. Rev. E* **68**, 040101 (2003).
- [63] K. Gustavsson, E. Meneguz, M. Reeks, and B. Mehlig, *New J. Phys.* **14**, 115017 (2012).

- [64] K. Gustavsson and B. Mehlig, Phys. Rev. E **87**, 023016 (2013).
- [65] A. N. Youdin and J. Goodman, Astrophys. J. **620**, 459 (2005).
- [66] L. Pan, Astrophys. J. **898**, 8 (2020).
- [67] A. Ferrante and S. Elghobashi, Phys. Fluids **15**, 315 (2003).
- [68] P. Gualtieri, F. Battista, and C. M. Casciola, Phys. Rev. Fluids **2**, 034304 (2017).
- [69] P. Gualtieri, F. Picano, and C. Casciola, J. Fluid Mech. **715**, 134 (2013).
- [70] P. Muramulla, A. Tyagi, P. S. Goswami, and V. Kumaran, J. Fluid Mech. **889**, A28 (2020).
- [71] C. Poelma, J. Westerweel, and G. Ooms, J. Fluid Mech. **589**, 315 (2007).
- [72] J. Bec, F. Laenen, and S. Musacchio, arXiv:1702.06773 (2017).
- [73] G. Tryggvason, A. Esmaeeli, J. Lu, and S. Biswas, Fluid Dynamics Research **38**, 660 (2006).
- [74] A. Prosperetti and G. Tryggvason, *Computational methods for multiphase flow* (Cambridge University Press, 2007).
- [75] D. D. Joseph, *Stability of Fluid Motions II* (Springer Publishers, Berlin, 1976).
- [76] C. D. Ohl, A. Tijink, and A. Prosperetti, J. Fluid Mech. **482**, 271 (2003).
- [77] M. Tripathi, *Rising bubbles and falling drops*, Ph.D. thesis, Indian Institute of Technology, Hyderabad (2015).
- [78] M. K. Tripathi, K. C. Sahu, and R. Govindarajan, Nat. Commun. **6**, 6268 (2015).
- [79] J. C. Cano-Lozano, C. Martinez-Bazan, J. Magnaudet, and J. Tchoufag, Phys. Rev. Fluid **1**, 053604 (2016).
- [80] D. Bhaga and M. E. Weber, J. Fluid Mech. **105**, 61 (1981).

- [81] R. Clift, J. R. Grace, and M. E. Weber, *Bubbles, drops and particles* (Academic Press, New York, 1978).
- [82] W. L. Shew and J.-F. Pinton, Phys. Rev. Lett. **97**, 144508 (2006).
- [83] M. Lance and J. Bataille, J. Fluid Mech. **222**, 95 (1991).
- [84] G. Riboux, F. Risso, and D. Legendre, J. Fluid Mech. **643**, 509 (2010).
- [85] J. Rensen, S. Luther, and D. Lohse, J. Fluid Mech. **538**, 153 (2005).
- [86] V. N. Prakash, J. M. Mercado, L. van Wijngaarden, E. Mancilla, Y. Tagawa, D. Lohse, and C. Sun, J. Fluid Mech. **791**, 174 (2016).
- [87] A. Esmaeeli and G. Tryggvason, J. Fluid Mech. **314**, 315 (1996).
- [88] B. Bunner and G. Tryggvason, J. Fluid Mech. **466**, 17 (2002).
- [89] B. Bunner and G. Tryggvason, J. of Fluid Mech. **495**, 77 (2003).
- [90] B. Bunner and G. Tryggvason, J. Fluid Mech. **466**, 53 (2002).
- [91] I. Roghair, J. M. Mercado, M. V. S. Annaland, H. Kuipers, C. Sun, and D. Lohse, Int. J. Multiph. Flow **37**, 1093 (2011).
- [92] J. M. Mercado, D. G. Gómez, D. V. Gils, C. Sun, and D. Lohse, J. Fluid Mech. **650**, 287 (2010).
- [93] S. Mendez-Diaz, J. C. Serrano-Garcia, R. Zenit, and J. A. Hernández-Cordero, Phys. Fluids **25**, 043303 (2013).

Numerical methods for multiphase flows

2.1 Introduction

In this chapter, we describe in detail the Direct Numerical Simulation (DUNE'S) techniques for solving different types of multiphase flows. We shall first discuss the case of particle-laden flows which is studied using a one- and two-way coupling techniques. We shall then describe buoyancy-driven bubbly flows where the dispersed phase is an immiscible liquid with different density and viscosity. The main characteristic feature of such a flow is the presence of a sharp interface at the phase boundary [1, 2].

The level of carrier-fluid interaction or the coupling regimes for dispersed multiphase flows is classified based on the Stokes number, $St = \tau_p/\tau_\eta$ and the volume fraction Φ_V . Note that the Stokes number, $St \sim \left(\frac{\rho_p}{\rho_f}\right) \left(\frac{d_p}{\eta}\right)^2$ also gives an estimate of the relative size of the suspended particle. The classification map, recreated from Elgobashi [3] and Ref. [4] is shown in Fig. 2.1. In each regime, appropriate choice of computational method is decided based on the volume fraction Φ_V and St . Broadly, the following regimes are possible.

1. Dilute suspensions ($\Phi_V \leq 10^{-6}$): In this regime the effect of suspended particles on carrier phase is negligible and the multiphase flows are

- studied in the one-way coupling regime where only the fluid→particle interaction exists.
- Moderately dense suspensions ($10^{-6} \leq \Phi_V \leq 10^{-3}$): Here, the suspended particles can modify the flow significantly and the multiphase flows are treated using a two-way coupling scheme, where both the fluid→particle and particle→fluid interaction exists.

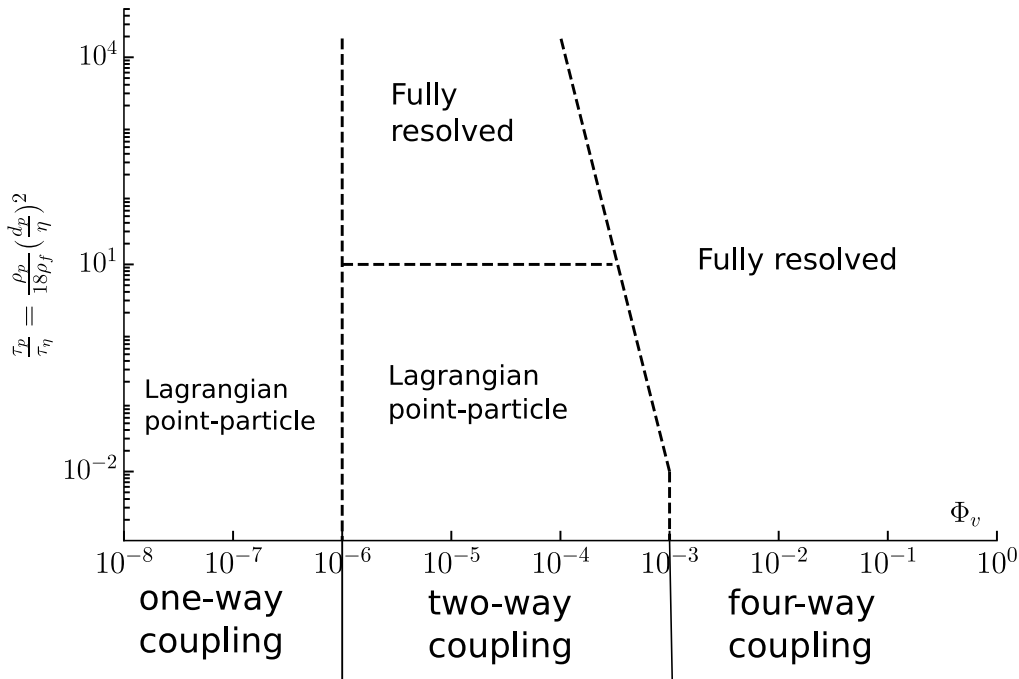


Figure 2.1: The phase plot showing the different carrier-phase coupling regimes for particle-laden flow and the appropriate choice of numerical model. The phase diagram is recreated from Elgobashi [3].

- Dense Suspensions ($\Phi_V > 10^{-3}$): The collisions between particles become significant and cannot be ignored and thus a four-way coupling scheme (fluid→particle, particle→fluid, and particle↔particle interactions) is needed to study the particle-laden flow.

The rest of the chapter is organized as follows: In [Sec. 2.2](#), we describe the pseudo-spectral method for the DNS of single phase. In [Sec. 2.3](#), we discuss the one- and two- way coupled DNS of multiphase flows. Finally in [Sec. 2.4](#),

we will describe the DNS methods for studying the buoyancy-driven bubbly flows, where $\Phi_V > 10^{-3}$ and size of each bubble is greater than η .

2.2 Single phase flow

The Navier-Stokes (NS) equations Eq. 1.1 and 1.2, governing the motion of a single phase fluid can also be written as,

$$\partial_t \mathbf{u} + \boldsymbol{\omega} \times \mathbf{u} = -\nabla p + \nu \nabla^2 \mathbf{u} + \mathbf{f}, \quad (2.1)$$

$$\nabla \cdot \mathbf{u} = 0, \quad (2.2)$$

where, $\boldsymbol{\omega} = \nabla \times \mathbf{u}$ is the vorticity and we have used the relation $\mathbf{u} \cdot \nabla \mathbf{u} = \mathbf{u} \times \boldsymbol{\omega} + \frac{1}{2} \nabla u^2$ to obtain 2.1.

2.2.1 Pseudo-spectral solver

We now discuss the pseudo-spectral solver for the single phase NS equation. In a spectral decomposition, the velocity field \mathbf{u} is expanded in terms of an orthogonal basis functions ψ ,

$$\mathbf{u}(\mathbf{x}, t) = \sum_{\mathbf{k}} \mathbf{u}_{\mathbf{k}}(t) \psi_{\mathbf{k}}(\mathbf{x}). \quad (2.3)$$

The choice of ψ depends on the problem at hand. For example, in a channel flow where the domain is bounded, a class of Jacobi functions, the Legendre, or Chebyshev polynomials of the first kind are used. When the domain is $\mathbf{L} = (L_x, L_y, L_z)$ -periodic, as in our case, the natural choice of the basis functions are the Fourier series,

$$\psi_{\mathbf{k}}(\mathbf{x}) = \exp(i\mathbf{k} \cdot \mathbf{x}), \quad (2.4)$$

where $\mathbf{k} = (k_x, k_y, k_z)$ are the wave-numbers. In physical space, the continuous field \mathbf{u} is approximated using N_x, N_y and N_z discrete points respectively along each component of \mathbf{L} . This sets the wavenumbers along each direction,

$$k_i \in \frac{2\pi}{L_i} \left[-\frac{N_i}{2} + 1, \dots, -1, 0, 1, \dots, \frac{N_i}{2} \right]. \quad (2.5)$$

We now write the 2.1 and 2.2 in Fourier basis,

$$\partial_t \mathbf{u}_k + \mathbf{W}_k = -ik p_k - \nu k^2 \mathbf{u}_k + \mathbf{f}_k, \quad (2.6)$$

$$ik \cdot \mathbf{u}_k = 0, \quad (2.7)$$

where \mathbf{W}_k is the Fourier transform of the nonlinear term. We can eliminate the pressure by using the incompressibility 2.7 to obtain,

$$\partial_t \mathbf{u}_k + \mathfrak{P} [\mathbf{W}_k - \mathbf{f}_k] = -\nu k^2 \mathbf{u}_k, \quad (2.8)$$

where $\mathfrak{P} = \mathbf{I} - \frac{\mathbf{k}\mathbf{k}}{k^2}$ is the projection operator.

2.2.2 The nonlinear term and the aliasing error

The nonlinear term, a product in the real space becomes convolution in the Fourier space,

$$(W_k)_i = -\epsilon_{ijk} \sum_{\mathbf{q}+\mathbf{p}=\mathbf{k}} (u_q)_j (\omega_p)_k, \quad (2.9)$$

where ϵ_{ijk} is the Levi-Civita tensor.

The evaluation of the convolution in spectral space is expensive as it requires $\mathcal{O}(N^2)$ operations, where $N = N_x \times N_y \times N_z$ is the total number of collocation points. This problem was overcome by Orzag [5, 6], where the evaluation of convolution was avoided by shifting \mathbf{u}_k and $\boldsymbol{\omega}_k$ back to the real space to calculate $\mathbf{u} \times \boldsymbol{\omega}$. Since the evaluation of nonlinear term involves transforming back and forth between real and Fourier space, these methods are called pseudo-spectral.

The use of discrete Fourier transform to evaluate the nonlinear term leads to aliasing errors. Since in a discrete Fourier transform, only a finite number of wave-numbers are resolved, the unresolved modes generated due to coupling gets folded back leading to errors in the solution. To demonstrate the aliasing error we expand 2.9, based on whether the condition $N_i \mathbf{e}_i < (\mathbf{p} + \mathbf{q})_i < N_i \mathbf{e}_i$, is satisfied or not, into the following terms [7],

$$\begin{aligned}
(W_{\mathbf{k}})_i = & -\epsilon_{ijk} \sum_{\mathbf{q}+\mathbf{p}=\mathbf{k}}^{-N_l \mathbf{e}_l < \mathbf{k}_l < N_l \mathbf{e}_l} (u_{\mathbf{q}})_j (\omega_{\mathbf{p}})_k - \epsilon_{ijk} \left[\sum_{\mathbf{q}+\mathbf{p}=\mathbf{k} \pm N_x \mathbf{e}_x} (u_{\mathbf{q}})_j (\omega_{\mathbf{p}})_{k+} \right. \\
& \sum_{\mathbf{q}+\mathbf{p}=\mathbf{k} \pm N_y \mathbf{e}_y} (u_{\mathbf{q}})_j (\omega_{\mathbf{p}})_k + \sum_{\mathbf{q}+\mathbf{p}=\mathbf{k} \pm N_z \mathbf{e}_z} (u_{\mathbf{q}})_j (\omega_{\mathbf{p}})_k + \sum_{\mathbf{q}+\mathbf{p}=\mathbf{k} \pm N_x \mathbf{e}_x \pm N_y \mathbf{e}_y} (u_{\mathbf{q}})_j (\omega_{\mathbf{p}})_{k+} \\
& \left. \sum_{\mathbf{q}+\mathbf{p}=\mathbf{k} \pm N_y \mathbf{e}_y \pm N_z \mathbf{e}_z} (u_{\mathbf{q}})_j (\omega_{\mathbf{p}})_{k+} + \sum_{\mathbf{q}+\mathbf{p}=\mathbf{k} \pm N_x \mathbf{e}_x \pm N_z \mathbf{e}_z} (u_{\mathbf{q}})_j (\omega_{\mathbf{p}})_{k+} + \sum_{\mathbf{q}+\mathbf{p}=\mathbf{k} \pm N_x \mathbf{e}_x \pm N_y \mathbf{e}_y \pm N_z \mathbf{e}_z} (u_{\mathbf{q}})_j (\omega_{\mathbf{p}})_k \right],
\end{aligned} \tag{2.10}$$

where \mathbf{e}_x is a unit vector along x . The second third and fourth terms in the RHS of Eq. 2.10, represent singly aliased contributions. The next three terms represent the doubly aliased contributions and the last term is the triply aliased contribution.

The general rule of eliminating the aliased terms is by spherical truncation [6, 7], where all Fourier amplitudes for modes $|\mathbf{k}| \geq \frac{2k_{max}}{3}$ are eliminated. Here $k_{max} = \left(\frac{2\pi}{L_x}\right) \frac{N_x}{2}$, and the number of collocation points are assumed to be same along each direction $N_x = N_y = N_z$. This rule is also known as 2/3 rule in the literature.

The key to all pseudo-spectral solvers are the Fast Fourier Transform (FFT) algorithms which requires $\mathcal{O}(N \log_2 N)$ operations. The FFT algorithms make pseudo-spectral code competitive to any other finite-difference solvers [7, 8].

2.2.3 Two-dimensions

In two-dimensions where $\mathbf{u} = (u_x, u_y)$ is restricted in $x-y$ plane only, it is easy to define a scalar function (Ψ) such that the continuity equation $\nabla \cdot \mathbf{u} = 0$ is identically satisfied,

$$u_x = \partial_y \Psi, \tag{2.11}$$

$$u_y = -\partial_x \Psi. \tag{2.12}$$

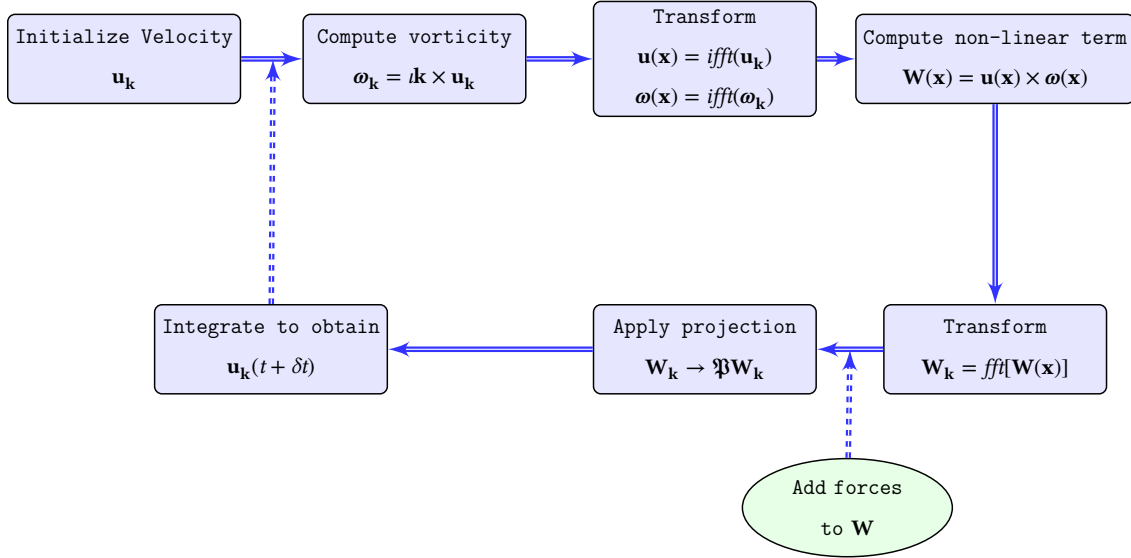
From 2.11 and 2.12, one finds $\omega = \nabla^2 \Psi$. In two-dimension, instead of \mathbf{u} , it is convenient to numerically integrate the vorticity equation,

$$\partial_t \omega + \mathbf{J}(\omega, \Psi) = \nu \nabla^2 \omega + (\nabla \times \mathbf{f}) \cdot \mathbf{e}_z, \tag{2.13}$$

where $J(\omega, \Psi) \equiv \partial_x \omega \partial_y \Psi - \partial_y \omega \partial_x \Psi$ is the Jacobian, and \mathbf{e}_z is a unit vector along z .

Pseudo-spectral algorithm

The schematic diagram for the algorithm of a pseudo-spectral code is shown below:



We use the FFTW (Fastest Fourier Transform in the West) library [9] to carry out all the Fourier transforms. Since we are interested in large scale simulations, we use the mpi version of the FFTW library for the parallel domain decomposition.

2.3 One- and two-way coupling

As discussed in the introduction, the equations of motion for a sub-Kolmogorov particle [10] are (1.23 and 1.24);

$$\begin{aligned} \frac{d\mathbf{X}_i(t)}{dt} &= \mathbf{V}_i(t), \\ \frac{d\mathbf{V}_i(t)}{dt} &= \frac{1}{\tau_p} [\mathbf{u}(\mathbf{X}_i, t) - \mathbf{V}_i(t)], \end{aligned}$$

where $i = 1, \dots, N_p$ is the particle index and N_p is the total number of particles in the suspension.

We use a second-order Runge-Kutta scheme [11, 12] to integrate 1.23 and 1.24 along each particle. Since the fluid equation is solved on a fixed Eulerian grids, which in general does not coincide with the positions of particles, $\mathbf{u}(\mathbf{X}_i)$ is obtained as,

$$\mathbf{u}(\mathbf{X}_i, t) = \sum_{\mathbf{x}} \mathbf{u}(\mathbf{x}, t) \delta(\mathbf{x} - \mathbf{X}_i) d\mathbf{x}, \quad (2.14)$$

where $\delta(\cdot)$ is a numerical approximation of the delta function. In this thesis, we use the Peskin [13] cosine function as the numerical delta function,

$$\delta(x - X) = \begin{cases} \frac{1}{4h} \left\{ 1 + \cos \left[\frac{\pi(x - X)}{2h} \right] \right\}, & |x - X| \leq 2h, \\ 0 & \text{otherwise,} \end{cases} \quad (2.15)$$

where h is the smallest grid spacing.

One-way coupling: At low Φ_V and mass-loading, the back-reaction of the particle on the fluid is ignored.

Two-way coupling: At high mass-loading the back-reaction force from the particle can not be ignored. From the Newton's third law of motion, the force density, due to the presence of particles is,

$$\mathbf{F}^{d \rightarrow g}(\mathbf{x}, t) = \sum_i \mathbf{f}_i^{d \rightarrow g} \delta(\mathbf{x} - \mathbf{X}_i), \quad (2.16)$$

where $\mathbf{f}_i^{d \rightarrow g} = \frac{m_p}{\tau_p} [\mathbf{V}_i(t) - \mathbf{u}(\mathbf{X}_i, t)]$, and m_p is the mass of a particle. The back-reaction from each particle is spread over a certain volume of the computational grid using 2.15. We shall refer to this method as particle in cell [14], which is extensively used in plasma physics. For convergence, it is recommended to have the more than one particle per cell [15, 16].

Exact Regularized Point Particle (ERPP)

In the method described above the forces from sub-grid size particle is instantly extrapolated to the fluid grid. Gualtieri *et al.* [16] and Ref. [15] introduced a new method which takes into consideration the time T_R required by the forces 2.16 at particle positions to reach the nearby grids. The total force density in the ERPP prescription is given by,

$$\mathbf{F}^{d \rightarrow g}(\mathbf{x}, t) = \sum_i \mathbf{f}_i^{d \rightarrow g}(t - T_R) g(\mathbf{x} - \mathbf{X}_i(t - T_R), T_R). \quad (2.17)$$

For more details of ERPP we refer the readers to Refs. [15, 16]. The explicit form of $g(\mathbf{x} - \mathbf{X}_i(t - T_R), T_R)$, is obtained by solving the diffusion equation for the disturbance generated by a particle,

$$g(\mathbf{x}, T_R) = \frac{1}{[4\pi\nu T_R]^{3/2}} \exp\left[-\frac{|\mathbf{x}|^2}{4\pi T_R}\right]. \quad (2.18)$$

The standard deviation of the Gaussian kernel given by 2.18 is taken, approximately as the grid spacing h , from which we estimate,

$$T_R = \frac{h^2}{2\nu}. \quad (2.19)$$

We remark that the Gaussian kernel given by 2.18 is similar to the one used in the earlier studies of Capecelatro and Desjardins [17].

2.3.1 Test case

We now compare the results obtained from the particle in cell method with the ERPP. For comparison we consider the case of a particle settling under gravity (\mathbf{g}), where,

$$\frac{d\mathbf{V}(t)}{dt} = \frac{1}{\tau_p} [\mathbf{u}(\mathbf{X}, t) - \mathbf{V}(t)] + m_p \mathbf{g}. \quad (2.20)$$

We place the particle in top of a two-dimensional domain of length $L_x = L_y = 2\pi$, discretized using 64 collocation points along each direction. The parameters for the study is given in Fig. 2.2. The particle after an initial acceleration attains a terminal velocity V_T as shown in the figure. We find that the both particle in cell and ERPP predicts the same V_T . A slight departure from the theoretical solution $V(t) = V_T [1 - \exp(-t/\tau_p)]$, is observed in both the methods [16].

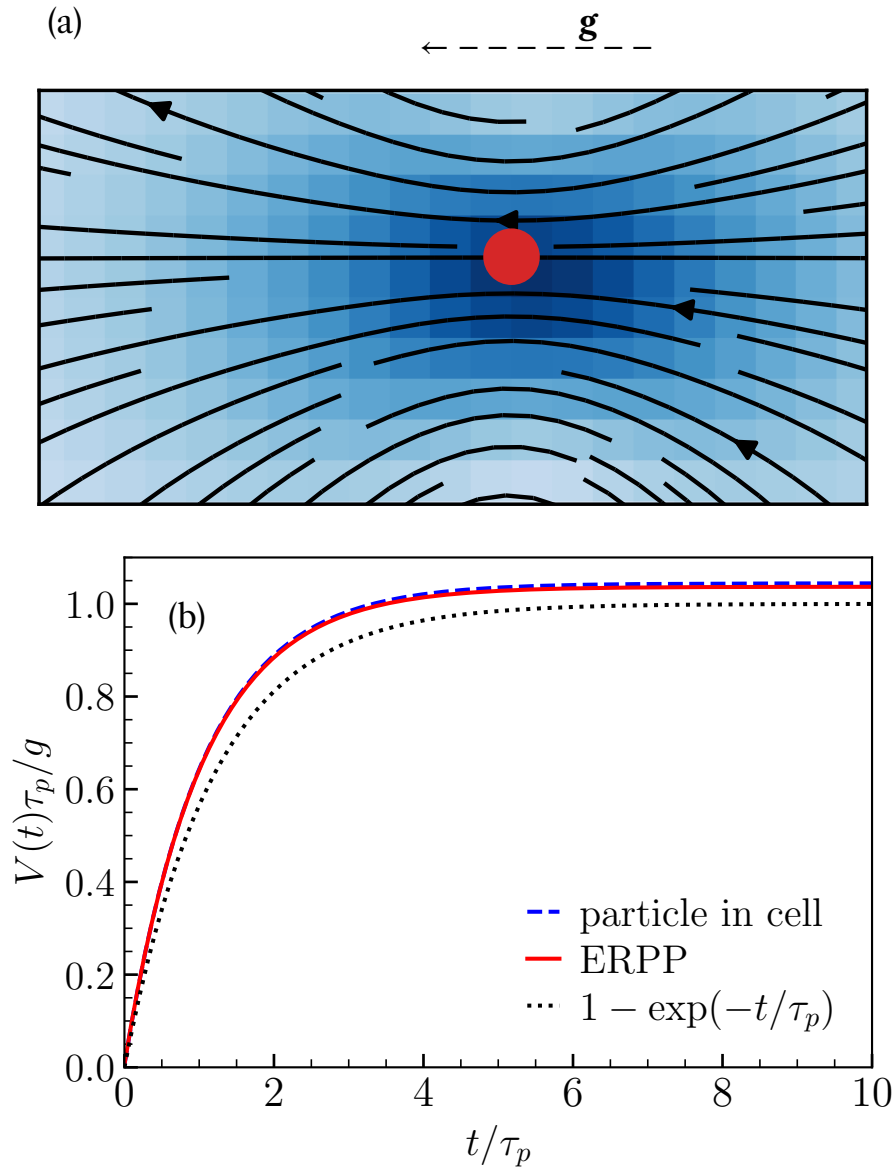


Figure 2.2: (a) The velocity streamlines overlaid over the pseudo-color plot of $|\mathbf{u}|$ at time $t = 3.0\tau_p$. The bright blue color indicates the region with high velocity. The arrow in the top marks the direction of gravity and red dot indicates the particle position. (b) The normalized settling velocity of the particle obtained using ERPP and particle in cell. We take $\tau_p = 1.0$, $m_p = 0.33$, $g = 0.2$ and $\nu = 1.6$.

In the particle equation of motion 1.24, $\mathbf{u}(\mathbf{X}, t)$ represents the undisturbed fluid velocity. A two-way coupling introduces small self-induced disturbances around the particle, leading to the observed error in the estimated value of the terminal velocity [Fig. 2.2(b)] [16, 18].

2.4 Buoyancy-driven bubbly flows

We begin by rewriting the NS equations 1.25 and 1.26 for an incompressible velocity field \mathbf{u} governing the buoyancy-driven bubbly flows,

$$\rho [\partial_t \mathbf{u} + \mathbf{u} \cdot \nabla \mathbf{u}] = -\nabla p + \nabla \cdot [2\mu \nabla \mathcal{S}] + \mathbf{F}^\sigma + \mathbf{F}^g, \quad (2.21)$$

$$\partial_t \rho + \mathbf{u} \cdot \nabla \rho = 0, \quad (2.22)$$

where $\mathbf{F}^\sigma = \sigma \kappa \mathbf{n}$, is the force density due to surface tension, defined in terms of σ , the coefficient of surface tension, κ , the curvature and \mathbf{n} , the unit normal to the interface, and $\mathbf{F}^g = (\rho - \rho_a) \mathbf{g}$, is the buoyancy force density, in which \mathbf{g} is the acceleration due to gravity, ρ_a is the average density.

Here it is convenient to define, the density, and the viscosity using the marker function c ,

$$\rho = \rho_f c + \rho_b (1 - c), \quad (2.23)$$

$$\mu = \mu_f c + \mu_b (1 - c). \quad (2.24)$$

where,

$$c = \begin{cases} 1, & \text{in the fluid phase,} \\ 0, & \text{in the bubble phase.} \end{cases} \quad (2.25)$$

2.4.1 Non-dimensional numbers

The NS 2.21 is non-dimensionalized using the transformation $x^* \rightarrow \frac{x}{d}$, $u_i^* = \frac{u_i}{U}$ and $t^* \rightarrow \frac{tU}{d}$, where d is the diameter of the bubble, and U is the characteristic velocity scale to obtain,

$$\partial_t \mathbf{u}^* + \mathbf{u}^* \cdot \nabla^* \mathbf{u}^* = -\nabla^* p^* + \frac{1}{\text{Ga}} \nabla^{*2} \mathbf{u}^* + \frac{1}{\text{Bo}} \mathbf{F}^{*\sigma} + \frac{1}{\text{Fr}} \mathbf{F}^{*g}. \quad (2.26)$$

Here $\text{Ga} = \rho_f U d / \mu_f$ is the Galilei number, $\text{Bo} = \rho_f U^2 d / \sigma$ is the Bond number, and $\text{Fr} = U^2 / |\mathbf{g}| d$ is the Froude number. In buoyancy-driven bubbly flows, the characteristic velocity scale is defined using d , $U = \sqrt{\delta \rho g d / \rho_f}$ ($\delta \rho = \rho_f - \rho_b$). Replacing, we get $\text{Ga} = \sqrt{g \rho_f \delta \rho d^3} / \mu_f$, $\text{Bo} = \delta \rho g d^2 / \sigma$, and $\text{Fr} = \delta \rho / \rho_f$. In addition,

the other important non-dimensional numbers here, are the viscosity ratio $\mu_r = \mu_f/\mu_b$, and the Atwood number $At = \delta\rho/(\rho_f + \rho_b)$. Physically, Ca gives the relative strength of the buoyancy and the viscous forces, and Bo gives the relative strength of buoyancy and the surface tension forces. The Galilei number Gal , gives the relative strength of the buoyancy and the viscous forces, and the Bond number Bo , gives the relative strength of buoyancy and the surface tension forces.

Note that the Reynolds number $Re = V_0 d/\nu$ in buoyancy-driven bubbly flows is defined using the rise velocity V_0 , of an isolated bubble.

2.4.2 Boussinesq approximation

In the regime where the viscosity μ_f is comparable to μ_b , and the density difference is small, the Navier-Stokes 2.21 gets simplified to [19],

$$\partial_t \mathbf{u} + \mathbf{u} \cdot \nabla \mathbf{u} = \frac{-\nabla p}{\rho_a} + \nu \nabla^2 \mathbf{u} + \frac{\mathbf{F}^\sigma}{\rho_a} + \frac{\delta\rho c}{\rho_a} \mathbf{g}, \quad (2.27)$$

where, the contribution due to the density difference $\delta\rho$ is retained only in the external forcing and ignored everywhere else. Here, the simplified form of the viscous term can be dealt accurately using exponential integrators [20]. In the next section, we describe the front-tracking method to evaluate the surface tension and the gravity force densities.

2.4.3 Front-tracking (FT)

This method was developed by Peskin [13] and Unverdi and Tryggvason [21] to solve the multiphase flows consisting of two-fluids mixture. In this method, the interface of two-phase, also known as the front, is tracked in the fluid as a Lagrangian mesh. In Fig. 2.3 we show illustrative diagram depicting the front-tracking method in both two- and three-dimensions. The front is represented by a set of points (\mathbf{x}_p), which are connected by elements. In two-dimensions the element is a line, whereas, in three-dimensions the element is a triangle (or any two-dimensional geometric shape).

The NS equations are solved on a fixed grid but the front-properties such as surface tension are calculated at the front point \mathbf{x}_p , which does not nec-

essarily, coincide with the fluid grid. Hence, all the quantities that exist at \mathbf{x}_p needs to be extrapolated to the fluid grid points \mathbf{x} . Any front quantity, say α_p evaluated at \mathbf{x}_p , is approximated on the underlying grid points (\mathbf{x}) as

$$\alpha(\mathbf{x}) = \sum_p \alpha_p \delta(\mathbf{x} - \mathbf{x}_p), \quad (2.28)$$

where $\delta(\mathbf{x} - \mathbf{x}_p) = \delta(x - x_p)\delta(y - y_p)\delta(z - z_p)$ is a three- (or two-) dimensional Dirac-delta function. The numerical approximation of δ function that we use is given by 2.15.

Estimation of surface tension

The surface tension force on each front element is given by,

$$\delta\mathbf{F}^\sigma = \int dS \sigma \kappa \mathbf{n}, \quad (2.29)$$

where the integration is over an element of a front. From the relation, $\kappa \mathbf{n} = \mathbf{n} \times \nabla \mathbf{n}$ this force gets simplified to,

$$\delta\mathbf{F}^\sigma = \int dl \sigma (\mathbf{t} \times \mathbf{n}), \quad (2.30)$$

where \mathbf{t} is the vector tangent to the edge of the element and the integration is over the line dl . The force given in 2.30 can be evaluated at each element and extrapolated to fluid grid using 2.28.

In two-dimensions, the curvature $\kappa \mathbf{n} = \frac{\partial \mathbf{t}}{\partial t}$ and the surface tension term over a small line element gets simplified to

$$\delta\mathbf{F}^\sigma = \sigma (\mathbf{t}_2 - \mathbf{t}_1), \quad (2.31)$$

where \mathbf{t} is the tangent to the interface.

Evaluation of c

At the interface, it is easy to see that, $\nabla c(\mathbf{x}) = \mathbf{n} \delta(\mathbf{x} - \mathbf{x}_p)$. Using the approximate value of ∇c at the fluid grid \mathbf{x} , the marker function can be evaluated by solving the following Poisson equation,

$$\nabla^2 c(\mathbf{x}) = \nabla \cdot \sum_p \mathbf{n} \delta(\mathbf{x} - \mathbf{x}_p). \quad (2.32)$$

The 2.32 can be easily inverted in the Fourier space.

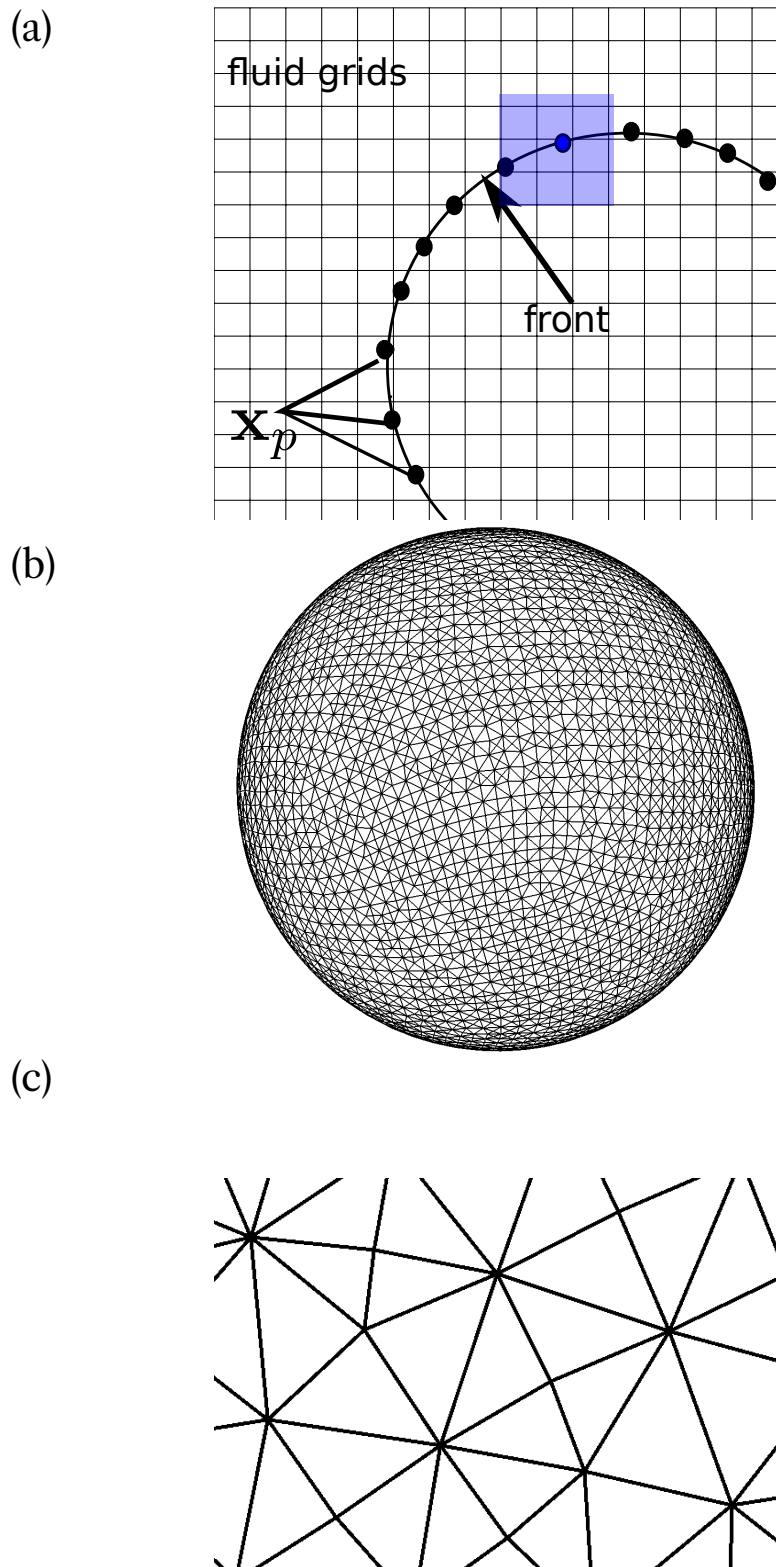


Figure 2.3: (a) The two-dimensional front constructed by connecting the points \mathbf{x}_p . The fluid grids are fixed in space but the front is evolved as Lagrangian points. The blue shaded region in the figure represents the two-dimensional approximation of $\delta(\mathbf{x})$ at the blue point. (b) A spherical front in three-dimensions and (c) a section showing the triangular elements.

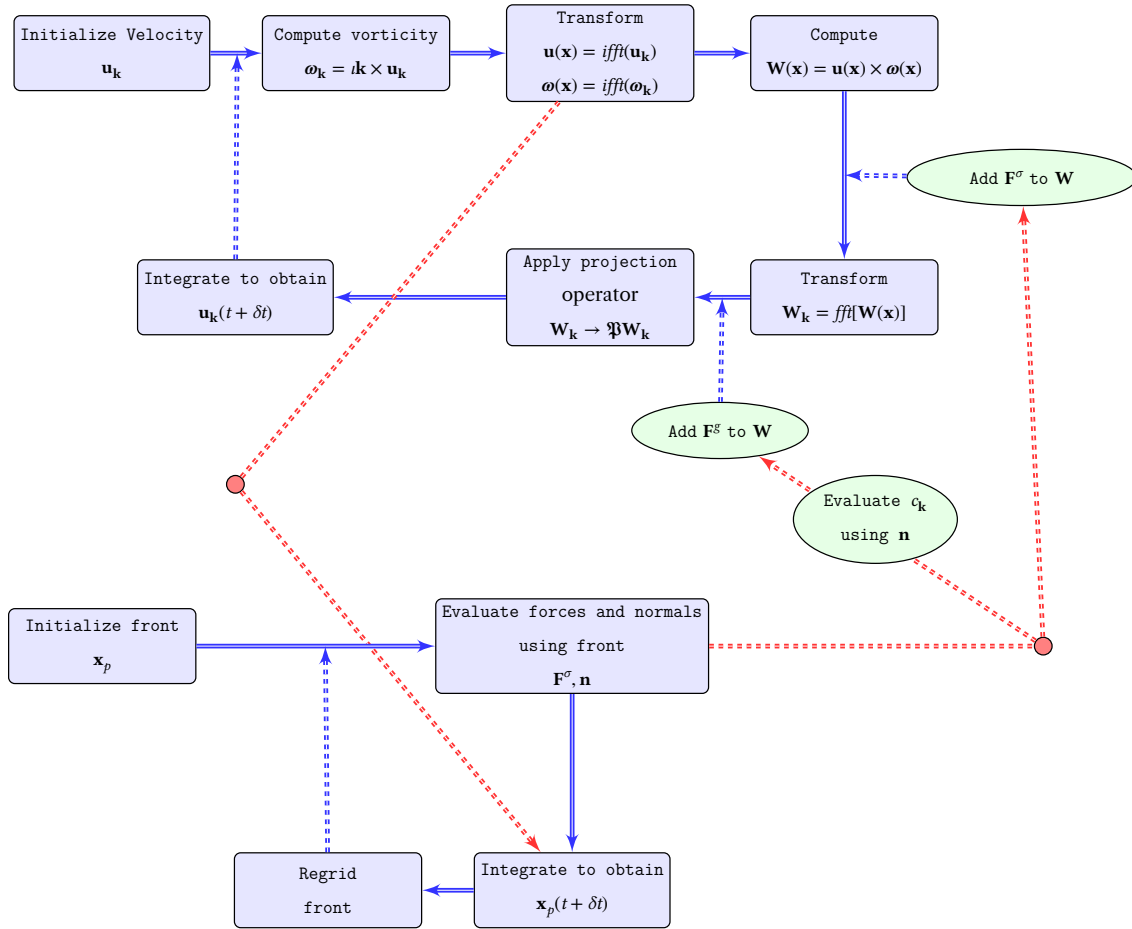
Advancing the front

The front point are advanced in time as $\mathbf{x}_p(t + \delta t) = \mathbf{x}_p + \delta t \mathbf{u}(\mathbf{x}_p)$, where

$$\mathbf{u}(\mathbf{x}_p) = \sum_{\mathbf{x}} \mathbf{u}_{\mathbf{x}} \delta(\mathbf{x} - \mathbf{x}_p) h^3. \quad (2.33)$$

Pseudo-Spectral Front-Tracking (PSFT) algorithm

The schematic of Pseudo-Spectral Front-Tracking (PSFT) algorithm for buoyancy-driven bubbly flow is shown below



Time step

The time step in the solver is decided by the Courant-Friedrichs-Lewy condition,

$$\max ((|u_x|, |u_y|, |u_z|)) \frac{\delta t}{h} < 1/2 \quad (2.34)$$

where $\max(\cdot)$ represents the maximum value of the argument.

2.5 PARIS

PARIS (PARallel Robust Interface Simulator) [22] is an open source multi-phase solver which has the option to select either, volume-of-fluid [23] or front-tracking to simulate the bubbles. In this thesis, we use the front-tracking.

We now validate the front-tracking in PARIS and contrast the result with the study of Cano-Lozano *et al.* [24], conducted using an open-source volume-of-fluid solver Gerris [25]. For the comparison, we consider the isolated bubble simulation “Bubble-26” in Ref. [24] (parameters given in Table 2.1). The bubble rises in a spiraling trajectory and the structure of the vorticity along gravity direction $\omega_z = (\nabla \times \mathbf{u})_z$ consists of a streamwise pair intertwined like a cork-screw (See Fig. 10 and 11 in [24]). We conduct the simulation in a domain of size $4.8d \times 4.8d \times 60d$, and discretize it uniformly by taking 2×10^8 collocation points which implies 55 grids points along bubble diameter. The simulation is expensive and takes about 9 seconds per iterations on 501 Intel(R) Xeon(R) (E5-2620) processors. We take a periodic boundary on all sides, in contrast to Cano-Lozano *et al.* [24] where outflux boundary at the top, and wall boundary at the remaining sides was taken.

We show the trajectory of the bubble obtained from PARIS in Fig. 2.4 and the iso-vorticity contours corresponding to $\omega_z = \pm 0.24$ when $Z/d = 120$ in Fig. 2.5. We find that the wake structure as well as the trajectory is identical to the one reported by [24]. However, a minor difference is observed in the diameter of the spiral (Fig. 2.4). As opposed to the reported value of $0.28d$, we find the diameter to be $0.2d$. This difference can be attributed to the different boundary conditions, and the domain size considered in our simulation.

Ga	Bo	At $\times g$	μ_f/μ_b
100.25	10.0	0.999×1	100

Table 2.1: The non-dimensional parameters from the simulation of Cano-Lozano *et al.* [24]. The density contrast ρ_f/ρ_b , between the phases is taken to be 10^3 .

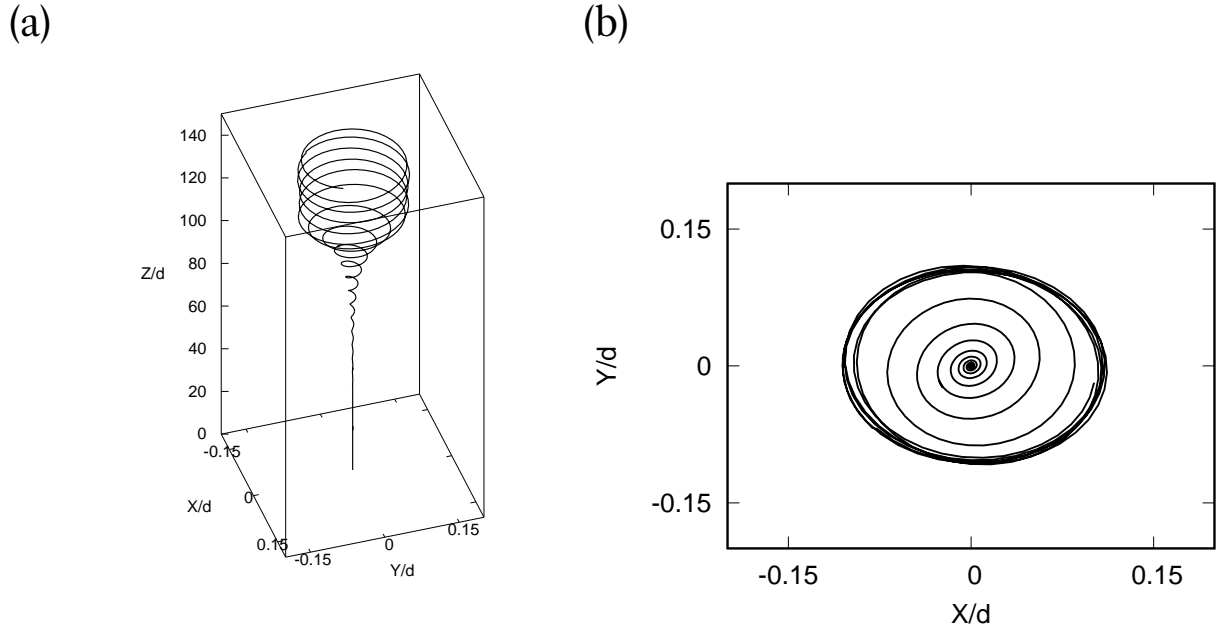


Figure 2.4: (a) The three dimensional trajectory of the bubble for parameters given in Table 2.1. (b) The trajectory in (a) projected in the x-y plane.

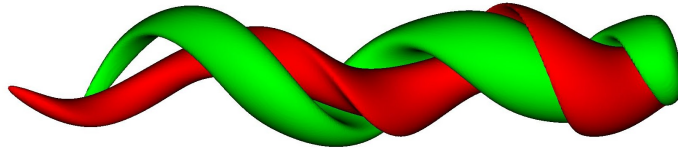


Figure 2.5: The iso-vorticity contour of ω_z corresponding to values $\omega_z = \pm 0.24$ ($\omega_z = 0.24$ is shown in green).

2.6 Test Cases

Since the PSFT code is valid only for low At numbers, we focus on the cases where the density difference between the two fluids is small and their viscosity is identical. For the tests, we consider the case of a single bubble rising under gravity. Table (2.2) summarizes the parameters used in our DNS.

We consider a cuboidal domain of dimensions $L_x = L_y$ and $L_z = 2L_x$. We find that this choice ensures that the effect of the bubble-wake interaction is minimal. All the results are presented in the units of the bubble diameter

d and the number of grid point along the bubble diameter d , $N_g = d/h$. We fix $L_z = 10.8d$ and apply periodic boundary conditions at all sides.

In the following sub-sections, we present the two methods to integrate the forces from the front to the fluid grid. We shall also contrast the results from the PSFT simulation with the solutions obtained using an open-source interface solver, PARIS [22, 26], which we have validated in the previous section.

Ga	Bo	At \times g
296.0	1.95	0.04×10.5

Table 2.2: The non-dimensional numbers for the single bubble test case.

2.6.1 Method-1

We begin by examining the effect of de-aliasing adopted in PSFT code on the numerical delta function (2.15). We first define an operator \mathbb{P} , which eliminates all the Fourier amplitudes greater than the aliasing mode k_a . Using \mathbb{P} , the de-aliasing operation on any periodic function $f(\mathbf{x})$ is defined as,

$$\mathbb{P}f(\mathbf{x}) \equiv \sum_{m \leq k_a} \exp(i\mathbf{m} \cdot \mathbf{x})f_{\mathbf{m}}, \quad (2.35)$$

where $f_{\mathbf{m}}$ is the Fourier transform of $f(\mathbf{x})$.

In Fig. 2.6, we show $\mathbb{P}\delta(x - x_p)$ for one-dimensional delta function. It is evident that the aliasing correction results in grid size oscillations.

The error due to aliasing correction can be resolved by choosing a $\delta(x - x_p)$ consistent with the 2/3 de-aliasing adopted in the PSFT algorithm. To find a consistent δ , we make the transformation $h \rightarrow 3h/2$ to obtain,

$$\delta(x - x_p) = \begin{cases} \frac{1}{6h} \left[1 + \cos\left(\frac{\pi(x-x_p)}{3h}\right) \right], & |x - x_p| \leq 3, \\ 0 & \text{otherwise.} \end{cases} \quad (2.36)$$

In Fig. 2.7 we show that using 2.36 for numerical approximation of $\delta(\cdot)$, the grid-size oscillations obtained previously gets suppressed.

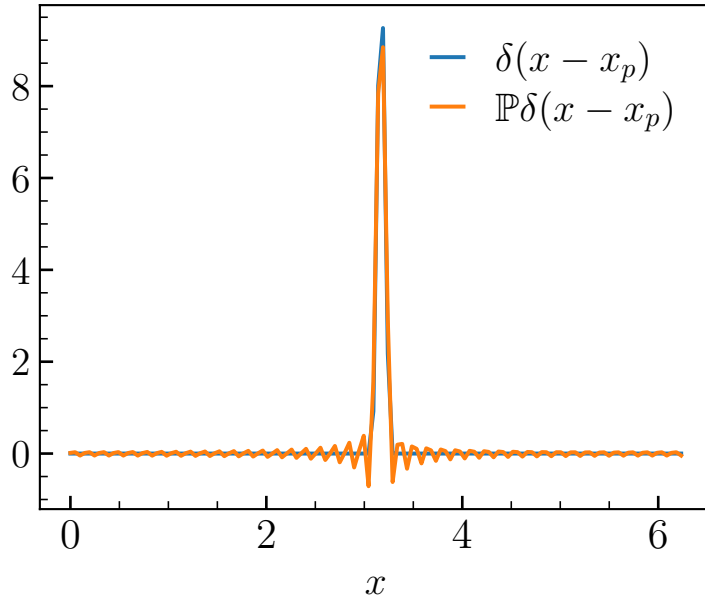


Figure 2.6: The numerical approximation of one-dimensional delta function $\delta(x - x_p)$ and $\mathbb{P}\delta(x - x_p)$. For the study we take $h = \frac{2\pi}{64}$. De-aliasing of δ results in small scale grid size oscillations

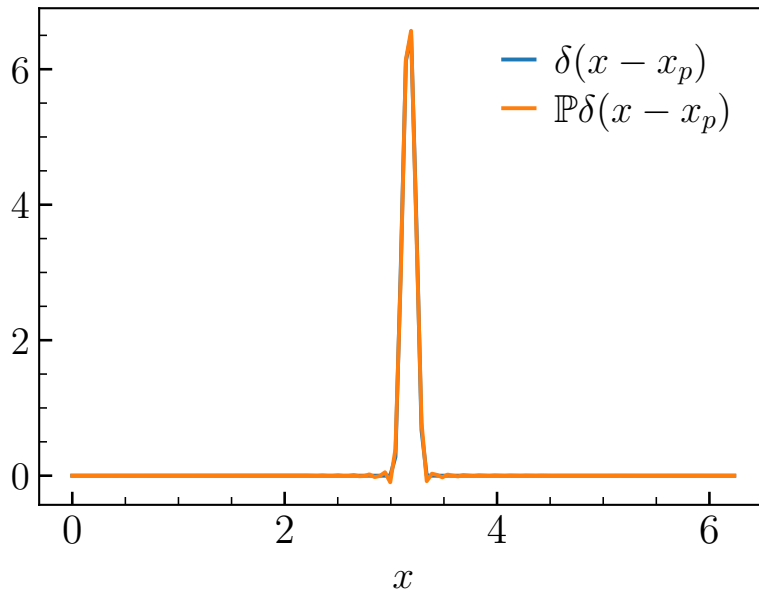


Figure 2.7: The $\delta(x - x_p)$ and $\mathbb{P}\delta(x - x_p)$ for the delta function given by 2.36.

We conduct the single bubble test using 2.36 for front-grid communication. In Fig. 2.8, we show the z-component of the vorticity, $\omega_z = (\nabla \times \mathbf{u})_z$, at $t = 9.0$, at three different resolutions $N_g = 24, 48$ and 70 . For a direct comparison, we show the ω_z obtained from the PARIS simulation at same time

and resolutions in Fig. 2.9. Clearly the ω_z resembles only qualitatively and spurious structures are present near bubble interface.

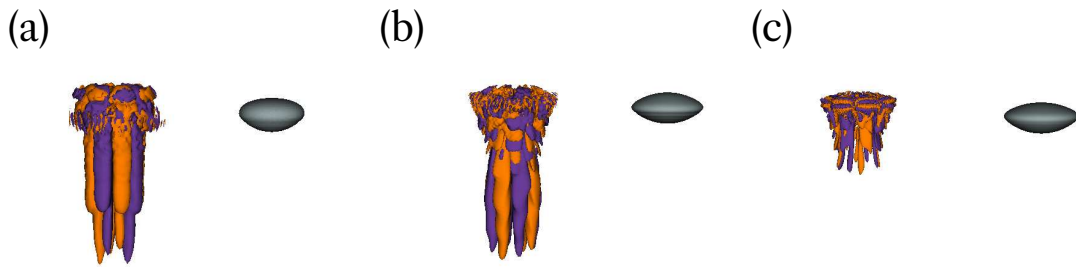


Figure 2.8: The iso-contour plot of ω_z and the bubble shape at time $t = 9.0$ obtained from PSFT simulation of a rising bubble at $Ga = 296$. For the front to grid communication we use the modified delta function given by 2.36. We show the iso-vorticity contours corresponding to $\omega_z = -0.01$ (orange) and $\omega_z = 0.01$ (purple). The results are shown for (a) $N_g = 24$, (b) $N_g = 48$, and (c) $N_g = 70$.

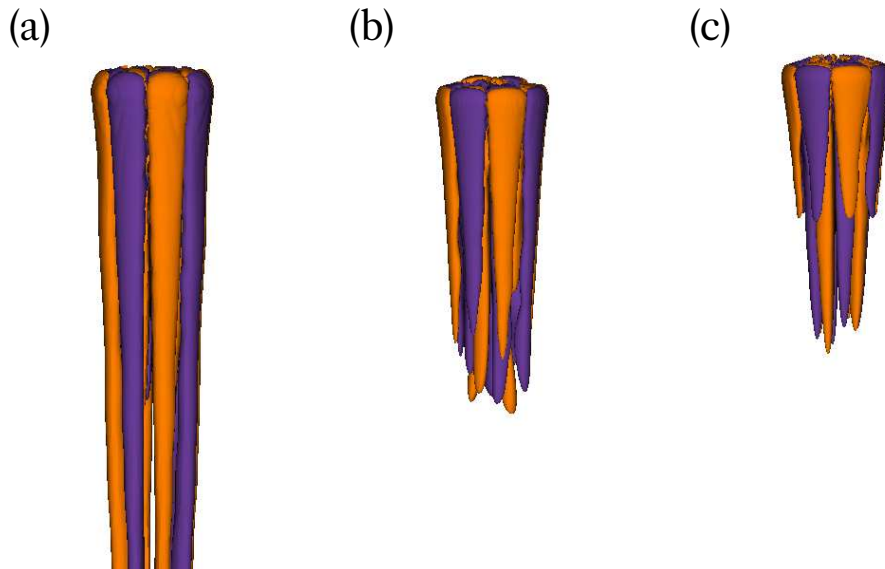


Figure 2.9: The iso-contour plot of ω_z at time $t = 9.0$ obtained from PARIS simulation of a rising bubble at $Ga = 296$. We show the iso-vorticity contours corresponding to $\omega_z = -0.01$ (orange) and $\omega_z = 0.01$ (purple). The results are shown for (a) $N_g = 24$, (b) $N_g = 48$, and (c) $N_g = 70$.

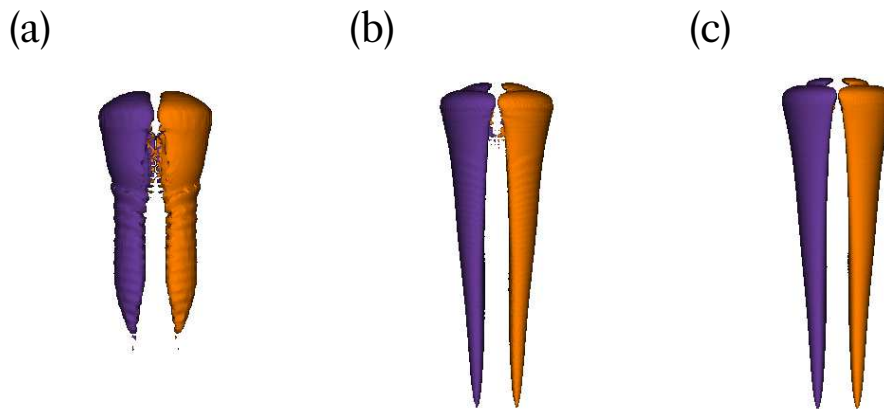


Figure 2.10: The iso-contour plot of ω_x at time $t = 9.0$ obtained from PSFT simulation of a rising bubble at $Ga = 296$. We show the iso-vorticity contours corresponding to $\omega_x = -1.0$ (orange) and $\omega_x = 1.0$ (purple). The results are shown for (a) $N_g = 24$, (b) $N_g = 48$, and (c) $N_g = 70$.

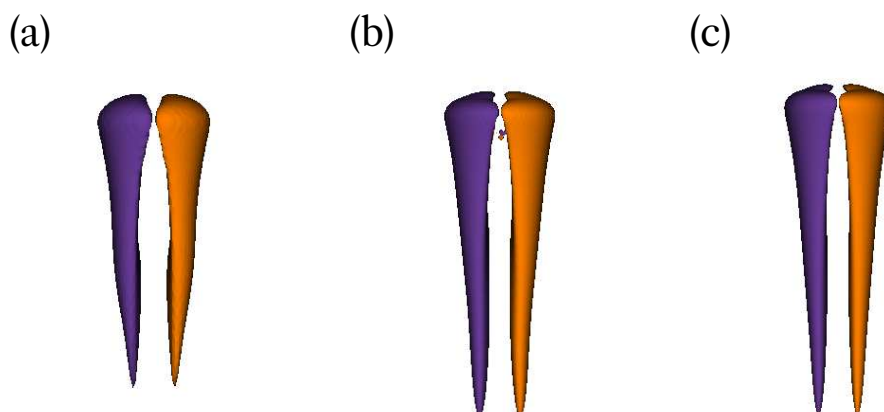


Figure 2.11: The iso-contour plot of ω_x at time $t = 9.0$ obtained from PARIS simulation of a rising bubble at $Ga = 296$. We show the iso-vorticity contours corresponding to $\omega_x = -1.0$ (orange) and $\omega_x = 1.0$ (purple). The results are shown for (a) $N_g = 24$, (b) $N_g = 48$, and (c) $N_g = 70$.

We further compare the one of the lateral component of the vorticity, ω_x , where we show the results from PSFT simulation in [Fig. 2.10](#) and PARIS in

Fig. 2.11. We find that the ω_x obtained from PSFT is identical to PARIS simulation. We have verified that, in PSFT, the spurious effects are present only in ω_z and all the other fields including velocity and the other components of the vorticity are smooth.

2.6.2 Method-2

In the previous section, we observed that the proper choice of δ function and aliasing correction leads to a considerable reduction in the grid-level oscillations. However, the resulting structure of ω_z obtained using PSFT is considerably different in comparison with PARIS. We now show how an improved implementation of the surface tension term leads to flow structures consistent with other solvers (PARIS and Basilisk).

The numerical delta function given by 2.36 is differentiable only upto second-order [27]. Therefore, we find the solenoidal component of \mathbf{F}^σ using a scheme consistent with the second-order differentiability of the delta function. To obtain the solenoidal component of the surface tension (\mathbf{F}_s^σ) we solve the following vector identity,

$$\nabla \times \nabla \times \mathbf{F}^\sigma = \nabla^2 \mathbf{F}_s^\sigma(\mathbf{x}) \quad (2.37)$$

for \mathbf{F}_s^σ . The above equation (2.37) is inverted in the Fourier space using a central-difference scheme described below.

The derivative of a general function $f(x)$ can be approximated as,

$$\partial_x f(x) = \frac{f(x+h) - f(x-h)}{2h}. \quad (2.38)$$

Taking the Fourier transform of the right hand side of 2.38, we obtain,

$$\frac{f(x+h) - f(x-h)}{2h} = \sum_k \frac{[f_k \exp(ik(x+h)) - f_k \exp(ik(x-h))]}{2h}, \quad (2.39)$$

which can be simplified to,

$$\frac{f(x+h) - f(x-h)}{2h} = i \sum_k \frac{\sin(kh)}{h} [f_k \exp(ikx)]. \quad (2.40)$$

Following similar steps in three-dimensions to estimate ∇ and ∇^2 2.37 can be trivially inverted to obtain \mathbf{F}_s^σ . The resultant \mathbf{F}_s^σ is then added to the nonlinear terms during the evolution of NS equation.

We show ω_z as obtained in Fig. 2.12. For front to grid communication, we use δ given by 2.36. Evidently, when the derivative of F^σ is evaluated using a central-difference scheme, the obtained vorticity structure resembles with the PARIS simulation.

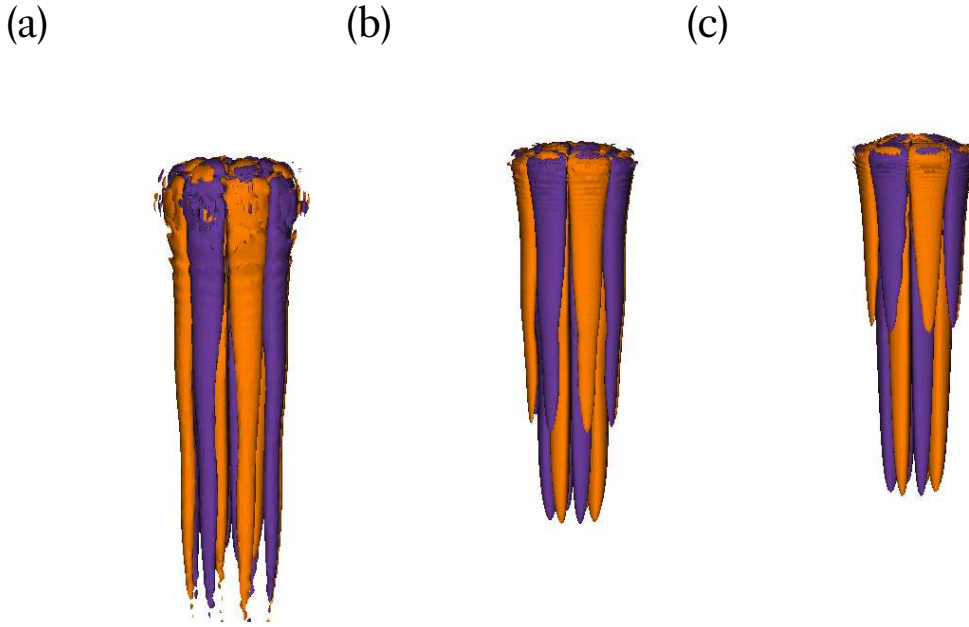


Figure 2.12: The iso-contour plot of ω_z at time $t = 9.0$ obtained from PSFT simulation of a rising bubble at $Ga = 296$ using method-2. We show the iso-vorticity contours corresponding to $\omega_z = -0.01$ (orange) and $\omega_z = 0.01$ (purple). The results are shown for (a) $N_g = 24$, (b) $N_g = 48$, and (c) $N_g = 70$.

We now compare all the three schemes PSFT, front-tracking from PARIS and volume-of-fluid from Basilisk [28] by conducting a simulation of an isolated bubble for the parameters given in Table (2.3).

Ga	Bo	At \times g
93.1	1.44	0.04 \times 2.5

Table 2.3: The non-dimensional numbers for the single bubble test case. We take a cubic domain of length $L_x = 5d$ and discretize each side with $N_x = 128$ points.

Note that PARIS and Basilisk have been validated in many previous studies [22, 24, 29–31]. In Fig. 2.13 we show the position of the z-component

of the bubble center of mass with time and find very minor differences in the trajectory. We show the iso-contour of the streamwise vorticity overlaid on the bubble position in Fig. 2.14. The core structure of ω_z consists of three pairs of counter-rotating vortices. We note that the choice of different algorithms to evaluate surface tension results in minor differences in flow structure around the bubble.

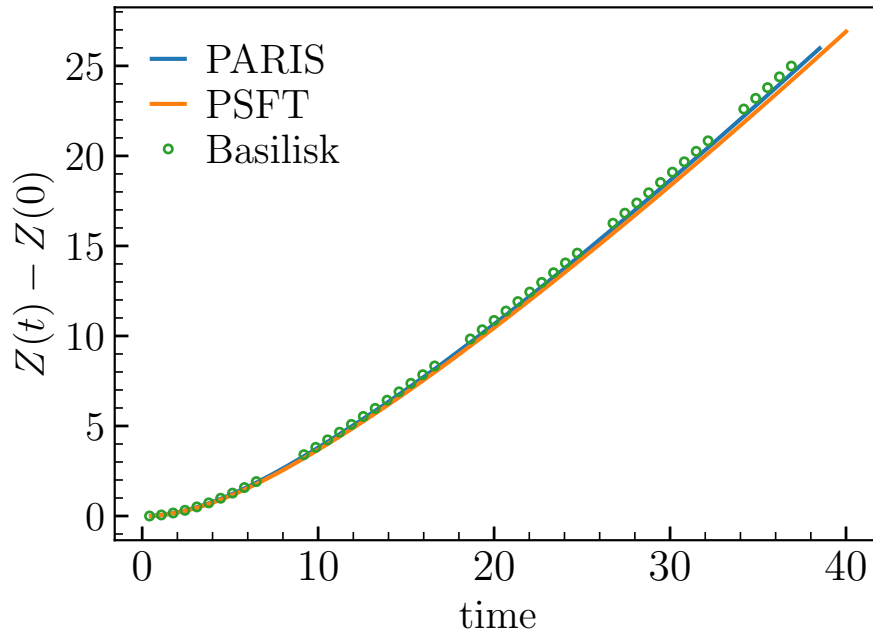


Figure 2.13: The z-component of the bubble center-of-mass with time predicted by different solvers.

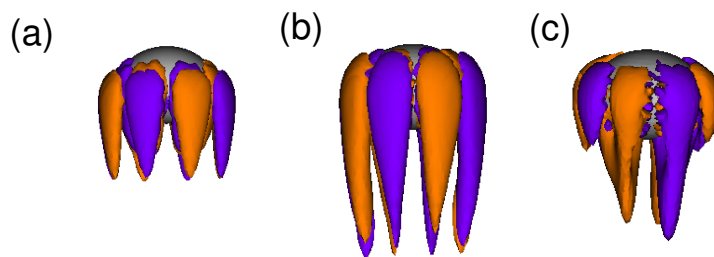


Figure 2.14: The iso-contour plot of ω_z at time $t = 10.0$ for (a) PSFT, (b) PARIS, and (c) Basilisk simulation. We show the iso-vorticity contours corresponding to $\omega_z = -0.01$ (orange) and $\omega_z = 0.01$ (purple).

2.6.3 Bubble shape and the Reynolds number

In this section, we compare the bubble shapes obtained from different simulations at time $t = 9.0$ and the bubble Reynolds number for parameters given in Table (2.2). We begin by showing the bubble shape obtained using method-1 at different resolutions in Fig. 2.15. We find the bubble is ellipsoidal and has grid size ripples on the bottom. The ripples at the bottom is clearly a numerical artifact as at highest resolution ($N_g = 70$), it become insignificant. A similar conclusion can be drawn from Fig. 2.16, where we show the bubble shapes obtained using PARIS.

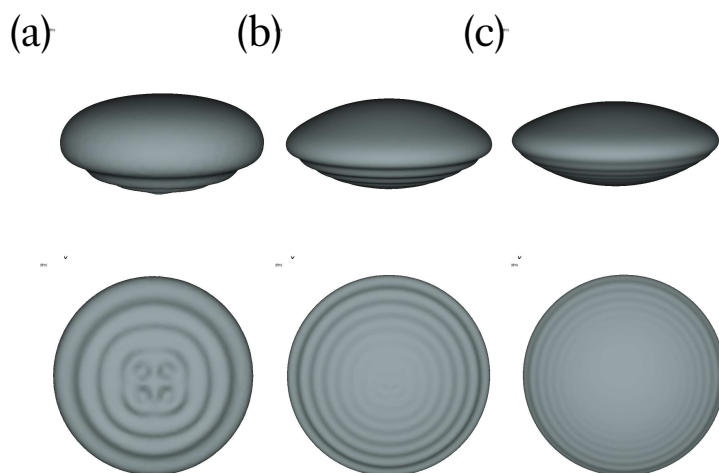


Figure 2.15: Side and bottom view of the bubble at $t = 9.0$ from the simulation conducted using the method described in method-1 above for (a) $N_g = 24$, (b) $N_g = 48$, and (c) $N_g = 70$.

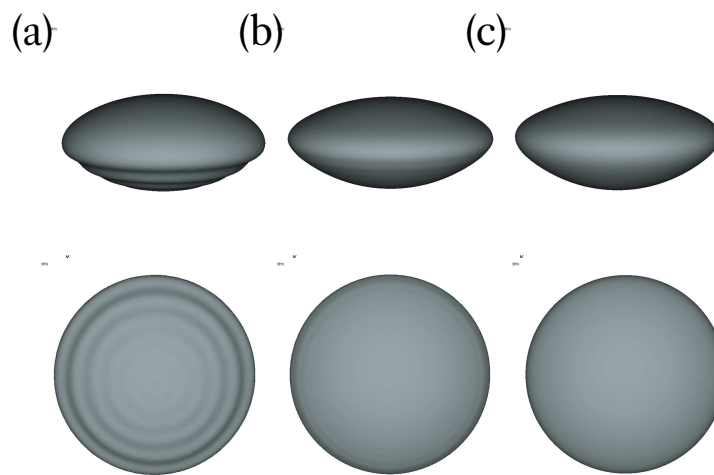


Figure 2.16: Side and bottom view of the bubble at $t = 9.0$ from the simulation conducted using PARIS for (a) $N_g = 24$, (b) $N_g = 48$, and (c) $N_g = 70$.

In [Fig. 2.17](#) we plot the bubble Reynolds number Re as obtained from simulation conducted as described in method-1 and 2 above. For each of the cases, we compare the Re from PSFT at three resolutions namely $N_g = 24$, 48 and $N_g = 70$ with the results of PARIS. We find the steady state value of the Re to be identical in all the cases.

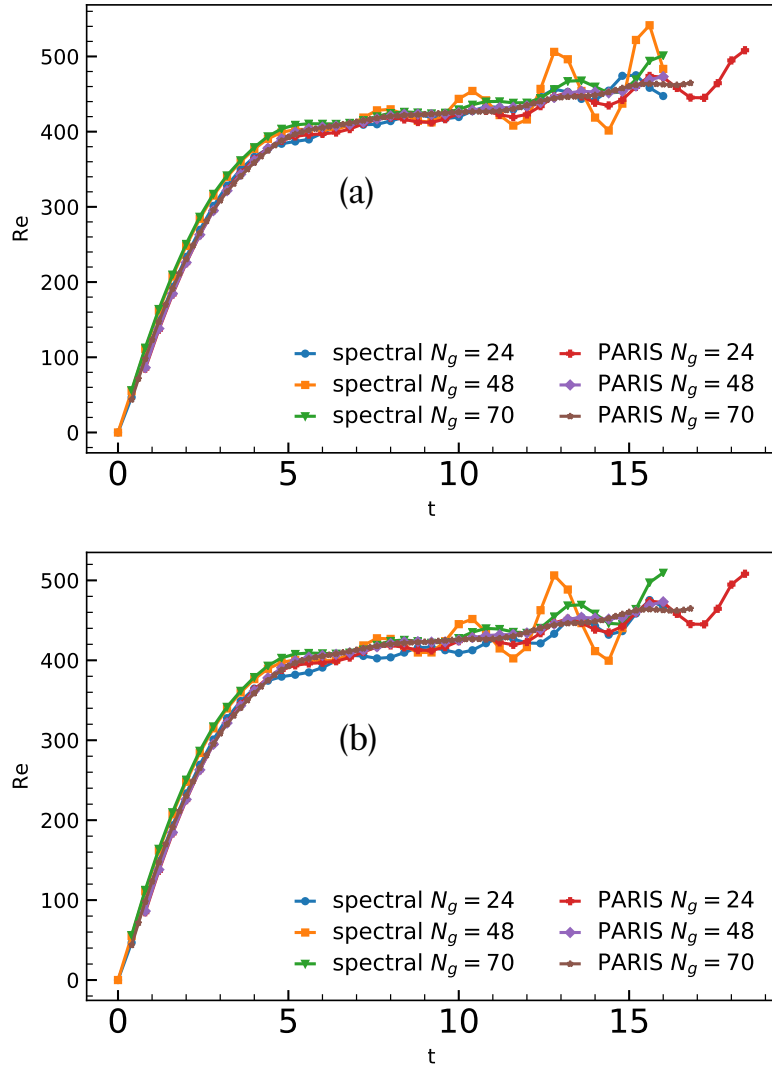


Figure 2.17: The comparison of the bubble Reynolds number as obtained from the simulation done using (a) method-1 and (b) method-2 with PARIS.

2.6.4 Two-dimensional test

In this section, we conduct the single bubble test in two-dimension and contrast it with the results obtained using the code ‘f2c2d-pv’ [32]. F2c2d-pv is an open-source two-dimensional front-tracking simulator developed by Trygvasson and similar to PARIS is second-order accurate in both space and time. Same as three-dimensions here we compare the ω for the parameters given in Table (2.2).

In Fig. 2.18 we show the ω obtained using the method-1 version of the algorithm described in previous section. Here we find the error in ω to be

minimal and the small scale vorticity structure are insignificant. Moreover, upon increasing the resolution these structures disappears. In Fig. 2.19, we further show the results obtained from f2c2d-pv. It is very evident that the ω obtained here is comparable with the method-1. We find that the bubble trajectory obtained using f2c2d-pv.f deviates from straight trajectory earlier compared to PSFT simulation and thus results in the tilted vorticity structure.

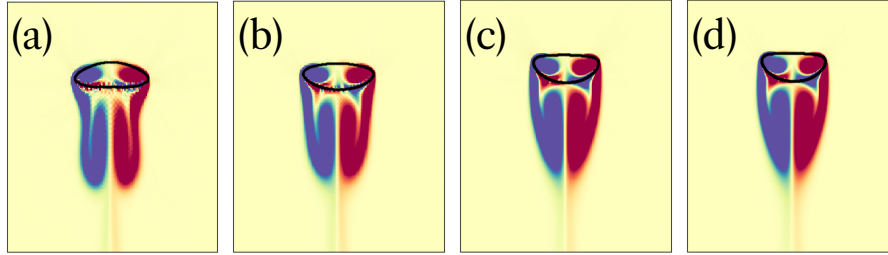


Figure 2.18: The pseudo-color plot of ω at time $t = 9.0$ obtained from PSFT simulation of a rising bubble at $Ga = 296$ in two-dimension using method-1. The color blue corresponding to $\omega = -1.8$ and red corresponds to $\omega = 1.8$. The results are shown for (a) $N_g = 24$, (b) $N_g = 48$, and (c) $N_g = 70$ and (d) $N_g = 96$. The bubble is drawn using black line in all the figures.

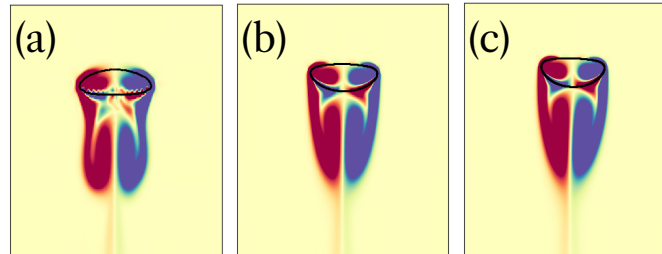


Figure 2.19: The pseudo-color plot of ω at time $t = 9.0$ obtained using f2c2d-pv [32]. The color blue corresponding to $\omega = -1.8$ and red corresponds to $\omega = 1.8$. The results are shown for (a) $N_g = 24$, (b) $N_g = 48$, and (c) $N_g = 70$ and (d) $N_g = 96$. The bubble is drawn using black line in all the figures.

In two-dimensions, the stream-function vorticity formulation gives tremendous advantage as the pressure gets eliminated completely and both vorticity and velocity fields is obtained from same scalar Ψ . This could be the reason that the spurious effects are insignificant here compared to three-dimensional study.

Before proceeding further we shall summarize the main results of this section below.

- The front-tracking method can be coupled to PSFT Navier-Stokes equation to study multiphase flows in the low At number regime.
- The aliasing correction on the numerical approximation of δ results in small grid size oscillations. With the proper choice of $\delta(x)$ these small scale structures can be reduced or eliminated.
- We find that 48 grids per bubble diameter to be enough to resolve the vorticity structures and bubble shape accurately at $Ga \approx 300$.

2.6.5 Multiple bubbles

We shall now compare the statistical properties of the flow generated by multiple bubbles rising under gravity. For simplicity and ease of simulation, we choose only $N_b = 4$ bubbles at $Ga = 296$ in a domain of size $L_x = L_y = L_z = 5.4d$ and resolve individual bubbles by taking $N_g = 24$. Clearly, at this N_g , the ω_z structure obtained from PSFT simulation have small scale spurious structures [section (2.6)]. Here, we show that in the multiple bubble study such structures disappears when bubbles' wake interactions are stronger.

The main motivation to conduct simulation with just 4 bubbles is to get insights into the time and computational resources required to conduct multiple bubble studies. We provide the details of the simulation parameters in Table (2.4). We note that the PSFT code is ten times faster than PARIS at same resolutions. The difference in timings is because, in all the finite-difference solvers the pressure Poisson equation is inverted using computationally expensive iterative methods (We use Gauss-Seidel solver in [22]).

Ga	Bo	$At \times g$	N_b
296.0	1.95	0.04×10.5	4

Table 2.4: The parameters for the multiple bubble simulation. We resolve individual bubbles by taking $N_g = 24$ in both PARIS and PSFT. For 100 iteration on 9 Intel(R) Xeon(R) CPU, PARIS took 360 seconds while PSFT took 34 seconds.

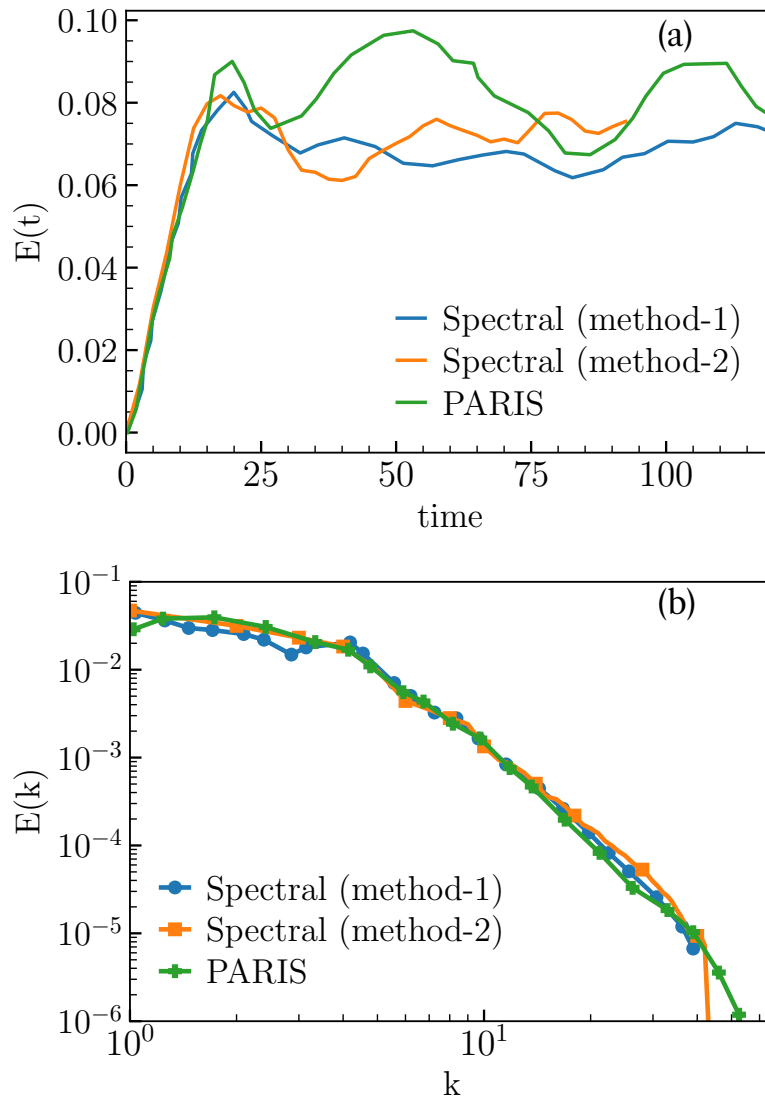


Figure 2.20: (a) The time evolution of the total kinetic energy for the multiple bubbles test case. (b) The kinetic energy spectrum ($E(k)$) evaluated in steady state.

We plot the time evolution of the total kinetic energy in Fig. 2.20. The

initial growth till $t = 20$ is identical with both PARIS and PSFT solvers. After an initial transient, the kinetic energy shows turbulence like behavior, where steady-state fluctuates about the same mean value for both PARIS and PSFT. The kinetic energy spectrum $E(k) = \sum_{m-1/2 < k < m+1/2} |\mathbf{u}_m|^2$ evaluated in the steady-state obtained shows the same scaling. As opposed to section 2.6, we find that the ω_z obtained using method-1, shown in Fig. 2.21, is also similar to PARIS result.

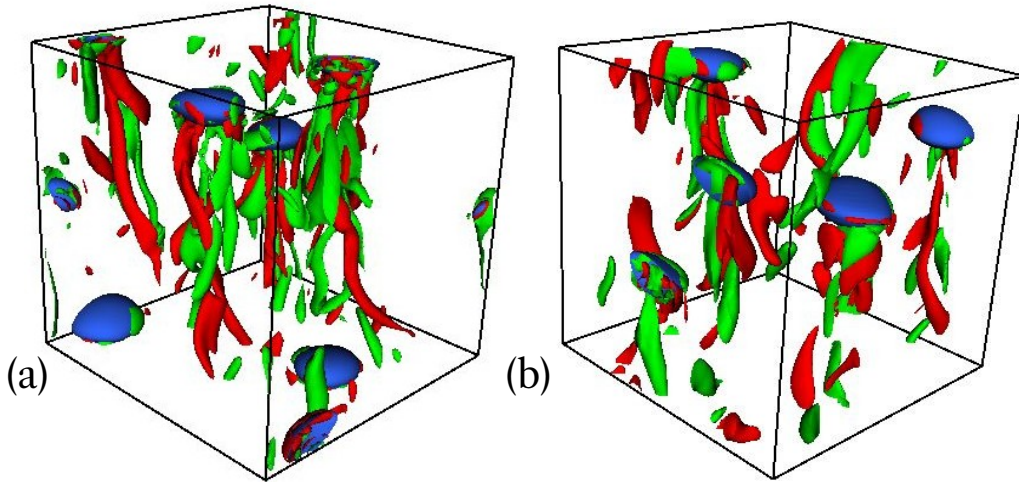


Figure 2.21: The iso-vorticity contour of ω_z and the bubbles, at a time in steady-state from (a) PSFT (method-1) $N_g = 24$ (b) PARIS $N_g = 24$ simulation. We plot iso-contours corresponding to $\pm(\omega_z)_{max}/5$, where $(\omega_z)_{max}$ is the maximum value of ω_z at the given time instant.

2.7 Conclusion

In this chapter, we outlined the procedure for writing a pseudo-spectral solver to numerically solve the single phase NS equation. Then we discussed the DNS methods for solving different multiphase flows. In the later chapters, we shall adopt these methods to study the statistical properties particle-laden and buoyancy-driven bubbly flows.

The DNS of buoyancy-driven bubbly flows poses considerable challenges. We show that, in the regime where the density and viscosity of two phases are comparable, the front-tracking could easily be coupled with a pseudo-

spectral solver. The PSFT solver provides a massive advantage over PARIS in terms of speed. A simulation that takes an hour with PSFT takes about 10hrs in PARIS. In chapter 5 and 6, we will primarily use the PSFT code for all the low Atwood simulations.

References

- [1] R. Scardovelli and S. Zaleski, *Annu. Rev. Fluid Mech.* **31**, 567 (1999).
- [2] G. Tryggvason, B. Bunner, A. Esmaeeli, D. Juric, D. Al-Rawahi, W. Tauber, J. Han, S. Nas, and Y. J. Jan, *J. Comput. Phys.* **169**, 708 (2001).
- [3] S. Elgobashi, in *IUTAM Symposium on Computational Approaches to Multiphase Flow* (Springer Netherlands, Dordrecht, 2006) pp. 3–10.
- [4] S. Balachandar and J. K. Eaton, *Annu. Rev. Fluid Mech.* **42**, 111 (2010).
- [5] S. A. Orszag, *Phys. Fluids* **12**, 250 (1969).
- [6] S. A. Orszag and G. S. Patterson, *Phys. Rev. Lett.* **28**, 76 (1972).
- [7] C. Canuto, Y. Hussaini, A. Quarteroni, and T. Zang, *Spectral methods: evolution to complex geometries and applications to fluid dynamics*, 1st ed., Scientific Computation (Springer, 2007).
- [8] J. P. Boyd, *Chebyshev and Fourier spectral methods* (Courier Corporation, 2001).
- [9] M. Frigo and S. G. Johnson, *Proceedings of the IEEE* **93**, 216 (2005).
- [10] M. R. Maxey and J. J. Riley, *Phys. Fluids* **26**, 883 (1983).
- [11] C. Runge, *Mathematische Annalen* **46**, 1432 (1985).
- [12] M. Kutta, *Zeitschrift für Mathematik und Physik* **46**, 435 (1901).
- [13] C. S. Peskin, *Acta Numer.* **11**, 479 (2002).
- [14] J. M. Dawson, *Rev. Mod. Phys.* **55**, 403 (1983).
- [15] P. Gualtieri, F. Battista, and C. M. Casciola, *Phys. Rev. Fluid* **2**, 034304 (2017).
- [16] P. Gualtieri, F. Picano, G. Sardina, and C. Casciola, *J. Fluid Mech.* **773**, 520 (2015).

- [17] J. Capecelatro and O. Desjardins, *J. Comput. Phys.* **238**, 1 (2013).
- [18] J. A. K. Horwitz and A. Mani, *J. Comput. Phys.* **318**, 85 (2016).
- [19] S. Chandrasekhar, *Hydrodynamic and Hydromagnetic Stability*, Dover Books on Physics Series (Dover Publications, 1981).
- [20] S. M. Cox and P. C. Matthews, *J. Comput. Phys.* **176**, 430 (2002).
- [21] S. O. Unverdi and G. Tryggvason, *J. Comput. fluid* , 25 (1992).
- [22] W. Aniszewski, T. Arrufat, M. Cialesi-Esposito, S. Dabiri, D. Fuster, Y. Ling, J. Lu, L. Malan, S. Pal, R. Scardovelli, G. Tryggvason, P. Yecko, and S. Zaleski, *Computer Physics Communications* **263**, 107849 (2021).
- [23] C. Hirt and B. Nichols, *J. Comput. Phys.* **39**, 201 (1981).
- [24] J. C. Cano-Lozano, C. Martinez-Bazan, J. Magnaudet, and J. Tchoufag, *Phys. Rev. Fluid* **1**, 053604 (2016).
- [25] S. Popinet, <http://gfs.sourceforge.net> (2001).
- [26] PARIS Software, <http://www.ida.upmc.fr/~zaleski/paris/> (2010).
- [27] Y. Bao, J. Kaye, and C. S. Peskin, *J. Comput. Phys.* **316**, 139 (2016).
- [28] Basilisk Software, <http://www.basilisk.fr>.
- [29] A. Menchaca-Rocha, A. Martínez-Dávalos, R. Núñez, S. Popinet, and S. Zaleski, *Phys. Rev. E* **63**, 046309 (2001).
- [30] J. C. Cano-Lozano, P. Bohorquez, and C. Martínez-Bazán, *Int. J. Multiph. Flow* **51**, 11 (2013).
- [31] A. R. Premlata, M. K. Tripathi, B. Karri, and K. C. Sahu, *Physics of Fluids* **29**, 033103 (2017).
- [32] F2C2D a fortran-77 solver for binary-liquid flows, <https://www3.nd.edu/~gtryggva/MultiphaseDNS/simple2dFTC.html>.

Caustics in turbulent flow

3.1 Introduction

In nature, flows with small particles are very common. Typical examples include gas flows in proto-planetary disks with small dust particles [1] and air flows in a cloud with water droplets [2]. In both of the cases the small particles collide and merge leading to the formation of planetesimals in former and rain droplets in latter. The crucial problem here, is to understand the dynamics of the formation of large objects (planetesimals, rain drops) from small particles.

In the clouds small water droplets form by condensation in a super-saturated environment. If only condensation and evaporation determines the evolution of the size of the droplets then, it can be estimated that, it would take an unnaturally long time for raindrops to form in clouds. Clearly, the droplets can either coalesce or bounce off after collision. The collision between droplets is set by their relative velocities. If the velocity field of the droplets is smooth everywhere then the relative velocities between droplets go to

¹This work is a result of collaborative effort with Jan Meibohm, Bernhard Mehlig, Kristian Gustavsson, Dhruvaditya Mitra, and Akshay Bhatnagar. All the 3D simulations were done by Akshay Bhatnagar. The stability analysis presented in the second last section was done by Jan Meibohm. Some part of this chapter is published in Ref. [3].

zero as their relative distances go to zero. In this case, both the frequency of collisions and collision velocities remains small [4] and the estimated time to form raindrops is still unnaturally long. One way out of this conundrum is to consider the possibility that the velocity field of the droplets does not remain smooth but develop singularities – such that the relative velocity between two infinitesimally close droplets remains finite. Such singularities which can invariably develop in the particle velocity gradients are also known as caustics [5]. The indirect effects of these singularities, namely the increase in the rate of collision has been observed in many earlier works [6–11].

In this chapter, we study the rate at which the caustics develop in the gradients of particle velocity field and its dependence on the fluid Reynolds number and the Stokes number (St). The earlier studies, Falkovich and Pumir [12] have also calculated the rate of the formation of singularities. But their data, was not extensive enough to determine how the rate depends on the Stokes number in the limit $St \rightarrow 0$. In this chapter, we show that in the limit $St \rightarrow 0$, the rate of caustic formation $\mathcal{J} \sim \exp\left(-\frac{C}{St}\right)$, where C is a constant, in both two- and three-dimensions.

The rest of the chapter is organized as follows: In the next [Sec. 3.2](#) we discuss the model equations and give theoretical arguments to derive the expression for \mathcal{J} in both two- and three-dimensions. We then in [Sec. 3.3](#), give all the simulation details used in this study. In the later sections, we discuss the results of the study in detail.

3.2 Model

We assume that the size of the inertial particles are smaller than η and a dust grain or a droplet obey [1.23](#) and [1.24](#),

$$\begin{aligned}\frac{d\mathbf{X}(t)}{dt} &= \mathbf{V}(t), \\ \frac{d\mathbf{V}(t)}{dt} &= \frac{1}{\tau_p} [\mathbf{u}(\mathbf{X}, t) - \mathbf{V}(t)],\end{aligned}$$

We shall also use the word “heavy inertial particle” to mean a particle which obey [1.23](#) and [1.24](#). The major non-dimensional number which govern the

dynamics of inertial particle is the $St = \frac{\tau_p}{\tau_\eta}$, where τ_η is the Kolmogorov time scale.

In the Lagrangian frame of this heavy inertial particle the equation of evolution of the gradient of its velocity matrix, Z , with components $Z_{\alpha\beta} \equiv \partial_\beta V_\alpha$ ($\alpha, \beta = 1, \dots, \mathfrak{D}$ in \mathfrak{D} dimensions), [12–15] is given by

$$\frac{dZ_{\alpha\beta}}{dt} + Z_{\alpha\gamma}Z_{\gamma\beta} + \frac{1}{\tau_p}Z_{\alpha\beta} = \frac{1}{\tau_p}A_{\alpha\beta}. \quad (3.1)$$

In above 3.1, $A_{\alpha\beta} \equiv \partial_\beta u_\alpha$ are the components of the fluid velocity-gradient matrix, Z . This equation contains the possibility that elements of Z can become infinitely large in finite time. To see this first consider the same equation in one-dimension. Now both the particle velocity-gradient ($Z \equiv \partial_x V$), and the fluid velocity-gradients ($A \equiv \partial_x u$) are scalars and 3.1 simplifies to

$$\frac{dZ}{dt} + Z^2 + \frac{1}{\tau_p}Z = \frac{1}{\tau_p}A. \quad (3.2)$$

The solution for the Z , assuming A to be a constant, reads

$$Z(t) = \frac{a - b \exp((t - t^*)(b - a))}{1 - \exp((t - t^*)(b - a))}, \quad (3.3)$$

where $a, b = -\frac{1}{2\tau_p} \left(1 \pm \sqrt{1 + 4A\tau_p}\right)$. It is evident from 3.3 that the solution develops singularity when

$$t = t^* \equiv \frac{1}{a - b} \log \left(\frac{Z(0) - a}{Z(0) - b} \right). \quad (3.4)$$

In order to gain further physical insights on the process of caustic formation, we rewrite 3.2 using a potential $V(Z)$,

$$\frac{dZ}{dt} = -\frac{\partial V(Z)}{\partial Z}, \quad (3.5)$$

where $V(Z) = \frac{Z^3}{3} + \frac{1}{\tau_p} \left(\frac{Z^2}{2} - AZ \right)$, and we have assumed A is constant. In Fig. 3.1, we show the plot of one-dimensional potential $V(Z)$ for the case $\tau_p = 1$, and $A = 0$. The system has a stable fixed point at the minima, and an unstable fixed point at the maxima. The trajectory of Z always remain concentrated at the minima until a large fluctuation in A pushes it to $-\infty$.

In principle, 3.2 is an inappropriate model for flows in clouds because the incompressibility criterion dictates A to be identically zero. Let us, nevertheless, model the effects of turbulence in 3.2 by replacing A by a Gaussian,

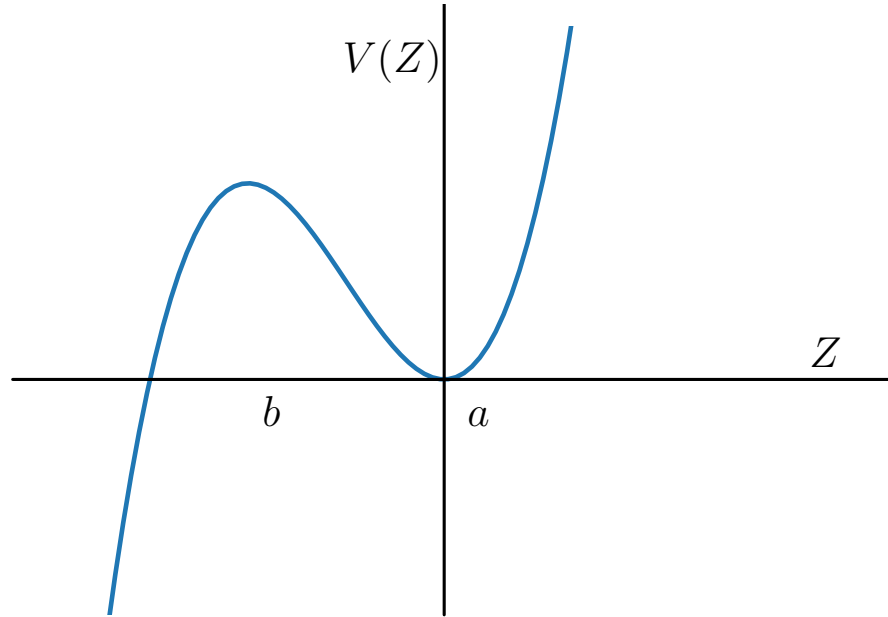


Figure 3.1: The potential $V(Z) = \frac{Z^3}{3} + \frac{1}{\tau_p}(\frac{Z^2}{2} - AZ)$ [see 3.5]. In the plot we have chosen $\tau_p = 1$ and $A = 0$.

white-in-time noise. This turns 3.2 into a stochastic differential equation. From the corresponding Fokker-Planck equation Wilkinson and Mehlig [5] evaluated the rate of formation of singularities

$$\mathcal{J} \sim \exp\left(-\frac{C}{\tau_p}\right). \quad (3.6)$$

In higher dimension we study the invariants of the velocity gradient tensor $\mathbb{Z} = \partial_\alpha V_\beta$. We rewrite the evolution of \mathbb{Z} below,

$$\frac{d\mathbb{Z}}{dt} + \mathbb{Z}^2 + \frac{1}{\tau_p}\mathbb{Z} = \frac{1}{\tau_p}\mathbb{A}. \quad (3.7)$$

In two- and three-dimensions appearance of singularities implies that the trace of the matrix \mathbb{Z} will become infinitely large [see e.g., 14, section 4.1]. Thus we can study formation of singularities by investigating the evolution of $\mathcal{T}r[\mathbb{Z}]$,

$$\frac{d\mathcal{T}r[\mathbb{Z}]}{dt} + \mathcal{T}r[\mathbb{Z}^2] + \frac{1}{\tau_p}\mathcal{T}r[\mathbb{Z}] = 0, \quad (3.8)$$

where $\mathcal{T}r[\mathbb{A}] \equiv 0$ because of incompressibility. In two-dimension in the limit

of $\tau_p \rightarrow 0$ the 3.8 can be simplified to

$$\frac{d\mathcal{T}r[\mathbb{Z}]}{dt} + \{\mathcal{T}r[\mathbb{Z}]\}^2 + \frac{1}{\tau_p}\mathcal{T}r[\mathbb{Z}] = 2\mathcal{D}et[\mathbb{A}]. \quad (3.9)$$

Here the leading order term is $\mathcal{O}(\frac{1}{\tau_p})$ and we have ignored terms of $\mathcal{O}(\tau_p)$ and higher [15]. Similarly in three-dimensions the equation for $\mathcal{T}r[\mathbb{Z}]$ can be simplified to

$$\frac{d\mathcal{T}r[\mathbb{Z}]}{dt} + \{\mathcal{T}r[\mathbb{Z}]\}^2 + \frac{1}{\tau_p}\mathcal{T}r[\mathbb{Z}] = 2\mathcal{Q}[\mathbb{A}], \quad (3.10)$$

where $\mathcal{Q}[\mathbb{A}]$ is the quadratic invariant of the matrix \mathbb{A} , i.e., $\mathcal{Q}[\mathbb{A}] \equiv \lambda_1\lambda_2 + \lambda_2\lambda_3 + \lambda_3\lambda_1$. Here λ_1, λ_2 , and λ_3 are the three eigenvalues of the matrix \mathbb{A} . To arrive at 3.10, we have again ignored terms of order τ_p and higher [15]. Note that 3.10 is equivalent to 3.9 because in two-dimensions $\mathcal{T}r[\mathbb{A}^2] = 2\mathcal{D}et[\mathbb{A}]$.

Assuming that the $\mathcal{Q}[\mathbb{A}]$ and $\mathcal{D}et[\mathbb{A}]$ is Gaussian, form the Fokker-Planck equation for $\mathcal{T}r[\mathbb{Z}]$ above we predict that the rate of caustics formation will be given by 3.6 in both two- and three-dimensions.

3.3 Simulation details

In both two- and three-dimensions we solve the Navier–Stokes equation given by

$$\partial_t \mathbf{u} + \mathbf{u} \cdot \nabla \mathbf{u} = -\nabla p + \nu \nabla^2 \mathbf{u} + \mathbf{f}, \quad (3.11)$$

where \mathbf{u} is the incompressible velocity field, p is the pressure, ν is the viscosity and \mathbf{f} is the external force. Along with 3.11 we evolve N_p particles governed by 1.23 and 1.24. In addition to tracking the heavy inertial particles, we solve 3.7 on each of the particles. We choose $\mathbb{Z} = 0$, the zero matrix, on all the particles at $t = 0$. We monitor $\mathcal{T}r[\mathbb{Z}]$, every time it becomes less than a large negative threshold, A_{th} , – we have used several values for this threshold – we set \mathbb{Z} back to zero matrix and count this event to be the formation of a singularity.

In two-dimensions, we solve 3.11 using a pseudo-spectral solver in vorticity stream-function formalism. We add a Ekman drag term ($\alpha \mathbf{u}$) to the

RHS of 3.11, to avoid accumulation of energy at small wave modes. In three-dimensions we use the pencil-code [16].

We give the parameters for the simulation in Table (3.1). For the two-dimensional simulations we use a variety of different situations. We use a deterministic Kolmogorov forcing $\mathbf{f} = f_0 \sin(k_f x) \mathbf{e}_y$, where f_0 is the forcing amplitude, in runs 2d1–2d8, and a stochastic forcing in runs 2d9–2d11. The Kolmogorov force is always limited to a single wave-number k_f . For a small k_f we develop a direct cascade, whereas for a large k_f we develop a large range of inverse cascade. We also change the threshold of detection of singularities, A_{th} , as we shall show later, has no appreciable effect on the dependence of \mathcal{J} (rate of formation of singularities) on the Stokes number.

In Fig. 3.2 we show the snapshot of vorticity along with particles position from the two-dimensional simulation 2d10 and in Fig. 3.3 we show the snapshot from three-dimensional simulation 3d1. As expected the density of the heavy inertial particle is higher in the strain dominated regions of the flow [17].

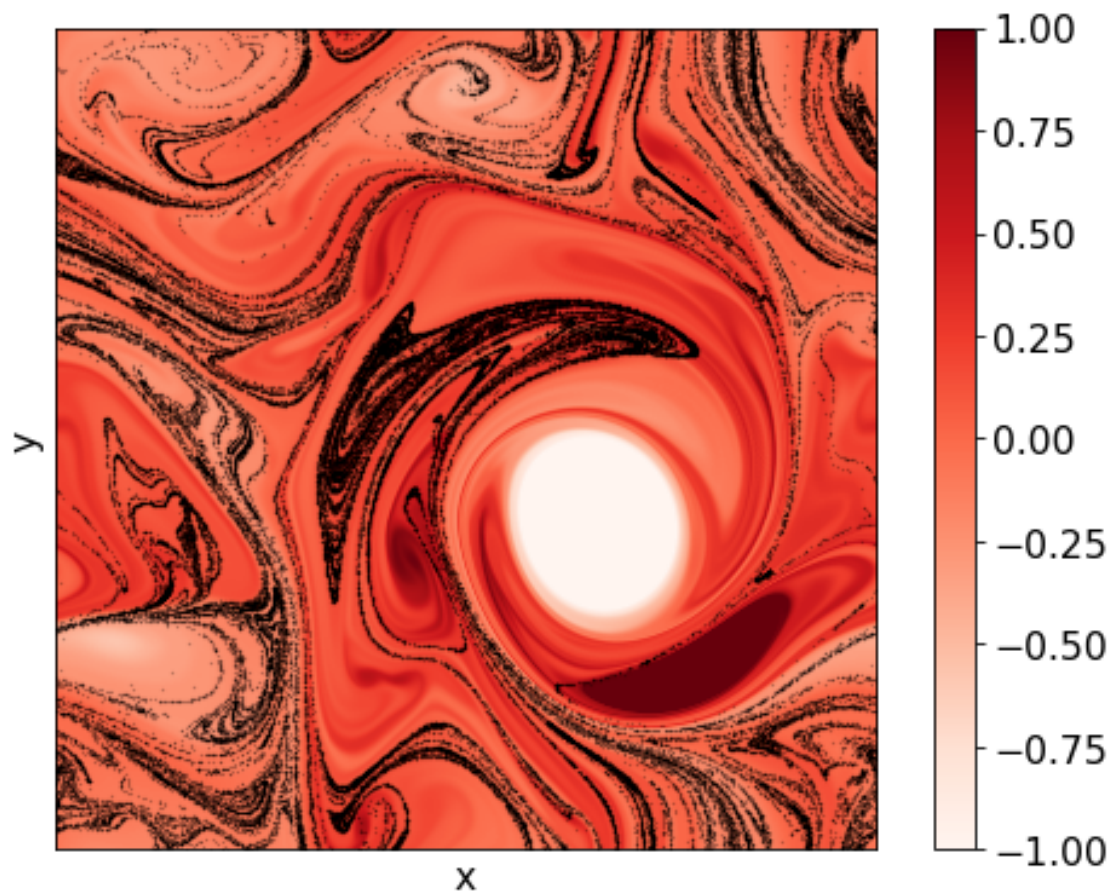


Figure 3.2: Representative snapshot of vorticity overlaid with the positions of particles ($St = 0.22$) from one of our two-dimensional simulations 2d9.

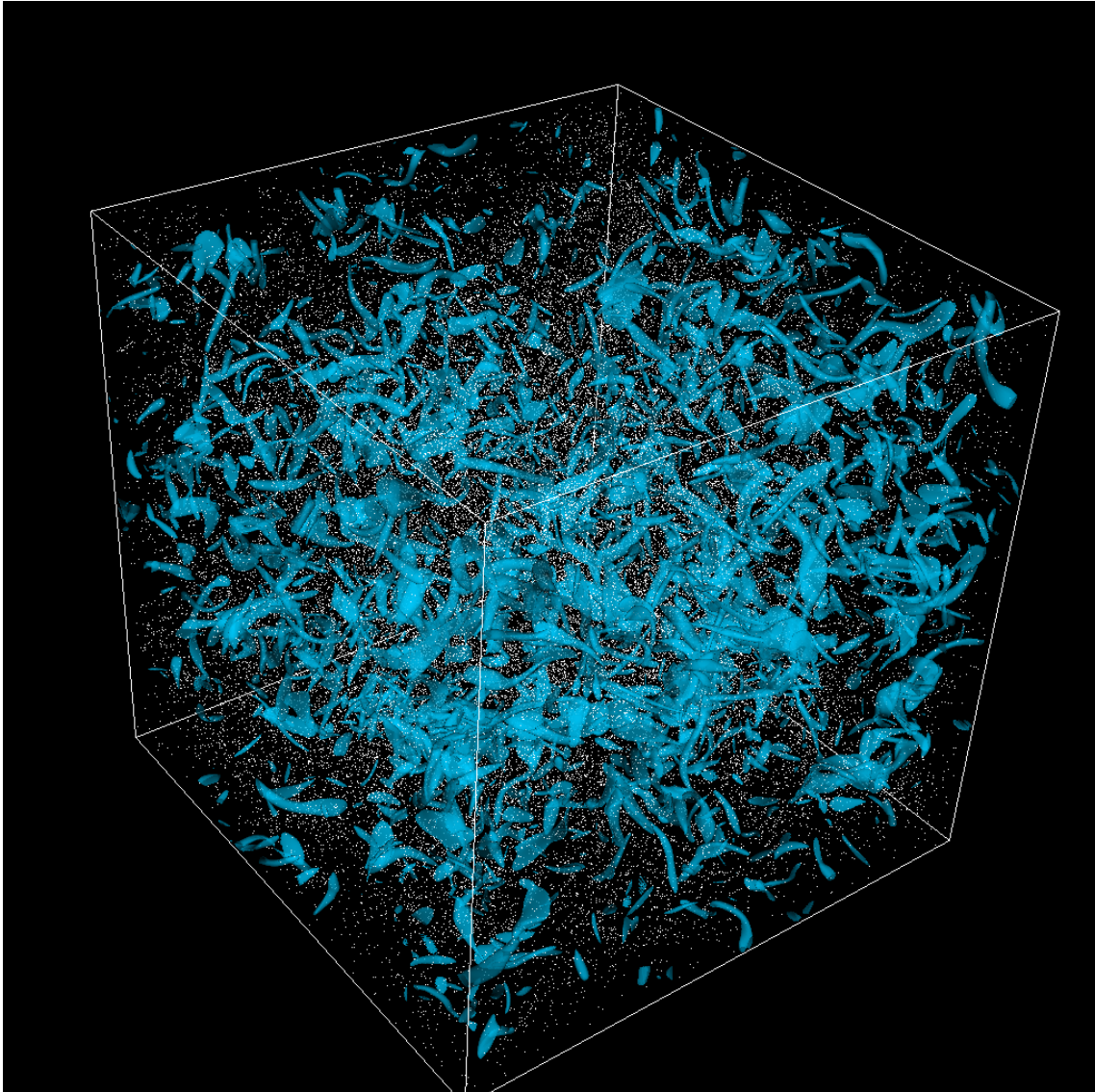


Figure 3.3: A representative snapshot showing the positions of the particles and iso-surface of $|\omega|$ from our three-dimensional simulation (3d1).

<i>runs</i>	N	Re_λ	λ	τ_η	$\eta \cdot 10^{-3}$	$f_o \cdot 10^{-3}$	k_f	τ_{ℓ_0}	$dt \cdot 10^{-3}$	$-A_{\text{th}}$
2d1	1024	1311	0.28	2.9	5	5	4	15.0	5	10^{10}
2d2	1024	1311	0.28	2.9	5	5	4	15.0	5	10^7
2d3	1024	1311	0.28	2.9	5	5	4	15.0	5	10^2
2d4	1024	1311	0.28	2.9	5	5	4	15.0	5	10
2d5	512	395	0.27	4.6	7	2.5	4	26.0	5	10^7
2d6	512	395	0.27	4.6	7	2.5	4	26.0	10	10^7
2d7	1024	395	0.11	1.6	4	5	35	2.64	5	10^{10}
2d8	1024	77	0.05	1.4	3.7	5	100	0.74	5	10^7
2d9	1024	4100	0.41	2.1	5	5	2 – 3	12.55	1	10^7
2d10	512	720	0.4	2.2	10	5	2 – 3	13.9	2.5	10^7
2d11	512	26	0.04	1.32	8	5	40 – 41	4.84	5	10^7
3d1	512	90	0.2	0.39	14	0.05	5	5.46	—	10^{10}
3d2	512	170	0.27	1.56	14	0.01	2	36.98	—	10^{10}

Table 3.1: Parameters used in both our three dimensional simulations are listed here. The two-dimensional runs are marked with the prefix 2d and the three dimensional ones are marked with the prefix 3d. Definition of symbols: N , number of grid points in one direction, $2 - \mathfrak{D}$ runs have N^2 number of grid points and $3 - \mathfrak{D}$ runs have N^3 grid points in simulation domain; dt , time-step used in the $2 - \mathfrak{D}$ solver. ν , viscosity; f_o , amplitude of the force; $\langle \cdot \rangle$, spatial average over the computational box and temporal average over the statistically-stationary, non-equilibrium, state of turbulence; $u_0 = \sqrt{\frac{\langle u^2 \rangle}{\mathfrak{D}}}$, the root-mean-square velocity of the flow; k_f , the forcing wavenumber; $\ell_0 \equiv 2\pi/k_f$, the integral scale; $\tau_{\ell_0} = \ell_0/u_0$, the large-eddy-turnover-time; $\omega_0 = \sqrt{\langle \omega^2 \rangle}$, root-mean-square vorticity; $\epsilon_\nu = \nu\omega_0^2$, the rate of energy dissipation; $\eta \equiv (\nu^3/\epsilon)^{1/4}$, Kolmogorov (dissipation) length scale, $\lambda = u_0/\omega_0$, the Taylor microscale; $\text{Re}_\lambda = u_0\lambda/\nu$, the Taylor microscale Reynolds number; $\text{St} = \tau_p/\tau_\eta$. We use $\text{St} = 0.1 - 3.1$ in three-dimensions and $\text{St} = 0.12 - 1.1$ in two-dimensions. We use a drag coefficient of 10^{-2} in all the $2 - \mathfrak{D}$ runs except for 2d7 and 2d11, where $\alpha = 10^{-3}$, and 2d8 where $\alpha = 2 \cdot 10^{-4}$. All the values of St used in different runs are given in Table (3.2).

<i>runs</i>	St
2d1	0.18, 0.20, 0.21, 0.24, 0.26, 0.28, 0.31, 0.34, 0.41, 0.46, 0.52, 0.69, 0.76
2d2	0.28, 0.31, 0.34, 0.41, 0.46, 0.52, 0.62, 0.69, 0.76
2d3	0.22, 0.26, 0.28, 0.31, 0.34, 0.41, 0.46, 0.52
2d4	0.18, 0.20, 0.21, 0.22, 0.24, 0.26, 0.28, 0.31, 0.34, 0.38, 0.41
2d5	0.22, 0.24, 0.26, 0.28, 0.32, 0.39, 0.43, 0.52, 0.54, 0.78
2d6	0.18, 0.19, 0.20, 0.21, 0.22, 0.24, 0.26, 0.30, 0.32, 0.39, 0.43, 0.48
2d7	0.14, 0.15, 0.17, 0.19, 0.22, 0.25, 0.28, 0.31, 0.47, 0.62, 1.00
2d8	0.13, 0.14, 0.16, 0.18, 0.21, 0.29, 0.36, 0.43
2d9	0.17, 0.18, 0.19, 0.21, 0.24, 0.29, 0.38, 0.48, 0.52, 0.62, 0.71
2d10	0.15, 0.16, 0.17, 0.18, 0.20, 0.22, 0.28, 0.36, 0.45, 0.50, 0.60, 0.68
2d11	0.12, 0.15, 0.17, 0.19, 0.23, 0.26, 0.30, 0.34, 0.38, 0.45, 0.53, 0.76
3d1	0.10, 0.11, 0.12, 0.14, 0.15, 0.16, 0.17, 0.27, 0.53, 0.69, 0.98
3d2	0.10, 0.11, 0.12, 0.14, 0.15, 0.20, 0.25, 0.30, 0.40, 0.50, 0.70

Table 3.2: Values of St used in different simulations

As the heavy inertial particles are much smaller than the energy containing scales of the flow we use the Kolmogorov length scale η and time scale τ_η as our characteristic length and time scales. In addition to usual Reynolds number, we use the Stokes number $St \equiv \tau_p/\tau_\eta$ to study the dynamics. The St we use in our study are typical of cumulus clouds where droplets are of size 10 to 60 micrometer [18–20] (St varies from 0.01 to 2). We use $St = 0.1$ to 3.1 in three-dimensions and $St = 0.12$ to 1.1 in two-dimensions. In Table (3.2) we give a complete list of Stokes numbers used in each of our simulations.

3.4 Rate of caustics formation

Let $N_c(t)$ be the total number of caustics recorded till time t . Then the rate of caustics formation is defined as

$$\bar{j} = \lim_{t \rightarrow \infty} \frac{N_c(t)}{t}. \quad (3.12)$$

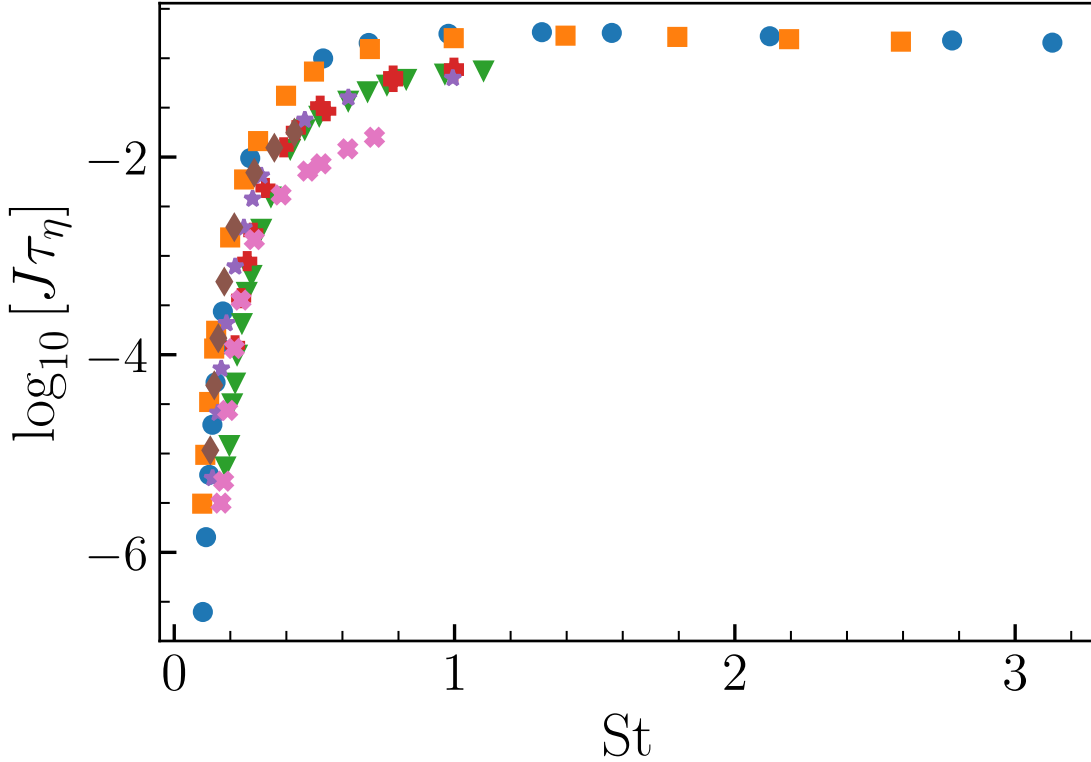


Figure 3.4: The rate-of-formation of singularities \mathcal{J} , non-dimensionalized by multiplying it with τ_η the Kolmogorov time scale, as a function of the Stokes number, St . The different symbols used are: blue circle (3d1), orange square (3d2), green triangle (2d1), red plus (2d5), purple star (3d7), brown diamond (2d8), and pink cross (2d9).

In Fig. 3.4, we plot the non-dimensional, rate-of-formation of singularities, $\log_{10}(\mathcal{J}\tau_\eta)$, as a function of the Stokes number St from all our simulations. As shown, the rate \mathcal{J} obtained from all the simulations has a universal behavior, where all the data converge to a single curve. We verify that the rate of caustic formation $\mathcal{J} \sim \exp(-C/St)$, by plotting $\log_{10}[-\log_{10} \mathcal{J}]$, vs on $1/St$, in Fig. 3.5. The data for all the runs at large $1/St$ falls over a line of slope unity, implying that the relation (3.6) holds. This shows the remarkable universality of 3.6. In Fig. 3.4 and 3.5 we show data from simulations in both three- and two-dimensions. In two-dimensions, depending on which length-scale is being forced, the turbulence may be dominated by either direct cascade of enstrophy (e.g., run 2d2) or inverse cascade of energy (e.g., run 2d8). In some two-dimensional simulations we have used a deterministic, Kolmogorov, ex-

ternal force in others we have used a stochastic, white-in-time, force. We have changed our Reynolds number over a large range, from approximately 70 to about 4000.

In the limit of small St , 3.6 holds in all of these cases, i.e., it is universal, but, as expected, the constant C is not. Earlier work [13] had assumed a dependence of $\mathcal{J} \sim \exp(-\frac{C}{St^2})$. We find that this assumption does not hold.

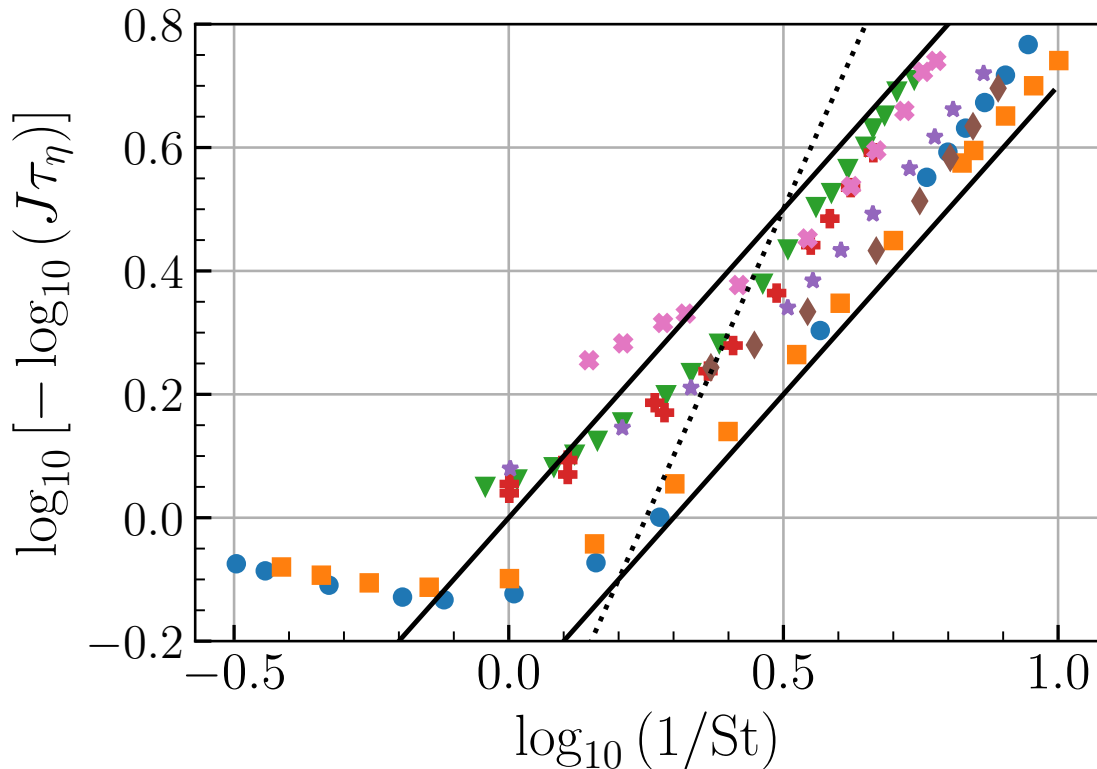


Figure 3.5: The plot of $\log_{10} [-\log_{10}(\tau_{\eta}\mathcal{J})]$ as a function of $\log_{10}(1/St)$. A slope of unity in this plot implies that 3.6 holds. Two continuous lines with slope unity are also plotted. For comparison, we plot a dashed line with slope of two as well. For definition of symbols see Fig. 3.4.

3.5 Statistical properties of \mathbb{Z} and \mathbb{A}

Several assumptions have been made to derive the expression of \mathcal{J} given by 3.6. In this section, we shall examine each of the assumption and make comparison with the data from the simulations.

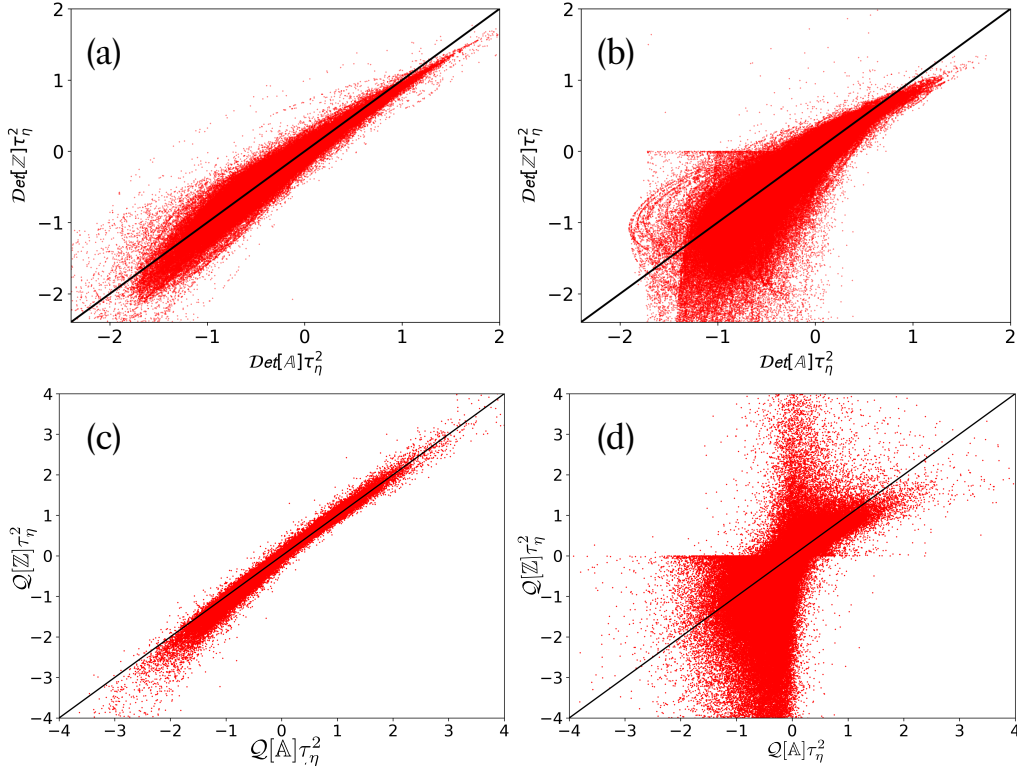


Figure 3.6: (top panels) Scatter plots of $\mathcal{D}et[Z]$ vs. $\mathcal{D}et[A]$ from our two dimensional simulation 2d1 at two different values of St : (a) $St = 0.18$, and (b) $St = 0.31$. (bottom panels) Scatter plots of $\mathcal{Q}[Z]$ vs. $\mathcal{Q}[A]$ from simulation 3d1 for two different values of (a) $St = 0.12$ and (b) 0.53 . Black solid line in all the plots from top panels represents $\mathcal{D}et[Z] = \mathcal{D}et[A]$ while it represents $\mathcal{Q}[Z] = \mathcal{Q}[A]$ in the figures in bottom panel.

The right hand side of 3.9 and 3.10 is derived using a perturbative expansion on τ_p [15], where in the limit $St \rightarrow 0$, we assume $\mathcal{D}et[Z] = \mathcal{D}et[A]$ in two-dimensions and $\mathcal{Q}[Z] = \mathcal{Q}[A]$ in three-dimensions. In Fig. 3.6(a,b) we show the scatter plot of $\mathcal{D}et[Z]$ vs $\mathcal{D}et[A]$ for $St = 0.18$ and 0.31 from the simulation 2d1. Similarly, in Fig. 3.6(c,d) we show the scatter plot of $\mathcal{Q}[Z]$ vs $\mathcal{Q}[A]$ for $St = 0.12$ and 0.53 , from the three-dimensional simulation. The black diagonal line in the figures represent $\mathcal{D}et[Z] = \mathcal{D}et[A]$ in two-dimensions and $\mathcal{Q}[Z] = \mathcal{Q}[A]$ in three-dimensions. For the smallest St in both two- and three-dimensions the dispersion about the diagonal is small. At larger Stokes the higher order terms in the expansion becomes more significant and thus the dispersion about the diagonal increases.

In one-dimension, to be able to calculate the rate-of-formation of singularities analytically we must assume that the RHS of 3.2, is a Gaussian, white-in-time, noise. Similarly, 3.6 to hold in two- and three-dimensions, $\mathcal{D}et[A]$ and $\mathcal{Q}[A]$ respectively must also be Gaussian and white-in-time. In Fig. 3.7, we show the probability distribution of $\mathcal{D}et[A]$ and Fig. 3.8 we show the distribution of and $\mathcal{Q}[A]$. Neither the probability distribution function of $\mathcal{D}et[A]$ in two-dimensions nor the probability distribution function of $\mathcal{Q}[A]$ in three-dimensions is Gaussian. An important implication could be that 3.6 holds even for a non Gaussian noise, but such a proof does not exist.

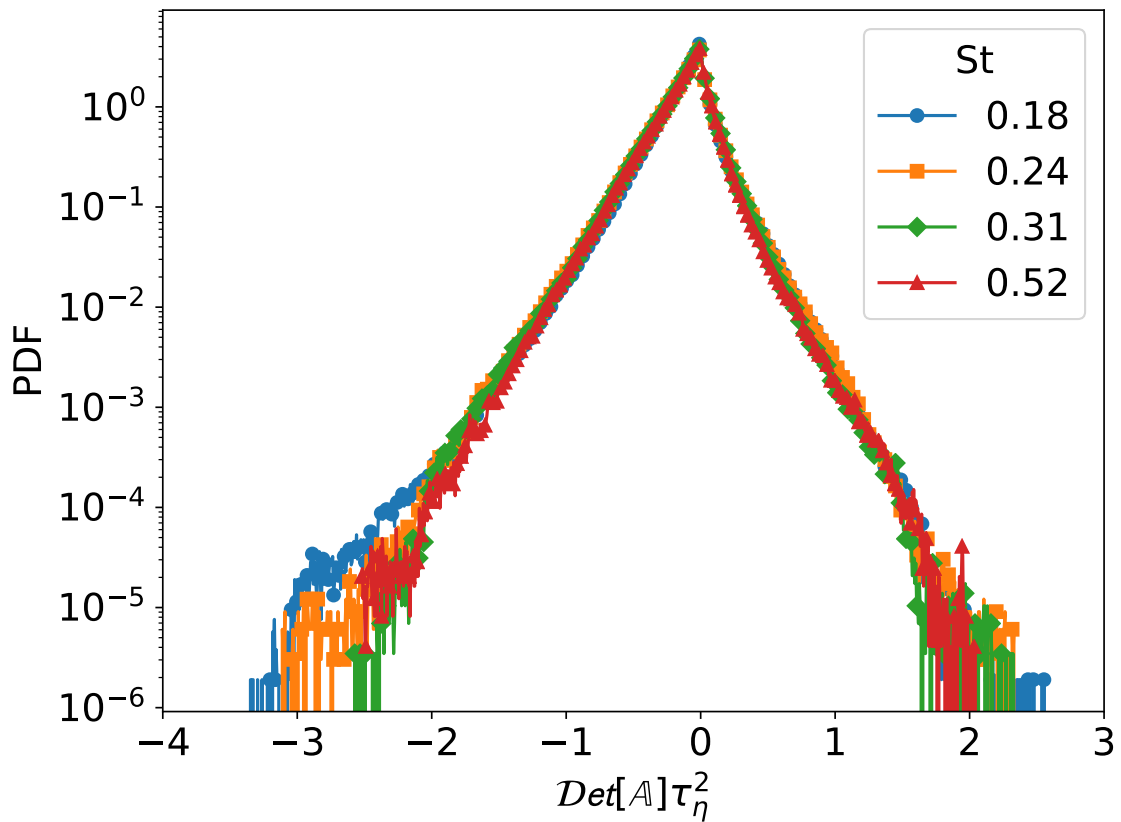


Figure 3.7: The probability distribution function of $\mathcal{D}et[A]$ at the location of heavy inertial particles from one of our two-dimensional simulations –run 2d1 at different St .

Note that in two-dimensions $\mathcal{D}et[A]$ is also known as the Okubo-Weiss parameter [21, 22], Λ_o . Its auto-correlation function calculated along Lagrangian trajectories, or at fixed Eulerian points in space, is exponential in time with a characteristic decay time of the order of one to two Kolmogorov

time [23] – characteristic time scale of the viscous scales of turbulence. It is safe to assume that the same holds for the correlation function of Λ_o along trajectories of heavy inertial particles, particularly in the limit of small τ_p . Hence for time scales much larger than Kolmogorov time we can consider the RHS of 3.9 to be white-in-time. The effect of non-zero correlation time of $\mathcal{D}et[\mathbb{A}]$ may manifest itself as corrections to leading order behavior in 3.6 or may just modify the constant C .

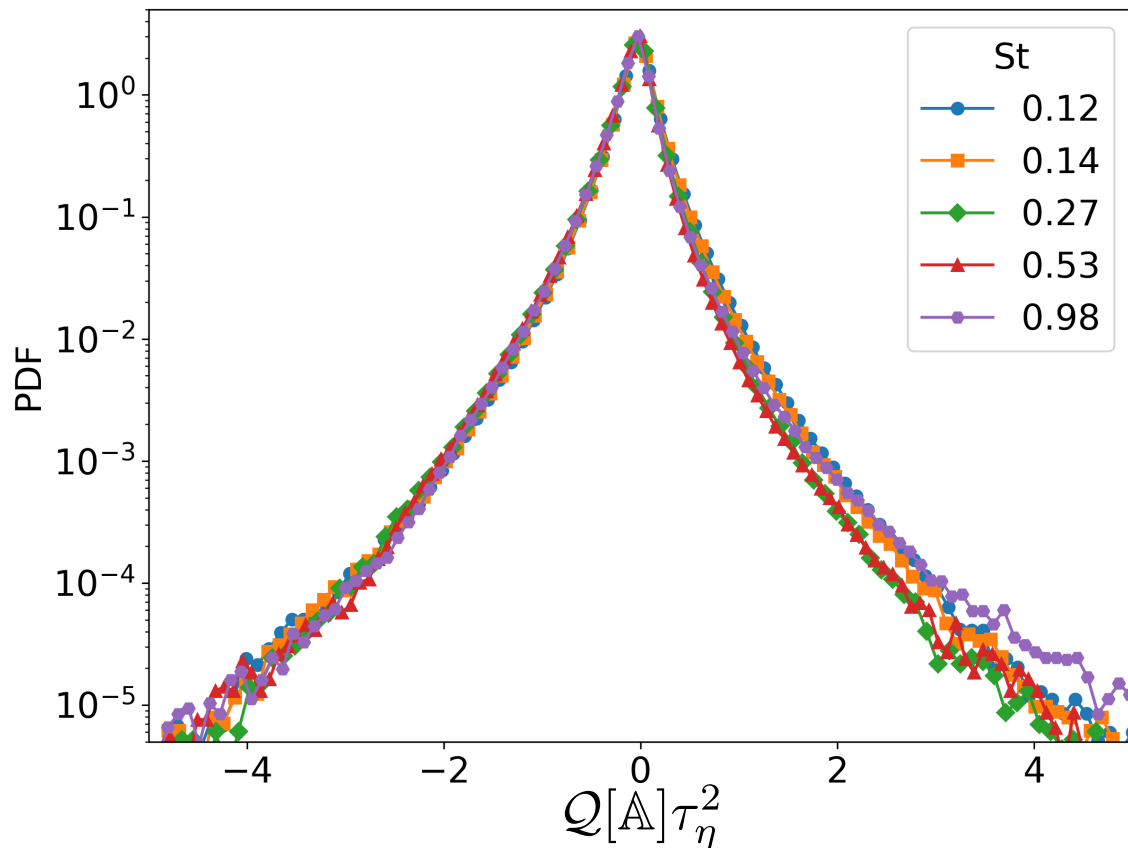


Figure 3.8: The probability distribution function of $Q[\mathbb{A}]$ at the location of heavy inertial particles from one of our three-dimensional simulations –run 3d1.

3.6 Path to caustics formation

The heavy inertial particles are preferentially ejected from regions of flow where the vorticity is large [17]. This suggests that particle-particle collisions are more likely to happen in regions where the flow vorticity is small. The

particle-particle collisions with large relative velocities necessarily correspond to formation of singularities of $\mathcal{T}r[\mathbb{Z}]$. 3.9 shows that in two-dimensions $\mathcal{T}r[\mathbb{Z}]$ can become singular only if $\mathcal{D}et[\mathbb{A}]$ is negative. These correspond to regions of the flow that are topologically hyperbolic points [22]. To demonstrate this we plot in Fig. 3.9 $\mathcal{T}r[\mathbb{Z}]$ as a function of time for several heavy inertial particles from our two-dimensional simulation 2d1 at $St = 0.31$. The lines are colored by red or blue depending on whether the flow at the position of the particle is topologically in a hyperbolic (red) or an elliptic (blue) point, respectively. Clearly the caustic formation primarily occurs when the region is hyperbolic.

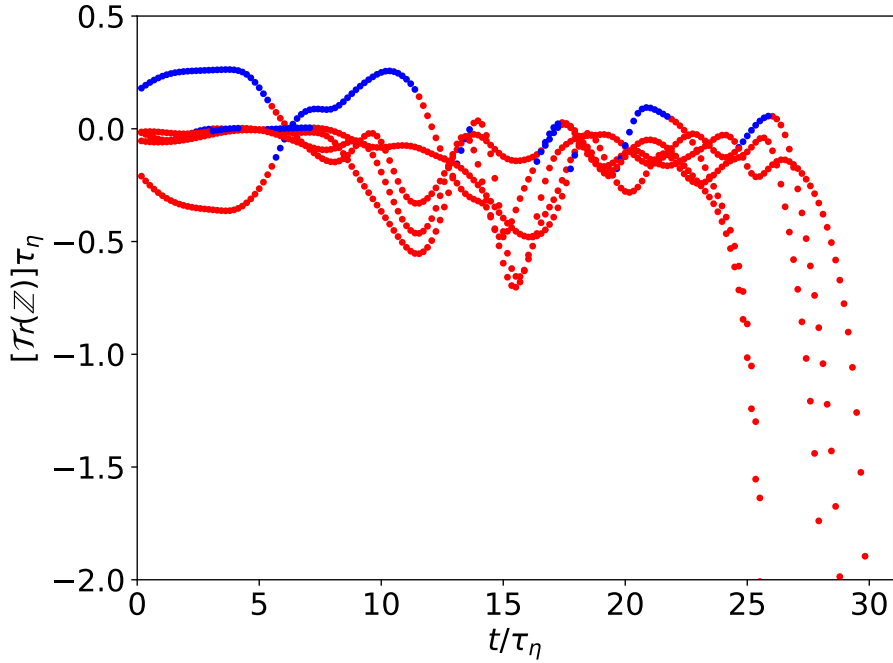


Figure 3.9: Typical time traces of $\mathcal{T}r[\mathbb{Z}]$ from our two-dimensional run 2d1 at $St = 0.31$. In the plot blue and red colors correspond to the positive and negative sign of $\mathcal{D}et[\mathbb{A}]$ respectively.

This observation can be understood by doing a stability analysis [24] of 3.7. We first non-dimensionalize 3.7 using the transformation $t \rightarrow t/\tau_p$ to get,

$$\frac{d\mathbb{Z}}{dt} = \mathbb{Z}^2 - \mathbb{Z} + \mathbb{A}. \quad (3.13)$$

We then expand \mathbb{Z} in the orthogonal basis $\mathbf{e}_0 = \begin{pmatrix} 1 & 0 \\ 0 & 1 \end{pmatrix}$, $\mathbf{e}_1 = \begin{pmatrix} 0 & -1 \\ 1 & 0 \end{pmatrix}$, $\mathbf{e}_2 =$

$\begin{pmatrix} 1 & 0 \\ 0 & -1 \end{pmatrix}$, and $\mathbf{e}_3 = \begin{pmatrix} 0 & 1 \\ 1 & 0 \end{pmatrix}$ as,

$$\mathbb{Z} = \sum_{i=0}^3 z_i \mathbf{e}_i, \quad (3.14)$$

where $z_i = \mathbb{Z} \cdot \mathbf{e}_i$ and the dot product is defined as $\mathbb{X} \cdot \mathbb{Y} = \frac{1}{2} \mathcal{T}r(\mathbb{X}\mathbb{Y})$. In this convention $A_0 = \mathbb{A} \cdot \mathbf{e}_0 = 0$ because of incompressibility.

We further make the assumption that the particle can either be in a strain dominated region or vortical. For the case in which the region is strain dominated, the eigenvalues of \mathbb{A} is real ($\pm \tilde{\lambda}$) or,

$$\mathbb{A} = \tilde{\lambda} \mathbf{e}_2. \quad (3.15)$$

In the vortical region the eigenvalues of \mathbb{A} is imaginary ($\pm i\tilde{\omega}$) or

$$\mathbb{A} = \tilde{\omega} \mathbf{e}_3 \quad (3.16)$$

Thus, the dynamical equation for z_i using 3.15 and 3.16 are,

$$\frac{dz_0}{dt} = -z_0 - z_0^2 - z_1^2 - z_2^2 - z_3^2 \quad (3.17)$$

$$\frac{dz_1}{dt} = -z_1 - 2z_0z_1 \quad (3.18)$$

$$\frac{dz_2}{dt} = -z_2 - 2z_0z_2 + \tilde{\lambda} \quad (3.19)$$

$$\frac{dz_3}{dt} = -z_3 - 2z_0z_3 + \tilde{\omega} \quad (3.20)$$

These dynamical equations can be separated based on the eigenvalues of \mathbb{A} . For the case when the eigenvalues of \mathbb{A} is real, the equations are,

$$\frac{dz_0}{dt} = -z_0 - z_0^2 - z_2^2 \quad (3.21)$$

$$\frac{dz_2}{dt} = -z_2 - 2z_0z_2 + \tilde{\lambda}, \quad (3.22)$$

and when eigenvalues of \mathbb{A} is imaginary, the relevant equations are,

$$\frac{dz_0}{dt} = -z_0 - z_0^2 - z_3^2 \quad (3.23)$$

$$\frac{dz_3}{dt} = -z_3 - 2z_0z_3 + \tilde{\omega} \quad (3.24)$$

Let us first consider the 3.21 and 3.22. The fixed points z_0^*, z_2^* can be determined by setting the RHS to 0. For $\tilde{\lambda} = 0$, the trivial solution is $z_0^* = z_2^* = 0$.

The other fixed points are $z_0^* = 0, z_2^* = -1, z_0^* = z_2^* = -1/2$ and $z_0^* = 1/2, z_2^* = -1/2$. A saddle node bifurcation occurs at $z_0^* = z_2^* = -1/2$.

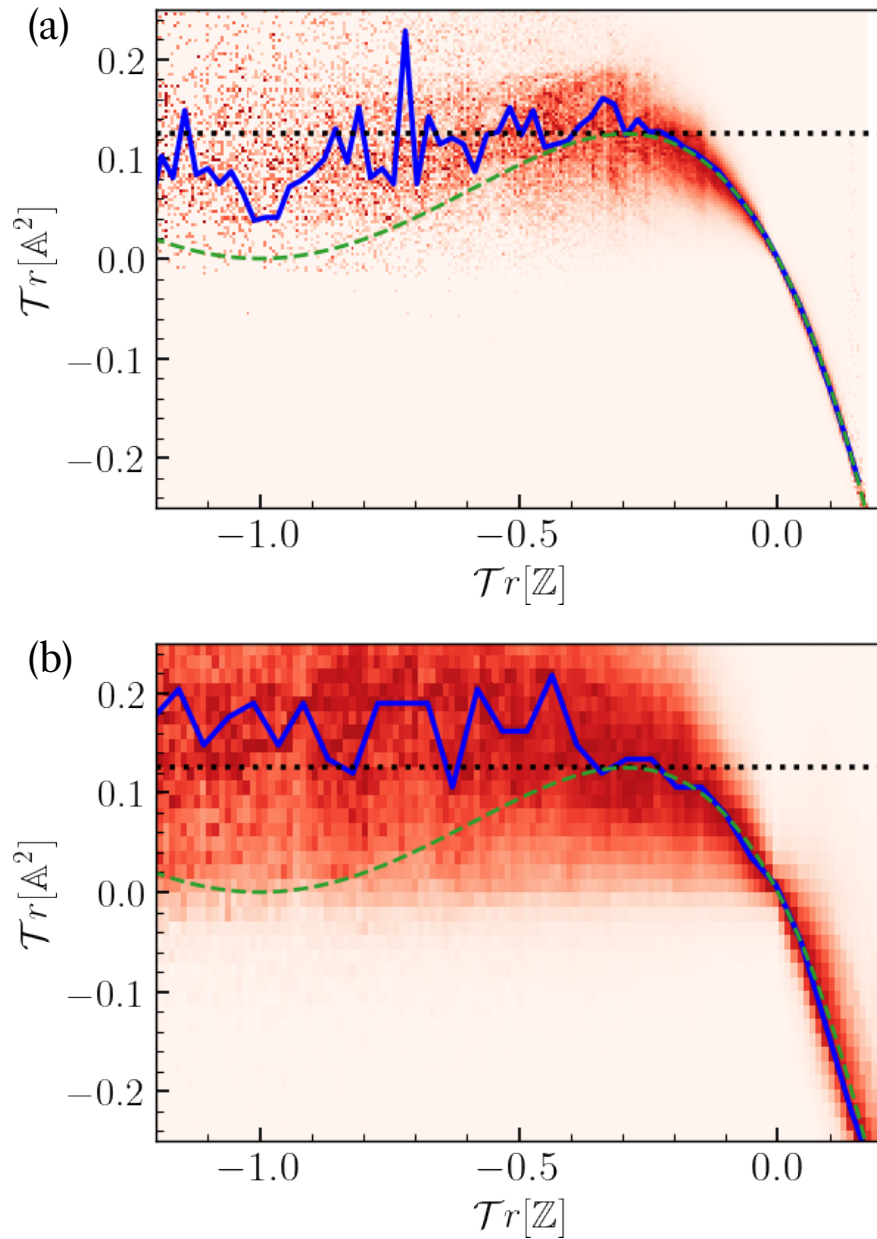


Figure 3.10: The joint distribution of $\mathcal{T}r[\mathbb{Z}]$ and $\mathcal{T}r[\mathbb{A}^2]$ for (a) $St = 0.26$, and (b) $St = 0.50$. Each vertical slice in the distribution is normalized to unity. Thus, the dark red represents the value 1 and the faint red 0. The optimal trajectory is plotted in blue and the trajectory of the fixed-point is marked in dashed green. Horizontal dashed line represents $\mathcal{T}r[\mathbb{A}^2] = 1/8$.

When $\tilde{\lambda}$ is finite, one obtain the following parametric equation

$$\tilde{\lambda}^2 = -z_0(z_0 + 1)(2z_0 + 1)^2, \quad (3.25)$$

and the bifurcation here occurs for $\{z_0^*, z_2^*\} = \{(-\frac{1}{4}(2 \pm \sqrt{2}), \pm \frac{1}{2\sqrt{2}})\}$ and $\tilde{\lambda}^2 = \frac{1}{16}$.

When the eigenvalues are imaginary or the dynamics is governed by 3.23 and 3.24, fixed points are stable and non-stable spirals. This implies no caustics can form in the vortical region.

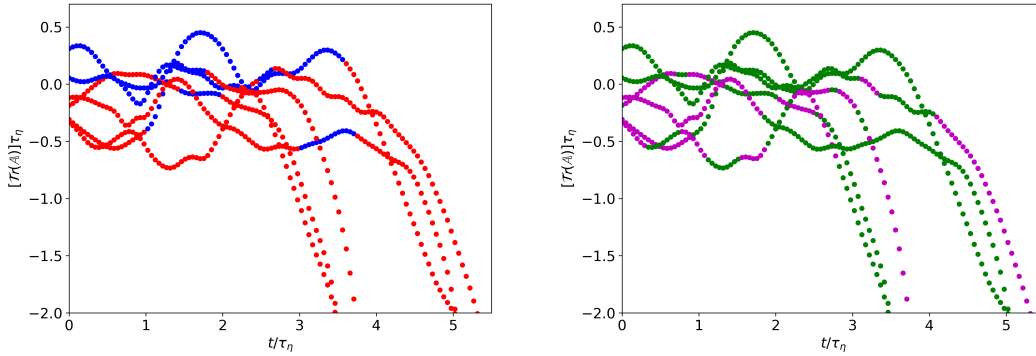


Figure 3.11: Typical time traces of $\mathcal{T}r[\mathbb{Z}]$ from our three-dimensional run 3a1. In the left plot blue and red colors correspond to the positive and negative sign of $\mathcal{Q}[\mathbb{A}]$, respectively. In the right plot green and magenta colors corresponds to the positive and negative sign of $\Delta[\mathbb{A}] = \frac{27}{4}\mathcal{R}[\mathbb{A}]^2 + \mathcal{Q}[\mathbb{A}]^3$, respectively, where $\Delta[\mathbb{A}]$ is the discriminant of the characteristic polynomial of \mathbb{A} . The traces are colored according to the topological character of the flow at the location of the particle. If the flow is topologically an elliptic point (a vortex) we use the color blue. If the flow is topologically a hyperbolic point (a strain dominated point) we use the color red.

Note that $\mathcal{T}r[\mathbb{A}^2] = 2(\tilde{\lambda}^2 + \tilde{\omega}^2)$ and $\mathcal{T}r[\mathbb{Z}] = 2z_0$. Thus,

$$\mathcal{T}r[\mathbb{A}^2] = -\mathcal{T}r[\mathbb{Z}] \left(\frac{\mathcal{T}r[\mathbb{Z}]}{2} + 1 \right) \left(\mathcal{T}r[\mathbb{Z}] + 1 \right)^2. \quad (3.26)$$

From the stability analysis, we can conclude that the caustic can occur only in the strain dominated when $\mathcal{T}r[\mathbb{A}^2]$ exceeds $\frac{1}{8}$. In Fig. 3.10 we plot $\mathcal{T}r[\mathbb{A}^2]$ vs. $\mathcal{T}r[\mathbb{Z}]$ obtained from our two-dimensional simulation 2d4. The optimal trajectory is obtained by finding the most probable $\mathcal{T}r[\mathbb{A}^2]$ for a given $\mathcal{T}r[\mathbb{Z}]$. In the plot we show this optimal trajectory using the blue line and the

trajectory of fixed point is plotted using the dashed green line. The optimal trajectory closely follows fixed point till bifurcation, or $\mathcal{T}r[\mathbb{A}^2] = 1/8$ marked by horizontal dashed line. Beyond that $\mathcal{T}r[\mathbb{Z}] \rightarrow -\infty$ almost vertically.

In Fig. 3.11 we show the evolution of $\mathcal{T}r[\mathbb{Z}]$ for three-dimensional simulation. Similar to two-dimension, we find the formation of singularities – large negative excursions of $\mathcal{T}r[\mathbb{Z}]$ – starts when the flow is hyperbolic in nature. In three-dimensions 3.10 shows that $\mathcal{T}r[\mathbb{Z}]$ can become singular only if $\mathcal{Q}[\mathbb{A}]$ is negative – these too correspond to regions of the flow which are topologically hyperbolic [25].

3.7 Conclusion

In this chapter we investigated the rate of caustic formation in a particle laden turbulent flow. The rate, given by 3.6 was first derived for the one dimensional model, 3.2 in Ref. [5]. This work has been extended to two- and three-dimensions in Refs [26, 27] respectively. Similar to this chapter, in both of these studies, 3.6 was argued to hold by analogy in two- and three-dimensions, but no systematic derivation was provided. In most of the earlier studies except Ref. [12], the fluctuations in \mathbb{A} was assumed to be Gaussian, in this study, we make no such assumptions. Furthermore our study brings out the clear nature of scaling for the rate of caustics formation in the limit $St \rightarrow 0$.

Singularities found in a numerical simulations are necessarily not true singularities – their detection depends on the threshold value we use. We have checked that by changing our threshold value $-A_{th}$ from 10^2 to 10^{10} the rate-of-formation of singularities itself changed, by small amounts, but its dependence on Stokes, 3.6, remains unchanged. This is expected, because in 3.2 once $\mathcal{T}r[\mathbb{Z}] < -1/\tau_p$ the dynamics is determined by the nonlinear term $[\mathcal{T}r[\mathbb{Z}]]^2$. Hence any stochastic trajectories of \mathbb{Z} where $\mathcal{T}r[\mathbb{Z}]$ becomes smaller than $-1/\tau_p$ will reach blowup.

Possible effects the non-zero correlation time of the flow may have on the rate-of-formation of singularities have been explored in a series of pa-

pers [28]. None of these consider actual turbulent flows but synthetic flows (statistical models) with a characteristic length scale (l), a characteristic velocity scale (v) and a characteristic time scale (τ) all three of which can be chosen independent of one another. This way, a new dimensionless number, the Kubo number, $Ku \equiv v\tau/l$, can be introduced. The rate-of-formation of caustics for such models, in one dimension, was calculated numerically [28] and compared with analytical perturbation theory. In the limit of white-noise 3.6 was recovered. But for finite Ku the rate-of-formation of singularities on St is not universal but depends on Ku too. In turbulent flows Ku is unity because the characteristic time scale, $\tau_\eta = \eta/u_\eta$, where u_η is the characteristic velocity scale at the Kolmogorov scale. For $Ku = 1$, the simulations of the statistical model confirmed 3.6.

In one dimensions, from 3.2 the rate-of-formation of singularities can be calculated exactly and 3.6 is the leading order term in the expression. But the mapping of the two-and three-dimensional problems to 3.6 holds only for small τ_p , equivalently small St . Hence, in two-and three-dimensions 3.6 hold only in the limit of small St . Simulations in two-dimensions [15] have shown that for small St , the approximation, $\mathcal{D}et[Z] \approx \mathcal{D}et[A]$ holds.

The formation of caustics occur predominantly in the strain-dominated region of the flow. In two-dimension this can be understood using a simple stability analysis (Ref. [3] for more details). A similar analysis although possible, is much difficult in three-dimension and is left for future studies.

References

- [1] P. J. Armitage, *Astrophysics of Planet Formation* (Cambridge University Press, Cambridge, UK, 2010).
- [2] H. Pruppacher and J. Klett, *Microphysics of Clouds and Precipitation*, Vol. 18 (Springer Science & Business Media, Berlin, Heidelberg, Dordrecht, and New York City, 2010).
- [3] J. Meibohm, V. Pandey, A. Bhatnagar, K. Gustavsson, D. Mitra, P. Perlekar, and B. Mehlig, “Paths to caustic formation in turbulent aerosols,” (2020), arXiv:2012.08424 [physics.flu-dyn] .
- [4] P. G. Saffman and J. S. Turner, *J. Fluid Mech.* **1**, 16 (1956).
- [5] M. Wilkinson and B. Mehlig, *Phys. Rev. E* **68**, 040101 (2003).
- [6] M. Voßkuhle, A. Pumir, E. Lévêque, and M. Wilkinson, *J. Fluid Mech.* **749**, 841 (2014).
- [7] V. E. Perrin and H. J. Jonker, *Phys. Rev. E* **92**, 043022 (2015).
- [8] A. Bhatnagar, K. Gustavsson, and D. Mitra, *Phys. Rev. E* **97**, 023105 (2018).
- [9] A. Bhatnagar, K. Gustavsson, B. Mehlig, and D. Mitra, *Phys. Rev. E* **98**, 063107 (2018).
- [10] S. L. Rani, R. Dhariwal, and D. L. Koch, *J. Fluid Mech.* **871**, 477 (2019).
- [11] R. Dhariwal and A. D. Bragg, *J. Fluid Mech.* **839**, 594 (2018).
- [12] G. Falkovich and A. Pumir, *J. Atmos. Sci.* **64**, 4497 (2007).
- [13] G. Falkovich, A. Fouxon, and M. Stepanov, *Nature, London* **419**, 151 (2002).
- [14] K. Gustavsson and B. Mehlig, *Adv. Phys.* **65**, 1 (2016).
- [15] D. Mitra and P. Perlekar, *Phys. Rev. Fluid* **3**, 044303 (2018).
- [16] A. Brandenburg and W. Dobler, *Comput. Phys. Commun.* **147**, 471 (2002).

- [17] M. Maxey, J. Fluid Mech. **174**, 441 (1987).
- [18] R. A. Shaw, Annu. Rev. Fluid Mech. **35**, 183 (2003).
- [19] O. Ayala, B. Rosa, L.-P. Wang, and W. W. Grabowski, N. J. Phys. **10**, 075015 (2008).
- [20] W. W. Grabowski and L.-P. Wang, Annu. Rev. Fluid Mech. **45**, 293 (2013).
- [21] A. Okubo, Deep sea research **17**, 445 (1970).
- [22] J. Weiss, Physica D: Nonlinear Phenomena **48**, 273 (1991).
- [23] P. Perlekar, S. Ray, D. Mitra, and R. Pandit, Phys. Rev. Lett **106**, 054501 (2011).
- [24] S. Strogatz, *Nonlinear Dynamics and Chaos*, Studies in Nonlinearity (Avalon Publishing, 2016).
- [25] M. Chong, A. Perry, and B. Cantwell, Phys. Fluids. A **3**, 765 (1990).
- [26] M. Wilkinson and B. Mehlig, EPL (Europhysics Letters) **71**, 186 (2005).
- [27] K. Duncan, B. Mehlig, S. Östlund, and M. Wilkinson, Phys. R. Lett. **95**, 240602 (2005).
- [28] K. Gustavsson and B. Mehlig, Phys. Rev. E **87**, 023016 (2013).

Clustering and energy spectra in dusty-gas turbulence

4.1 Introduction

In the previous chapter-3, the back-reaction from particle was ignored to study the multiphase flow. In this chapter, we consider a problem in the regime of moderately dense suspension, where the flow is affected by the particles. For notational convenience, in the rest of this chapter, we shall call the solvent phase “gas” and the particles “dust”. As discussed in chapter-2, the simplest model of such multiphase flows is based on the assumption that the dust is a collection of heavy inertial particles (HIPs).

In the absence of dust, the turbulence in the gas phase has been extensively studied [1–3]. The pioneering work of Kolmogorov [4] has established that in three-dimensions the (angle-integrated) energy spectrum of the gas shows power-law behavior $E(k) \sim k^{-5/3}$ within the inertial range followed by the dissipation range where the energy spectrum shows exponential decay¹. More importantly, the inertial range spectral exponent is universal, i.e. it

¹Experiments and recent numerical simulations have demonstrated that the Kolmogorov picture is not complete, but must include corrections due to intermittency. The intermittency corrections to the energy spectrum is small and is ignored.

does not depend on the Reynolds number and the mechanism of turbulence generation. Does the presence of dust modify this energy spectrum? Obviously, in general, the answer depends on the number, size, and shape of the dust grains. In this chapter, we study this question using direct numerical simulations (DNS) of the dusty gas flow.

Previous studies [5] has suggested that in the presence of dust a new power-law behavior can emerge where $E(k) \sim k^{-4}$ in three dimensions. Is this exponent universal, in the sense that, is it independent of the particle properties such as Stokes number and the dust concentration? It is difficult to provide an answer to this question because an accurate determination of the exponent requires obtaining clean scaling of the energy spectrum over at least a decade. This is a formidable task in three dimensions but is a much simpler proposition in two-dimensions. Hence to understand the universality (or lack thereof) we study this problem in two dimensions.

Two-dimensional turbulence is the simplest model to investigate flows in the atmosphere and oceans [1, 3, 6]. A key feature of two-dimensional turbulence is that it supports a bi-directional cascade, an inverse cascade of energy from forcing scales to larger scales and a forward enstrophy cascade from forcing scales to smaller scales [7–12]. As we are interested in investigating how dust modifies small scale flow properties, we concentrate on the forward enstrophy cascade.

In two-dimensional gas turbulence, forced at large scales (small k) and in the presence of air-drag friction (α), the scaling exponent of the energy spectrum is universal with respect to the Reynolds number but *non-universal* in general – it depends on the air-drag-friction coefficient [13, 14]. The scaling exponent and its non-universality can be understood as an effect of the loss of enstrophy due to air-drag-friction [15]. In our simulations, we choose an α such that in the absence of dust $E(k) \sim k^{-3.9}$. We then perform extensive simulations of the dusty-gas flow by varying both the Stokes number and the mass-loading-parameter (ϕ_m , ratio of the total mass of the dust to the total fluid mass).

The rest of this chapter is organized in the following manner. We first

present the model of dust grains and fluid and describe the numerical method used to study the problem in Sec. 5.2. In Sec. 5.9, we study the pair distribution function of dust particles where we show that increasing mass-loading parameter reduces the clustering of dust. In Sec. 4.4 and 4.5, we study the kinetic energy spectra and scale-by-scale enstrophy budget for the gas phase. We show that in the presence of dust-gas coupling, a new scaling range, which we call the dust-dissipative range, emerges in the kinetic energy spectra of the gas. Furthermore, using a scale-by-scale enstrophy budget analysis we show that the new scaling regime appears due to a balance between the injection (from the dust to the gas) and viscous dissipation. Our main result is that the scaling exponent is *not universal* but depends on both St and the mass-loading parameter ϕ_m .

4.2 Simulation details

We model the gas phase in the Eulerian-framework using the Navier-Stokes equation in the vorticity-streamfunction formulation,

$$\partial_t \omega + \mathbf{u} \cdot \nabla \omega = \nu \nabla^2 \omega - \alpha \omega + f^k + \nabla \times \mathbf{F}^{d \rightarrow g}, \quad (4.1)$$

where $\omega(\mathbf{x}, t) \equiv \nabla \times \mathbf{u}(\mathbf{x}, t)$ is the vorticity field, $\mathbf{u}(\mathbf{x}, t)$ is the incompressible velocity field, ν is the viscosity, and α is the Ekman drag coefficient. To sustain turbulence we force the equation with the Kolmogorov driving of the form $f^k(\mathbf{x}, t) = -f_0 k_f \cos(k_f y)$, where f_0 is the amplitude and k_f is the forcing wave-mode. The last term $\mathbf{F}^{d \rightarrow g}$ is the back-reaction from the dust phase to the gas.

We solve 4.1 in the vorticity-stream function formulation in a square periodic box of length L and generate a stationary turbulence by forcing at wave-mode $k_f = 4$. The domain is discretized taking N collocation points along each direction. For time evolution we employ a second-order Runge-Kutta scheme [16]. We take $\omega(\mathbf{x}, 0) = -f_0 k_f \nu [\cos(k_f x) + \cos(k_f y)]$. In Fig. 4.1 we show a representative snapshot of the vorticity field in the steady state for the case where $\mathbf{F}^{d \rightarrow g} = 0$, from the simulation.

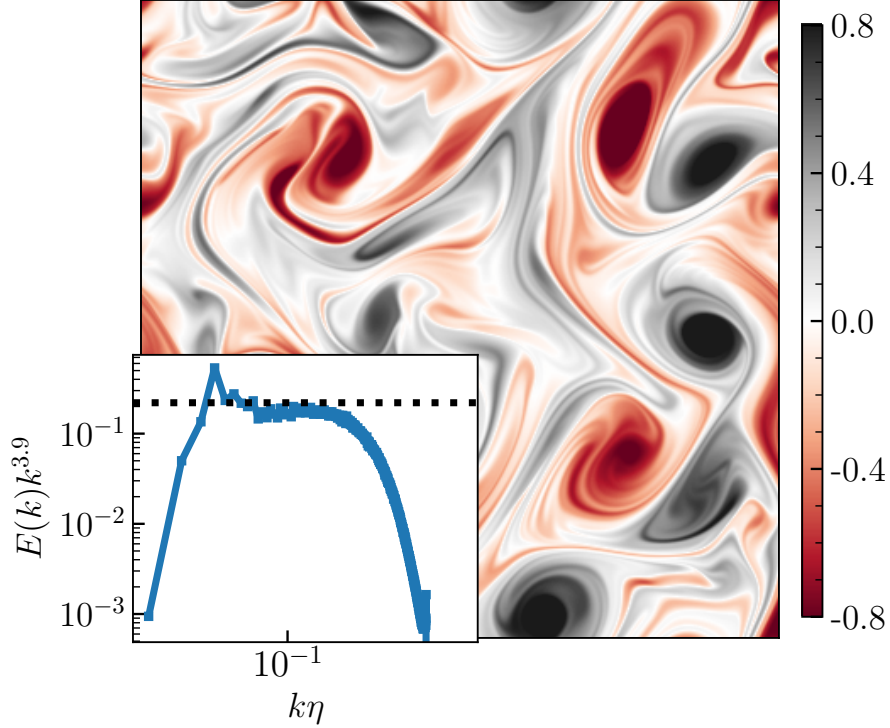


Figure 4.1: Representative steady-state snapshot of vorticity field (ω) from the simulation of pure gas phase. (Inset) Log-log plot of compensated energy spectrum $[k^{3.9}E(k)]$ versus $k\eta$, where η is the Kolmogorov dissipation length scale. To generate turbulent flow we use the following parameters: $\alpha = 10^{-2}$, $f_0 = 5 \times 10^{-3}$, $k_f = 4$ and $\nu = 10^{-5}$. We vary $N = 1024$ and 4096 . We find: the Kolmogorov dissipation length $\eta \left(\equiv \sqrt[4]{\nu^3/\epsilon} \right) = 5.4 \times 10^{-3}$, the Kolmogorov dissipation time scale $\tau_\eta \left(\equiv \sqrt{\nu/\epsilon} \right) = 2.9$, and enstrophy dissipation rate $\beta = 2.8 \times 10^{-4}$.

The details of modeling the dust phase is given in chapter 2. For completeness here we rewrite the equations of motion for a grain of dust (1.23 and 1.24),

$$\begin{aligned} \frac{d\mathbf{X}(t)}{dt} &= \mathbf{V}(t), \\ \frac{d\mathbf{V}(t)}{dt} &= \frac{1}{\tau_p} [\mathbf{u}(\mathbf{X}, t) - \mathbf{V}(t)], \end{aligned}$$

where \mathbf{X} is the position, \mathbf{V} is the velocity of a dust particle, \mathbf{u} is the velocity of the gas at a point \mathbf{X} , and $\tau_p \equiv 2\rho_p a^2 / 9\rho_f \nu$ is the particle relaxation time.

In Fig. 4.2, we show that comparison of kinetic energy spectrum of the fluid as obtained using the ERPP and the particle in cell. We find that the scaling in the spectra is independent of the choice of method used to distribute the back-reaction forces. Due to the ease of computation we use particle in cell for all the dns in this chapter.

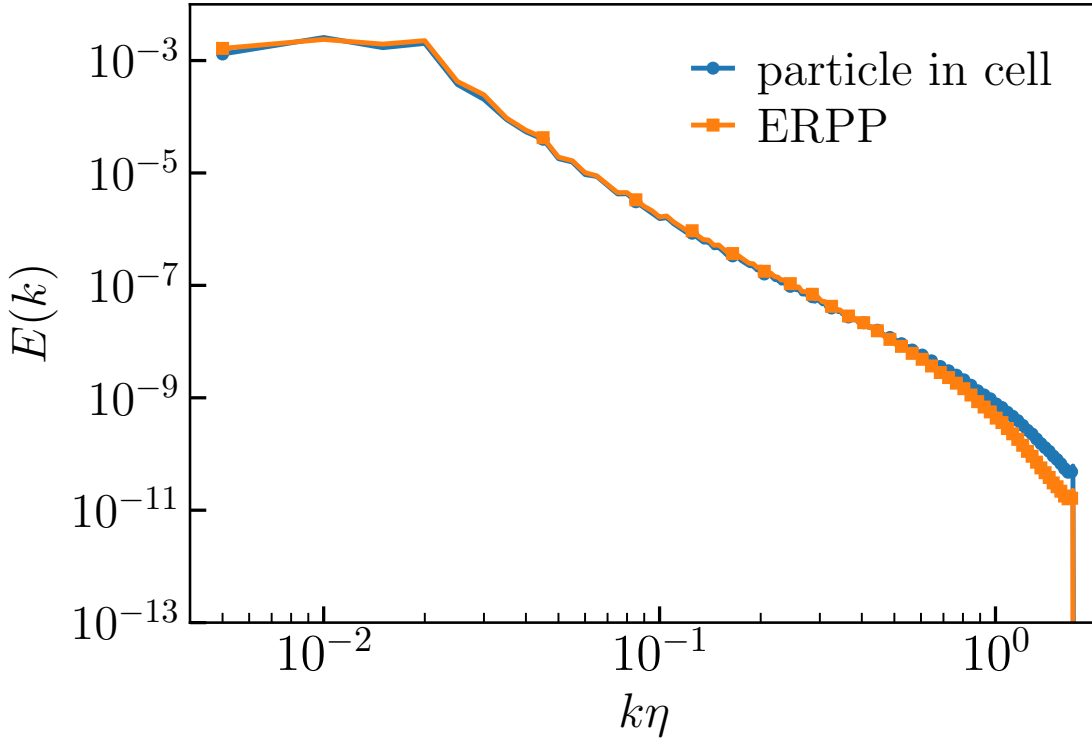


Figure 4.2: Comparison of the kinetic energy spectrum for the cases where the particle back-reaction is treated using ERPP and particle in cell. The simulation is conducted at $St = 0.33$, $\phi_m = 1$ and $N = 1024$. In the ERPP simulation we take $T_R = h^2/2\nu = 1.89$.

We further compare the kinetic energy spectra obtained for two resolution $N = 1024$ and 4096 from particle in cell simulation. Such comparisons are important to determine the convergence of the solution. In Fig. 4.3, we show the energy spectra for $St = 0.33$ and $\phi_m = 1$ at both the resolutions. The spectra shows the same scaling in the inertial range for both $N = 1024$ and 4096 . We find that, increasing the resolution only extends the scaling range to smaller scales.

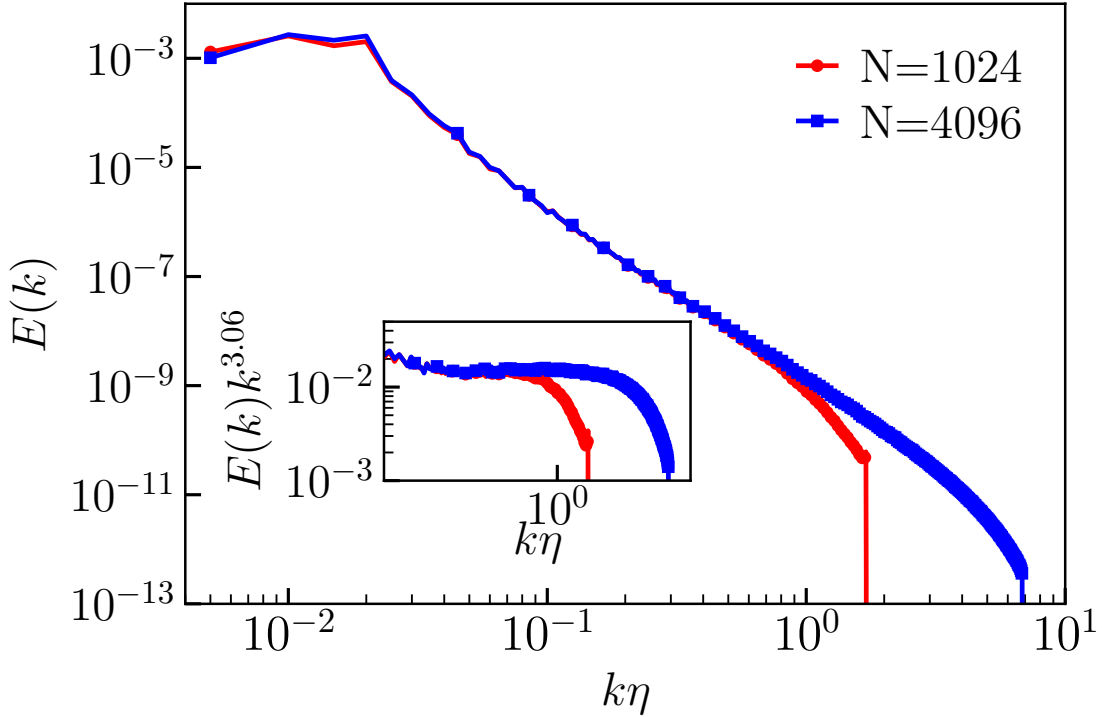
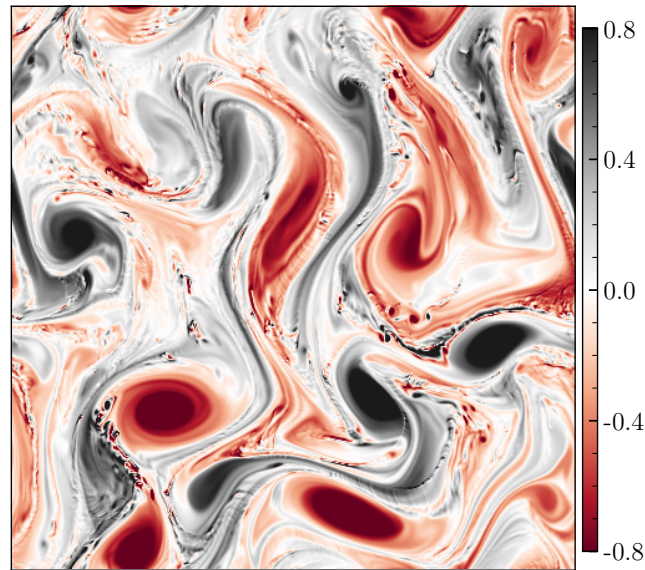


Figure 4.3: Comparison of the kinetic energy spectrum for $St = 0.33$ and $\phi_m = 1$ at two resolutions. Inset shows the compensated plot showing the scaling range.

In Fig. 4.4 we show a representative pseudo-color plot of the vorticity field at high mass-loading $\phi_m = 1$. In contrast to the case where $\phi_m = 0$, here we observe small-scale vortices form in the regions where dust particle cluster. Our observation is consistent with the earlier study of two-dimensional dusty-gas turbulence [17].

In the statistically stationary state, we continue the DNS for another $35\tau_{\ell_0}$ to collect statistics of the turbulent flow. Here $\tau_{\ell_0} \equiv 2\pi/k_f u_0$ is the large-eddy-turnover-time and the Kolmogorov time scale $\tau_\eta \equiv \sqrt{\nu/\epsilon}$ is approximately $\tau_{\ell_0}/16$ in our simulation. Similar to aerosols in clouds [18], we assume that ratio of material density of dust over the gas density is $\rho_p/\rho_f \sim 10^3$.

(a)



(b)

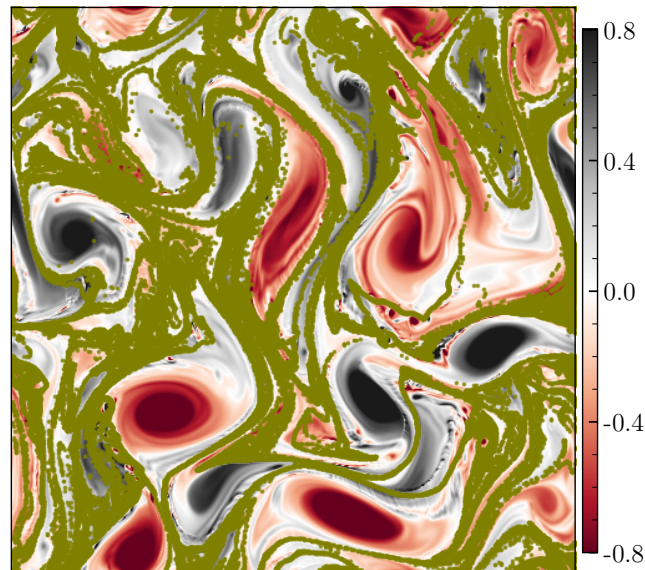


Figure 4.4: (a) Representative snapshot of ω during steady state for $St = 0.33$ and $\phi_m = 1.0$. (b) The positions of all the dust particles are overlaid as olive dots on the underlying vorticity plot of (a). The diameter of each dust particle is assumed to be much smaller than η . We vary St in the range $0.17 - 1.67$ and N_p in range $1.5 \cdot 10^4 - 1.5 \cdot 10^5$ to achieve mass-loading (ϕ_m) of $0.1 - 1.0$ respectively. Only exception is made for $St = 0.17$ for results shown in [Sec. 4.4](#) and [Sec. 4.5](#) where we take $N_p = 4.5 \cdot 10^5$ to achieve $\phi_m = 1$.

4.3 Clustering

We quantify the clustering by using the cumulative pair distribution function

$$N(r) \equiv \left\langle \frac{2}{N_p(N_p - 1)} \sum_{i < j} \Theta(r - |\mathbf{X}_i - \mathbf{X}_j|) \right\rangle. \quad (4.2)$$

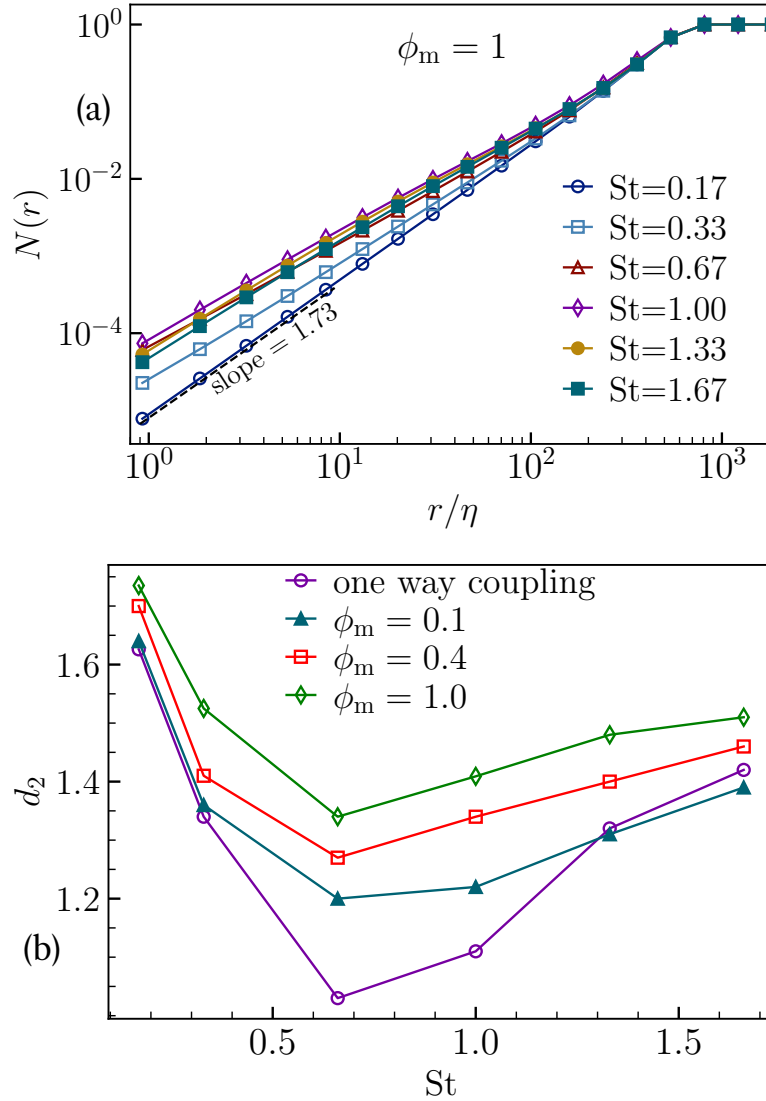


Figure 4.5: (a) Log-log plot of the cumulative distribution function $N(r)$ vs. r/η for $\phi_m = 1$ and different St . The dashed line represents least square fit with corresponding value of the slope. (b) The correlation dimension d_2 vs. St for different ϕ_m .

Here Θ is the Heaviside function and the angular brackets denote averaging over different stationary-state turbulent configurations. In Fig. 4.5(a),

we plot $N(r)$ versus r for fixed $\phi_m = 1$ and with different St . In the limit $r \rightarrow 0$, $N(r) \sim r^{d_2}$, where d_2 is the correlation dimension [19]. We obtain d_2 by performing a least square fit in the range $1 < r\eta < 10$.

In Fig. 4.5(b) we plot the correlation dimension d_2 as a function of St for different values of ϕ_m . In the limit $St \rightarrow 0$, 1.24 gives $\mathbf{V}(\mathbf{X}, t) = \mathbf{u}(\mathbf{X}, t)$, which implies that the spatial distribution of the particles is uniform ($d_2 = 2$). The opposite limit $St \rightarrow \infty$, corresponds to the ballistic regime where the inertial particles detach from the underlying flow, again resulting to a uniform spatial distribution. At intermediate St , the correlation dimension $d_2 < 2$, as the particles preferentially cluster in the strain dominated regions of the flow. Hence we expect a non-monotonic behavior in d_2 as the St is increased from 0 Fig. 4.5. We find that d_2 attains a minimum value, which corresponds to maximum clustering, around $St \approx 0.6$ [20]. We observe that for all the values of ϕ_m this is indeed the case. However, the amount of clustering (d_2) decreases (increases) with increasing ϕ_m . We find that for a fixed St , the maximum clustering is obtained for one-way coupled simulations where the back-reaction from the dust is ignored. Similar results have also been observed for particle-laden turbulent homogeneous shear flows [21, 22]. Qualitatively, the small-scale vortices produced in presence of mass-loading expel particles hence clustering reduces as with ϕ_m increases.

4.4 Energy spectra

In this section, we study the angle averaged velocity power spectrum,

$$E(k) \equiv \frac{1}{2} \left\langle \sum_{k-1/2 \leq |\mathbf{m}| < k+1/2} |\mathbf{u}_{\mathbf{m}}|^2 \right\rangle, \quad (4.3)$$

where $\mathbf{u}_{\mathbf{m}}$ is the velocity at the fourier mode \mathbf{m} . In the absence of dust particles ($\phi_m = 0$), the energy spectrum [Fig. 4.1] shows inertial range scaling $E(k) \sim k^{-3.9}$ for $0.03 \leq k\eta \leq 0.1$ and decays exponentially in the dissipation range ($k\eta > 0.10$) [23].

We find that once the feedback from the dust to the gas phase is included, the energy spectra changes dramatically in the following manner: the inertial

range scaling with an exponent of $k^{-3.9}$ persists till a critical wave number K_c ; for $k > K_c$, we observe a new power-law $E(k) \sim k^{-\xi}$ with $\xi < 3.9$. This scaling range, which we henceforth call *dust-dissipative* range, continues, in some cases, almost up to the dealiasing scale k_{\max} . The new scaling exponent ξ is *non-universal* – it depends on both St and the mass-loading parameter ϕ_m . To demonstrate this we first compare the energy spectra for the case with no feedback (dashed black line) with three representative cases with feedback: $\phi_m = 1$ and three different values of St, in Fig. 4.6(a). For $k < K_c$ all the four spectra show the same scaling behavior. But for $k > K_c$ the spectrum without feedback ($\phi_m = 0$) falls off very sharply compared to the ones with feedback. To explore the scaling behavior of the spectra in detail, in Fig. 4.6(b) we plot the same spectra compensated with $k^{3.9}$. For $k < K_c$ all the compensated spectra look horizontal, with fluctuations. In contrast, for $k > K_c$ the compensated spectrum for the case with no feedback ($\phi_m = 0$) falls off sharply, indicating an exponential fall off, whereas the ones with feedback grows with k suggesting the emergence of a new scaling regime with an exponent $\xi < 3.9$. Next we calculate ξ by a least-square fit to the tail of the spectra with feedback. The values of ξ we obtain depends on St.

Next, in Fig. 4.6(c) we plot the three spectra with feedback again, this time compensated with k^ξ . The range over which the spectra are horizontal shows the extent of new dust-dissipative range. Next we do a similar analysis where we compare the case with no feedback again with three cases with feedback; but this time we hold $St = 0.67$ fixed and consider three different values of ϕ_m . The corresponding figures are shown in the right column of Fig. 4.6. We systematically calculate the scaling exponent ξ for three values of St between 0.17 and 1.67 with $\phi_m = 1$ and for three values of ϕ_m between 0.1 and 1 with $St = 0.67$. With St, we find that ξ first decreases, reaches its minimum value $\xi \sim 3$ for $St = 0.33$ [see Fig. 4.6(d,e)] and then increases again. For a fixed $St = 0.67$, ξ reduces monotonically as ϕ_m is increased [Fig. 4.6(b,d, and f)].

In Table 4.1 we list the scaling exponent ξ , obtained from the energy spectra, with its error estimate. It is not trivial to estimate the error in measurement of ξ . We select the scaling range as the range over which the scaling

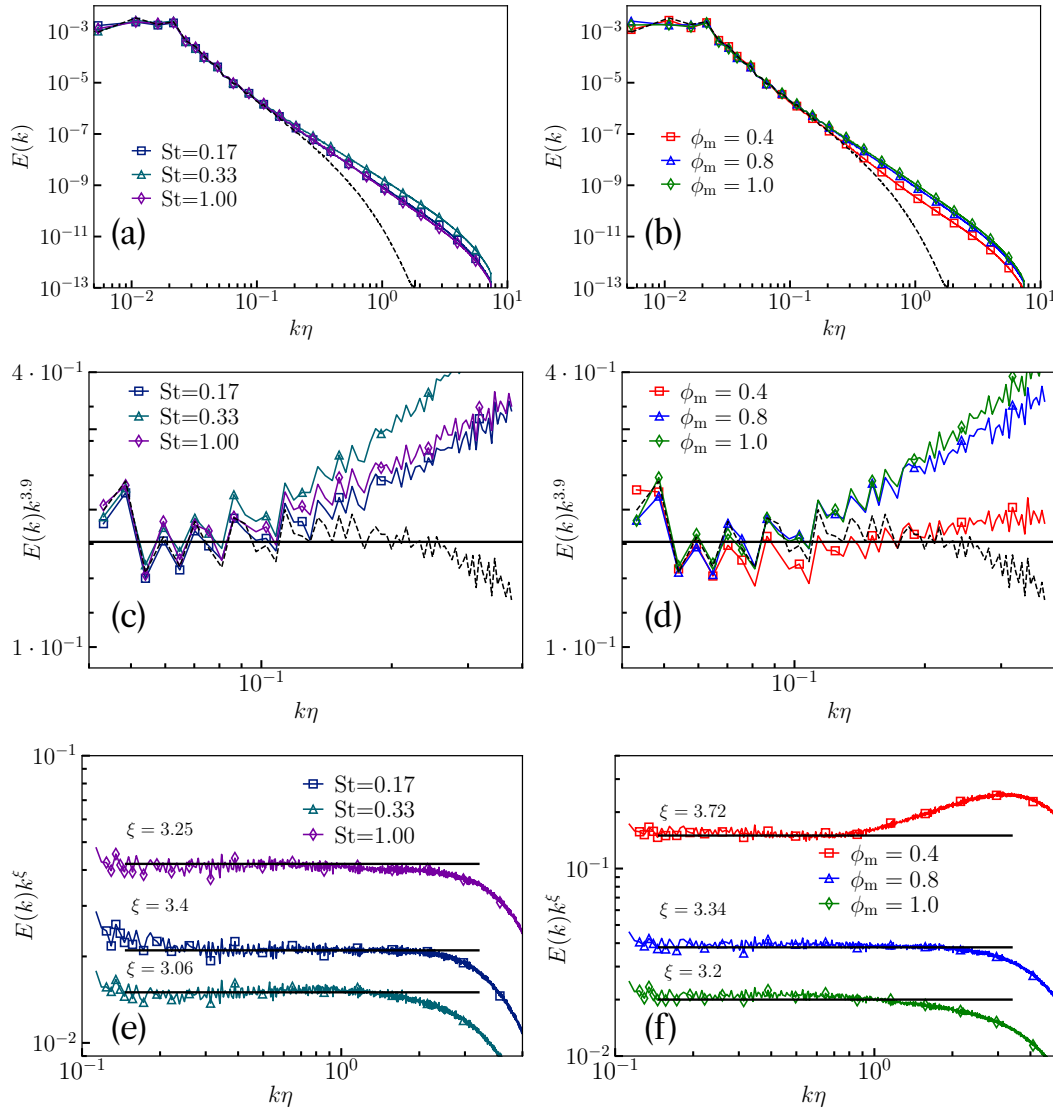


Figure 4.6: Log-log plot of energy spectra for (a) $\phi_m = 1.0$, different values of St , (b) $St = 0.67$, different values of ϕ_m . Black dashed line shows $E(k)$ for $\phi_m = 0$. (c,d) Log-log plot of energy spectra $E(k)$ compensated by $k^{3.9}$. The black dashed lines shows the compensated spectra for the case $\phi_m = 0$, i.e., no feedback. Once the feedback is included, the compensated spectra show a rise at large wavenumbers, i.e., a new scaling regime emerges. (e,f) Log-log plot of energy spectra compensated by k^ξ where the exponents ξ for each St and ϕ_m is given in the figure. In (c) and (e) the mass loading $\phi_m = 1$, while $St = 0.67$ in (d) and (f). The scaling exponents of energy spectra in the dust-dissipative range is obtained by doing a local slope analysis. The maximum standard error [24] on the local slope for each data set is around ± 0.05 .

exponent (obtained from local slope) of the energy spectra is within ± 0.1 of its mean value. We use the maximum standard error [24] of the local slope as a reasonable estimate of error. We have checked that, if we calculate the exponents ξ over half the data-set the values obtained remain within the range of error. Note that the range of the scaling regime is not very large even in the best cases. Consequently, sub-leading terms in scaling behavior may contribute significantly [25]. The actual error in the determination of the scaling exponents is likely to be larger than the values we quote. In the next section, we calculate the exponent in another manner.

4.5 Enstrophy budget

To understand the scaling behavior we now study the scale-by-scale enstrophy budget equation:

$$\Pi^\omega(k) = \mathcal{D}^\omega(k) - \alpha\Omega(k) + \mathcal{F}^k(k) + \mathcal{R}(k). \quad (4.4)$$

Here

$$\Omega(k) \equiv \left\langle \sum_{m \leq k} |\omega_{\mathbf{m}}|^2 \right\rangle \quad (4.5a)$$

is the cumulative enstrophy up to wave-number k ,

$$\Pi^\omega(k) \equiv \left\langle \sum_{m \leq k} \omega_{\mathbf{m}} (\mathbf{u} \cdot \nabla \boldsymbol{\omega})_{-\mathbf{m}} \right\rangle \quad (4.5b)$$

is the enstrophy flux through a sphere of radius k in Fourier space due to the non-linear term,

$$\mathcal{D}^\omega(k) \equiv -\nu \left\langle \sum_{m \leq k} m^2 |\omega_{\mathbf{m}}|^2 \right\rangle \quad (4.5c)$$

is cumulative enstrophy dissipation rate, $-\alpha\Omega(k)$ is the contribution due to the Ekman friction,

$$\mathcal{F}^k(k) \equiv \left\langle \sum_{m \leq k} \omega_{\mathbf{m}} f_{-\mathbf{m}}^k \right\rangle \quad (4.5d)$$

is the cumulative enstrophy injected due to Kolmogorov forcing, and

$$\mathcal{R}(k) \equiv \left\langle \sum_{m \leq k} \omega_{\mathbf{m}} (\nabla \times \mathbf{F}^{d \rightarrow g})_{-\mathbf{m}} \right\rangle \quad (4.5e)$$

is the contribution because of the back reaction from the dust particles to the gas.

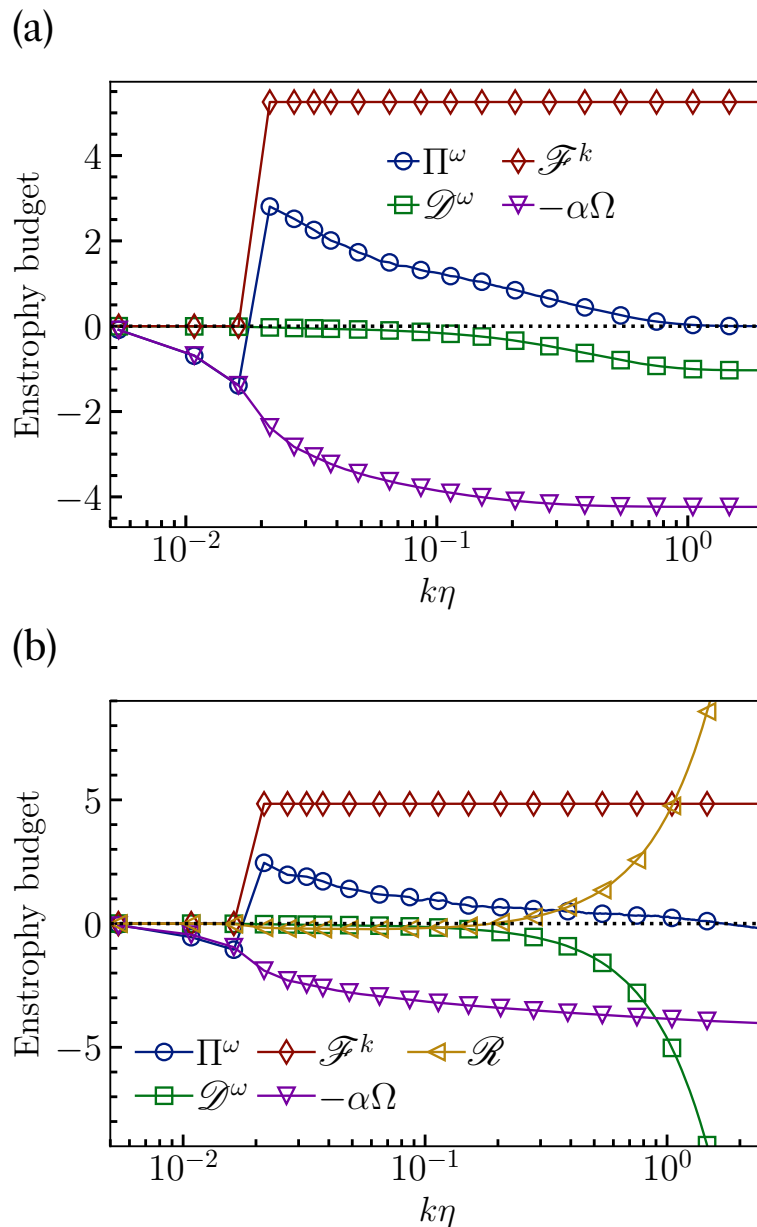


Figure 4.7: Semi-log (X-axis in log scale) plot of scale-by-scale enstrophy budget for (a) $\phi_m = 0$, (b) $St = 0.67$ and $\phi_m = 1$. The ordinates of figure (a) and (b) are normalized by the enstrophy dissipation rate β .

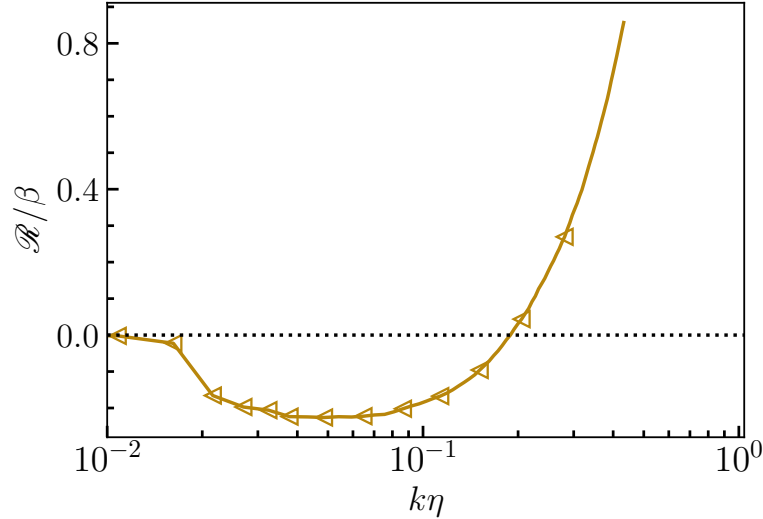


Figure 4.8: Semi-log plot of $\mathcal{R}(k)$ zoomed for $k_\eta \leq 0.4$. Note that $\mathcal{R}(k)$ changes sign from negative to positive at K_c . The ordinates of the figure is normalized by the entrophy dissipation rate β .

In Fig. 4.7(a) we plot the entrophy budget for the gas in the absence of particles ($\phi_m = 0$). Similar to earlier studies, we observe that at large scales entrophy injected by external forcing is primarily balanced by the Ekman drag and the entrophy flux $\Pi^\omega(k)$ decreases with increasing k [11].

We now show that the presence of dust particles dramatically alters the entrophy budget in the range of wavenumber which belongs to the dissipation range for the case with no feedback. In Fig. 4.7(b) we plot the cumulative contributions of all the terms in budget for $St = 0.67$ and $\phi_m = 1.0$. The dust particles inject entrophy (\mathcal{R}) at large k which is then balanced by viscous dissipation \mathcal{D}^ω . We find a negligible change in shape of Π^ω , \mathcal{F}^k and the Ekman drag term in the inertial range. A closer look at \mathcal{R} [Fig. 4.8] reveals that it makes a net negative contribution to budget till a wavenumber K_c after which it turns positive. Clearly, the particles extracts entrophy from the flow at small k (large scales) but injects entrophy at large k (small scales). Furthermore, for $k > K_c$ the two dominant terms that balance each other are the contribution because of the back reaction from the dust particles to the gas \mathcal{R} and the cumulative entrophy dissipation due to viscosity \mathcal{D}^ω , i.e. $\nu \sum_{m \leq k} m^4 E(m) \sim \mathcal{R}(k)$. Taking the derivative with respect to k , we get

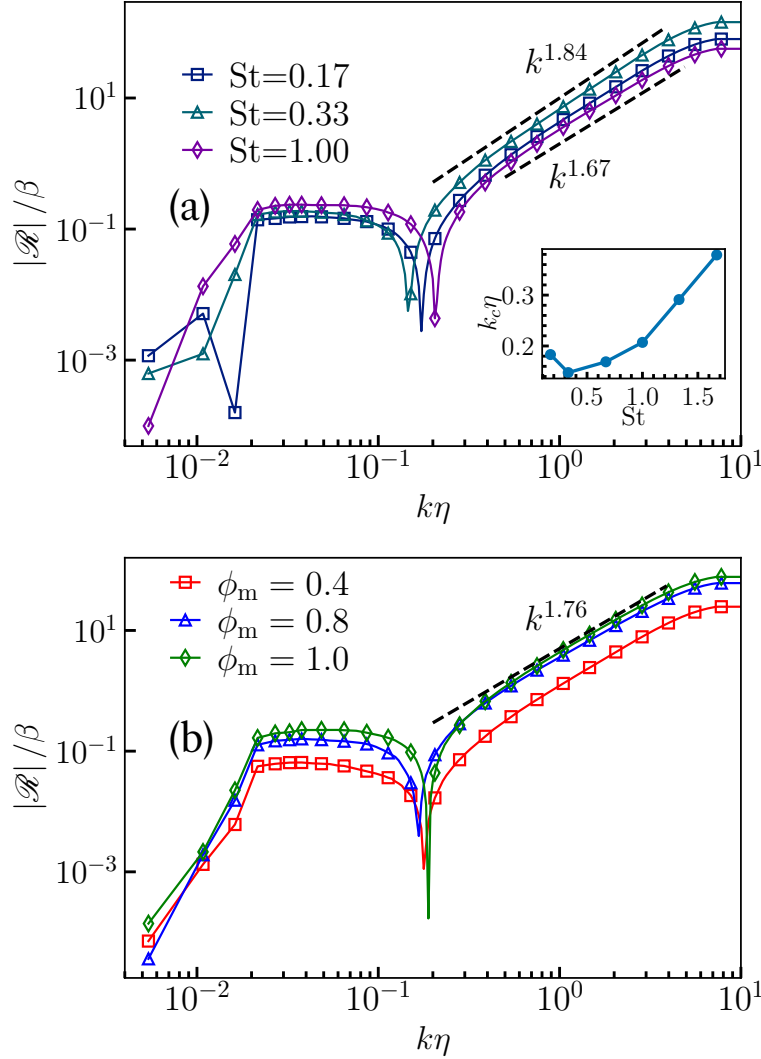


Figure 4.9: Log-log plot of $\mathcal{R}(k)$ for (a) $\phi_m = 1$, different values of St and (b) $St = 0.67$, different values of ϕ_m . (Inset) Linear plot of $K_c\eta$ (mode where $\mathcal{R}(k)$ changes sign) vs. St . Dashed lines in both (a) and (b) shows the scaling for $\mathcal{R}(k)$.

$$E(k) \sim k^{-4} \frac{d\mathcal{R}(k)}{dk} \quad (4.6)$$

for $k > K_c$. In Fig. 4.9(a,b) we show that $\mathcal{R}(k) \sim k^\gamma$ for $k > K_c$. Using 4.6 and noting that $E(k) \sim k^{-\xi}$, we get $\xi = 5 - \gamma$. In Table 4.1, we present the scaling exponent ξ evaluated using the dominant balance discussed above with those obtained from Fig. 4.6. Except for $\phi_m = 0.4$, the two different methods for estimating ξ are in reasonable agreement. Note that the range over which scalings are observed in Fig. 4.6 and Fig. 4.9 are slightly different.

We would like to point out that using arguments similar to the paragraph above, an equivalent prediction for the scaling of the energy spectrum can be also obtained from the steady-state spectral kinetic energy transfer equation [3, 6]

$$T(k) = \mathcal{D}(k) - \alpha E(k) + \mathcal{F}(k) + R(k), \quad (4.7)$$

where

$$T(k) \equiv \left\langle \sum_{k-1/2 \leq m \leq k+1/2} \mathbf{u}_m(\mathbf{u} \cdot \nabla \mathbf{u})_{-m} \right\rangle \quad (4.8)$$

is the transfer function,

$$R(k) \equiv \left\langle \sum_{k-1/2 \leq m \leq k+1/2} \mathbf{u}_m(\mathbf{F}^{d \rightarrow g})_{-m} \right\rangle \quad (4.9)$$

is the contribution due to particle fluid coupling, $\mathcal{D}(k) \equiv -\nu k^2 E(k)$ is the viscous dissipation rate, $-\alpha E(k)$ is the dissipation rate due to Ekman drag, and $\mathcal{F}(k)$ is the energy injection rate due to Kolmogorov forcing. Since $T(k)$ is negligible for $k \geq K_c$, the scaling exponent for the energy spectrum can also be obtained from the balance between $\mathcal{D}(k)$ and $R(k)$.

St	ϕ_m	$\xi \equiv 5 - \gamma$	ξ (Fig. 4.6)
0.17	1.0	3.24	3.25
0.33	1.0	3.16	3.06
0.67	1.0	3.24	3.20
1.00	1.0	3.33	3.40
0.67	0.8	3.30	3.34
0.67	0.4	3.20	3.72

Table 4.1: Scaling exponent $\xi = \gamma - 5$ obtained from dominant balance of the viscous term (\mathcal{D}) and the contribution because of back reaction from the dust particles to the gas (\mathcal{R}) [see 4.6] for different values of the particle inertia (St) and the mass-loading parameter (ϕ_m). For comparison, in the last column we provide the value of the same exponent ξ as obtained from the energy spectrum [Fig. 4.6]. The maximum standard error in estimation of the scaling exponents is around ± 0.05 .

4.6 Conclusion

We use the Eulerian-Lagrangian formalism to study the effects of dust to gas coupling in two-dimensional turbulence. The dust are modeled as heavy inertial particles immersed in the gas. We solve gas equations on fixed Eulerian grids by incorporating the forces [2.16] due to dust. The main problem with this technique is that to have a smooth Eulerian representation of the feedback, the number of particles per cell needs to be equal or greater than a certain threshold (≈ 1) [26, 27]. We choose N_p such that in the stationary state, i.e. after the dust have clustered, the above constraint is satisfied for almost all the St. Furthermore, we use higher order weight function for extrapolation to ensure a smoother approximation of back reaction on the fluid grids. We obtain reasonable scaling range for nearly all the St and ϕ_m .

The Eulerian-Lagrangian formalism has been extensively used to study how the interaction between dust and gas modifies three-dimensional turbulence. Here, we shall review some of them with an emphasis on energy spectra (see [26, 28] and references therein for more details). Refs. [29, 30] studied the effects of dust in isotropic stationary turbulence using direct numerical simulations while similar studies in decaying turbulence were done by Refs. [31, 32]. The key results of these studies are: (a) particle injects energy at large k and reduces it at small k , and (b) increasing mass loading leads to reduction of the total kinetic energy. But, the effects of changing the inertia of the dust particles (St) or the mass-loading parameter (ϕ_m) on the scaling of the energy spectra remained unclear as these simulations were done at small or moderate resolution. More recently, Refs. [33–35] introduced new numerical scheme to model coupling between gas and dust. In brief, let us point out that the mollification function that we use spreads the back-reaction of a single particle up to sixteen neighboring grid points and is similar to the Gaussian kernel used in Refs. [33, 34]. We avoid additional computational cost, by not implementing the additional diffusion filter of Ref [33] or the exact regularization protocol of Ref. [34]. One major advantage of the method of Ref. [34] is that the number of particles need not be comparable to

number of grid cells for smooth feedback. Unfortunately, the method is computationally expensive and not easily parallelizable on distributed-memory machines. By studying dust laden homogeneous shear turbulent flow using this technique, Ref. [5] reported a scaling exponent of -4 in gas kinetic energy spectrum [for $St = 1$ and $\phi_m = (0.4, 0.8)$]. They argued that the new scaling appears due to the balance of viscous forces with the back reaction from dust. In Ref. [5], the critical wave number beyond which the new scaling was observed was found to be $K_c\eta \geq 1$, whereas our two-dimensional study shows $K_c\eta \sim 0.2$. Clearly, the crucial problem with our and similar studies is that there is, as yet, no well-established algorithm to numerically calculate the feedback in DNS.

For good reasons, the most important one being difficulties in experimental realization, turbulence in flows of dust and gas has been rarely studied in two dimensions. Ref. [17] using Eulerian description of dust found a scaling exponent of -2 in the gas energy spectra, that emerges due to balance of the non-linear transfer against the feedback, for $St \ll 1$ and ϕ_m between $0.1 - 0.4$. To numerically smoothen the caustics that invariably develops in such a computation a synthetic hyper-viscous term was added in the Eulerian description. Ekman drag coefficient was chosen such that the pure gas spectra (without dust coupling) scale with an exponent -3.3 . Notably, the new scaling here starts at much small k compared to what we find.

To summarize our main results: (a) presence of dust-gas coupling decreases clustering of dust particles, (b) a new scaling regime emerges in the kinetic energy spectrum, (c) scale-by-scale enstrophy budget, suggests that the new scaling is because of gas viscosity dissipating the enstrophy injected by dust at those scales. (d) dust has a net negative contribution to budget till a wavenumber K_c and injects enstrophy at higher fourier modes, (e) as the form of dust-gas coupling term varies with both ϕ_m and more importantly St , the scaling exponent is non-universal and a function of both. Even in two dimensions, where we have been able to do large-scale simulations for long enough time, the appearance of the new scaling regime is not always prominent. We cannot rule out the possibility that there may be no scaling range

at all. But we can and do conclude that the spectra is *non-universal*.

It is quite difficult to perform a DNS of similar resolution, with feedback from particles, in three dimensions. So it is unlikely that in near future we shall observe clear scaling behavior in analogous cases in three dimensions. But based on our result we speculate that the same *non-universal* nature of spectra will be true in three-dimensions too.

References

- [1] U. Frisch, *Turbulence the legacy of A.N. Kolmogorov* (Cambridge University Press, Cambridge, 1996).
- [2] S. Pope, *Turbulent Flows* (Cambridge University Press, Cambridge, 2000).
- [3] P. Davidson, *Turbulence* (Oxford University Press, New York, 2004).
- [4] A. Kolmogorov, Dokl. Acad. Nauk USSR **30**, 4 (1941).
- [5] P. Gualtieri, F. Battista, and C. Casciola, Phys. Rev. Fluids **2**, 034304 (2017).
- [6] M. Lesieur, *Turbulence in Fluids*, Fluid Mechanics and Its Applications, Vol. 40 (Springer, Netherlands, 1997).
- [7] R. Fjørtoft, Tellus **5**, 226 (1953).
- [8] R. Kraichnan, Physics of Fluids **10**, 1417 (1967).
- [9] G. Batchelor, Phys. Fluids Suppl. II **12**, 233 (1969).
- [10] C. Leith, Physics of Fluids **11**, 671 (1968).
- [11] G. Boffetta and R. E. Ecke, Annu. Rev. Fluid Mech. **44**, 427 (2012).
- [12] R. Kraichnan and D. Montgomery, Rep. Prog. Phys **43**, 548 (1980).
- [13] K. Nam, E. Ott, T. Antonsen, and P. Guzdar, Phys. Rev. Lett **84**, 5134 (2000).
- [14] G. Boffetta, A. Cenedese, S. Espa, and S. Musacchio, Europhys. Lett. **71**, 590 (2005).
- [15] M. K. Verma, Europhys. Lett. **98**, 14003 (2012).
- [16] W. Press, B. Flannery, S. Teukolsky, and W. Vetterling, *Numerical Recipes in Fortran* (Cambridge University Press, Cambridge, 1992).

- [17] J. Bec, L. François, and M. Stefano, arXiv.org (2017).
- [18] R. A. Shaw, *Annu. Rev. Fluid Mech.* **35**, 183 (2003).
- [19] P. Grassberger and I. Procaccia, *Phys. Rev. Lett.* **50**, 346 (1983).
- [20] J. Bec, L. Biferale, M. Cencini, A. Lanotte, S. Musacchio, and F. Toschi, *Phys. Rev. Lett.* **98**, 084502 (2007).
- [21] P. Gualtieri, F. Picano, G. Sardina, and C. M. Casciola, *J. Phys.: Conf. Ser.* **333**, 012007 (2011).
- [22] P. Gualtieri, F. Battista, and C. M. Casciola, *Phys. Rev. Fluids* **2**, 034304 (2017).
- [23] P. Perlekar, S. Ray, D. Mitra, and R. Pandit, *Phys. Rev. Lett* **106**, 054501 (2011).
- [24] I. Hughes and T. Hase, *Measurements and Their Uncertainties: A Practical Guide to Modern Error Analysis* (Oxford University Press, Oxford, 2010).
- [25] D. Mitra, J. Bec, R. Pandit, and U. Frisch, *Phys. Rev. Lett* **94**, 194501 (2005).
- [26] S. Balachandar and J. K. Eaton, *Annu. Rev. Fluid Mech.* **41**, 111 (2010).
- [27] P. Gualtieri, F. Picano, and C. Casciola, *J. Fluid Mech.* **715**, 134 (2013).
- [28] C. Poelma and G. Ooms, *Appl. Mech. Rev.* **59**, 217 (2006).
- [29] K. D. Squires and J. K. Eaton, *Phys. Fluids A: Fluid Dyn.* **2**, 1191 (1990).
- [30] M. Boivin, O. Simonin, and K. D. Squires, *J. Fluid Mech.* **375**, 235 (1998).
- [31] A. Ferrante and S. Elghobashi, *Phys. Fluids* **15**, 315 (2003).
- [32] S. Sundaram and L. R. Collins, *J. Fluid Mech.* **379**, 105 (1999).
- [33] J. Capecelatro and O. Desjardins, *J. Comput. Phys.* **238**, 1 (2013).
- [34] P. Gualtieri, F. Picano, G. Sardina, and C. M. Casciola, *J. Fluid Mech.* **773**, 520 (2015).

- [35] G. Sardina, K. Jareteg, H. Ström, and S. Sasic, Chem. Eng. Sci. **201**, 58 (2019).

Statistical properties of pseudo-turbulence generated by buoyancy-driven bubbly flows

5.1 Introduction

In this chapter, we study the statistical properties of the buoyancy-driven bubbly flows. Bubble laden flow appears in a variety of natural [1, 2] and industrial [3] processes. Presence of bubbles dramatically alters the transport properties of a flow [4–11]. A single bubble of diameter d , because of buoyancy, rises under gravity. Its trajectory and the wake flow depend on the density and viscosity contrast with the ambient fluid, and the surface tension [1, 12, 13]. A suspension of such bubbles at moderate volume fractions generates complex spatiotemporal flow patterns that are often referred to as pseudo-turbulence or bubble-induced agitation [4, 8].

Experiments have made significant progress in characterizing velocity fluctuations of the fluid phase in pseudo-turbulence. A key observation is the robust power-law scaling in the energy spectrum with an exponent of -3 either in frequency $\tilde{\nu}$ or the wave-number k space [14–16]. The scaling range, however, remains controversial. Riboux *et al.* [15] investigated tur-

bulence in the wake of a bubble swarm and found the k^{-3} scaling for length scales larger than the bubble diameter d (i.e., $k < 2\pi/d$), whereas Mercado *et al.* [14], Prakash *et al.* [17] observed this scaling for scales smaller than d in a steady state bubble suspension. Experiments on buoyancy driven bubbly flows in presence of grid-turbulence [17–19] observe Kolmogorov scaling for scales larger than the bubble diameter and smaller than the forcing scale and a much steeper k^{-3} scaling for scales smaller than the bubble diameter and larger than the dissipation scale. Lance and Bataille [18] argued that, assuming production because of wakes to be local in spectral space, balance of production with viscous dissipation leads to the observed k^{-3} scaling.

Fully resolved numerical simulations of three-dimensional (3D) bubbly flows for a range of Reynolds number $O(10) < \text{Re} < O(10^3)$ [20–22] found the k^{-3} scaling for length scales smaller than d ($k > 2\pi/d$) and attributed it to the balance between viscous dissipation and the energy production by the wakes [18].

Two mechanisms proposed to explain the observed scaling behavior in experiments are: (i) superposition of velocity fluctuations generated in the vicinity of the bubbles [23], and (ii) at high Re, the instabilities in the flow through bubble swarm [4, 8, 18]. In an experiment or a simulation, it is difficult to disentangle these two mechanisms.

In classical turbulence, a constant flux of energy is maintained between the injection and dissipation scales [24, 25]. In pseudo-turbulence, on the other hand, it is not clear how the energy injected because of buoyancy is transferred between different scales. In particular, the following key questions remain unanswered: (i) How do liquid velocity fluctuations and the pseudo-turbulence spectrum depend on the Reynolds number (Re)? (ii) What is the energy budget and the dominant balances? (iii) Is there an energy cascade (a non-zero energy flux)?

In this chapter, we address all of the above questions for experimentally relevant Reynolds (Re) and Atwood (At) numbers. We first investigate the dynamics of an isolated bubble and show that the wake flow behind the bubble is in agreement with earlier experiments and simulations. Next for a bubbly

suspension we show that the liquid velocity fluctuations are in quantitative agreement with the experiments of Riboux *et al.* [15] and the bubble velocity fluctuations are in quantitative agreement with the simulations of Roghair *et al.* [22]. We then proceed to derive the scale-by-scale energy budget equation and investigate the dominant balances for different Re and At. We find that for scales smaller than the bubble diameter, viscous dissipation balances net nonlinear transfer of energy because of advection and the surface tension to give k^{-3} pseudo-turbulence spectrum. The dominant balances are robust and do not depend on the density contrast (At).

5.2 Model and simulation details

We model the multiphase flows using the Navier Stokes (NS) equations 1.25 and 1.26

$$\begin{aligned}\rho [\partial_t \mathbf{u} + \mathbf{u} \cdot \nabla \mathbf{u}] &= \nabla \cdot [2\mu \mathcal{S}] - \nabla p + \mathbf{F}^\sigma + \mathbf{F}^g, \\ \nabla \cdot \mathbf{u} &= 0.\end{aligned}$$

We solve the non-Boussinesq NS equations using the open source finite-volume-front-tracking solver PARIS [26]. The details of the solver is given in chapter-2. For the Boussinesq approximated 2.27, we use a 2/3 dealiased pseudo-spectral front-tracking solver [26–28]. For time marching we use a second-order Adams-Bashforth scheme. Note that low-At DNS of bubbly flows are much easier and such flows with same viscosity and comparable density can be experimentally realized in near critical binary-fluids and certain mixtures of oils [29, 30].

runs	L	N	N_b	d	g	μ_f	$\Phi_V\%$	Ga	At	Bo	Re	ℓ_0	τ_{ℓ_0}
R1	256	512	60	24	1.0	0.32	2.6	104	0.04	1.8	150	11.3	36.6
R2	256	512	60	24	1.0	0.20	2.6	166	0.04	1.0	298	9.88	26.3
R3	128	432	10	22	8.75	0.42	2.6	206	0.04	2.1	315	8.51	8.1
R4	128	432	10	22	10.5	0.32	2.6	296	0.04	1.9	462	7.35	6.1
R5	256	256	40	24	0.1	0.32	1.7	113	0.90	2.0	173	10.0	38.7
R6	256	256	40	24	1.0	0.32	1.7	345	0.80	2.4	465	8.12	7.7
R7	256	256	40	24	1.0	0.32	1.7	358	0.90	1.9	546	7.31	7.0

Table 5.1: Table of parameters used in our DNS. Here, $\delta\rho \equiv \rho_f - \rho_b$ is the density difference, $\text{Ga} \equiv \sqrt{\rho_f \delta\rho g d^3} / \mu_f$ is the Galilei number, $\text{Bo} \equiv \delta\rho g d^2 / \sigma$ is the Bond number, $\text{At} = \delta\rho / (\rho_f + \rho_b)$ is the Atwood number, and $\text{Re} \equiv \rho_f V_0 d / \mu_f$ is the bubble Reynolds number, where V_0 is the rise velocity of an isolated bubble, $\ell_0 \equiv \sqrt{10\mu_f E / \rho_f \epsilon_\mu}$ is the integral length scale, and $\tau_{\ell_0} \equiv \ell_0 / \sqrt{2E/3\rho_f}$ is the integral time scale. The simulations R5 – 7 is conducted using the open source solver PARIS

We use a cubic periodic box of volume L^3 and discretize it with N^3 collocation points. We initialize the velocity field $\mathbf{u} = 0$ and place the centers of N_b bubbles at random locations such that no two bubbles overlap. The Reynolds number Re , the Bond number Bo , and the bubble volume fraction $\Phi_V \equiv [\int (1 - c) d\mathbf{x}] / L^3$ that we use (see Table (5.1)) are comparable to the experiments [15, 16].

5.3 Single bubble dynamics

In this section, we study the dynamics of an initially spherical bubble as it rises because of buoyancy. The seminal work of Bhaga and Weber [12], Wu and Gharib [31], Tchoufag *et al.* [32] characterized the shape and trajectory of an isolated bubble in terms of Reynolds and Bond number. Experiments on turbulent bubbly flows [17, 18, 33] observe ellipsoidal bubbles. In the following, we characterize the dynamics of an isolated bubble for the parameters

used in our simulations.

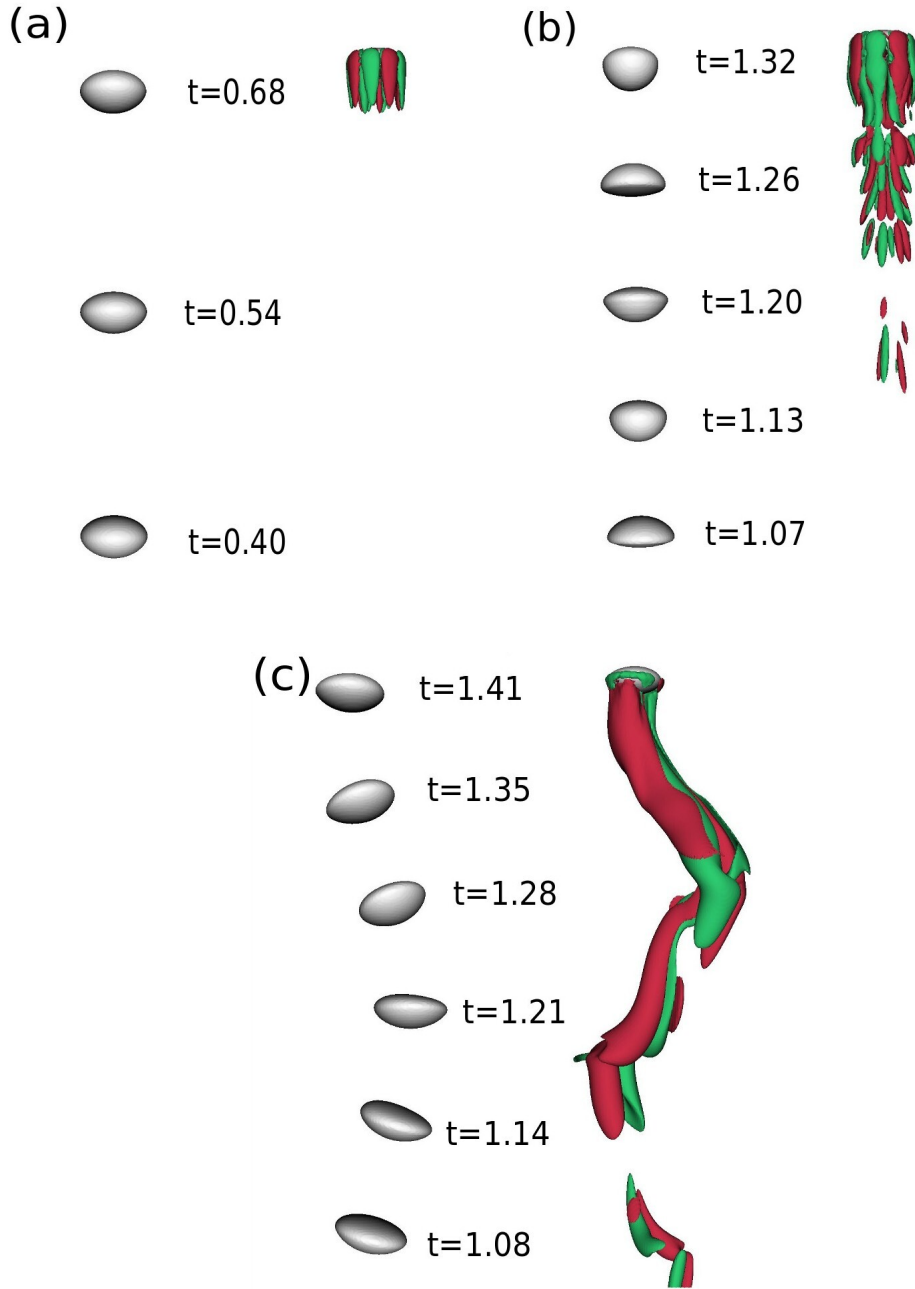


Figure 5.1: Bubble positions at different times (in units of $\tau_s \equiv L/\sqrt{\delta\rho g d/\rho_f}$) and the z-component of the vorticity ($\omega_z = \partial_x u_y - \partial_y u_x$) for the case of single bubble rising under gravity. The non-dimensional parameters in representative cases are taken the same as run R1 in panel (a), run R4 in panel (b), and run R6 in panel (c). Green region corresponds to $\omega_z < 0$, whereas red region corresponds to $\omega_z > 0$. We plot iso-contours corresponding to $|\omega_z| = \pm 10^{-3}$ in (a), $|\omega_z| = \pm 10^{-2}$ in (b), and $|\omega_z| = \pm 10^{-1}$ in (c).

To avoid the interaction of the bubble with its own wake, we use a vertically elongated cuboidal domain of dimension $5d \times 5d \times 21d$. After the bubble rise velocity attains steady-state, Fig. 5.1(a-c) shows the bubble shape and the vertical component of the vorticity $\omega_z = (\nabla \times \mathbf{u}) \cdot \hat{z}$. For $\text{Re} = 150$ and $\text{At} = 0.04$ (run R1), the bubble shape is oblate ellipsoid and it rises in a rectilinear trajectory. On increasing the $\text{Re} = 462$ (run R4), the bubble pulsates while rising and sheds varicose vortices similar to Pivello *et al.* [34]. Finally, for high $\text{At} = 0.80$ and $\text{Re} = 465$ (run R6), similar to region III of Tripathi *et al.* [13], we find that the bubble shape is oblate ellipsoid and it follows a zigzag trajectory.

5.4 Bubbles suspension

We now study the pseudo-turbulence properties due to swarm of buoyant bubbles rising under gravity. The plots in Fig. 5.2(a,b) show the representative steady state iso-vorticity contours of the z -component of the vorticity along with the bubble interface position for our bubbly flow configurations. As expected from our isolated bubble study in the previous section, we observe rising ellipsoidal bubbles and their wakes which interact to generate pseudo-turbulence. The individual bubbles in the suspension show shape undulations which are similar to their isolated bubble counterparts. Furthermore, for comparable $\text{Bo} \approx 2$, the average bubble deformation $\langle\langle S(t)/S(0) \rangle\rangle$ increases with increasing Re (Fig. 5.3). Here, $\langle\langle \cdot \rangle\rangle$ denote temporal averaging over bubble trajectories in the statistically steady state, $S(t)$ is the surface area of the bubble, and $S(0) = \pi d^2$.

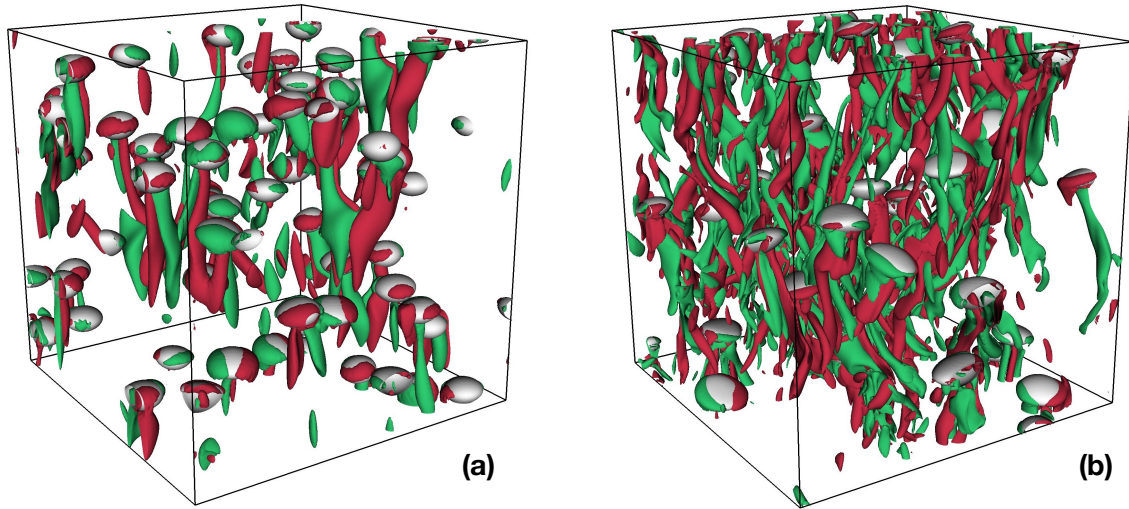


Figure 5.2: Representative steady-state snapshot of the bubbles overlaid on the iso-contour plots of the z -component of the vorticity field $\omega_z \equiv [\nabla \times \mathbf{u}] \cdot \hat{\mathbf{z}}$ for $\text{Re} = 150$, $\text{At} = 0.04$ (a) and for $\text{Re} = 465$, $\text{At} = 0.8$ (b). Regions with $\omega_z = 2\sigma_\omega(-2\sigma_\omega)$ are shown in red (green), where σ_ω is the standard deviation of ω_z . As expected, bubble-wake interactions become more intense on increasing Re .

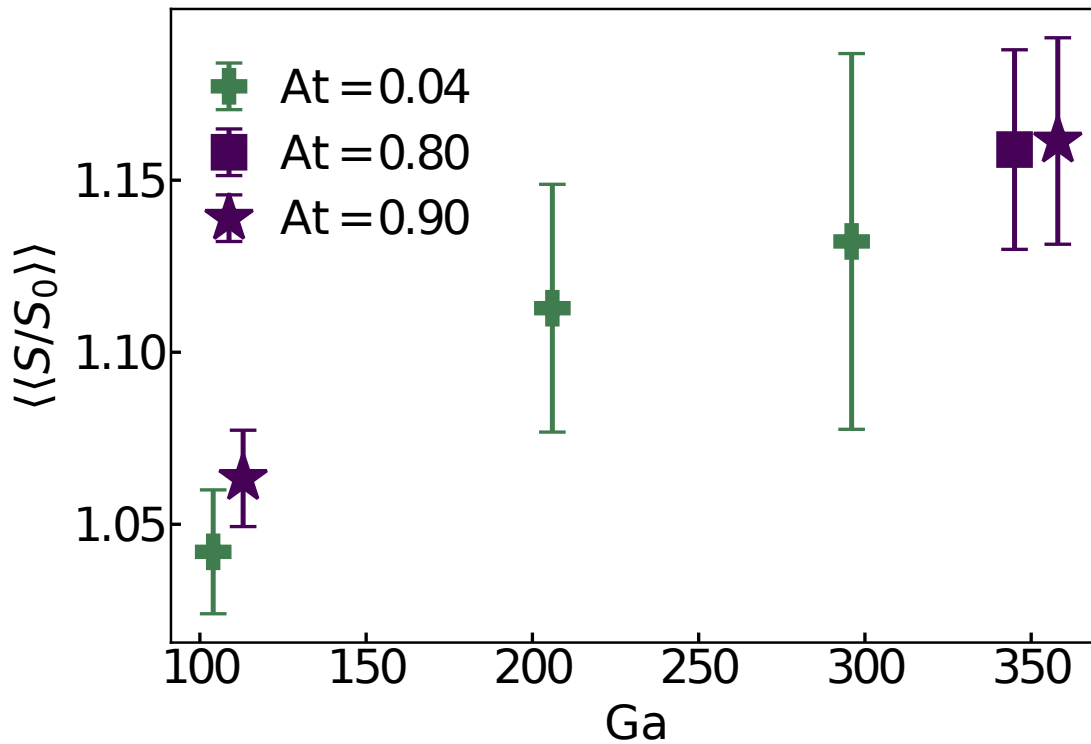


Figure 5.3: Average bubble deformation $\langle\langle S(t)/S(0) \rangle\rangle$ versus Ga for low and high At numbers

5.5 Total kinetic energy

The time evolution of the kinetic energy $E = \langle \rho u^2 / 2 \rangle$ for runs R1 – R7 is shown in Fig. 5.2(a). A statistically steady state is attained around $t \approx 20\tau_{\ell_0}$, where τ_{ℓ_0} is the integral time scale (see table Table (5.1)). Using Eq. 1.25 and 1.26, we obtain the total kinetic energy E balance equation as

$$\partial_t \underbrace{\left\langle \frac{\rho u^2}{2} \right\rangle}_E = \underbrace{\langle \mathbf{u} \cdot (\nabla \cdot 2\mu \mathcal{S}) \rangle}_{\epsilon_\mu} + \underbrace{\langle [\rho_a - \rho(c)] u_z g \rangle}_{\epsilon_g} + \underbrace{\langle \mathbf{F}^\sigma \cdot \mathbf{u} \rangle}_{\epsilon_\sigma}, \quad (5.1)$$

where, $\langle \cdot \rangle$ represents spatial averaging, ϵ_μ is the total dissipation rate, ϵ_g is the energy injection rate due to buoyancy and ϵ_σ is the contribution due to surface-tension. The total dissipation rate can further be simplified as

$$\epsilon_\mu = \langle \mathbf{u} \cdot [\nabla \cdot (2\mu \mathcal{S})] \rangle = - \langle 2\mu \nabla \mathbf{u} : \mathcal{S} \rangle. \quad (5.2)$$

Since ϵ_μ is scalar, the following relation should hold

$$\epsilon_\mu = - \langle 2\mu (\nabla \mathbf{u})^T : \mathcal{S} \rangle. \quad (5.3)$$

From 5.2 and 5.3 we obtain the total dissipation rate

$$\epsilon_\mu = - \langle 2\mu \mathcal{S} : \mathcal{S} \rangle. \quad (5.4)$$

In the approximation $\rho_a \approx \rho_f$ valid for low At or in a very dilute bubble suspension, the injection rate simplifies to

$$\epsilon_g \approx \frac{1}{V} \delta \rho g \int u_z (1 - c) dV. \quad (5.5)$$

Since $c = 0$ inside the bubble and 1 in the liquid phase, 5.5 reduces to

$$\epsilon_g \approx \Phi_V \delta \rho g \langle U \rangle, \quad (5.6)$$

Where $\langle U \rangle = 1/V_b \int u_z (1 - c) dV$ is the average bubble rise velocity.

In steady state, the energy injected by buoyancy ϵ_g is balanced by viscous dissipation ϵ_μ . The contribution due to $\epsilon_\sigma = -\partial_t \int \sigma dS$ [35], where dS is the bubble surface element, is zero in the steady-state. In Fig. 5.4 we show the steady state values of ϵ_μ and ϵ_g .

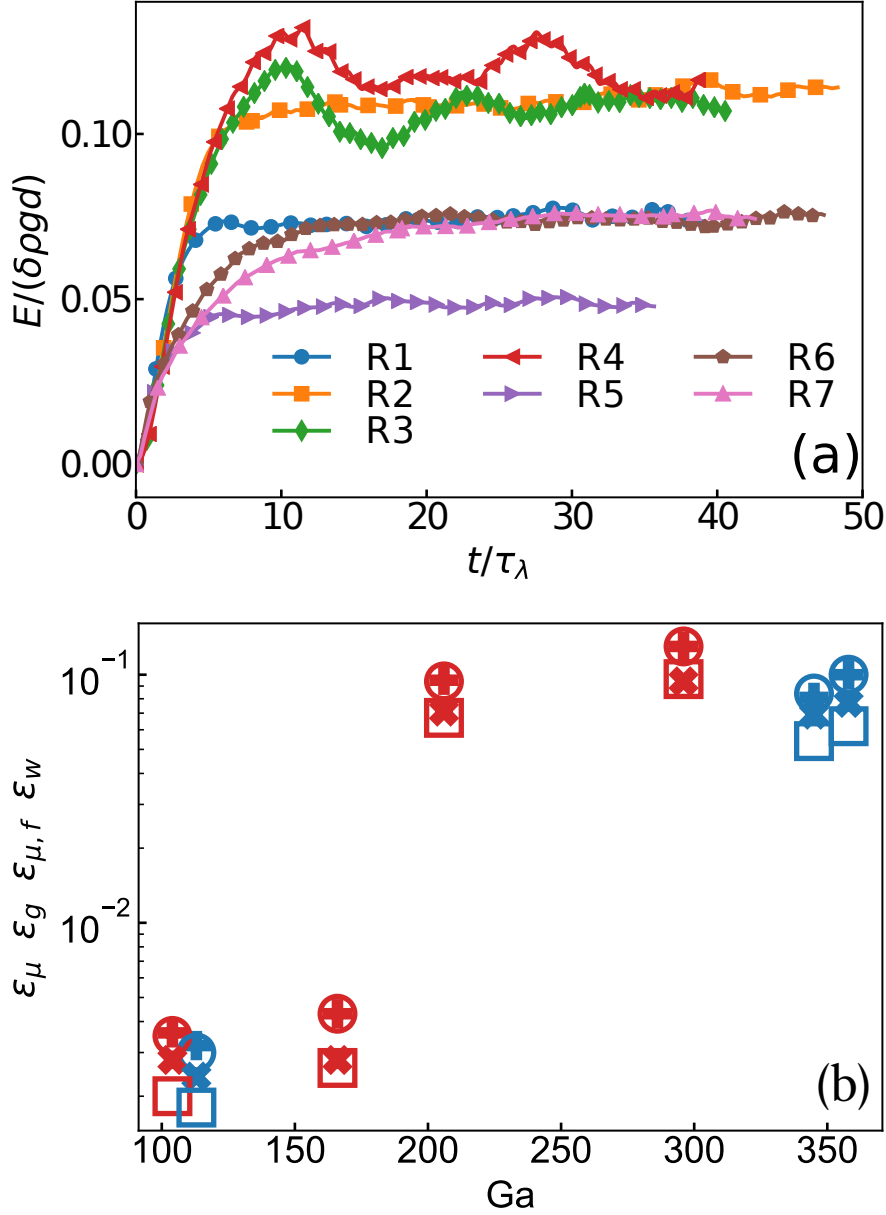


Figure 5.4: (a) Kinetic energy evolution for the runs given in Table (5.1). (b) Energy dissipation rate ϵ_μ (filled plus), the estimation of the liquid dissipation rate $\epsilon_w \equiv \Phi_V(\delta\rho gd/\rho_f)^{3/2}/d$ (empty squares) because of the bubble wakes [18], the dissipation rate in the fluid $\epsilon_{\mu,f}$ (filled cross) and, the energy injection rate ϵ_g (empty circles) for runs R1 – R7. The low At runs are marked in red and the high At runs are marked in blue.

Lance and Bataille [18] argued that the energy injected by the buoyancy is dissipated in the wakes on the bubble. The energy dissipation in the wakes can be estimated as $\epsilon_w = C_d\Phi_V((\delta\rho/\rho_f)gd)^{3/2}/d$, where C_d is the drag coefficient.

Assuming $C_d = O(1)$, we find that ϵ_w comparable to the viscous dissipation in the fluid phase $\epsilon_{\mu,f}$ (see Fig. 5.4).

5.6 Liquid and bubble velocity fluctuations

In this section, we will discuss the results for the liquid and bubble velocity distribution functions. We shall first discuss the distribution for the liquid phase and then present the results for the bubble center-of-mass velocity. In both the cases we contrast our results with the previous studies.

5.6.1 Probability distribution of the liquid velocity

We first discuss the probability distribution function (pdf) of the velocity fluctuations in the liquid phase ($\mathbf{u}^f = \mathbf{u}c$). In Fig. 5.5(a,b) we plot the probability distribution function of the fluid velocity fluctuations. Both the horizontal and vertical velocity pdf's are in quantitative agreement with the experimental data of Riboux *et al.* [15] and Risso [8]. The pdf of the velocity fluctuations of the horizontal velocity components are symmetric about origin whereas the vertical velocity fluctuations are positively skewed [15, 17, 19]. The skewness in the distribution in the vertical component of velocity has also been observed in thermal convection with bubbles [6].

According to Risso [36], liquid velocity fluctuations in pseudo-turbulence is a result of the combined effects of i) potential disturbance around a bubble, ii) bubble wakes, and iii) the turbulent fluctuations due to flow instabilities. A combination of these three contributions results in a probability distribution of the form $\sim \exp(-\xi|u_i|/\langle u_i^2 \rangle^{1/2})$, for both horizontal ($i = x$ or y) and vertical component ($i = z$) of the velocity, with successively decreasing ξ . Since the contribution due to bubble wake is present only in the vertical direction, the initial decay in the pdf of horizontal component is primarily due to turbulent fluctuations ($\xi = \sqrt{2}$) [36]. We verify the model of Risso [36] in Fig. 5.6, where we plot the pdf for the horizontal component along with the function $\exp(-\sqrt{2}|u_x|/\langle u_x^2 \rangle^{1/2})$. Indeed, we find that the function

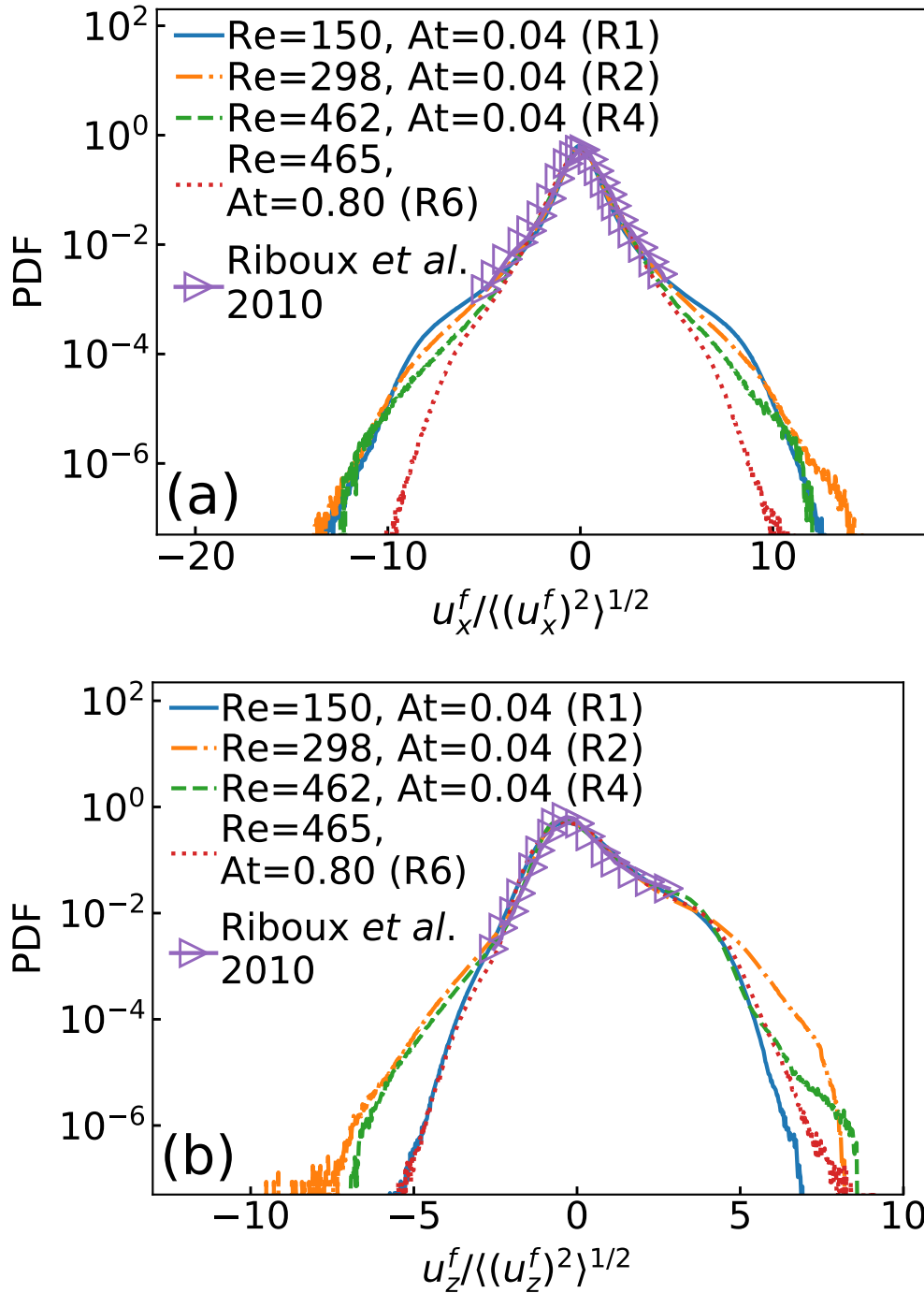


Figure 5.5: The probability distribution function of the (a) horizontal component (b) vertical component of the liquid velocity fluctuations for runs given in Table (5.1). The pdf obtained from our DNS are in excellent agreement with the experimental data of Riboux *et al.* [15] [Data extracted using [engauge https://markummittchell.github.io/engauge-digitizer/](https://markummittchell.github.io/engauge-digitizer/)].

accurately represents the initial decay of the pdf. The skewness in the pdf

of the vertical velocity is due to the presence of bubble wakes.

Although we find all the pdf to be identical around the mean for both horizontal and vertical velocity, there are deviations in the tail. This deviation is probably because of the differences in the wake flow for different Re and At (see Fig. 5.1).

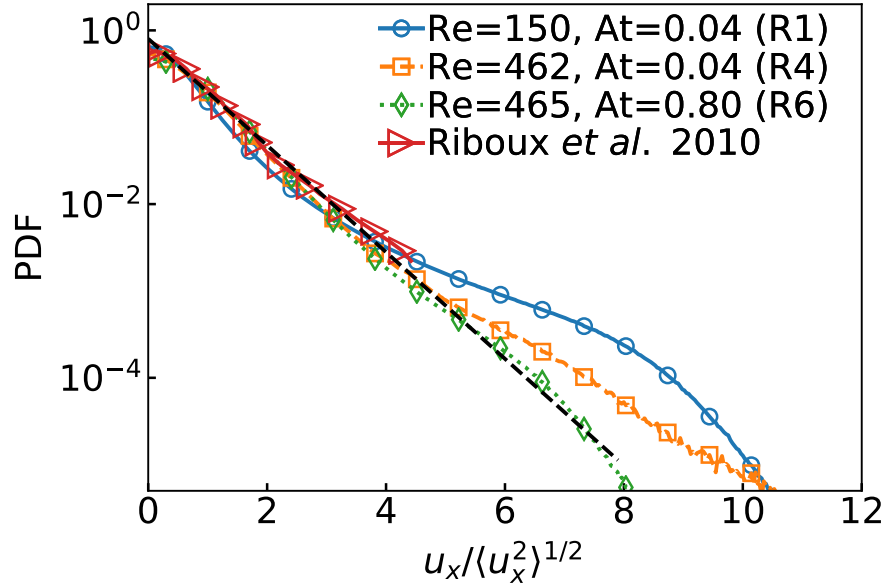


Figure 5.6: Probability distribution function of the horizontal component of the liquid velocity fluctuations. The black dashed line shows the exponential distribution $\sim \exp(-\sqrt{2\xi}|u_x|/\langle u_x^2 \rangle^{1/2})$.

5.6.2 Probability distribution of the bubble velocity

In this section, we characterize the fluctuations in the velocity of the center-of-mass of bubbles using a probability distribution function. Since we evolve the bubbles using front tracking, we use marker points to estimate the location and velocity of the individual bubbles [20]. A typical front depicting the marker points from the simulation is shown in Fig. 5.7. The volume V_i^b and centroid position \mathbf{x}_i^b of bubble i^{th} are

$$V_i^b = \int_{V_b} dV_b = \int_{V_b} \nabla \cdot \mathbf{x} dV_b = \frac{1}{3} \oint_{S_i} \mathbf{x} \cdot \mathbf{dS}, \quad (5.7)$$

$$\mathbf{x}_i^b = \frac{1}{V_b} \int_{V_b} \mathbf{x} dV_b = \frac{1}{2V_b} \int_{V_b} \nabla(\mathbf{x} \cdot \mathbf{x}) dV_b = \frac{1}{2V_b} \oint_{S_i} \mathbf{x} \cdot \mathbf{dS}. \quad (5.8)$$

Where, the volume integrals are converted into surface integrals using the Gauss divergence theorem. We then estimate the bubble velocity using the centroid trajectory

$$\mathbf{u}_i^b = \frac{d\mathbf{x}_i^b}{dt}. \quad (5.9)$$

Here, we note that \mathbf{u}_i^b can also be determined using the surface information of the bubble as

$$\mathbf{u}_i^b = \frac{1}{V_b} \int_{V_b} \mathbf{u} dV_b = \frac{1}{V_b} \int_{V_b} \nabla \cdot (\mathbf{x}\mathbf{u}) dV_b = \frac{1}{V_b} \oint_{S_i} \mathbf{x}(\mathbf{u} \cdot d\mathbf{S}), \quad (5.10)$$

We have verified numerically that both 5.10 and (5.9) give identical results.

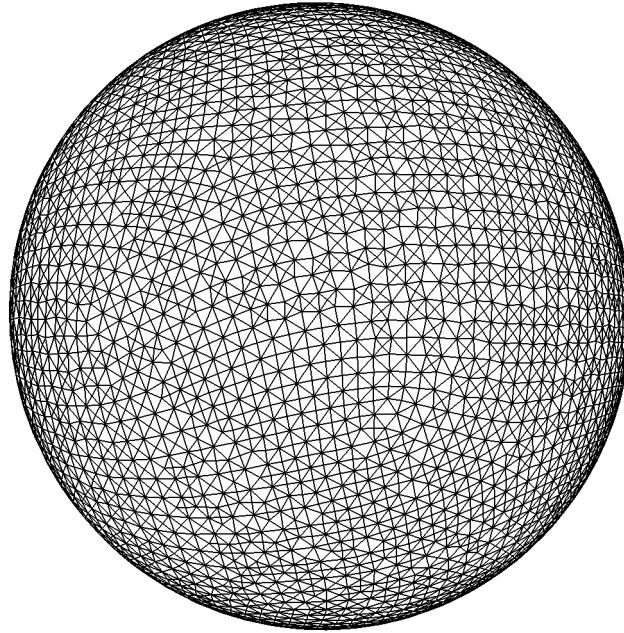


Figure 5.7: A typical front with marker points connected by lines.

We show the pdf of the bubble velocity in Fig. 5.8. In agreement with the earlier simulations of Roghair *et al.* [22] and Esmaeeli and Tryggvason [37], the pdf's of the bubble velocity fluctuation are Gaussian (see Fig. 5.8). The departure in the tail of the pdf is evident in comparison with the experimental data of Mercado *et al.* [14]. The reason probably is the formation of large scale structures in the experimental water channel, which are absent in the simulations with periodic boundary [22].

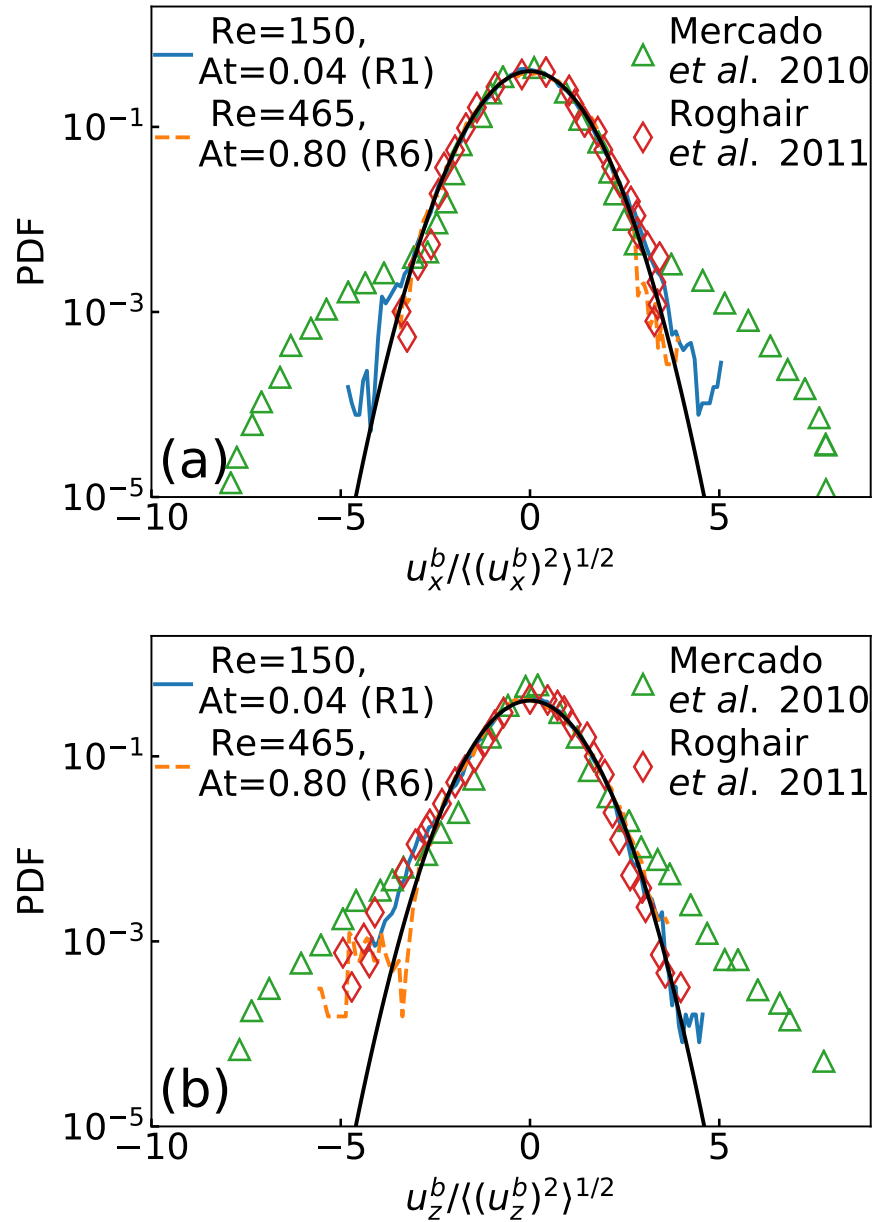


Figure 5.8: The probability distribution function of (a) the horizontal and (b) the vertical component of the bubbles velocity fluctuations for runs R1 and R6 (see Table (5.1)). The experimental data of Mercado *et al.* [14] and numerical results of Roghair *et al.* [22] is also shown for comparison. The black continuous line represents a Gaussian distribution.

5.7 Energy spectra and scale-by-scale budget

In this section we discuss the kinetic energy spectra and the scale-by-scale energy budget. Homogeneous and isotropic turbulence is characterized by a energy spectra with scaling of $k^{-5/3}$ in the inertial range [24, 38]. The energy spectra in pseudo-turbulence, on the otherhand, have a scaling of k^{-3} [17, 18]. To understand the scaling behavior we derive the scale-by-scale energy budget equation for pseudo-turbulence.

5.7.1 Energy spectra

The kinetic energy spectrum for a velocity field \mathbf{u} is defined as

$$E_k^{uu} \equiv \sum_{k-1/2 < m < k+1/2} |\hat{\mathbf{u}}_m|^2, \quad (5.11)$$

where \mathbf{u}_m is the Fourier transform of the velocity field $\mathbf{u}(\mathbf{x})$. Since density of the bubble is different than that of the fluid, we also define the co-spectrum

$$E_k^{\rho uu} \equiv \sum_{k-1/2 < m < k+1/2} \Re[(\hat{\rho}\mathbf{u})_{-m} \hat{\mathbf{u}}_m] \equiv d\mathcal{E}/dk. \quad (5.12)$$

5.7.2 Scale-by-scale energy budget

Here we derive the scale-by-scale energy budget equation. For the derivation, we closely follow section 2.4 of Frisch [24]. We start by introducing the concept of scale using a Fourier transform. Any periodic function $f(\mathbf{x})$ can be represented using the Fourier series as

$$f(\mathbf{x}) = \sum_{\mathbf{m}} \exp(i\mathbf{m} \cdot \mathbf{x}) f_{\mathbf{m}}, \quad (5.13)$$

given a scale $k = 2\pi/l$,

$$f(\mathbf{x}) = \sum_{m \leq k} \exp(i\mathbf{m} \cdot \mathbf{x}) f_{\mathbf{m}} + \sum_{m > k} \exp(i\mathbf{m} \cdot \mathbf{x}) f_{\mathbf{m}}, \quad (5.14)$$

or

$$f(\mathbf{x}) = f_k^<(\mathbf{x}) + f_k^>(\mathbf{x}). \quad (5.15)$$

Here $f_k^<$ (pronounced as f-lesser) is a *low pass* filtered function with a filtering scale of k . Similarly, $f_k^>$ is a *high pass* filtered function.

We now define an operator \mathbb{P}_k , which, when operated on any periodic function, eliminates all the wave-modes $\geq k$.

$$\mathbb{P}_k f(\mathbf{x}) \equiv f^<(\mathbf{x}). \quad (5.16)$$

It is important to note the following properties of \mathbb{P} :

- The operator \mathbb{P}_k commutes with ∇ and ∇^2

$$\langle \mathbb{P}_k(\nabla f) \rangle = \langle \nabla(\mathbb{P}_k f) \rangle \quad (5.17)$$

- \mathbb{P}_k is a Hermitian

$$\langle f(\mathbb{P}_k g) \rangle = \langle (\mathbb{P}_k f)g \rangle \quad (5.18)$$

A low-pass filtered function is orthogonal to any high-pass filtered function with the same filtering scale k

$$\langle f^< g^> \rangle = 0. \quad (5.19)$$

We now re-write the Navier Stokes equation for $\rho \mathbf{u}$ and \mathbf{u} below,

$$\partial_t \rho \mathbf{u} + \mathbf{u} \cdot \nabla \rho \mathbf{u} = \nabla \cdot (2\mu \mathcal{S}) - \nabla p + \mathbf{F}^\sigma + \mathbf{F}^g, \quad (5.20)$$

$$\partial_t \mathbf{u} + \mathbf{u} \cdot \nabla \mathbf{u} = \frac{1}{\rho} [\nabla \cdot (2\mu \mathcal{S}) - \nabla p + \mathbf{F}^\sigma + \mathbf{F}^g]. \quad (5.21)$$

The equation for low-pass field $(\rho \mathbf{u})_k^<$ and $\mathbf{u}_k^<$ is obtained by applying \mathbb{P}_k to 5.20 and (5.21)

$$\partial_t \rho \mathbf{u}_k^< + \mathbb{P}_k(\mathbf{u} \cdot \nabla \rho \mathbf{u}) = \mathbb{P}_k [-\nabla p + \nabla \cdot (2\mu \mathcal{S}) + \mathbf{F}^\sigma + \mathbf{F}^g], \quad (5.22)$$

$$\partial_t \mathbf{u}_k^< + \mathbb{P}_k(\mathbf{u} \cdot \nabla \mathbf{u}) = \mathbb{P}_k \left\{ \frac{1}{\rho} [-\nabla p + \nabla \cdot (2\mu \mathcal{S}) + \mathbf{F}^\sigma + \mathbf{F}^g] \right\}. \quad (5.23)$$

The scale-by-scale budget equation is finally obtained by taking a dot product of $\mathbf{u}_k^<$ with 5.22, $(\rho \mathbf{u})_k^<$ with 5.23, and adding them both. The final expression can be written as

$$\partial_t \mathcal{E}_k + \Pi_k + \mathcal{F}_k^\sigma = \mathcal{P}_k - \mathcal{D}_k + \mathcal{F}_k^g. \quad (5.24)$$

Here, $2\mathcal{E}_k = \langle \mathbf{u}_k^< \cdot (\rho \mathbf{u})_k^< \rangle$ is the cumulative energy up to wave-number k , $2\Pi_k = \langle (\rho \mathbf{u})_k^< \cdot (\mathbf{u} \cdot \nabla \mathbf{u})_k^< \rangle + \langle \mathbf{u}_k^< \cdot (\mathbf{u} \cdot \nabla \rho \mathbf{u})_k^< \rangle$ is the energy flux through wave-number k , $2\mathcal{D}_k = -[\langle (\rho \mathbf{u})_k^< \cdot (\nabla \cdot [2\mu \mathcal{S}]/\rho)_k^< \rangle + \langle \mathbf{u}_k^< \cdot (\nabla \cdot [2\mu \mathcal{S}])_k^< \rangle]$ is the cumulative energy dissipated upto k , $2\mathcal{F}_k^\sigma = -[\langle (\rho \mathbf{u})_k^< \cdot (\mathbf{F}^\sigma/\rho)_k^< \rangle + \langle \mathbf{u}_k^< \cdot (\mathbf{F}^\sigma)_k^< \rangle]$ is the cumulative energy transferred from the bubble surface tension to the fluid upto k , $2\mathcal{F}_k^g = \langle (\rho \mathbf{u})_k^< \cdot (\mathbf{F}^g/\rho)_k^< \rangle + \langle \mathbf{u}_k^< \cdot (\mathbf{F}^g)_k^< \rangle$ is cumulative energy injected by buoyancy upto k . In crucial departure from the uniform density flows, we find a non-zero cumulative pressure contribution $2\mathcal{P}_k = \langle (\rho \mathbf{u})_k^< \cdot (\nabla p/\rho)_k^< \rangle$. The \mathcal{P}_k represents the ‘‘baropycnal work’’ done by pressure-gradient against sub-scale mass flux [39].

In the Boussinesq regime (small At), the individual terms in the scale-by-scale budget simplify to their uniform density analogues: $\mathcal{E}_k = \rho_a \langle \mathbf{u}_k^< \cdot \mathbf{u}_k^< \rangle / 2$, $\Pi_k = \rho_a \langle \mathbf{u}_k^< \cdot (\mathbf{u} \cdot \nabla \mathbf{u})_k^< \rangle$, $\mathcal{D}_k = -\mu \langle |\nabla \mathbf{u}_k^<|^2 \rangle$, $\mathcal{F}_k^\sigma = -\langle \mathbf{u}_k^< \cdot (\mathbf{F}^\sigma)_k^< \rangle$, $\mathcal{F}_k^g = \langle \mathbf{u}_k^< \cdot (\mathbf{F}^g)_k^< \rangle$, and $\mathcal{P}_k = 0$.

5.7.3 Low At (runs R1 – R4)

We first discuss the results for the Boussinesq regime (low At). For scales smaller than the bubble diameter ($k > k_d$), the energy spectrum (Fig. 5.9) shows a power-law behavior $E(k) \sim k^{-\beta}$ for different Re . The exponent $\beta = 4$ for $Re = 150$, it decreases on increasing the Re and becomes close to $\beta = 3$ for the largest $Re = 462$.

We now investigate the dominant balances using the scale-by-scale energy budget analysis. In the statistically steady-state $\partial_t \mathcal{E}_k = 0$, and $\Pi_k + \mathcal{F}_k^\sigma = -\mathcal{D}_k + \mathcal{F}_k^g$ (note that $\mathcal{P}_k = 0$ for low At). In Fig. 5.10(a) and 5.10(b) we plot different contributions to the cumulative energy budget for $Re = 150$ and $Re = 462$ and make the following observations:

1. Cumulative energy injected by buoyancy \mathcal{F}_k^g saturates around $k \approx k_d$. Thus buoyancy injects energy at scales comparable to and larger than the bubble diameter.
2. Energy flux $\Pi_k > 0$ around $k \approx k_d$ and it vanishes for $k \gg k_d$.

3. Especially for scales smaller than the bubble diameter, the cumulative energy transfer from the bubble surface tension to the fluid is the dominant energy transfer mechanism.

4. Consistent with the earlier predictions [15], for our highest $Re = 462$ simulation provides a direct evidence that the balance of total production $d(\Pi_k + \mathcal{F}_k^\sigma)/dk \sim k^{-1}$ with viscous dissipation [$d\mathcal{D}_k/dk = \nu k^2 E(k)$] gives the pseudo-turbulence spectra $E(k) \sim k^{-3}$ [15, 18, 22].

Our scale-by-scale analysis, therefore, suggests the following mechanism of pseudo-turbulence. Buoyancy injects energy at scales comparable and larger to the bubble size. A part of the energy injected by buoyancy is absorbed in stretching and deformation of the bubbles and another fraction is transferred via wakes to scales comparable to bubble diameter. Similar to polymers in turbulent flows [40–42], the relaxation of the bubbles leads to injection of energy at scales smaller than the bubble diameter.

Note that for low At , Boussinesq regime $\rho = \rho_a$, there is no distinction between a droplet and a bubble. Therefore, our results for low At buoyancy driven bubbly flows are equally valid for a suspension of sedimenting droplets.

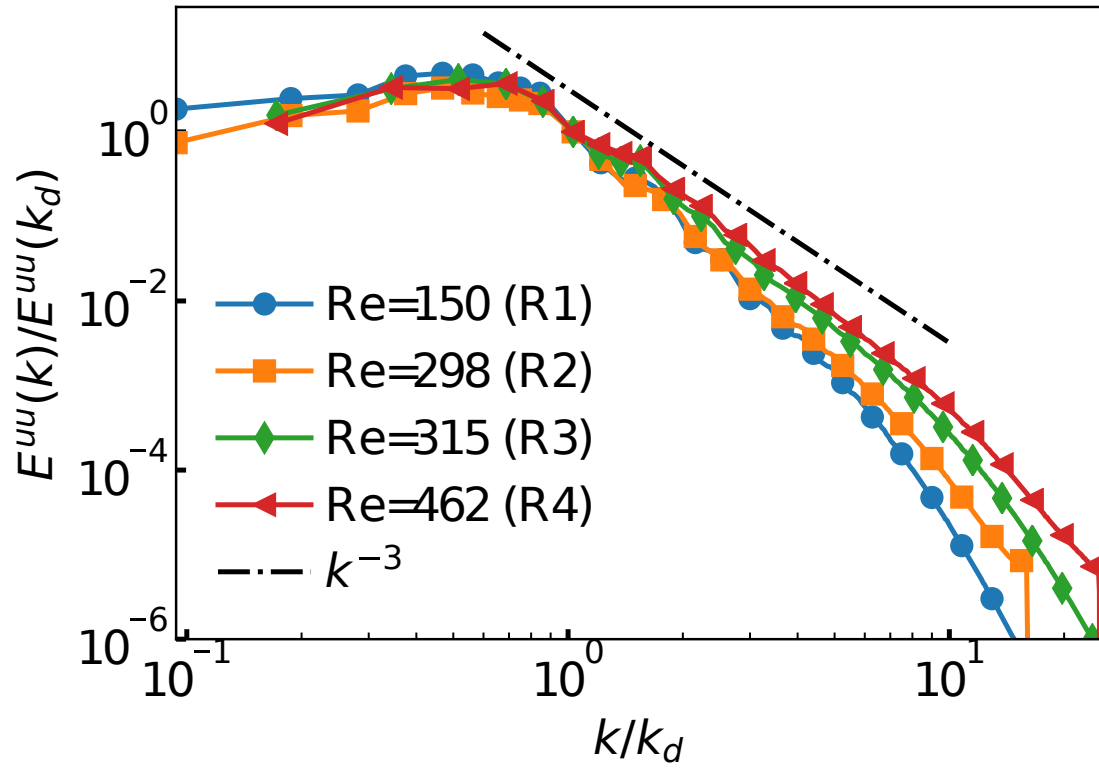


Figure 5.9: Log-log plot of energy spectra E_k^{uu} versus k/k_d for our high Re low At runs R1 - R4. Dashed dotted line indicates the k^{-3} scaling.

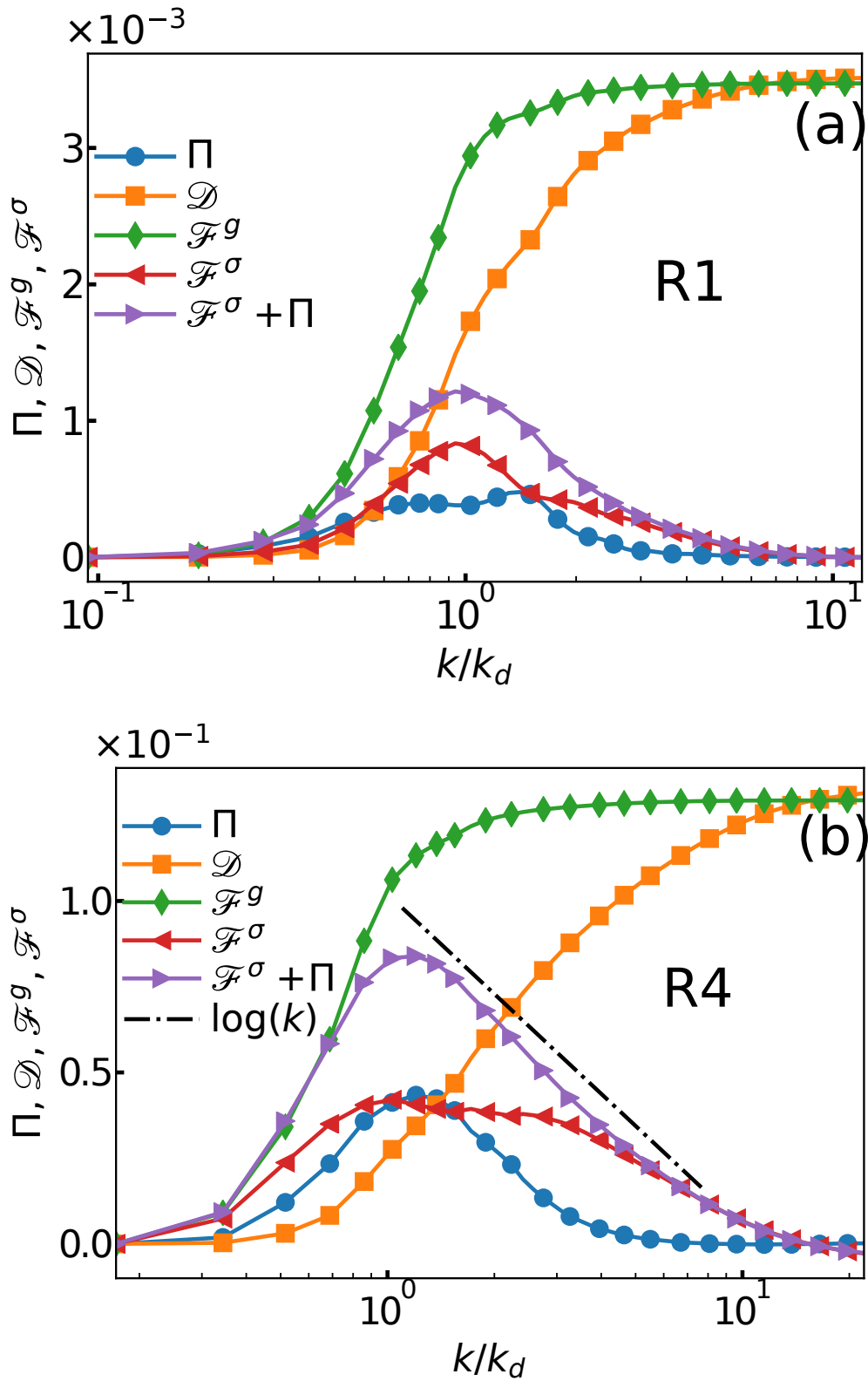


Figure 5.10: Cumulative contribution of viscous dissipation \mathcal{D}_k , energy injected because of buoyancy \mathcal{F}_k^g and the surface tension contribution \mathcal{F}_k^σ versus k/k_d for (a) run R1 and (b) run R4. Note that, for $k > k_d$, the balance between $d\mathcal{F}_k^\sigma/dk$ and $d\mathcal{D}_k/dk$ is more prominent in panel (b) compared to (a).

5.7.4 High At (runs R5 – R7)

Similar to earlier section, here also the energy spectrum and the co-spectrum shows a scaling of k^{-3} at high $\text{Re} = 546$ [22] and the spectrum becomes steeper $E(k) \sim k^{-3.6}$ [20] on decreasing the $\text{Re} = 173$ (Fig. 5.11). However, because of density variations the scale-by-scale energy budget becomes more complex. Now, in the statistically steady state $\Pi_k + \mathcal{F}_k^\sigma = \mathcal{P}_k - \mathcal{D}_k + \mathcal{F}_k^g$.

In Fig. 5.12 we plot the scale-by-scale energy budget for our high At run R6. We find that the cumulative energy injected by buoyancy and the pressure contribution $\mathcal{F}_k^g + \mathcal{P}_k$ reaches a peak around $k \approx k_d$ and then decrease mildly to ϵ_g . Similar to the low At case, we find a non-zero energy flux for $k \approx k_d$ and a dominant surface-tension contribution to the energy budget for $k \gg k_d$. Finally, similar to last section, for $k > k_d$ the net production $d(\Pi + \mathcal{F}^\sigma)/dk \sim k^{-1}$ balances viscous dissipation $\nu k^2 E(k)$ to give $E(k) \sim k^{-3}$.

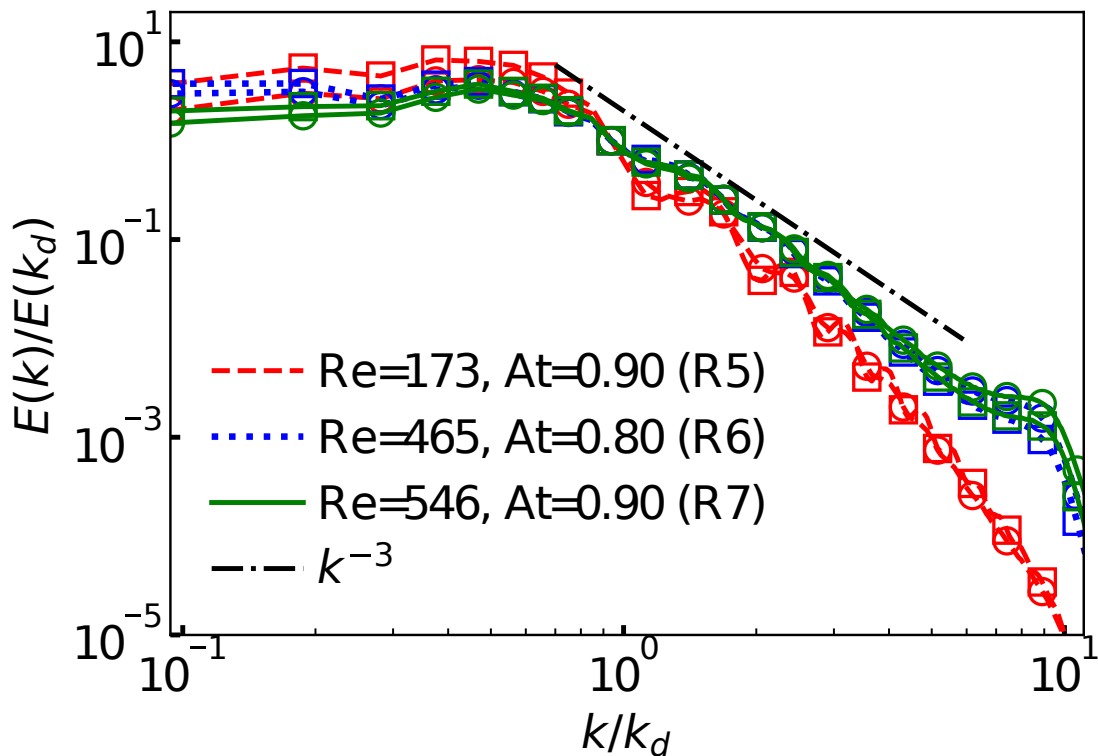


Figure 5.11: Log-log plot of energy spectra (○) E_k^{uu} and co-spectrum (□) $E_k^{\rho uu}$ versus k/k_d for our high Re high At runs R5 – R7. Dashed dotted line indicates the k^{-3} scaling.

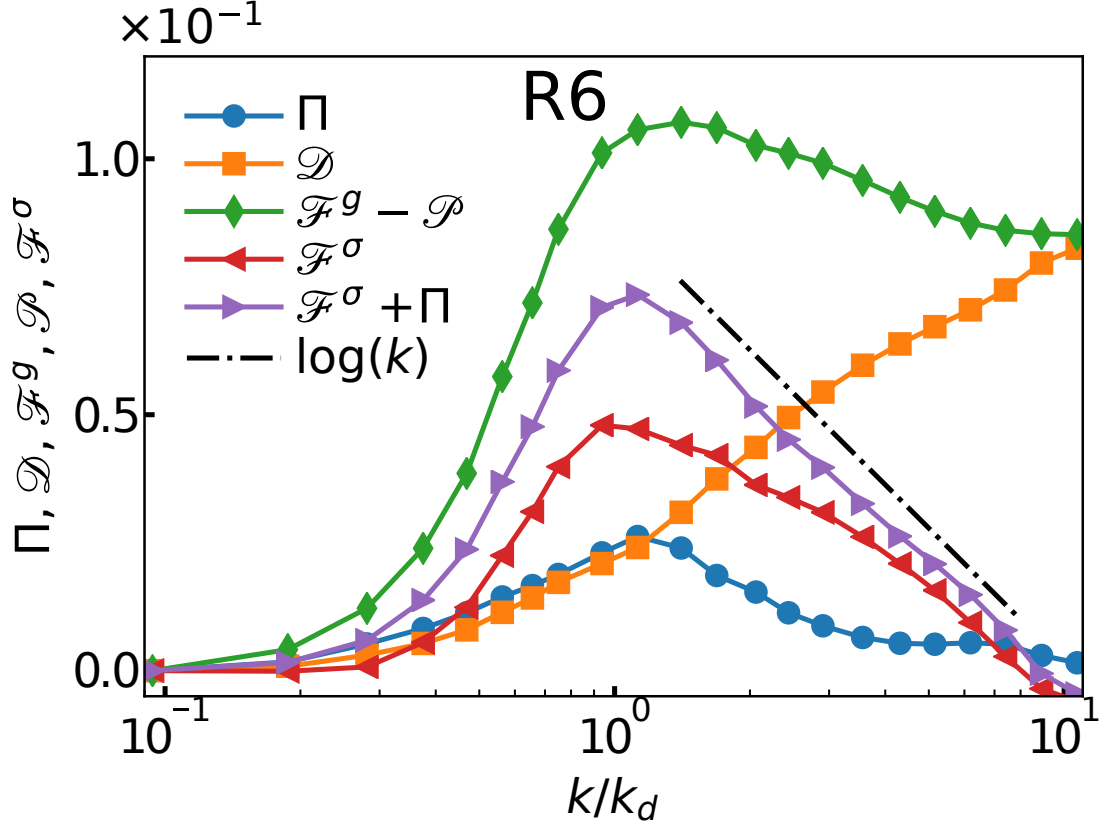


Figure 5.12: Cumulative contribution of the viscous dissipation \mathcal{D}_k , the contribution due to buoyancy and pressure $\mathcal{F}_k^g - \mathcal{P}_k$, the energy flux Π_k and the surface tension contribution \mathcal{F}_k^σ versus k/k_d for run R6.

5.7.5 Frequency spectrum of pseudo-turbulence

To investigate the frequency spectrum of pseudo-turbulence, we now conduct a time-series analysis similar to Roghair *et al.* [22] and Prakash *et al.* [17] for our high $At = 0.8$, high $Re = 465$ run R6. We monitor the time-evolution of the three components of the velocity and the density ρ for time $t = 90\tau_{\ell_0}$, with sampling time $8 \times 10^{-3}\tau_{\ell_0}$, on 32^3 equally spaced Eulerian points within our simulation domain. From these signals, we select continuous segments of liquid velocity fluctuations of size $t_s \geq 19\tau_{\ell_0}$ and ignore regions where $\rho = \rho_b$. We then use the Welch method, with hamming windows, to obtain the energy spectrum [17, 43]. In Fig. 5.13(a) we plot the liquid velocity spectrum $E(\tilde{v})$ versus \tilde{v}/\tilde{v}_d and find it to be in excellent agreement with the experiments of Prakash *et al.* [17]. In Fig. 5.13(b) we show that the normalized

energy spectrum is not modified on doubling $t_s \geq 38\tau_{\ell_0}$. Similar to Prakash *et al.* [17], Alm eras *et al.* [19], Roghair *et al.* [22] we find that $E(\tilde{\nu}) \sim \tilde{\nu}^{-3}$ for frequencies $\tilde{\nu} > \tilde{\nu}_d$, where $\tilde{\nu}_d = \langle U \rangle / 2\pi d$ [17].

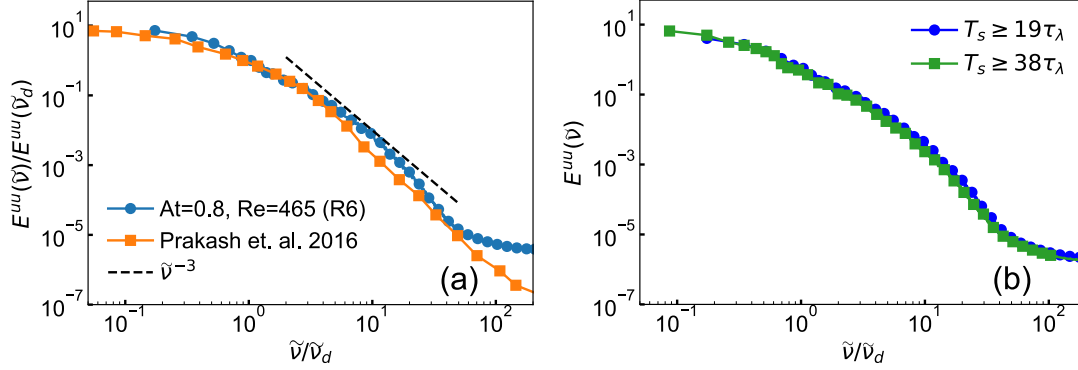


Figure 5.13: (a) Kinetic energy spectrum of the liquid velocity fluctuations $E(\tilde{\nu})$ versus $\tilde{\nu}/\tilde{\nu}_d$ for our run R6. We also overlay the spectrum obtained from the experiments of Prakash *et al.* [17] and find it to be in excellent agreement with our numerical simulation. (b) Comparison of the normalized energy spectrum obtained from liquid velocity segments of length $t_s \geq 19\tau_{\ell_0}$ ($1.9 \cdot 10^4$ trajectories) and $38\tau_{\ell_0}$ ($5 \cdot 10^3$ trajectories).

5.8 Length scales of pseudo-turbulence

We have used bubble diameter as a relevant scale of pseudo-turbulence [16, 17]. Riboux *et al.* [15] proposed an alternate length scale $\Lambda \propto V_0^2/g = 4\delta\rho d/(3\rho_f C_{d0})$, where V_0 is the single bubble rise velocity, and C_{d0} is the drag coefficient of an isolated bubble. Note that for large At , $\delta\rho/\rho_f \approx 1$. In Table 5.2 we present values of d and Λ obtained from our numerical simulations R1 – R7. For our large At runs, we find that bubble diameter is comparable to Λ ($d/\Lambda \approx 0.4 - 0.6$). On the other hand, for our small At runs, $d/\Lambda \approx 4 - 6$ indicating that k_Λ/k_d lies near the end of the k^{-3} scaling range. Thus Λ does not capture the beginning of the k^{-3} scaling for our low At runs.

runs	R1	R2	R3	R4	R5	R6	R7
Λ	4.0	6.2	4.1	4.3	52.9	38.4	53.3
d/Λ	6.0	3.8	5.4	5.1	0.5	0.6	0.4

Table 5.2: Length scale $\Lambda \propto V_0^2/g = 4\delta\rho d/(3\rho_f C_{d0})$ and the ratio d/Λ for our runs R1–R7.

5.9 Clustering of bubbles

In this section, we study the clustering of bubbles using Voronoï analysis, similar to Tagawa *et al.* [44]. In Voronoï tessellations, space is divided into cells based on the particle positions [45]. All the points inside a Voronoï cell are closest to the particle inside compared to its neighbors. The only exception to this rule being the vertices and edges of the Voronoï cell. For randomly distributed particles, the probability distribution of the volume of Voronoï cells is described using the following function, with a single fit parameter Σ [46]

$$P(x) = \frac{1}{\Sigma^{(2/\Sigma^2)}\Gamma(\frac{1}{\Sigma^2})} x^{(1/\Sigma^2-1)} \exp(-x/\Sigma^2). \quad (5.25)$$

Here $x = \mathcal{V}/\langle\mathcal{V}\rangle$ is the volume of Voronoï cell scaled by its mean.

For irregularly clustered particles, the standard deviation of the Voronoï (Σ) volume will be larger than the standard deviation of volumes (Σ_{rnd}) corresponding to randomly distributed particles. In other words, the indicator of clustering $\mathcal{E} \equiv \Sigma/\Sigma_{rnd} > 1$, for irregularly clustered particles. For the particles arranged in a regular lattice, the distribution of Voronoï volume will be a delta function and $\mathcal{E} < 1$. We illustrate the classification of clustering in Fig. 5.14 using two dimensional Voronoï tessellations.

A detailed analysis of the clustering of bubbles, in a buoyancy-driven flow, using Voronoï analysis was done by Tagawa *et al.* [44]. They varied Re , surface tension σ , d/L , and the volume fraction Φ_V (5–40%) and observed that the clustering depends on the bubbles' deformability.

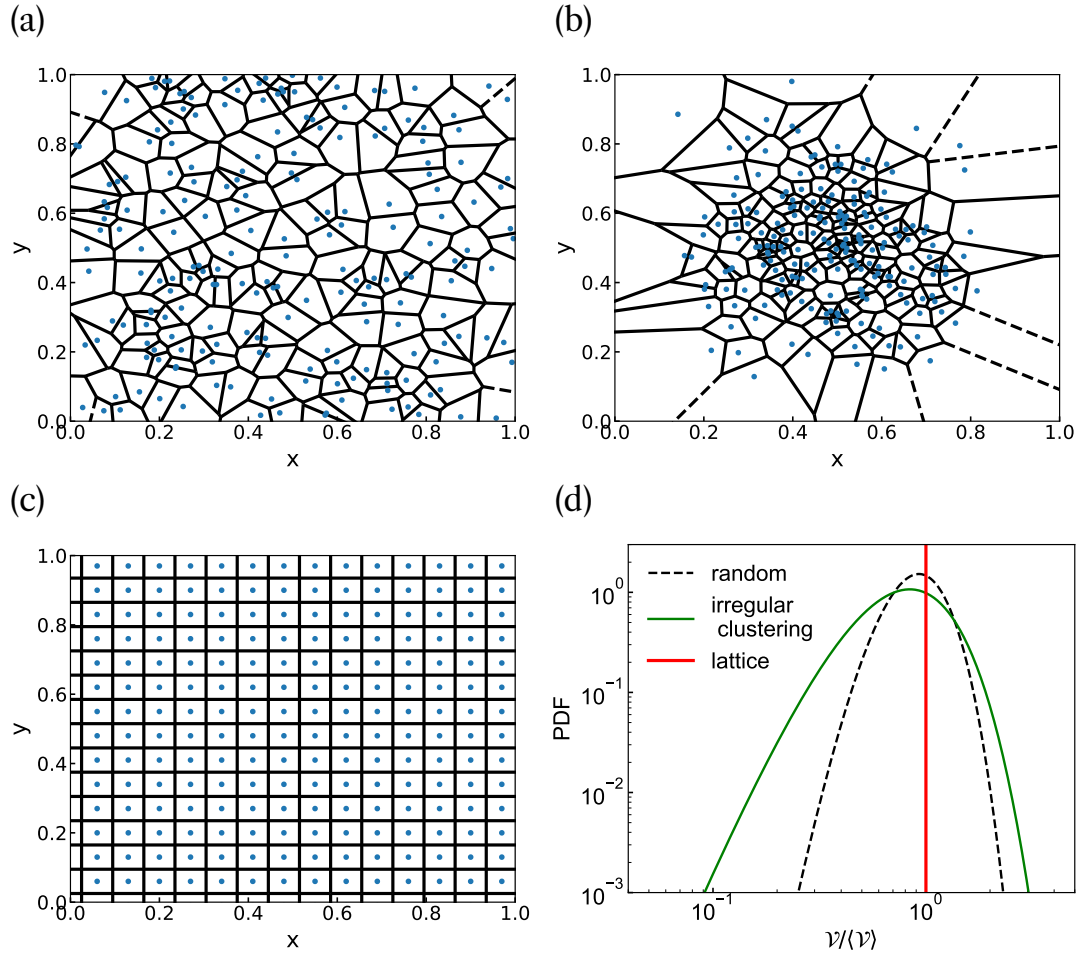


Figure 5.14: Schematic representation of clustering of 196 particles using Voronoi tessellation: (a) randomly distributed particles, (b) irregularly clustered particles, and (c) regular arrangement of particles. For the ease of visualization, we show tessellation in two-dimensional (d) The representative probability distribution function of the 3-d Voronoi volumes. For irregularly clustered particles $\Sigma/\Sigma_{rnd} > 1$, and for regular lattice arrangement of particles $\Sigma/\Sigma_{rnd} < 1$. Figure recreated from Tagawa *et al.* [44].

We investigate clustering in our numerical study on a much dilute bubbly flows ($\Phi_V = 1.7 - 2.6\%$) compared to Tagawa *et al.* [44]. For the construction of Voronoi tessellation, we use open source voro++ library [47]. We first generate 200 configurations of randomly positioned, non-overlapping, N_b bubbles of diameter d in a box of length L . Using the Voronoi tessellation of these random configurations, we determine the standard deviation Σ_{rnd} . Using the steady-state bubble configurations, we then estimate Σ for each simulation.

runs	R1	R2	R3	R4	R5	R6	R7
\mathcal{C}	1.3	1.3	1.1	1.1	1.3	1.0	0.9

Table 5.3: The clustering indicator \mathcal{C} for our runs R1–R7.

The clustering indicator \mathcal{C} for all the simulations is given in Table (5.3). We observe random or weakly irregular clustering for our runs R1 – R6 (see Table 5.3). For our high-Re, high-At run R7, $\mathcal{C} = 0.9$, which indicates a weakly regular lattice arrangement of bubbles.

We finally show the pdf of Voronoï volumes for a few representatives runs in Fig. 5.15. We find that the pdf is close to that of corresponding random configuration. For the Voronoï analysis, we are limited by i) the number of steady-state configurations, and ii) the number of bubbles in the domain, which are few. Although we do not quote the error in our estimation of \mathcal{C} , it is probably significant. Within the error, the steady-state bubbles configuration in all our simulations can be considered random.

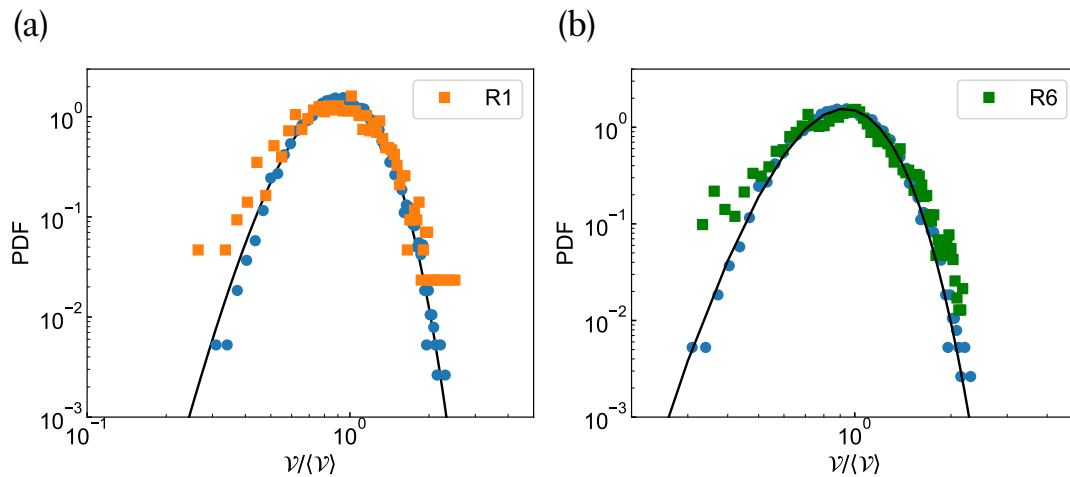


Figure 5.15: The probability distribution of the Voronoï volume ($\mathcal{V}/\langle\mathcal{V}\rangle$) for (a) R1 ($Re = 150, At = 0.04$) (b) R6 ($Re = 465, At = 0.80$). The blue filled circles represent the pdf of ($\mathcal{V}/\langle\mathcal{V}\rangle$) for the corresponding random configurations. The continuous black line shows the fit $P(x)$ (see 5.25).

5.10 Topological properties of fluid

The velocity-gradient tensor $\mathbb{A} = \nabla \mathbf{u}$ determines the local topology of a flow [48, 49]. If λ 's are the eigenvalues of tensor \mathbb{A} , then the characteristic equation for \mathbb{A} is

$$\lambda^3 + P\lambda^2 + Q\lambda + R = 0, \quad (5.26)$$

where P , Q , and R are the three invariants of tensor \mathbb{A} . Since, for incompressible flow,

$$P \equiv \mathcal{T}r[\mathbb{A}] \equiv 0, \quad (5.27)$$

the other invariants reduce to

$$Q \equiv \frac{P^2 - \mathcal{T}r[\mathbb{A}^2]}{2}, \quad (5.28)$$

and

$$R \equiv -\mathcal{D}et[\mathbb{A}]. \quad (5.29)$$

Here, $\mathcal{T}r[\cdot]$ denotes trace, and $\mathcal{D}et$ denotes determinant of a tensor.

The discriminant of 5.26, $\Delta = Q^3 + \frac{27}{4}R^2$ divides the $Q - R$ plane into two regions based on real and imaginary λ .

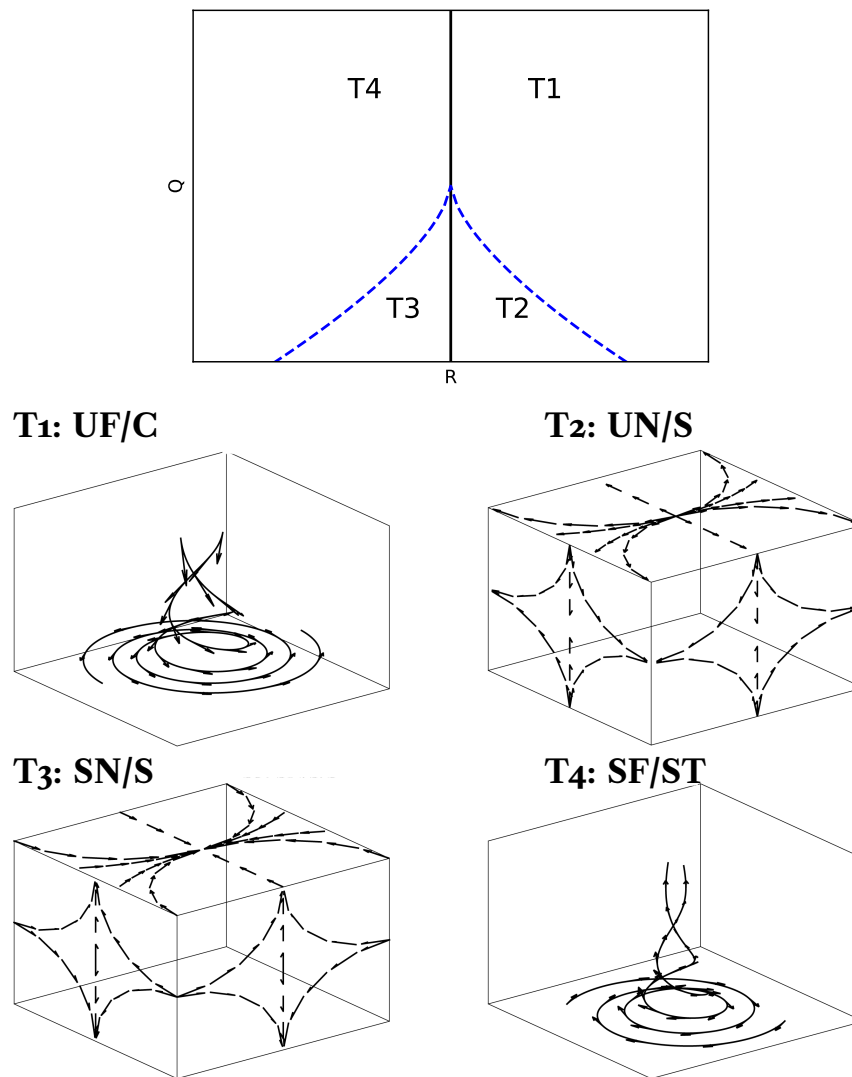


Figure 5.16: Showing the different regions in the Q - R plane and the schematic diagram of the flow topologies. Blue dashed line represents $D = 0$. The different topologies are: UF = unstable Focus, C = compressing UN = unstable node, S = saddle, SN = stable node, SF = stable focus, and ST = stretching.

- $\Delta < 0$ implies three real eigenvalues, and the topology is nodal.
- $\Delta > 0$ implies one real and two complex eigenvalues, and the topology is focal.

Furthermore, the $Q = 0$ line distinguishes the vorticity ($Q < 0$) and strain dominated ($Q > 0$) regions. The joint probability distribution function (pdf) of the invariants $Q - R$ determines the flow topology of incompressible flow. In [Fig. 5.16](#), we show all the flow topologies possible using a schematic diagram.

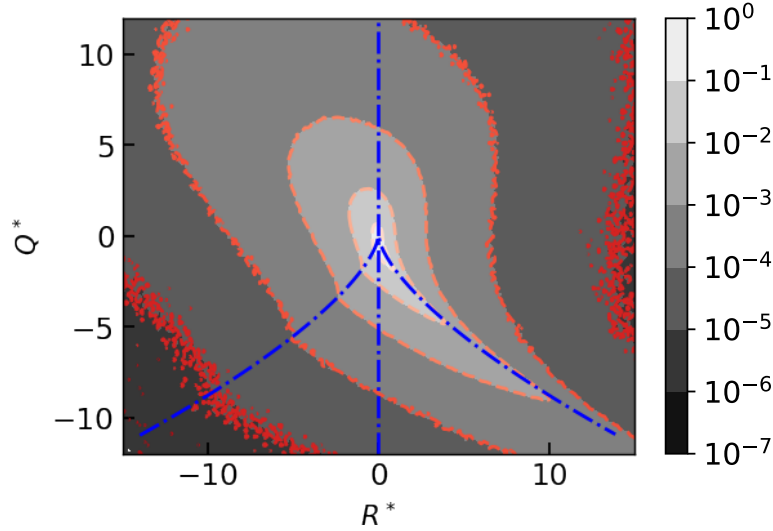


Figure 5.17: Representative joint probability distribution of $Q^* = Q/\epsilon_\mu$ and $R^* = R/\epsilon_\mu^{3/2}$ for homogeneous and isotropic turbulence.

In homogeneous isotropic turbulence, the joint probability distribution function (pdf) of $Q - R$ have a classical 'teardrop' shape [48, 50, 51]. We show a representative plot of the joint pdf for an isotropic and homogeneous turbulence in Fig. 5.17. Clearly, in the region where vorticity dominates ($Q > 0$), T4 is the most probable topology and in the region where strain dominates ($Q < 0$), the most probable topology is T2.

Although the shape of the joint pdf of $Q - R$ is well known for homogeneous and isotropic turbulence, the question still remains – what is the flow topology for a pseudo-turbulent flow? To answer this question, we show the joint pdf of $Q - R$ in Fig. 5.18 for different runs given in Table (5.1). We shall first discuss the topology for low $Re \sim 150$ [Fig. 5.18(a) and (c)]. Interestingly, we find topology to be similar for both high and low At . In contrast with the homogeneous and isotropic turbulence where the topology T4 was favored over T1 in the vorticity dominated region, we find that both T1 and T4 equally probable. Also, in the strain dominated region, we find a significant increase in T3 topology.

As a direct consequence of increased bubble wake interaction, interestingly, upon increasing the $Re \sim 450$, for both high and low At , we find the joint pdf starts to resemble with turbulence with T4 more probable than T1

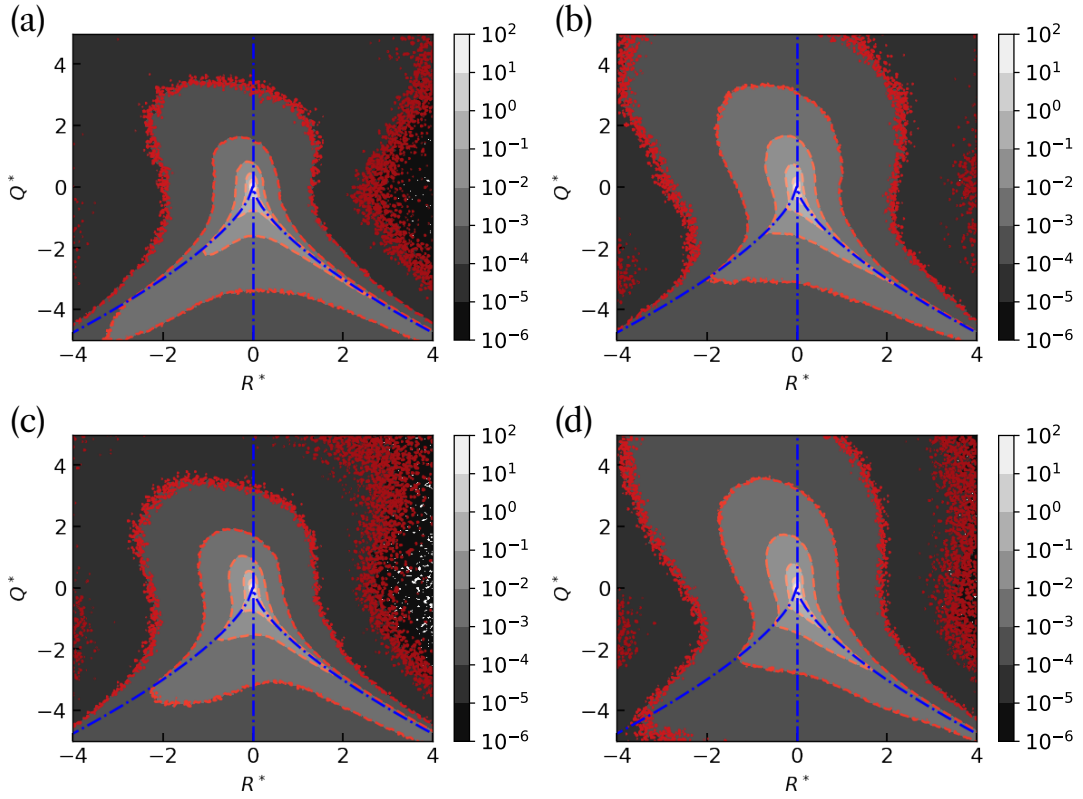


Figure 5.18: The joint probability distribution of $Q^* = Q/\epsilon_{\mu,f}$ and $R^* = R/(\epsilon_{\mu,f})^{3/2}$ for (a) $Re = 150$, $At = 0.04$ (R1), (b) $Re = 462$, $At = 0.04$ (R4), (c) $Re = 172$, $At = 0.90$ (R5) and (d) $Re = 465$, $At = 0.80$ (R6).

for $Q > 0$ and T2 favored over T3 for $Q < 0$.

5.11 Conclusion

In this chapter, we studied the statistical properties of pseudo-turbulence in buoyancy-driven bubbly flows using direct numerical simulations. We take a range of $Re \sim [100 - 600]$ and $At \sim [0.04 - 0.90]$. The Re that we have explored are consistent with the $Re \sim [300 - 1000]$ used in the experimental studies [15–17]. Even though the At in our simulations is much smaller than the experiments (~ 0.999), we find that the shape of pdf of the velocity fluctuations is consistent with the experiments. In the kinetic energy spectra, we show that for high Re and for low and high At , $E(k) \sim k^{-3}$ [22]. However, on reducing the Re , the spectral slope becomes steeper $E(k) \sim k^{-4}$ [20]. Our

scale by scale budget analysis shows that the scaling is because of the viscous dissipation of the energy transferred by surface tension and non-linear forces at scales smaller than the bubble diameter. We then show the energy spectra scales with frequency as $E(\tilde{\nu}) \sim \tilde{\nu}^{-3}$, consistent with the experiments of Prakash *et al.* [17].

In section 5.9 of this chapter, we study the clustering of bubbles. In a homogeneous and dilute bubble suspension at high Re, the spatial clustering of bubbles is not observed in earlier simulations [22, 37] or experiments [15, 52]. In line with the previous studies, we also find the spatial distribution of the bubbles nearly random for all the simulations.

In the last section 5.10, we study the topological properties of the fluid in pseudo-turbulence. We contrast our result with the topological structures observed in homogeneous and isotropic turbulence. The topology in pseudo-turbulence resembles homogeneous and isotropic turbulence for our highest Re simulation.

We finally would like to remark on the scaling of energy spectra in pseudo-turbulence. Experiments on pseudo-turbulence have investigated the liquid velocity fluctuations in the bubble swarm [14, 16, 17, 53] or the wake [15]. All these experiments show a robust -3 spectrum. However, Riboux *et al.* [15] also observed that the -3 spectrum is followed by nearly half a decade of $-5/3$ spectrum. Similar observation, albeit for a much smaller scaling range, was also made by Mendez-Diaz *et al.* [16]. Consistent with bubble swarm experiments, [14, 17, 53], we do not observe a $-5/3$ spectrum. A plausible reason for the observed discrepancy, as indicated by Riboux *et al.* [15], could be that strong flows generated in the vicinity of the bubbles are absent in the wake of the bubble swarm.

References

- [1] R. Clift, J. R. Grace, and M. E. Weber, *Bubbles, drops and particles* (Academic Press, New York, 1978).
- [2] H. M. Gonnermann and M. Manga, *Annu. Rev. Fluid Mech.* **39**, 321 (2007).
- [3] W.-D. Deckwer, *Bubbles Column reactors* (Wiley, 1992).
- [4] R. F. Mudde, *Annu. Rev. Fluid Mech.* **37**, 393 (2005).
- [5] S. L. Ceccio, *Annu. Rev. Fluid Mech.* **42**, 183 (2010).
- [6] L. Biferale, P. Perlekar, M. Sbragaglia, and F. Toschi, *Phys. Rev. Lett.* **108**, 104502 (2012).
- [7] R. Pandit, D. Banerjee, A. Bhatnagar, M. Brachet, A. Gupta, D. Mitra, N. Pal, P. Perlekar, S. S. Ray, V. Shukla, and D. Vincenzi, *Phys. Fluids* **29**, 111112 (2017).
- [8] F. Risso, *Annu. Rev. Fluid Mech.* **50**, 25 (2018).
- [9] E. Alm eras, V. Mathai, C. Sun, and D. Lohse, *Int. J. Multiphase Flow* **114**, 316 (2019).
- [10] S. Elghobashi, *Annu. Rev. Fluid Mech.* **51**, 217 (2019).
- [11] V. Mathai, D. Lohse, and C. Sun, *Annu. Rev. Condens. Matter Phys.* **11**, 1 (2019).
- [12] D. Bhaga and M. E. Weber, *J. Fluid Mech.* **105**, 61 (1981).
- [13] M. K. Tripathi, K. C. Sahu, and R. Govindarajan, *Nat. Commun.* **6**, 6268 (2015).
- [14] J. M. Mercado, D. G. G omez, D. V. Gils, C. Sun, and D. Lohse, *J. Fluid Mech.* **650**, 287 (2010).
- [15] G. Riboux, F. Risso, and D. Legendre, *J. Fluid Mech.* **643**, 509 (2010).

- [16] S. Mendez-Diaz, J. C. Serrano-Garcia, R. Zenit, and J. A. Hernández-Cordero, *Phys. Fluids* **25**, 043303 (2013).
- [17] V. N. Prakash, J. M. Mercado, L. van Wijngaarden, E. Mancilla, Y. Tagawa, D. Lohse, and C. Sun, *J. Fluid Mech.* **791**, 174 (2016).
- [18] M. Lance and J. Bataille, *J. of Fluid Mech.* **222**, 95 (1991).
- [19] E. Alméras, V. Mathai, D. Lohse, and C. Sun, *J. Fluid Mech.* **825**, 1091 (2017).
- [20] B. Bunner and G. Tryggvason, *J. Fluid Mech.* **466**, 53 (2002).
- [21] B. Bunner and G. Tryggvason, *J. Fluid Mech.* **466**, 17 (2002).
- [22] I. Roghair, J. M. Mercado, M. V. S. Annaland, H. Kuipers, C. Sun, and D. Lohse, *Int. J. Multiph. Flow* **37**, 1093 (2011).
- [23] F. Risso, *Phys. Fluids* **23**, 011701 (2011).
- [24] U. Frisch, *Turbulence, A Legacy of A. N. Kolmogorov* (Cambridge University Press, 1997).
- [25] R. Pandit, P. Perlekar, and S. S. Ray, *Pramana* **73**, 157 (2009).
- [26] W. Aniszewski, T. Arrufat, M. Cialesi-Esposito, S. Dabiri, D. Fuster, Y. Ling, J. Lu, L. Malan, S. Pal, R. Scardovelli, G. Tryggvason, P. Yecko, and S. Zaleski, “PARallel, Robust, Interface Simulator (PARIS),” (2019), hal-02112617.
- [27] C. Canuto, M. Y. Hussaini, A. M. Quarteroni, and T. A. Zang, *Spectral Methods in Fluid Dynamics* (Springer-Verlag, 2012).
- [28] G. Tryggvason, B. Bunner, A. Esmaeeli, D. Juric, N. Al-Rawahi, W. Tauber, J. Han, S. Nas, and Y.-J. Jan, *J. Comput. Phys.* **169**, 708 (2001).
- [29] P. Perlekar, *J. Fluid Mech.* **873**, 459 (2019).
- [30] I. Shukla, N. Kofman, G. Balestra, L. Zhu, and F. Gallaire, *J. Fluid Mech.* **874**, 1021 (2019).

- [31] M. Wu and M. Gharib, *Phys. Fluids* **14**, L49 (2002).
- [32] J. Tchoufag, J. Magnaudet, and D. Fabre, *J. Fluid Mech.* **751**, R4 (2014).
- [33] V. Mathai, S. G. Huisman, C. Sun, D. Lohse, and M. Bourgoïn, *Phys. Rev. Lett.* **121**, 054501 (2018).
- [34] M. R. Pivello, M. M. Villar, R. Serfaty, A. M. Roma, and A. Silveira-Neto, *Int. J. Multiph. Flow* **58**, 72 (2014).
- [35] D. D. Joseph, *Stability of Fluid Motions II* (Springer Publishers, Berlin, 1976).
- [36] F. Risso, *J. Fluid Mech.* **809**, 240 (2016).
- [37] A. Esmaeeli and G. Tryggvason, *Phys. Fluids* **17**, 093303 (2005).
- [38] S. Pope, *Turbulent Flows* (Cambridge University Press, 2012).
- [39] H. Aluie, *Physica D: Nonlinear Phenomena* **247**, 54 (2013).
- [40] P. Perlekar, D. Mitra, and R. Pandit, *Phys. Rev. Lett.* **97**, 264501 (2006).
- [41] P. Perlekar, D. Mitra, and R. Pandit, *Phys. Rev. E* **82**, 066313 (2010).
- [42] P. Valente, C. da Silva, and F. Pinho, *J. Fluid Mech.* **760**, 39 (2014).
- [43] P. Welch, *IEEE Trans. Audio Electroacoust.* **15**, 70 (1967).
- [44] Y. Tagawa, I. Roghair, V. N. Prakash, M. van Sint Annaland, H. Kuipers, C. Sun, and D. Lohse, *J. Fluid Mech.* **721**, 313 (2013).
- [45] A. Okabe, B. Boots, K. Sugihara, and S. Chiu, *Spatial tessellations* (John Wiley and Sons, 2000).
- [46] Y. Tagawa, J. M. Mercado, V. N. Prakash, E. Calzavarini, C. Sun, and D. Lohse, *J. Fluid Mech.* **693**, 201 (2012).
- [47] C. H. Rycroft, *Chaos: An Interdisciplinary Journal of Nonlinear Science* **19**, 041111 (2009).
- [48] M. S. Chong, A. E. Perry, and B. J. Cantwell, *Phys. Fluids A* **2**, 765 (1990).

- [49] J. Hasslberger, S. Marten, and M. Klein, *Fluids* **4**, 117 (2019).
- [50] B. J. Cantwell, *Phys. Fluids A* **4**, 782 (1992).
- [51] A. Tsinober, *Vortex Stretching versus production of Strain/Dissipation* (Cambridge University Press, 2000).
- [52] F. Alm eras, E. and Risso, V. Roig, S. Cazin, C. Plais, and F. Augier, *Journal of Fluid Mechanics* **776**, 458 (2015).
- [53] A. Larue De Tournemine, *Etude exp erimentale de l'effet du taux de vide en  coulement diphasique   bulles*, Ph.D. thesis, Institut National Polytechnique de Toulouse, France (2001).

Turbulence modulation by large buoyant bubbles

6.1 Introduction

In the previous chapter, we investigated the statistical properties of pseudo-turbulence. In this chapter, we study the interaction of pseudo-turbulence with externally driven turbulence. Pseudo-turbulence is the complex flow generated by a swarm of bubbles rising in an otherwise quiescent fluid. It has been studied by several experiments and numerical simulations over the last two decades [1–5].

A more complex but ubiquitous scenario is where large scale external forcing leads to a turbulent flow [4, 6, 7]. In the absence of bubbles, a non-linear transfer of energy (maintaining constant energy flux) from forcing to dissipation range characterizes turbulence [8–10]. How does the presence of bubbles modify this flow? The answer, in principle, depends on the ratio of the bubble diameter to the dissipation scale, the bubble volume fraction, and its density and viscosity contrast with the ambient fluid.

For sub-dissipation scale bubbles at low volume fraction, bubbles are passively advected, and the Maxey-Riley (MR) equations describe their dynamics [11, 12]. Indeed, numerical studies using MR equations have investigated

acceleration statistics of bubbles and found them to be in excellent agreement with the experiments [13–15]. For large bubbles, the MR equations are no longer valid, and the studies of acceleration statistics use numerical simulations that fully resolve the bubble-fluid interaction. At moderate volume fractions and for large bubbles, the bubble-wake interactions are relevant, and we expect it to have a non-trivial effect on the bubble acceleration as well as flow statistics.

Experiments with large scale forcing that generates nearly homogeneous, isotropic flows at large Reynolds numbers show that bubbles dramatically alter the energy spectrum for scales smaller than the bubble diameter [16, 17]. Although the liquid velocity fluctuations have been well-characterized, an understanding of the energy transfer mechanisms and the Lagrangian statistics of the bubbles remain mostly unexplored.

Direct Numerical Simulation (DNS) studies in this regime are limited to (a) buoyancy-driven bubbly flows in the absence of external driving, (b) low Reynolds numbers, (c) neutrally buoyant regime, and (d) wall-bounded flow to understand the influence of bubbles on the mean flow properties. The use of low-order finite-difference schemes and the requirement of substantial grid resolution to resolve bubbles at high-density and viscosity ratios, such as an air-water suspension, make the high Reynolds number simulations untenable.

Recent DNS studies of buoyancy-driven bubbly flow for a wide range of density and viscosity ratios have revealed that the statistical properties of pseudo-turbulence are robust [5]. Motivated by these findings, in this chapter, we investigate turbulence modulation in suspensions of weakly buoyant bubbles. Similar to the experiments, we characterize the flow in terms of the ‘bubblance’ parameter $b = \Phi_V V_0^2 / u_0^2$, where Φ_V is the bubble volume fraction, V_0 is the rise velocity of an isolated bubble in quiescent fluid, and u_0 is the rms velocity of the turbulent flow in the absence of bubbles. The two extreme limits $b = 0$ and $b = \infty$ correspond to pure fluid turbulence and buoyancy-driven bubbly flow, respectively.

6.2 Numerical Simulations

We use the Navier-Stokes (NS) equations with a surface tension force to investigate the suspension of bubbles. Since we are interested in studying the weakly buoyant regime, we invoke the Boussinesq approximation [5, 18] to get,

$$\partial_t \mathbf{u} + \mathbf{u} \cdot \nabla \mathbf{u} = -\nabla p + \nu \nabla^2 \mathbf{u} + \mathbf{F}^\sigma + \mathbf{F}^g + \mathbf{F}^t, \text{ and} \quad (6.1)$$

$$\nabla \cdot \mathbf{u} = 0. \quad (6.2)$$

Here \mathbf{u} is the hydrodynamic velocity field at position \mathbf{x} and time t , p is the pressure field, ν is the viscosity, the buoyancy force due to gravity $\mathbf{F}^g \equiv -2Atcg\hat{\mathbf{z}}$, the Atwood number $At \equiv (\rho_f - \rho_b)/(\rho_f + \rho_b)$, g is the acceleration due to gravity, \mathbf{z} is the unit vector in the positive z -direction, ρ_f (ρ_b) is the fluid (bubble) density, c is an indicator function whose value is 1 in the liquid phase and 0 in the bubble phase. The surface tension force is $\mathbf{F}^\sigma = \kappa\sigma\mathbf{n}$, where κ is the local curvature of the front, σ is the coefficient of surface tension and \mathbf{n} is the unit normal. We apply a large-scale forcing in Fourier space, $\mathbf{F}_k^t = \epsilon_t \mathbf{u}_k / \sum_k |\mathbf{u}_k|^2$ with $|\mathbf{k}| \leq 2$, which generates turbulence and ensures constant energy injection rate ϵ_t .

We use a pseudo-spectral method, described in chapter-2, for the direct numerical simulation (DNS) of the NS 6.1 and 6.2 in a cube with each side of length $L \equiv 2\pi$. We use periodic boundary conditions, discretize the simulation domain with N^3 collocation points, and place $N_b = 80$ non-overlapping spherical bubbles of diameter $d = 0.46$ at random locations. Bubbles are resolved using a front-tracking method [19]. For time-evolution, we use a second-order Adams-Bashforth scheme for 6.1 and a second-order Runge-Kutta scheme for the front positions. A substantial part of the computational effort undergoes in resolving the front; DNS with the bubbles is four times slower than the one without them. We initialize the simulation domain with $\mathbf{u} = 0$ and place the bubbles at random locations such that no two bubbles overlap. In Table 6.1, we present the parameters used in our DNS. We refer to chapter-2 for more details on numerical scheme.

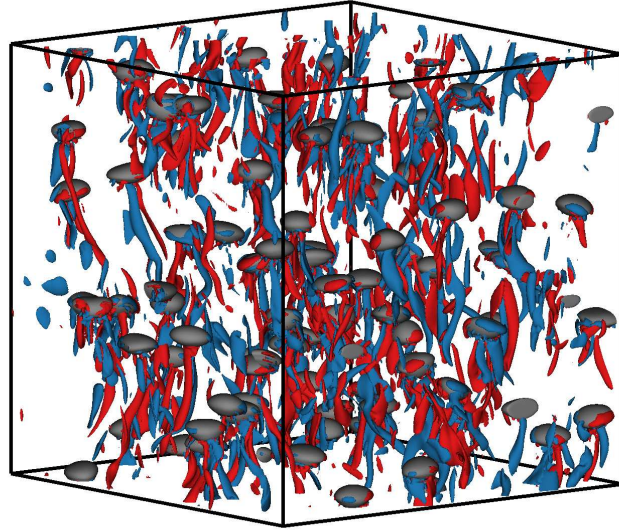
	N	Re_λ	ϵ_v	$\epsilon_t \cdot 10^{-2}$	$\epsilon_g \cdot 10^{-3}$	η	b
R0	546	—	0.007	—	7.0	—	∞
R1	512	79	0.009	0.25	6.8	0.02	0.35
R2	512	95	0.012	0.5	6.7	0.018	0.21
R3	512	110	0.015	1.0	6.0	0.015	0.13

Table 6.1: Parameters for our DNS runs R1 – 4, the Taylor-scale Reynolds number $\text{Re}_\lambda \equiv u_0 \sqrt{15/(\epsilon_t \nu)}$, $\nu = 8 \cdot 10^{-4}$ is the viscosity, u_0 is the root-mean-square velocity obtained from DNS in absence of bubbles but with turbulent driving, $\eta \equiv (\nu^3/\epsilon_t)^{1/4}$ is the Kolmogorov dissipation scale, $\epsilon_v = \nu \langle |\nabla \mathbf{u}|^2 \rangle$ is the viscous dissipation rate, the energy injection rates due to turbulent forcing and buoyancy are $\epsilon_t \equiv \langle \mathbf{u} \cdot \mathbf{F}^t \rangle$ and $\epsilon_g \equiv \langle \mathbf{u} \cdot \mathbf{F}^g \rangle$, respectively. The angular brackets denote spatio-temporal averaging in the statistically steady-state. For all the runs R0 – R4, the Galilei number $\text{Ga} \equiv \sqrt{\delta \rho g d^3 / \rho_f \nu} = 302$, the Bond number $\text{Bo} \equiv \delta \rho g d^2 / \sigma = 1.8$, the Atwood number $\text{At} = \delta \rho / (\rho_f + \rho_b) = 0.04$, the bubble diameter $d = 0.46$, the bubble volume fraction $\Phi_V \equiv N_b (\pi/6) (d/L)^3 = 1.64\%$, bubble Reynolds number $\text{Re} = 302$, and the bubble parameter $b \equiv \Phi_V V_0^2 / u_0^2$, where $V_0 \approx 0.8$. Note that $b = \infty$ for buoyancy-driven bubbly flows in the absence of large scale forcing, and $b = 0$ corresponds to homogeneous, isotropic turbulence without bubbles. All the simulations run for at least for a period of $\approx 5 \tau_{\ell_0}$ in the steady state, where $\tau_{\ell_0} \equiv \ell_0 / (2u_0)$ is the large eddy turn over time. Note that the values of Φ_V , Ga , Bo , and Re_λ used in our study are comparable to those used in the experiments [16, 17].

6.3 Results

In Fig. 6.1, we show the representative snapshot of vorticity ω_z from our simulation. We monitor the time evolution of the energy dissipation rate, the energy injected by buoyancy, and the center-of-mass $\mathbf{X}_i(t)$ of each bubble in the suspension after every $\delta t = 0.08 \tau_\eta$ time-interval, where i denotes the

(a)



(b)

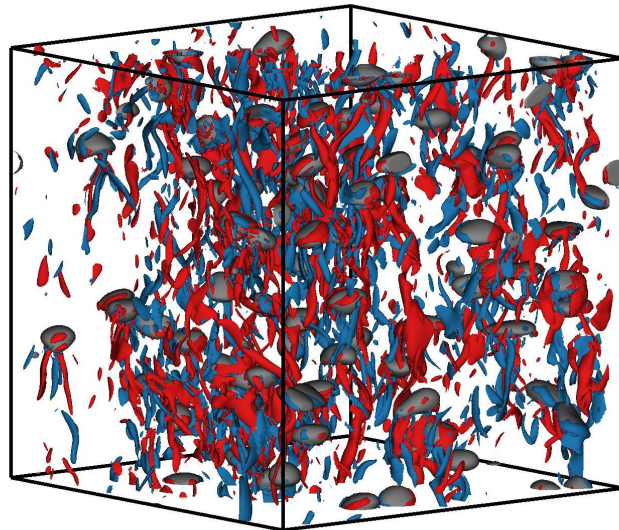


Figure 6.1: (a,b) Representative steady-state snapshot of the bubbles and super-imposed iso-vorticity surfaces (with iso-value $\pm 3 \langle \omega_z^2 \rangle^{1/2}$) from run (a) R1 and (b) R3.

bubble index. From the bubble tracks, we obtain the center-of-mass velocity $V_i(t)$ and the acceleration $A_i(t)$ using centered, second-order, finite-differences.

In the statistically steady-state, the viscous dissipation balances net energy injected by the large-scale turbulent forcing and buoyancy, i.e., $\epsilon_v \approx$

$\epsilon_t + \epsilon_g$ [5]. With increasing Re_λ (decreasing b), the large-scale forcing becomes the dominant energy injection mechanism (see Table 6.1).

In the following, we first investigate the statistical properties of the bubble rising in the turbulent flow, we then investigate the statistical properties of the fluid velocity fluctuations. Finally, we present the results for the spectral properties of the flow by using a scale-by-scale energy budget analysis.

6.3.1 Bubble trajectories and rise velocity

The plots in Fig. 6.2 show representative bubble trajectory in a swarm for $\text{Re}_\lambda = 79, b = 0.35$ and $\text{Re}_\lambda = 110, b = 0.13$. Clearly the trajectory for lower bubble size is more curved because of the increased turbulence-bubble interaction.

We characterize the trajectory by using local curvature $\kappa_t \equiv |\mathbf{A} \times \mathbf{V}|/|\mathbf{V}|^3$. Consistent with the observation that the trajectories are more curved for larger Re_λ , we find that the probability distribution function (pdf) $P(\kappa_t)$ is broader Fig. 6.3(a). Another consequence of large-scale turbulent stirring is that the average bubble rise velocity $\langle U \rangle \equiv \sum_{i=1}^{N_b} \mathbf{V}^i \cdot \hat{\mathbf{z}}/N_b$ (see Fig. 6.2) increases with increasing b (decreasing Re_λ). Using the definition of \mathbf{F}^g and noting that $\langle u_z \rangle = 0$ in the Boussinesq regime, we obtain $\epsilon_g = 2\text{At}g\Phi_V\langle U \rangle$ and verify it in Fig. 6.3(b). A decrease in the rise velocity of the bubbles is consistent with the observation that the drag on large particles increases with an increase in the turbulence intensity [20].

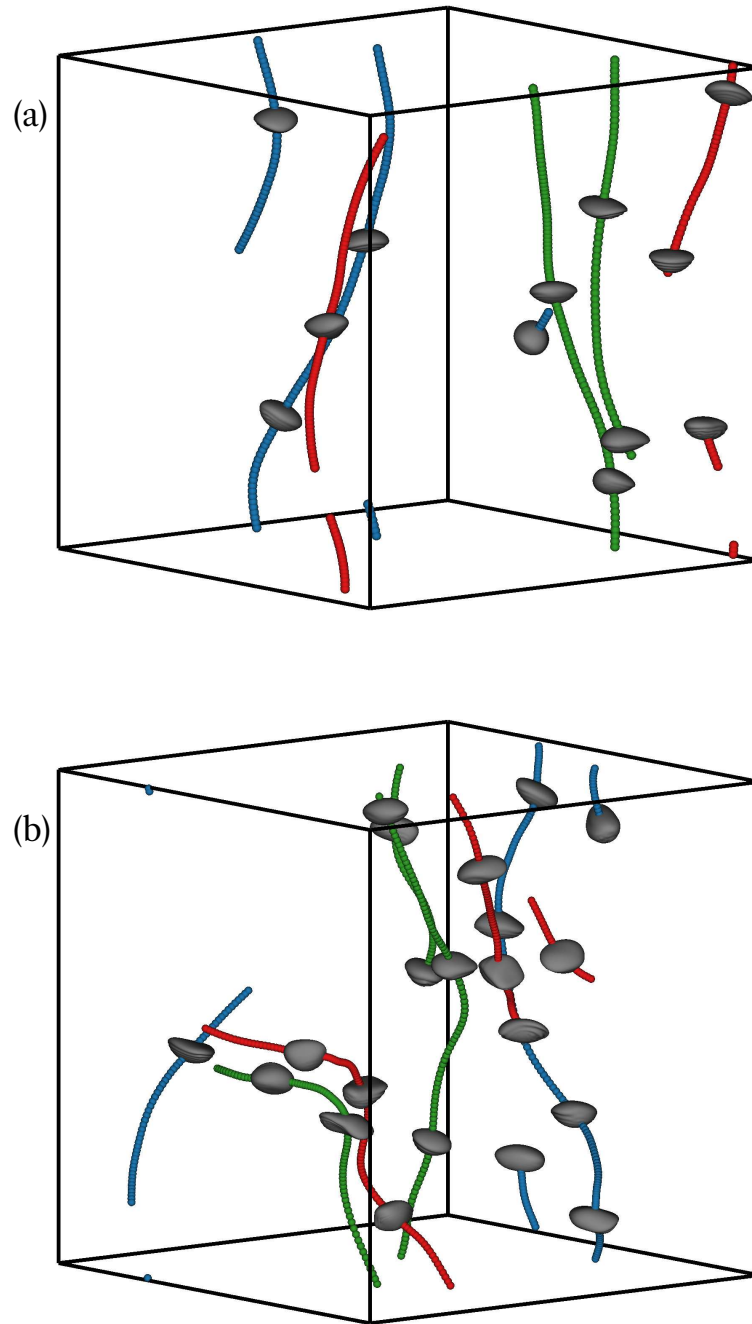


Figure 6.2: Typical trajectories of the center-of-mass of bubbles in a turbulent flow for runs (a) $Re_\lambda = 79$, $b = 0.35$ (R1) and (b) $Re_\lambda = 110$, $b = 0.13$ (R3).

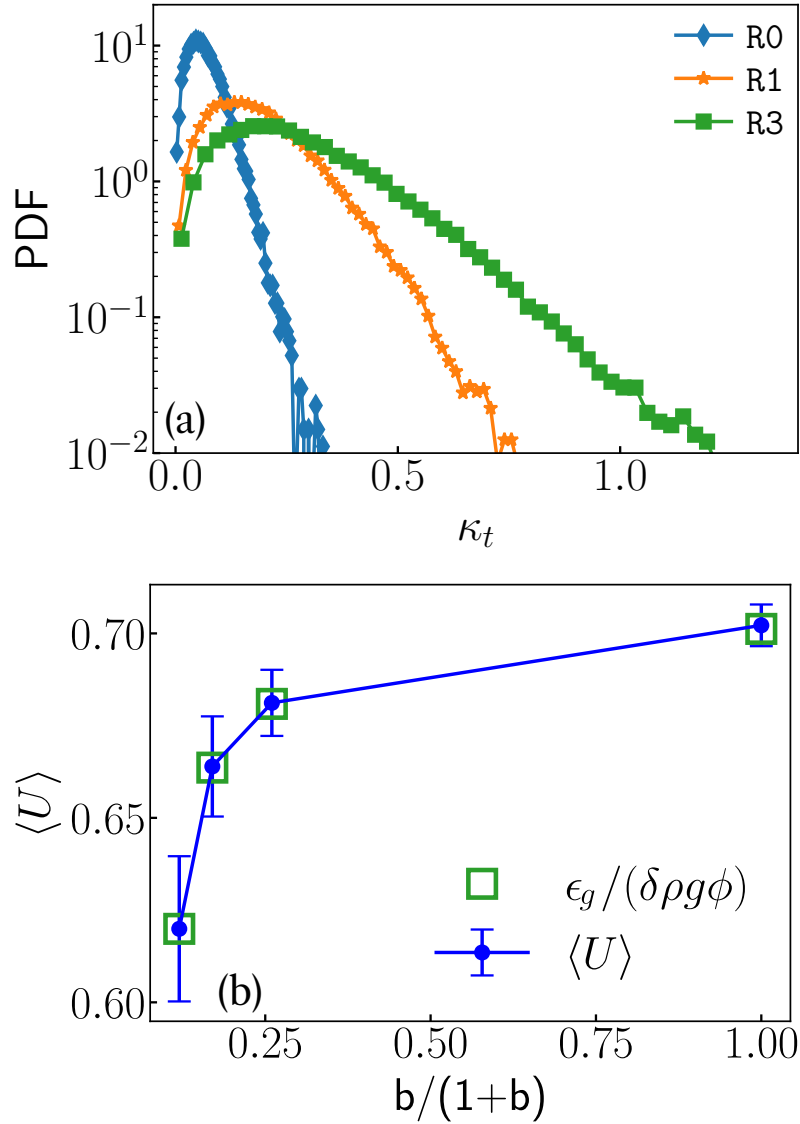


Figure 6.3: (a) The pdf of the curvature $P(\kappa_t)$ for $b = \infty$ (R0), $b = 0.35$ (R1), and $b = 0.13$ (R4). (b) Plot of $\langle U \rangle$ versus b . We find that $\langle U \rangle$ increases with increasing b or decreasing Re_λ . We also show that $\langle U \rangle$ obtained directly from the trajectories and from ϵ_g are in excellent agreement.

The pdf of the bubble velocity fluctuations is nearly Gaussian, and the normalized pdf of the horizontal components of the acceleration $A_h \equiv A_{x,y}$ [Fig. 6.4(a)] is well approximated by a log-normal distribution $P(A_i) = \exp(3\sigma^2/2) \{1 - \text{erf}[(\ln |A_i/\sqrt{3}| + 2\sigma^2)/\sqrt{2}\sigma]\}/4\sqrt{3}$ [21] with $\sigma^2 = 0.27$. Intriguingly, the core of the pdf fits well with the

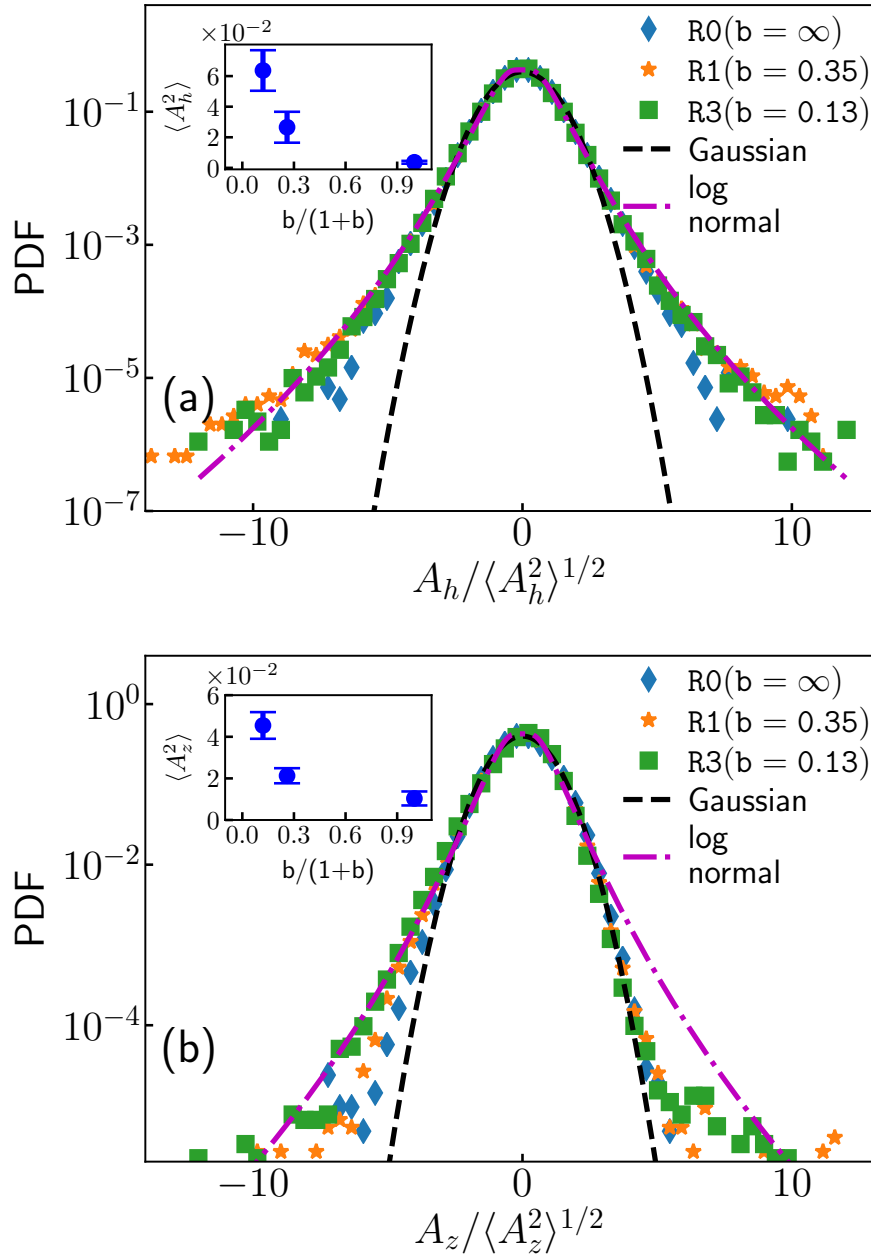


Figure 6.4: The probability distribution function (pdf) of the (a) horizontal A_h and the (b) vertical A_z acceleration. Inset shows the acceleration variance with varying b .

log-normal distribution even in absence of large-scale driving $b = \infty$. As expected, the variance $\langle A_h^2 \rangle$ decreases with increasing b (decreasing Re_λ). For a single buoyant bubble of diameter $d_b \approx 10\eta$ in turbulence at $\text{Re}_\lambda = 32$, Ref. [21] obtained a kurtosis $K \approx 10.3$; for a suspension of droplets with $d = 7\eta$ at $\text{Re}_\lambda = 65$, Ref. [22] obtained a much smaller value for kurtosis $K = 3.94$.

From the log-normal fit to our data, we get $K \equiv \langle A_h^4 \rangle / \langle A_h^2 \rangle^2 \approx 5.3$ which lies within the range of values reported in earlier studies. We find the pdf of vertical component of acceleration A_z is negatively skewed (see Fig. 6.4(b)).

6.3.2 Liquid velocity fluctuations

The pdf of the liquid velocity fluctuations with varying b is show in Fig. 6.5 and 6.6. The case of pseudo-turbulence ($b = \infty$) has already been discussed in the previous chapter-5, and earlier studies [5, 23]

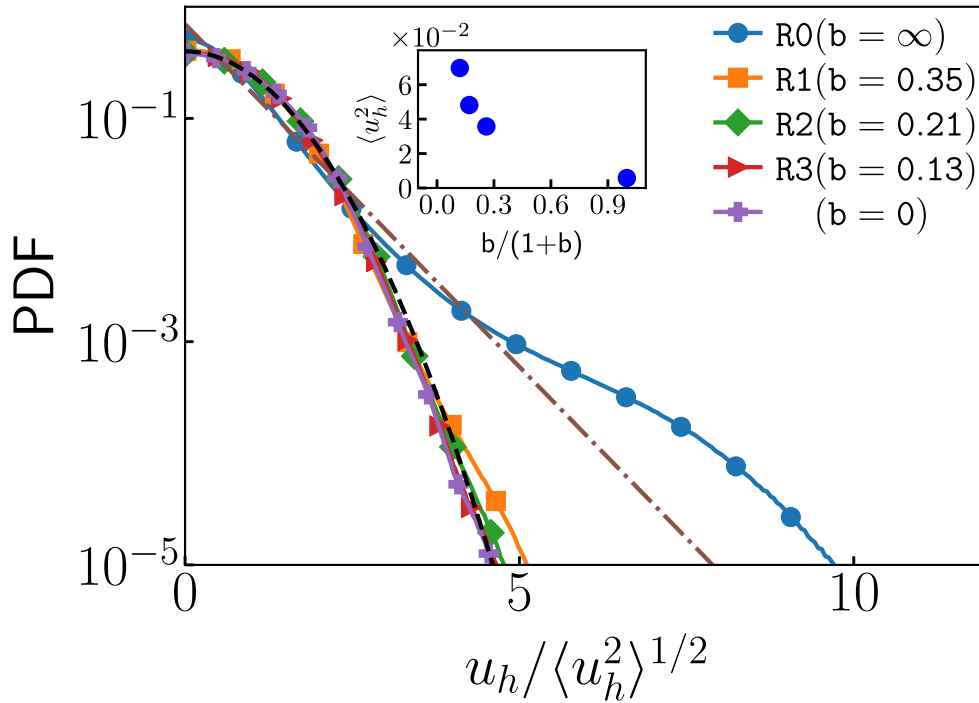


Figure 6.5: The probability distribution of the horizontal component of the liquid velocity fluctuations for different values of b . The black dashed line indicates a Gaussian distribution.

and we obtain a positively skewed distribution for the vertical component of the velocity and exponential tails for the horizontal component. In presence of large scale driving, the turbulent fluctuations overwhelm contribution due to wakes - velocity variance increases with increasing b (see inset to Fig. 6.5 and 6.6) - and the scaled pdf approaches a Gaussian distribution.

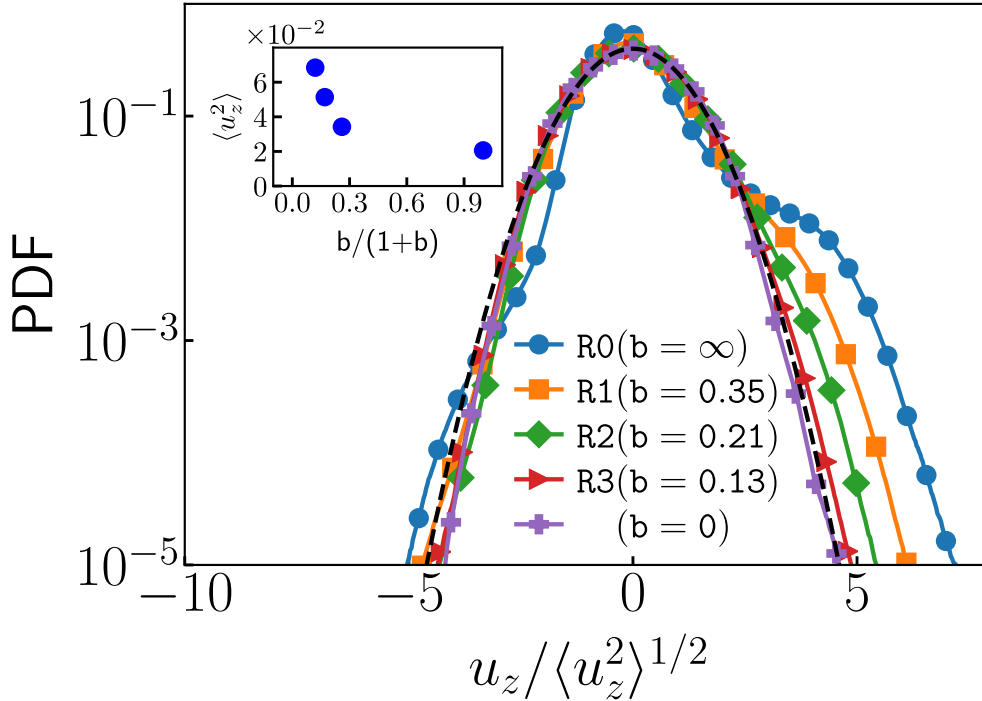


Figure 6.6: The probability distribution of the vertical component of the liquid velocity fluctuations for different values of b . The black dashed line indicates a Gaussian distribution and the brown dashed-dotted line shows the exponential distribution.

6.3.3 Energy spectrum and flux

Earlier DNS studies [5, 24] have only investigated the nature of the energy spectrum in the absence of large scale turbulent forcing. These studies, consistent with experiments, confirm the presence of a power-law scaling that appears because of the balance of net energy production in the wakes with viscous dissipation.

Experiments on buoyancy-driven bubbly flows in the presence of a large scale driving show a Kolmogorov spectrum for frequencies smaller than the bubble frequency and a pseudo-turbulence scaling for higher frequencies [1, 4, 16]. Using the Taylor hypothesis [25] and noting that bubbles inject energy at scales comparable to their diameter, we could argue that the flow resembles homogeneous, isotropic turbulence for wave-numbers $k < k_d$, and

it resembles pseudo-turbulence for $k > k_d$. Here $k_d \equiv 2\pi/d$ is the wave-number corresponding to the bubble diameter. In the following, we study the energy spectrum and the scale-by-scale energy budget to present direct evidence in support of the above arguments

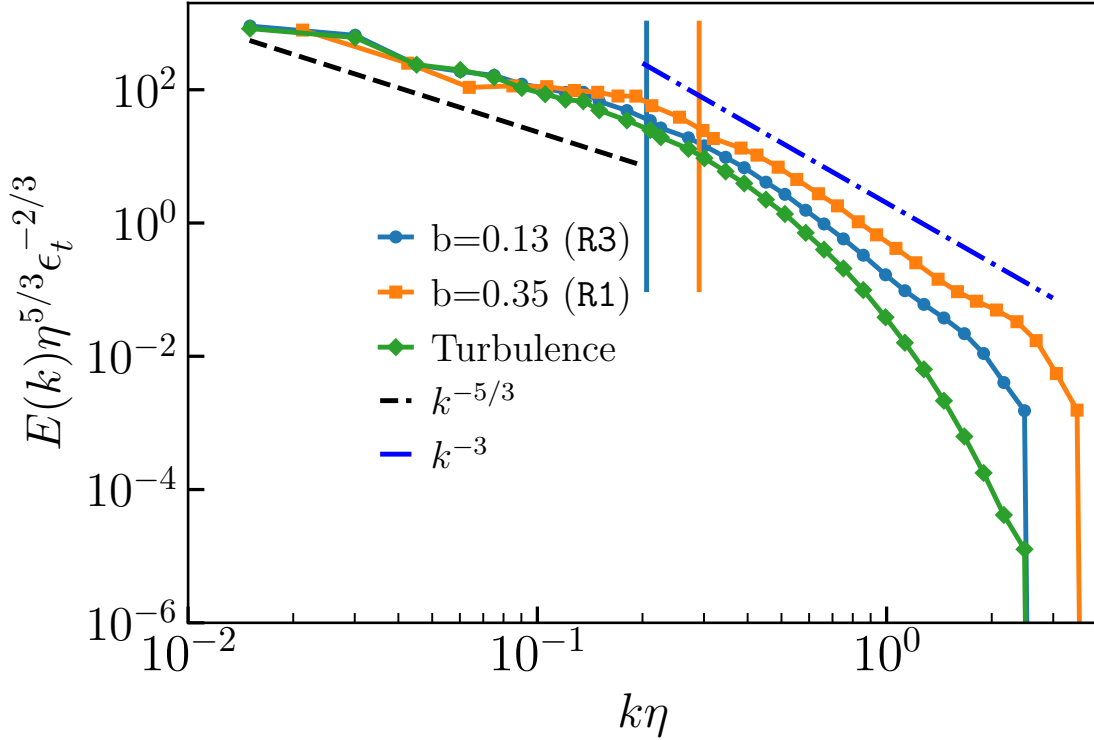


Figure 6.7: Log-log plot of the normalized kinetic energy spectrum $k\eta$ versus $E(k)\eta^{5/3}\epsilon_t^{-2/3}$ for different values of b . The wave-number corresponding to the bubble diameter is marked by green vertical line for $b = 0.35$ and by red vertical line for $b = 0.13$.

In Fig. 6.7, we plot the scaled energy spectrum for different values of b (Re_λ). Consistent with experiments, we observe Kolmogorov scaling $E(k) \sim k^{-5/3}$ for $k < k_d$ and a pseudo-turbulence scaling $E(k) \sim k^{-3}$ for $k > k_d$. Note that on decreasing b (increasing Re_λ), the energy spectrum tends to the homogeneous, isotropic turbulence spectrum ($b = 0$).

Following [5, 8], using 6.1 we get the following steady state, scale-by-scale energy budget equation

$$\Pi_k + \mathcal{F}_k^\sigma = -\mathcal{D}_k + \mathcal{F}_k^g + \mathcal{F}_k^t, \quad (6.3)$$

where the energy flux due to advective nonlinearity $\Pi_k = \langle \mathbf{u}_k^< \cdot (\mathbf{u} \cdot \nabla \mathbf{u})_k^< \rangle$, the cumulative viscous dissipation $\mathcal{D}_k = -\mu \langle |\nabla \mathbf{u}_k^<|^2 \rangle$, the energy transfer due to the surface tension term $\mathcal{F}_k^\sigma = -\langle \mathbf{u}_k^< \cdot (\mathbf{F}^\sigma)_k^< \rangle$, the cumulative energy injected due to buoyancy $\mathcal{F}_k^g = \langle \mathbf{u}_k^< \cdot (\mathbf{F}^g)_k^< \rangle$, the cumulative energy injected due to large scale forcing $\mathcal{F}_k^t = \langle \mathbf{u}_k^< \cdot (\mathbf{F}^t)_k^< \rangle$, and the superscript $<$ denotes a low-pass filtering of eddies of scale $2\pi/k$ [8]. By definition, $\mathcal{F}_k^t = \epsilon_t$ for $k \geq 2$.

In Fig. 6.8(a), we plot the energy budget for $b = \infty$, i.e., buoyancy-driven flow in absence of large scale forcing ($\mathcal{F}_k^t = 0$). The energy is injected by buoyancy \mathcal{F}_k^g at scales $k/k_d \approx 1$. Together advection and surface tension transfer this energy to small scales leading to net energy production $d(\Pi_k + \mathcal{F}_k^\sigma)/dk \sim k^{-1}$ [5]. The balance of total production with viscous dissipation then gives the $E(k) \sim k^{-3}$ spectrum [1, 5].

In the absence of bubbles ($\mathcal{F}_k^g = 0$ and $\mathcal{F}_k^\sigma = 0$) but with large scale forcing $b = 0$ ($\text{Re}_\lambda = 110$), we recover the energy budget for homogeneous, isotropic turbulence (see Fig. 6.8(b) [8, 26, 27]). Energy injected at large scales cascades to small scales in the inertial range while maintaining a constant energy flux $\Pi_k = \epsilon_t$. Finally, the viscosity leads to energy dissipation.

In Fig. 6.8(c-d), we plot the scale-by-scale energy budget when buoyancy injection due to bubbles as well as large-scale driving are present and make the following observations:

1. For $k \ll k_d$, the energy injected by large scale force is transferred to small scales by nonlinear flux. Here we observe the Kolmogorov scaling $E(k) \sim k^{-5/3}$.
2. For $k \gg k_d$, the surface tension contribution dominates the net production and balances viscous dissipation to give the pseudo-turbulence spectrum.
3. The situation is more complicated for k around k_d . Both the nonlinear flux Π_k and the surface tension \mathcal{F}_k^σ contribute towards net production. For $k > k_d$, the nonlinear flux dominates for small b , and the surface tension contribution dominates for large b . The wave-number at which the nonlinear flux becomes smaller than the surface tension contribution

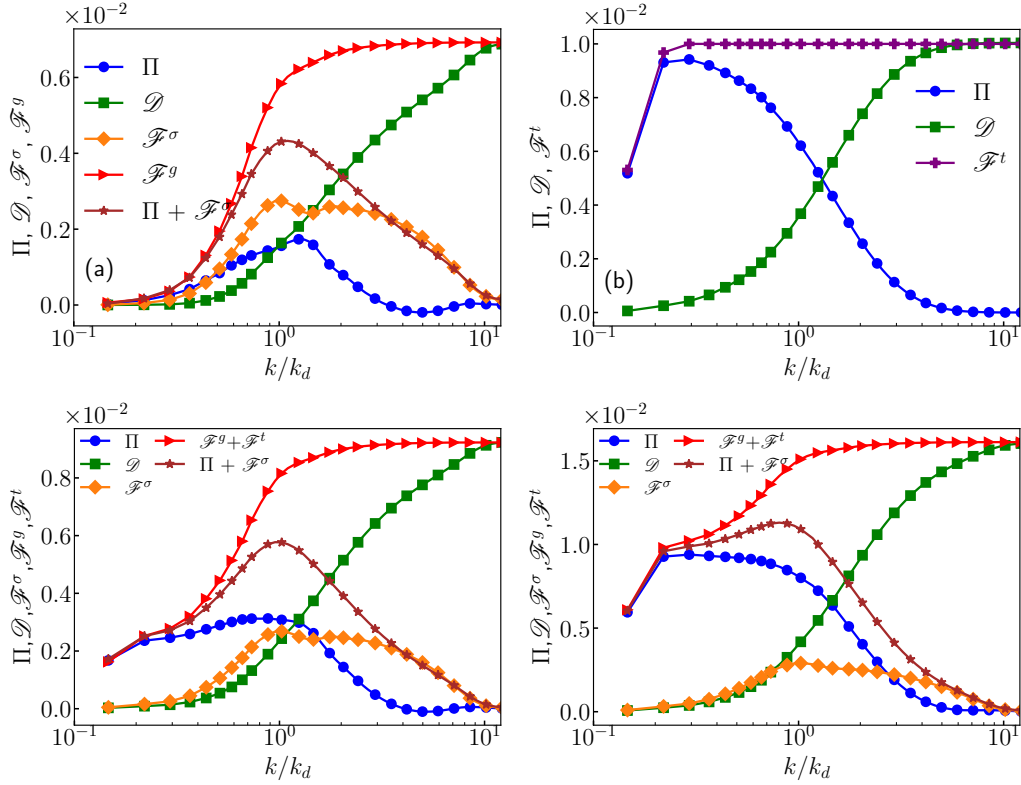


Figure 6.8: Scale-by-scale energy budget: plot of the energy flux Π_k , cumulative viscous dissipation \mathcal{D}_k , the surface tension contribution \mathcal{F}_k^σ , the cumulative energy injected due to buoyancy \mathcal{F}_k^g , and the energy injected due to turbulent forcing \mathcal{F}_k^t for $b = \infty$ (a), $b = 0$ (b), $b = 0.35$ (c), and $b = 0.13$ (d).

marks the transition from the Kolmogorov $E(k) \sim k^{-5/3}$ to the pseudo-turbulence $E(k) \sim k^{-3}$ scaling.

6.4 Conclusion

In this chapter, we presented a dns study of buoyancy-driven bubbly flows in the presence of turbulence. We show that the statistical properties of the flow are consistent with the earlier experiments conducted at similar values of Re_λ , Ga and Φ_V . The energy spectrum shows a Kolmogorov scaling for $k < k_d$ and a pseudo-turbulence scaling for $k > k_d$. We rationalize the scaling observed in the energy spectrum by using a scale-by-scale energy budget analysis. For $k < k_d$, energy flux is the dominant energy transfer mechanism.

The balance of net production with viscous dissipation leads to the pseudo-turbulence scaling for $k > k_d$.

References

- [1] M. Lance and J. Bataille, *J. Fluid Mech.* **222**, 95 (1991).
- [2] R. F. Mudde, *Annu. Rev. Fluid Mech.* **37**, 393 (2005).
- [3] F. Risso, *Annu. Rev. Fluid Mech.* **50**, 25 (2018).
- [4] V. Mathai, D. Lohse, and C. Sun, *Annu. Rev. Fluid Mech.* **11**, 529 (2020).
- [5] V. Pandey, R. Ramadugu, and P. Perlekar, *J. Fluid Mech.* , R6 (2020).
- [6] W. Deckwer, *Bubble Column Reactors* (Wiley, UK, 1992).
- [7] M. Tabib, S. Roy, and J. Joshi, *Chem. Engg. J.* **139**, 589 (2008).
- [8] U. Frisch, *Turbulence the legacy of A.N. Kolmogorov* (Cambridge University Press, Cambridge, 1996).
- [9] S. Pope, *Turbulent Flows* (Cambridge University Press, 2012).
- [10] A. Kolmogorov, *Dokl. Acad. Nauk USSR* **30**, 9 (1941).
- [11] M. Maxey and J. Riley, *Phys. Fluids* **26**, 883 (1983).
- [12] R. Gatignol, *J. Mec. Theor. Appl.* **1**, 143 (1983).
- [13] F. Toschi and E. Bodenschatz, *Ann. Rev. Fluid Mech.* **41**, 375 (2009).
- [14] J. Bec, L. Biferale, G. Boffetta, A. Celani, M. Cencini, A. Lanotte, S. Musacchio, and F. Toschi, *J. Fluid Mech.* **550**, 349 (2006).
- [15] E. Calzavarini, R. Volk, M. Bourgoïn, E. L  v  que, J.-F. Pinton, and F. Toschi, *J. Fluid Mech.* **630**, 179 (2009).
- [16] V. N. Prakash, J. M. Mercado, L. van Wijngaarden, E. Mancilla, Y. Tagawa, D. Lohse, and C. Sun, *J. Fluid Mech.* **791**, 174–190 (2016).
- [17] E. Alm  ras, V. Mathai, D. Lohse, and C. Sun, *J. Fluid Mech.* **825**, 1091 (2017).

- [18] S. Chandrasekhar, *Hydrodynamic and Hydromagnetic Stability*, Dover Books on Physics Series (Dover Publications, 1981).
- [19] G. Tryggvason, B. Bunner, A. Esmaeeli, D. Juric, N. Al-Rawahi, W. Tauber, J. Han, S. Nas, and Y.-J. Jan, *J. Comput. Phys.* **169**, 708 (2001).
- [20] H. Homann, J. Bec, and R. Grauer, *J. Fluid Mech.* **721**, 155 (2013).
- [21] A. Loisy and A. Naso, *Phys. Rev. Fluids* **2**, 014606 (2017).
- [22] A. Chouippe and M. Uhlmann, *Phys. Fluids* **27**, 123301 (2015).
- [23] F. Risso, *J. Fluid Mech.* **809**, 240 (2016).
- [24] I. Roghair, J. M. Mercado, M. V. S. Annaland, H. Kuipers, C. Sun, and D. Lohse, *Int. J. Multiph. Flow* **37**, 1093 (2011).
- [25] U. Frisch, *Turbulence, A Legacy of A. N. Kolmogorov* (Cambridge University Press, 1997).
- [26] R. Pandit, P. Perlekar, and S. S. Ray, *Pramana* **73**, 179 (2009).
- [27] T. Ishihara, T. Gotoh, and Y. Kaneda, *Ann. Rev. Fluid Mech.* **41**, 165 (2009).

Conclusion

In this thesis, we have carried detailed research to address several key problems in the field of multiphase flows using direct numerical simulations. In particular, we have focussed on inertial particles and buoyancy-driven bubbly flows. Below we summarize the significant findings of the study.

We began by exploring the simplest model of the multiphase flow. The dispersed phase consists of millions of spherical particles, of size smaller than η , the Kolmogorov length scale. These particles are inertial, i.e., the density is much larger than the underlying fluid. Such a system can be a model of clouds or dust in the atmosphere [1, 2]. At very low mass-loading (ϕ_m), the particles do not affect the flow [3–5] (one-way coupling). In chapter 3, we studied the statistics of singularities that occur in the particle velocity gradients. These singularities, also known as caustics, have major significance in accelerating raindrops’ formation in clouds [6]. We showed that the rate-of-formation of caustics in the flows of heavy inertial particles, advected by turbulent flows, in two and three dimensions is proportional to $\exp(-C/St)$ in leading order, at small Stokes. Here C is a constant that depends on the details of the flow.

In chapter 4, we considered the case where the mass-loading is significant, and back-reaction from the particle can modify the flow (two-way coupling) [4]. Here we conducted direct numerical simulation (DNS) study of

heavy inertial particles (which we called dust) immersed in a two-dimensional turbulent flow. We studied the clustering phenomenon and the gas phase kinetic energy spectra by varying the Stokes number and the mass-loading parameter. We showed that the dust-dust correlation dimension (d_2) also depends on ϕ_m . In particular, clustering decreases as mass-loading is increased. In the kinetic energy spectra of gas, we showed that a new scaling regime emerges, which we call the dust-dissipative range. The scaling exponent in this regime is not universal but rather a function of both St and ϕ_m . Using a scale-by-scale enstrophy budget analysis, we showed that in the new scaling regime, viscous dissipation of the gas balances the back-reaction from the dust.

When the particle size $d \gg \eta$, the shape and deformations also play a crucial role in the dynamics [2, 7]. Here we studied the statistical properties pseudo-turbulence generated by the buoyancy-driven bubbly flows and turbulence modulation in the presence of bubbles. In chapter 5, we investigated the pseudo-turbulence for At ranging 0.04 – 0.9 and experimentally relevant Re 150 – 450 [8, 9]. We showed the probability distribution function (pdf) of the horizontal and vertical liquid velocity fluctuations is in quantitative agreement with the experiments [9]. The energy spectrum shows the k^{-3} scaling at high Re and becomes steeper on reducing the Re. Using scale-by-scale budget analysis, we showed that, for scales smaller than the bubble diameter, the net transfer because of the surface tension and the kinetic energy flux balances viscous dissipation to give the k^{-3} scaling in the energy spectrum for both low and high At.

In the final chapter 6, we studied the statistical properties of buoyancy-driven bubbly flows in the presence of large scale driving that generates turbulence. The pseudo-turbulent intensity is characterized using the bubble parameter b [10, 11]. Although our bubbles are weakly buoyant, we showed that the flow's statistical properties are consistent with experiments on air bubbles in the water. We showed that the pdf of the horizontal component of the acceleration has a log-normal distribution, and the pdf of the vertical component is negatively skewed. Finally, we investigate the statis-

tics of the liquid velocity fluctuations. Consistent with the experiments [12], we showed that the energy spectrum shows a pseudo-turbulence scaling for length scales smaller than the bubble diameter and a Kolmogorov scaling for scales larger than the bubble diameter.

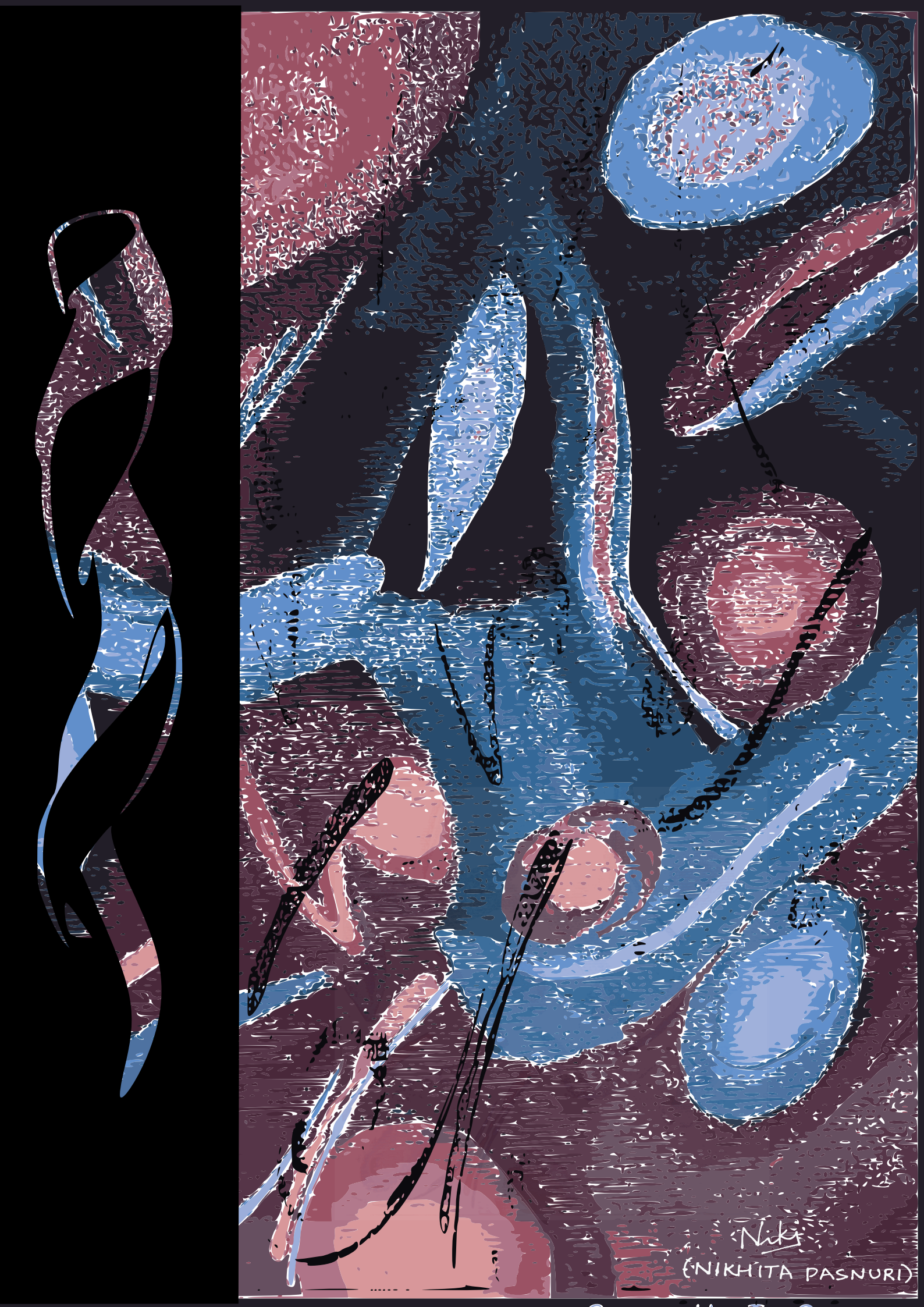
In the future, the research conducted in this thesis can be extended to study the following problems. For the case of caustics formation, one can perform a detailed analysis of the path in the phase-space of $\mathcal{T}r[\mathbb{Z}]$ and $\mathcal{T}r[\mathbb{A}]$ leading caustic formation in three-dimensions. A similar extension is also possible to study the scaling of energy spectra in the three-dimensional particle-laden turbulent flow.

In the case of buoyancy-driven flow, one can investigate the mixing of scalars in pseudo-turbulence. Experiments of Alm eras *et al.* [12] have shown that the dispersion of scalars in buoyancy-driven can be modeled as a normal diffusion process. Albeit the study of Alm eras *et al.* [12] was conducted for high Re gas bubbles in the water. The direct numerical simulations allow for this investigation to be carried at both low and high Re bubbles. A further extension can be made to study the dispersion of bubbles in pseudo-turbulence.

The previous investigation of bubbles' acceleration in an externally driven flow has observed an offset of $\sim g^2$ in the vertical component of acceleration compared to horizontal [13]. In this study, we do not find such a discrepancy. Thus further investigation by varying At would be helpful to understand the acceleration pdf.

References

- [1] R. A. Shaw, *Annual Review of Fluid Mechanics* **35**, 183 (2003).
- [2] S. Balachandar and J. K. Eaton, *Annu. Rev. Fluid Mech.* **42**, 111 (2010).
- [3] S. Sundaram and L. R. Collins, *J. Fluid Mech.* **335**, 75 (1997).
- [4] S. Elgobashi, in *IUTAM Symposium on Computational Approaches to Multiphase Flow* (Springer Netherlands, Dordrecht, 2006) pp. 3–10.
- [5] S. Elghobashi, *Annu. Rev. Fluid Mech.* **51**, 217 (2019).
- [6] G. Falkovich, A. Fouxon, and M. G. Stepanov, *Nature* **419**, 151 (2002).
- [7] M. K. Tripathi, K. C. Sahu, and R. Govindarajan, *Sci. Rep.* **4**, 4771 (2014).
- [8] F. Risso, *Annu. Rev. Fluid Mech.* **50**, 25 (2018).
- [9] G. Riboux, F. Risso, and D. Legendre, *J. Fluid Mech.* **643**, 509 (2010).
- [10] J. Rensen, S. Luther, and D. Lohse, *J. Fluid Mech.* **538**, 153 (2005).
- [11] V. N. Prakash, J. M. Mercado, L. van Wijngaarden, E. Mancilla, Y. Tagawa, D. Lohse, and C. Sun, *J. Fluid Mech.* **791**, 174 (2016).
- [12] E. Alm eras, V. Mathai, D. Lohse, and C. Sun, *J. Fluid Mech.* **825**, 1091 (2017).
- [13] V. N. Prakash, Y. Tagawa, E. Calzavarini, J. M. Mercado, F. Toschi, D. Lohse, and C. Sun, *New J. Phys.* **14**, 105017 (2012).



Nika
(NIKHITA PASNURI)